

ULTRAVIOLET RESONANCE RADIATION
AND
THE STRUCTURE OF THE HELIOSPHERE

by
Doyle Thomas Hall

A Dissertation Submitted to the Faculty of the
DEPARTMENT OF PLANETARY SCIENCES
In Partial Fulfillment of the Requirements
For the Degree of
DOCTOR OF PHILOSOPHY
In the Graduate College
THE UNIVERSITY OF ARIZONA

1 9 9 2

INFORMATION TO USERS

This manuscript has been reproduced from the microfilm master. UMI films the text directly from the original or copy submitted. Thus, some thesis and dissertation copies are in typewriter face, while others may be from any type of computer printer.

The quality of this reproduction is dependent upon the quality of the copy submitted. Broken or indistinct print, colored or poor quality illustrations and photographs, print bleedthrough, substandard margins, and improper alignment can adversely affect reproduction.

In the unlikely event that the author did not send UMI a complete manuscript and there are missing pages, these will be noted. Also, if unauthorized copyright material had to be removed, a note will indicate the deletion.

Oversize materials (e.g., maps, drawings, charts) are reproduced by sectioning the original, beginning at the upper left-hand corner and continuing from left to right in equal sections with small overlaps. Each original is also photographed in one exposure and is included in reduced form at the back of the book.

Photographs included in the original manuscript have been reproduced xerographically in this copy. Higher quality 6" x 9" black and white photographic prints are available for any photographs or illustrations appearing in this copy for an additional charge. Contact UMI directly to order.



University Microfilms International
A Bell & Howell Information Company
300 North Zeeb Road, Ann Arbor, MI 48106-1346 USA
313/761-4700 800/521-0600

Order Number 9307702

**Ultraviolet resonance radiation and the structure of the
heliosphere**

Hall, Doyle Thomas, Ph.D.

The University of Arizona, 1992

U·M·I

300 N. Zeeb Rd.
Ann Arbor, MI 48106

ULTRAVIOLET RESONANCE RADIATION
AND
THE STRUCTURE OF THE HELIOSPHERE

by
Doyle Thomas Hall

A Dissertation Submitted to the Faculty of the
DEPARTMENT OF PLANETARY SCIENCES
In Partial Fulfillment of the Requirements
For the Degree of
DOCTOR OF PHILOSOPHY
In the Graduate College
THE UNIVERSITY OF ARIZONA

1 9 9 2

THE UNIVERSITY OF ARIZONA
GRADUATE COLLEGE

As members of the Final Examination Committee, we certify that we have
read the dissertation prepared by Doyle Thomas Hall

entitled Ultraviolet Resonance Radiation and
the Structure of the Heliosphere

and recommend that it be accepted as fulfilling the dissertation
requirement for the Degree of Doctor of Philosophy

D. E. Schumacher

09/11/92

Date

A. Burrows

9/11/92

Date

Leo J. Kerner

9/11/92

Date

J. R. K. Jones

9/11/92

Date

Heidi Kling

11 Sept. 1992

Date

Final approval and acceptance of this dissertation is contingent upon
the candidate's submission of the final copy of the dissertation to the
Graduate College.

I hereby certify that I have read this dissertation prepared under my
direction and recommend that it be accepted as fulfilling the dissertation
requirement.

D. E. Schumacher
Dissertation Director

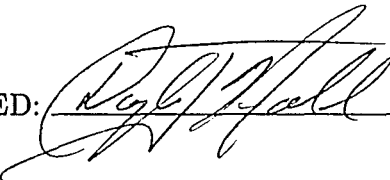
09/11/92
Date

STATEMENT BY AUTHOR

This dissertation has been submitted in partial fulfillment of requirements for an advanced degree at The University of Arizona and is deposited in the University Library to be made available to borrowers under the rules of the Library.

Brief quotations from this dissertation are allowable without special permission, provided that accurate acknowledgment of source is made. Requests for permission for extended quotation from or reproduction of this manuscript in whole or part may be granted by the head of the major department or the Dean of the Graduate College when in his or her judgement the proposed use of the material is in the interests of scholarship. In all other instances, however, permission must be obtained from the author.

SIGNED:

 *D. G. Hall* Sept 21, 1992

ACKNOWLEDGEMENTS

The Voyager UVS experiment succeeded thanks to the skills and expertise of its designers and builders. I would like to collectively thank the entire Voyager project and UVS team for their efforts. Particularly, I am very grateful to Lyle Broadfoot, Terry Forrester, Floyd Herbert, Jay Holberg, Bill Sandel, Don Shemansky and Roger Yelle.

On a personal note, I would like to thank my advisor, Don Shemansky, and his wife, Livia. Amazingly enough, I met Livia first—because, at the time, I was teaching her son to play the drums. Eventually, Don invited me into the UVS lab, and hired me soon thereafter. I have enjoyed working with Don Shemansky through the years. He has a relaxed manner but an incisive intellect.

My fellow Planetary Sciences students and colleagues deserve praise for tolerating me and my antics during the last four years. This is particularly true for the present and past members of Hawthorne House. I appreciate that no one has ever been so irritated with me as to injure me physically, or prosecute me through our civil lawsuit system.

I am grateful to my brothers, sister and late father for supporting me and indulging my eccentricities over the years. I especially thank my brother David, who played a key role in my academic development, and my sister Ann, who, even though five years my younger, has always been more mature than I. Of course the most fundamental thanks that any of us have to offer is to our mothers, who have labored for our births. And so, I thank you Mom.

TABLE OF CONTENTS

LIST OF ILLUSTRATIONS	8
LIST OF TABLES	17
ABSTRACT	19
1 INTRODUCTION	20
1.1 Summary of this Research	21
1.2 The Setting of the Sun and Heliosphere	22
1.2.1 The Galaxy and the Interstellar Medium	22
1.2.2 The Local Interstellar Medium	23
1.2.3 The Very Local Interstellar Medium	24
1.3 The Heliosphere	25
1.3.1 The Solar Wind	26
1.3.2 The Solar Wind Termination Shock	28
1.3.3 The Heliopause	31
1.3.4 The Inner and Outer Heliosphere	32
1.4 Penetration of VLISM H and He into the Heliosphere	33
1.4.1 H-p Charge Exchange	33
1.4.2 Photoionization	34
1.5 Solar H Ly α	35
1.5.1 The Integrated Solar H Ly α Flux	35
1.5.2 The Solar H Ly α Line Shape	37
1.5.3 H Ly α Radiation Pressure	39
1.6 Heliospheric H and He Distributions	40
1.7 Resonantly Scattered Radiation	41
1.7.1 Inner Solar System Observations	42
1.7.2 Outer Solar System Ly α Observations	43
2 THE DISTRIBUTION OF H AND He IN THE HELIOSPHERE	47
2.1 Distribution Theory: The Boltzmann Formulation	48
2.1.1 The Integral Form of the Boltzmann Equation	49
2.1.2 H-p Charge Exchange	50
2.1.3 Solar EUV Photoionization	53
2.2 Distributions Neglecting Production Terms	55
2.2.1 Spherically Symmetric Distributions	56
2.2.2 The Cold Heliospheric Distribution	62

	6
2.2.3 The Hot Heliospheric Distribution	66
2.2.4 “Standard” H and He Hot Distributions	68
2.3 A Multi-Component H Distribution Model	72
2.3.1 The Plasma Model	74
2.3.2 Multi-Component Theory	80
2.3.3 The Splash Component	81
2.3.4 Numerical Algorithm	82
2.3.5 Calculated Results	85
3 HELIOSPHERIC RESONANCE SCATTERING	91
3.1 H and He Atomic Structure and Data	93
3.2 Resonance Line Radiative Transfer	95
3.2.1 The Resonance Scattering Process	95
3.2.2 The Scattering Coefficient and Optical Depth	96
3.2.3 The Absorption Profile	98
3.2.4 Interplanetary Absorption of H Ly α	100
3.2.5 The Redistribution Function	101
3.2.6 The Specific Intensity	104
3.2.7 The Equations of Resonance Radiative Transfer	106
3.2.8 Singly Scattered Photons	108
3.2.9 Multiply Scattered Photons	109
3.2.10 The Optically Thin Approximation	109
3.2.11 Radiation Pressure	110
3.2.12 An Iterative, Finite-Element RT Method	112
3.3 RT in a Uniform Medium with a Point Source	113
3.3.1 The Optically Thin Solution	113
3.3.2 Ivanov’s Solution for Conservative Scattering	114
3.3.3 Numerical Solution of the Uniform Problem	115
3.3.4 Line Intensities in a Uniform Medium	115
3.3.5 Radiation Pressure in a Uniform Medium	117
3.4 A Heliospheric H Ly α RT Model	117
3.4.1 Results for the “Standard” Hot H Distributions	120
3.4.2 Results for the Multi-Component H Distribution	123
4 PIONEER AND VOYAGER H Lyα OBSERVATIONS	127
4.1 Instrument Calibrations: Issues and Limitations	129
4.2 The Pioneer Spacecraft and H Ly α Observations	130
4.2.1 The Pioneer 10 UV Photometer Experiment	131
4.2.2 Pioneer 10 H Ly α Heliospheric Observations	131
4.3 The Voyager Spacecraft and Ultraviolet Spectrographs	134

	7
4.4 Voyager UVS H Ly α Calibration	135
4.5 Voyager Cruise Maneuver H Ly α Observations	137
4.5.1 A Simple Fit to the Cruise Maneuver Data	137
4.5.2 H Ly α Observations on 65° Antisolar Cones	141
4.5.3 Observations from 5 to 10 AU	141
4.5.4 Observations from 15 to 35 AU	143
4.5.5 Voyager 1 Observations Beyond 35 AU	144
4.6 Models of Voyager and Pioneer 10 H Ly α Observations	146
5 VOYAGER MUTUAL OBSERVATIONS	152
5.1 The Mutual Observation Method	153
5.2 Voyager Mutual Observation Measurements	156
5.3 Results and Limitations	156
6 CONCLUSIONS AND FUTURE WORK	160
A VOYAGER UVS DATA AND H Lyα CALIBRATION	163
A.1 UVS Instrument Design and Parameters	163
A.2 UVS Data Reduction	164
A.2.1 Fixed Patterned Noise	164
A.2.2 UVS Dark Counts	165
A.2.3 Internal Instrument Scattering	165
A.3 Voyager UVS H Ly α Sensitivity Calibrations	166
A.3.1 In-Flight Recalibration with Stellar Observations	167
A.3.2 The Degradation at the Voyager 1 Jupiter Encounter	167
A.3.3 Non-Uniform Degradation in the Ly α Region	169
A.3.4 The Relative UVS H Ly α Calibrations	172
A.4 The Absolute Voyager UVS H Ly α Calibrations	175
B VOYAGER CRUISE MANEUVER Lyα OBSERVATIONS	176
B.1 Voyager Spacecraft and Geometry	176
B.2 Cruise Maneuver Sequences	178
B.3 Initial Spacecraft Orientation and Spin Rate	180
B.4 Binning the Spectra	180
B.5 Cruise Maneuver H Ly α Observations	181
REFERENCES	234

LIST OF ILLUSTRATIONS

1.1	Two schematic diagrams of the VLISM and solar wind plasma interaction where the VLISM flow is subsonic (a) and supersonic (b). The solid lines with arrows show streamlines of the solar wind flow. The dashed lines show streamlines of the VLISM flow. The bold lines with no arrows show the SWTS and ISS shock structures. The dotted lines labeled A, B and C show VLISM neutral particle trajectories (Reproduced with permission from Holzer, 1989).	27
1.2	The total solar H Ly α flux at the Earth as determined by correlating to the solar He 10.8 μ m chromospheric feature (Skinner et al., 1988). The flux varies by a factor of ≈ 1.5 over the 11 year solar cycle.	36
1.3	The solar H Ly α line observed at 1 AU (Lemaire et al., 1978). The solar line has a characteristic self reversed shape and a total width of ~ 0.1 nm. The radiation pressure parameter is also shown.	38
1.4	Voyager and Pioneer 10 heliospheric Ly α observations adjusted to constant solar flux and normalized at 15 AU. In the top panel the 65° antisolar cone Voyager 1 and 2 data are shown. The dashed lines show how the power laws $r^{-0.7}$ and $r^{-0.8}$ fall. In the lower panel, the Pioneer 10 observations (collected on 20° anti-Earth cones) are shown with $r^{-1.0}$ and $r^{-1.1}$ power laws.	45
2.1	The normalized density and temperature of a neutral gas in a $1/r$ potential with no ionization. The density relative to the value at infinite distance is plotted as the solid curve and the normalized temperature as the dashed curve. For attractive potentials ($\lambda > 0$) the densities and temperatures are enhanced near the force center. Radiation pressure can create repulsive potentials ($\lambda < 0$), where the densities are diminished but the system is isothermal.	57
2.2	The normalized densities and radial velocities of a gas in a force-free system with a central ionization source. The density relative to the value at infinite distance is plotted as the solid line. As the ionization parameter, $A_i = (\beta_e r_e^2)/(rv_{th,\infty})$, is increased the density decreases. The radial speed relative to the thermal speed at infinity, $v_r/v_{th,\infty}$ is plotted as the dashed line.	60

- 2.3 Representative trajectories in the Heliospheric cold distribution. Here four trajectories are shown as dotted lines defining the cold distribution at three points **A**, **B** and **C**. The density of the penetrating neutrals at the points **A** and **B** is given by the sum of the densities of particles travelling along each of the two trajectories. Point **A** lies in the upstream region, implying that particles on one of the two trajectories have passed their perihelia, are outbound and have suffered more ionization loss than the inbound stream. Point **C** is located on the downstream axis where an infinite number of cold trajectories intersect and whose velocities lie on the illustrated cone. This effect leads to a singularity on the downstream axis where the cold density diverges. 64
- 2.4 The solar minimum standard heliospheric H hot distribution. The integrated H densities relative to the value at infinity are plotted for several axial angles. The upstream ($\theta = 0^\circ$), sidestream ($\theta = 90^\circ$) and downstream ($\theta = 180^\circ$) distributions are marked with squares, triangles and circles respectively. Intermediate values of the axial angle $\theta = 30, 60, 120$ and 150° are shown as the intervening dashed lines. The parameters used for this distribution are: $v_\infty = 20 \text{ km s}^{-1}$, $T_\infty = 10^4 \text{ K}$, $\beta_e = 5 \times 10^{-7} \text{ s}^{-1}$, and $\mu_\odot = 0.75$ 69
- 2.5 The solar maximum standard heliospheric H hot distribution. The integrated H densities relative to the value at infinity are plotted for several axial angles in the same format as described in the previous figure. The parameters used for this distribution are: $v_\infty = 20 \text{ km s}^{-1}$, $T_\infty = 10^4 \text{ K}$, $\beta_e = 10 \times 10^{-7} \text{ s}^{-1}$, and $\mu_\odot = 1.20$ 70
- 2.6 The standard heliospheric He hot distribution. The integrated He densities relative to the value at infinity are plotted for several axial angles in the same format as described in the two previous figures. The parameters are: $v_\infty = 20 \text{ km s}^{-1}$, $T_\infty = 10^4 \text{ K}$, $\beta_e = 7.5 \times 10^{-8} \text{ s}^{-1}$, and $\mu_\odot = 0.0$ 71
- 2.7 Heliopause shapes in the Suess and Nerney (1990, 1991) model for various values of ϵ_s . The shape of the heliopause is shown for $\epsilon_s = 0.05, 0.1, 0.2, 0.5, 1, 2$. The largest values of ϵ_s correspond to the smallest heliopause surfaces. For the heliosphere, $\epsilon_s \approx 0.1$ 77
- 2.8 Plasma streamlines for the Suess and Nerney (1990, 1991) model for $\epsilon_s = 0.1$. The spherical SWTS is illustrated as the dotted line. Plasma streamlines are shown as the dashed lines. The heliopause is shown as the dark line separating the VLISM streamlines from the subsonic solar wind streamlines. 78

- 2.9 Densities, temperatures, and velocities for component 1 (the thermal component) of the heliospheric H distribution using solar and VLISM parameters: $R_s = 70 \text{ AU}$, $\mu_\odot = 0.80$, $v_{sw} = 400 \text{ km s}^{-1}$, $n_{pe} = 8 \text{ cm}^{-3}$, $n_{p\infty} = 0.003 \text{ cm}^{-3}$, $n_{H\infty} = 0.1 \text{ cm}^{-3}$, $T_\infty = 10^4 \text{ K}$, and $v_\infty = 20 \text{ km s}^{-1}$. Values for lines of constant axial angle, θ , are shown as a function of heliocentric radius. The symbols correspond to the following axial angles: solid squares (0° -upstream), stars (30°), open circles (60°), triangles (90° -sidestream), asterices (120°), open squares (150°), and solid circles (180° -downstream). 86
- 2.10 Densities, temperatures, and velocities calculated for component 2 (the suprathermal component) of the heliospheric H distribution. The same solar and VLISM parameters are used as in the previous figure (as are the plotted symbols). Comparing this to the previous figure reveals that thermal densities are much larger than suprathermal densities everywhere except for $r < 2 \text{ AU}$ and in the downstream direction. At 10 AU downstream, $n_2/n_1 \approx 0.1$; at 2 AU downstream $n_2/n_1 \approx 1$. . . 87
- 2.11 Upstream and downstream densities for H components 1 and 2 obtained by varying R_s . The other solar and VLISM parameters are: $\mu_\odot = 0.80$, $v_{sw} = 400 \text{ km s}^{-1}$, $n_{pe} = 6 \text{ cm}^{-3}$, $n_{p\infty} = 0.003 \text{ cm}^{-3}$, $n_{H\infty} = 0.1 \text{ cm}^{-3}$, $T_\infty = 10^4 \text{ K}$, and $v_\infty = 20 \text{ km s}^{-1}$. The thermal component is plotted with solid lines and the suprathermal component with dotted lines. The symbols correspond to the following SWTS radii in AU: solid squares (50), asterices (75), solid circles (100), triangles (150), open squares (200). 89
- 2.12 Upstream and downstream densities for the thermal and suprathermal components of the heliospheric H distribution obtained by varying the solar wind density, n_{pe} . The other solar and VLISM parameters are: $R_s = 70 \text{ AU}$, $\mu_\odot = 0.80$, $v_{sw} = 400 \text{ km s}^{-1}$, $n_{p\infty} = 0.003 \text{ cm}^{-3}$, $n_{H\infty} = 0.1 \text{ cm}^{-3}$, $T_\infty = 10^4 \text{ K}$, and $v_\infty = 20 \text{ km s}^{-1}$. Component 1 is plotted with solid lines and component 2 dotted lines. The symbols correspond to the following n_{pe} in cm^{-3} : solid squares (4), asterices (6), solid circles (8), triangles (10), open squares (12). Inside the SWTS, the densities of both components vary strongly with n_{pe} 90
- 3.1 Voyager 2 UVS spectrum observed in the direction of the North Galactic Pole. The H Lyman series lines α (off scale), β and γ and the He 58.4 nm lines are produced by resonance scattering in the heliosphere. The total exposure duration is $\sim 1.5 \times 10^6$ seconds. (Reproduced with permission from Holberg, 1986.) 92

- 3.2 Schematic geometry of a resonance scattering interaction. The incident photon has direction and frequency $(\hat{\mathbf{n}}', \nu')$. The new photon has $(\hat{\mathbf{n}}, \nu)$. The two directions are separated by the scattering angle, θ_s 95
- 3.3 H Ly α line center optical depths between the Earth and the outer planets for the “standard” solar minimum and maximum H distributions shown in Figures 2.5 and 2.6. Shown are line center optical depths between Earth and Jupiter (panel a), Saturn (b), Uranus (c) and Neptune (d) (the solar maximum absorption is the lower curve in all cases). Cyclical variations associated with the orbital periods of both the Earth and the source planet are due to the Doppler shift associated with the net motion of the interplanetary H gas. All of these curves assume a VLISM H density of 0.10 cm^{-3} but optical depth scales linearly with this parameter. 99
- 3.4 The dimensionless emission rate for a uniform, motionless, conservative, isotropic and CFR scattering medium as a function of line center optical depth from a point source. The optically thin rate, τ_o^{-2} , is shown as the dashed line. The dash-dot line is the singly scattered emission rate, which falls rapidly because of attenuation of the solar source flux. The dotted line is the total emission rate calculated using an iterative, finite-element computer code. As a boundary condition, the solution is forced to match the Ivanov (1973) large- τ_o asymptote (shown as the solid line) for $\tau_o > 10$ 116
- 3.5 Line intensities looking radially outward, relative to the optically thin approximation. The multiply scattered intensities are within $\approx 10\%$ of the optically thin approximation for τ_o less than about 2. At larger τ_o , the ratio falls as τ_o^{-1} . Since optically thin intensities already fall as τ_o^{-1} , this implies that for outside a few line center optical depths, intensities measured in the antisolar direction in a uniform medium should fall as τ_o^{-2} , or alternatively as r^{-2} 118
- 3.6 The ratio of the radiation pressure parameter to the optically thin approximation. The solid line shows the ratio for the total radiation force, while the dotted and dashed line show the singly and multiply scattered values respectively. The total ratio is reduced by about 20% at $\tau_o \approx 1$. At $\tau_o \approx 10$, the reduction is $\approx 70\%$. This effect could be significant for the heliospheric H distribution, where one line center optical depth corresponds to a path of order 10 AU. 119

- 3.7 The volume emission rates and antisolar line intensities for $\text{Ly}\alpha$ scattering in the standard solar minimum hot H distribution shown in Figure 2.4. The symbols correspond to the following values of θ : solid squares (0°), stars (30°), open circles (60°), triangles (90°), asterices (120°), open squares (150°), solid circles (180°). In the top panel, the emission rates are shown as the solid lines. The dashed lines show the optically thin approximation. The lower panel shows the antisolar intensities, which tend to remain constant within the ionization cavity. 121
- 3.8 The total volume emission rates and antisolar line intensities for $\text{Ly}\alpha$ scattering in the standard solar maximum hot H distribution shown in Figure 2.5. The symbol and line format is the same as in the previous figure. Because the ionization cavity is larger and more depleted in this distribution than the previous case, the antisolar line intensities tend to remain constant further out from the Sun. 122
- 3.9 The total volume emission rates and antisolar line intensities for $\text{Ly}\alpha$ scattering in the multi-component heliospheric H distribution shown in Figures 2.9 and 2.10. The symbol format is the same as in the previous 2 figures. In the upper panel the solid and dashed lines correspond to the thermal and suprathermal H gases respectively. The general pattern of antisolar intensities is similar to that of the hot distribution. The critical difference is that a fraction of the $\text{Ly}\alpha$ intensity here is caused by scattering from the suprathermal component of the H distribution. 124
- 3.10 The H $\text{Ly}\alpha$ line shapes calculated in the upstream, sidestream and downstream directions in the multi-component heliospheric H distribution shown in Figures 2.10 and 2.11. The line shapes looking radially outward from 1 AU are shown for observation points lying upstream (squares), sidestream (triangles) and downstream (circles). The two H components combined produce line shapes that have two distinct parts. The central, thinner parts are due to scattering from component 1 of the H distribution. The wider parts are from the suprathermal component 2. In the downstream region, component 2 comprises a larger fraction of the total H density than in the upstream region; so the wide part of the line in the downstream direction makes up a larger part of the total line intensity. This effect could provide a means of estimating the density of component 2, which is sensitive to the distance to the solar wind termination shock. 125

- 4.1 The trajectories of the Voyager 1, Voyager 2, and Pioneer 10 spacecraft projected onto the ecliptic plane. For scale, the dotted circle represents the orbit of Jupiter. Both Voyagers are heading generally upstream, into the VLISM flow direction, illustrated as the dashed line. The Pioneer 10 trajectory lies nearly in the ecliptic plane directed downstream. Since its encounter with Saturn (≈ 10 AU), Voyager 1 has travelled northward of the ecliptic plane. Voyager 2 was redirected southward at Neptune (≈ 30 AU). The cones illustrate the directions the UV instruments aboard each spacecraft obtained Ly α observations. Pioneer 10 collects data averaged on a cone 20° from the anti-Earth direction. At each point marked on the Voyager trajectories, the spacecraft performed Cruise Maneuver observing sequences which are combined to produce averages over the schematically illustrated 65° antisolar cones. 128
- 4.2 Pioneer 10 heliospheric H Ly α observations adjusted to constant solar Ly α flux. The absolute intensity scale is determined by the calibration factors reported in Wu et al. (1981). The solar Ly α flux variation has been removed from the data via multiplication by the factor $(3 \times 10^{11} \text{ photons cm}^{-2} \text{ s}^{-1})/\pi\mathcal{F}_\odot$, where $\pi\mathcal{F}_\odot$ is the estimated sub-spacecraft, monthly averaged solar Ly α flux. Between 5 and 15 AU, the intensities decrease relatively slowly as a function of heliocentric distance. Beyond 15 AU, the data fall off as $r^{(-1.07 \pm 0.1)}$ 132
- 4.3 A scatter diagram showing the overall quality of a simple fit to the Voyager Cruise Maneuver cone-average intensities obtained between 15 and 35 AU. Despite the relative simplicity and phenomenological nature of the expansion, most of the data are reproduced to within error. 138
- 4.4 The best fit function $J(\Theta)$ derived from the combined Voyager 1 and 2 Cruise Maneuver Ly α data obtained between 15 and 35 AU. In an optically thin uniform system $J(\Theta) = \Theta/\sin \Theta$, shown as the dotted line. The best fit to the observations (points with error bars) indicates that the observed intensities increase less quickly than the optically thin result as the Θ approaches 180° . This probably is due to a combination of the H ionization cavity and radiative transfer effects. 140

- 4.5 Voyager heliospheric 65° $\text{Ly}\alpha$ cone-average observations adjusted to constant solar $\text{Ly}\alpha$ flux. The solar $\text{Ly}\alpha$ flux variation has been removed from the data via multiplication by the factor $(3 \times 10^{11} \text{ photons cm}^{-2} \text{ s}^{-1})/\pi\mathcal{F}_\odot$, where $\pi\mathcal{F}_\odot$ is a 6-day average of the estimated sub-spacecraft solar $\text{Ly}\alpha$ flux. Between 5 and 10 AU the Voyager 1 intensities are consistently lower than for Voyager 2. From 15 to 35 AU the intensities observed by each spacecraft are the same to within cross calibration uncertainty. The Voyager 1 intensities beyond ≈ 30 AU show a flat signature. 142
- 4.6 Voyager and Pioneer 10 heliospheric $\text{Ly}\alpha$ observations adjusted to constant solar flux and normalized at 15 AU plotted with solar minimum RT simulations. In the top panels the 65° Voyager 1 and 2 data are shown as circles and squares respectively. The solid and dotted lines show the solar minimum Voyager 1 and 2 simulations respectively. In the lower panels, the Pioneer 10 observations and models are shown. Five models are shown for each spacecraft, using the VLISM densities 0.04, 0.06, 0.08, 0.10, 0.12 and 0.14 cm^{-3} , from top to bottom in all cases. 147
- 4.7 Voyager and Pioneer 10 heliospheric $\text{Ly}\alpha$ observations adjusted to constant solar flux and normalized at 15 AU plotted with solar maximum RT simulations. See the previous figure for a description. 148
- 4.8 Voyager and Pioneer 10 heliospheric $\text{Ly}\alpha$ observations adjusted to constant solar flux and normalized at 15 AU plotted with RT simulations using the hot heliospheric distribution and including an additive upstream $\text{Ly}\alpha$ background. The line and symbol formats are the same as in the previous two figures. The parameters for the hot distribution are $v_\infty = 20 \text{ km s}^{-1}$, $T_\infty = 10^4 \text{ K}$, $\beta_e = 4 \times 10^{-7} \text{ s}^{-1}$, and $\mu_\odot = 0.75$. The upstream background is equal to 25% of the intensity observed at 15 AU. 149
- 5.1 An illustration of the Voyager Mutual Observation $\text{Ly}\alpha$ measurements. The $\text{Ly}\alpha$ line intensity measured by Voyager 1 when its UVS is pointed inward towards Voyager 2 is defined as A_i . The Voyager 1 intensity measured in the opposite direction is A_o . The Voyager 2 intensities B_i and B_o are defined similarly. The region between the spacecraft is filled with H gas that both scatters and absorbs $\text{Ly}\alpha$ photons. The goal of these measurements is to estimate the interspacecraft H density. 154

- 5.2 The interspacecraft H density determined from the Voyager Mutual Observations as a function of the Voyager 1 UVS Ly α sensitivity calibration factor. The Voyager 1 calibration factor is 218 ± 33 , where the error refers to the cross calibration uncertainty between the two UVS instruments. The densities calculated from measurements performed in 1990 and 1992 are shown as the solid and dashed lines respectively. The densities derived from the VMO observations are strong functions of the UVS Ly α cross calibration. The 15% cross calibration error dominates the uncertainty of the VMO determinations. 158
- A.1 The Voyager 1 UVS H Ly α line shape before and after Jupiter encounter. The solid and dotted lines show the Ly α line as detected in long duration sky background observation before and after Jupiter encounter. The line core and scattering wings are clearly visible. The histograms with the error bars show the spectra multiplied by a factor of 15 and illustrates the detailed shapes of the scattering wings. The cores of the lines (channels 70–78) are normalized to a count rate of 2 counts/sec. The difference in the spectral shapes in these core regions indicates that sensitivity changes that occurred at or near Jupiter encounter were non-uniform across the Ly α channels. The change in the ratio of the count rates in the scattering wings relative to the core indicates that the Ly α channels suffered a different level of degradation than adjacent channels. The channels near the Ly β line at 102.5 nm are not included, and the contribution from the scattering wings of the Ly β line is negligible. 171
- B.1 A drawing of the Voyager spacecraft indicating the location of various components. The UVS is mounted on the scan platform at the end of the science boom. The orientation of the roll, yaw and pitch axes are shown at the lower right. The High-Gain Antenna lies along the roll axis. (Reproduced with permission from Holberg and Watkins, 1992.) 177
- B.2 The pattern of UVS observations during two Voyager 2 cruise maneuvers. Each dot represents a UVS spectrum obtained at a particular Right Ascension and Declination (Earth Mean Equatorial, 1950). The pattern of stars detected in the Cruise Maneuver Observations allows the spacecraft spin rate and orientation to be determined. The spectra not polluted by starlight may then be compiled into maps of the sky in the heliospheric emissions. 179

B.3	The geometry of the coordinate system used to bin the Voyager Cruise Maneuver H Ly α observations. Panel a shows the EMec50 coordinate system with the spacecraft at heliocentric radius R , and ecliptic longitude and latitude λ and β . Panel b shows how the angles Θ and Ψ are related to the local unit vectors \hat{r} , $\hat{\lambda}$ and $\hat{\beta}$. The Cruise Maneuver Ly α data are tabulated in the angles Θ and Ψ	182
-----	---	-----

LIST OF TABLES

3.1	Heliospheric Resonance Line Atomic Data.	94
5.1	H Ly α Voyager Mutual Observations.	157
B.1	Voyager 1 Cruise Maneuver: 1979 Day 288	184
B.2	Voyager 1 Cruise Maneuver: 1980 Day 51	185
B.3	Voyager 1 Cruise Maneuver: 1980 Day 168	186
B.4	Voyager 1 Cruise Maneuver: 1981 Day 41	187
B.5	Voyager 1 Cruise Maneuver: 1981 Day 134	188
B.6	Voyager 1 Cruise Maneuver: 1981 Day 320	189
B.7	Voyager 1 Cruise Maneuver: 1982 Day 90	190
B.8	Voyager 1 Cruise Maneuver: 1982 Day 300	191
B.9	Voyager 1 Cruise Maneuver: 1983 Day 117	192
B.10	Voyager 1 Cruise Maneuver: 1983 Day 306	193
B.11	Voyager 1 Cruise Maneuver: 1984 Day 11	194
B.12	Voyager 1 Cruise Maneuver: 1984 Day 116	195
B.13	Voyager 1 Cruise Maneuver: 1984 Day 193	196
B.14	Voyager 1 Cruise Maneuver: 1985 Day 59	197
B.15	Voyager 1 Cruise Maneuver: 1985 Day 283	198
B.16	Voyager 1 Cruise Maneuver: 1986 Day 93	199
B.17	Voyager 1 Cruise Maneuver: 1986 Day 246	200
B.18	Voyager 1 Cruise Maneuver: 1986 Day 309	201
B.19	Voyager 1 Cruise Maneuver: 1987 Day 16	202
B.20	Voyager 1 Cruise Maneuver: 1987 Day 246	203
B.21	Voyager 1 Cruise Maneuver: 1988 Day 111	204
B.22	Voyager 1 Cruise Maneuver: 1988 Day 230	205
B.23	Voyager 1 Cruise Maneuver: 1988 Day 351	206
B.24	Voyager 1 Cruise Maneuver: 1989 Day 104	207
B.25	Voyager 1 Cruise Maneuver: 1989 Day 279	208
B.26	Voyager 2 Cruise Maneuver: 1980 Day 24	209
B.27	Voyager 2 Cruise Maneuver: 1980 Day 136	210
B.28	Voyager 2 Cruise Maneuver: 1980 Day 192	211
B.29	Voyager 2 Cruise Maneuver: 1980 Day 351	212
B.30	Voyager 2 Cruise Maneuver: 1981 Day 77	213
B.31	Voyager 2 Cruise Maneuver: 1981 Day 148	214
B.32	Voyager 2 Cruise Maneuver: 1981 Day 302	215
B.33	Voyager 2 Cruise Maneuver: 1982 Day 293	216

B.34 Voyager 2 Cruise Maneuver: 1983 Day 132	217
B.35 Voyager 2 Cruise Maneuver: 1983 Day 313	218
B.36 Voyager 2 Cruise Maneuver: 1984 Day 145	219
B.37 Voyager 2 Cruise Maneuver: 1984 Day 325	220
B.38 Voyager 2 Cruise Maneuver: 1985 Day 150	221
B.39 Voyager 2 Cruise Maneuver: 1986 Day 113	222
B.40 Voyager 2 Cruise Maneuver: 1986 Day 273	223
B.41 Voyager 2 Cruise Maneuver: 1986 Day 339	224
B.42 Voyager 2 Cruise Maneuver: 1987 Day 42	225
B.43 Voyager 2 Cruise Maneuver: 1987 Day 133	226
B.44 Voyager 2 Cruise Maneuver: 1987 Day 280	227
B.45 Voyager 2 Cruise Maneuver: 1988 Day 15	228
B.46 Voyager 2 Cruise Maneuver: 1988 Day 88	229
B.47 Voyager 2 Cruise Maneuver: 1988 Day 246	230
B.48 Voyager 2 Cruise Maneuver: 1988 Day 300	231
B.49 Voyager 2 Cruise Maneuver: 1990 Day 73	232
B.50 Voyager 2 Cruise Maneuver: 1990 Day 143	233

ABSTRACT

The solar system and heliosphere are embedded in a partially ionized medium flowing past the Sun at about 22 km s^{-1} . The Voyager and Pioneer 10 spacecraft are travelling upstream and downstream respectively, detecting $\text{Ly}\alpha$ radiation resonantly scattered from heliospheric hydrogen. None of the probes has encountered the solar wind termination shock, where the supersonic solar wind is believed to decelerate to subsonic speeds. Penetration of H atoms from the local interstellar flow is the principal source of heliospheric H. Solar gravitation, radiation pressure, and ionization processes largely control the H distribution. However, the presence of the solar wind termination shock is predicted to have two additional effects. H-p charge exchange reactions occurring in the hot, post-shock solar wind plasma should both reduce the number of penetrating H atoms and create a population of suprathermal H atoms. Therefore, heliospheric $\text{Ly}\alpha$ emission lines should be composed of narrow and wide components, which should be diagnostic of outer heliospheric structure. Previously unpublished Voyager Cruise Maneuver observations obtained between 15 and 40 AU reveal that upstream $\text{Ly}\alpha$ intensities fall as $r^{(-0.75 \pm 0.05)}$. Beyond 15 AU downstream, Pioneer 10 $\text{Ly}\alpha$ falls as $r^{(-1.07 \pm 0.1)}$. These trends cannot be simultaneously reproduced using models which do not include the termination shock. The Voyager data suggest an additional source of $\text{Ly}\alpha$ in the upstream region beyond 40 AU. This may be due to suprathermal H gas and/or gradients in the H density, both predicted to be associated with the termination shock. A new method of estimating the heliospheric H density between the two Voyager spacecraft is introduced. The results are ambiguous and suffer due to the uncertainty in relative instrumental $\text{Ly}\alpha$ sensitivities.

CHAPTER 1

INTRODUCTION

Currently four spacecraft, Voyager 1 and 2 and Pioneer 10 and 11, are venturing into the interstellar space beyond the solar system. As of this writing they have not passed outside the heliosphere, the region of space appreciably influenced by the Sun. For instance, each is still detecting the solar wind, a supersonic plasma flow continuously streaming outward from the Sun. The Sun and heliosphere lie within the very local interstellar medium (VLISM), a tenuous, partially ionized gas flowing past the solar system at a speed of about 22 km s^{-1} . It is generally believed that, as it expands into the VLISM, the solar wind eventually decelerates via a hydromagnetic shock—the solar wind termination shock (SWTS).

As the Voyager and Pioneer spacecraft head outward, the astrophysical community eagerly anticipates an encounter with the solar wind termination shock. However, even if such an encounter should occur, it is possible that it will be missed due to spotty Deep Space Network coverage or inevitable spacecraft failures. Therefore it is prudent to try to determine as much as is possible about heliospheric structure from the data already in hand. This allows the community to plan for the possibility of such an encounter. But more importantly, it provides fundamental information about the local interstellar environment.

The Pioneer and Voyager spacecraft are equipped with various instruments including magnetometers, high and low energy charged particle detectors, plasma wave detectors and ultraviolet (UV) radiation detectors. Many of these measure quantities associated with the immediate environment of the spacecraft. The magnetometers make such *in situ* measurements of magnetic fields. Other instruments measure particles or radiation originating from the outer heliosphere or beyond. Several of the

latter group may be able to sense outer heliospheric structures from afar. The observations of particular interest here are from the UV instruments aboard the Voyager and Pioneer 10 spacecraft. These detect photons resonantly scattered from neutral atomic hydrogen (H) and helium (He) in the heliosphere. By far, the strongest line is H Ly α with wavelength 121.6 nm.

1.1 Summary of this Research

Heliospheric Ly α observations conducted beyond 5 AU from the Sun are the subject of this dissertation. Two empirical studies are undertaken. First, the patterns of Ly α detected by the Voyager and Pioneer 10 spacecraft are compared. The Voyager data are from the Cruise Maneuver observing sequences, many of which have not been previously reduced or published. The combined Voyager and Pioneer data suggest that the distribution of heliospheric hydrogen is not adequately described unless the effects of the solar wind termination shock and associated outer heliospheric structures are considered. Second, an attempt to measure the heliospheric H density in the region between the two Voyager spacecraft yields ambiguous results and is limited by the poor instrument sensitivity calibration. The method is called the Voyager Mutual Observations and consists of measuring the Ly α intensities along the line connecting the spacecraft. The results are ambiguous probably because the spacecraft are separated by too many optical depths.

In Chapters 2 and 3, theories and models of the distribution of H and He and the radiative transfer of the associated resonance lines are developed. Chapter 4 contains descriptions and preliminary analyses of the Pioneer 10 and Voyager Ly α observations collected beyond 5 AU. The Voyager Mutual Observations are presented in Chapter 5. Appendix A describes the Voyager UVS instruments and data reduction procedure. A description and tabulation of the Voyager Cruise Maneuver heliospheric Ly α observations obtained between 5 and 40 AU are given in Appendix B.

1.2 The Setting of the Sun and Heliosphere

As pointed out by Thomas (1978) neutral interstellar gas is conveniently organized into structures of the following sizes in parsecs ($1 \text{ parsec} = 1 \text{ pc} \approx 3 \times 10^{18} \text{ cm}$): The Galaxy (10^4), large interstellar clouds and spiral arms (10^2 – 10^3), small clouds (10^0) and intercloud eddies (10^{-2} – 10^{-1}). Radioastronomical observations of the H 21 cm line probe the largest distances, 10^2 – 10^4 pc. Studies of the interstellar absorption of stellar spectra probe distances over the range 10^1 – 10^3 pc. Observations of resonantly scattered UV radiation probes to distances up to perhaps 200 AU, or 10^{-3} – 10^{-4} pc.

To present a comprehensive view of the heliosphere and its setting, a description proceeding from the very distant to the very local is employed here. A similar approach is used in the reviews of the interstellar medium (ISM) and its interaction with the solar environment presented by Holzer (1989) and Thomas (1978). The material presented here is mainly gathered from extensive review articles published within the last 15 years. For brevity, many of the observational details that are discussed in these reviews are not discussed explicitly.

1.2.1 The Galaxy and the Interstellar Medium

The Milky Way Galaxy is of spiral form with diameter $\sim 3 \times 10^4$ pc and thickness $\sim 10^3$ pc. The Sun is located in an outer spiral arm about 2/3 the way out from the Galactic center. The spiral arms contain stars and intervening gas and dust. The Galactic ISM is a collection of gas and dust phases which occupy a volume of order 10^{12} pc^3 .

The primary component of the neutral gas phase of the ISM is atomic hydrogen. Its Galactic distribution is reviewed by Dickey and Lockman (1990). The principal means of detecting distant (≥ 100 pc) hydrogen is by observing the H 21 cm hyperfine line (1420.4058 MHz). The 21 cm radioastronomy observations imply that H column

densities vary by more than a factor of 500 over the sky. In the central portions of the Galaxy the H is concentrated within 200 pc of the Galactic plane. Farther out, the H sheet is warped and extends 4 kpc out of the plane. The distribution is characterized by sheets, loops and arching filaments both within and extending out of the Galactic plane. These structures are very likely due to the action of supernovas and strong stellar winds creating expanding bubbles of tenuous and hot H gas bounded by denser filamentary structures (see the review by Spitzer, 1990).

Supernovas explosions are believed to play an important role in regulating the overall structure of the ISM. Early studies of the ISM energy and pressure balance considered the heating of a neutral interstellar gas by low-energy cosmic rays (Field et al., 1969; Goldsmith et al., 1969). These considerations led to the development of a two-phase model where the ISM is represented by two thermally stable phases in pressure equilibrium: a tenuous component with temperature $\sim 10^4$ K and density $(0.1-1) \text{ cm}^{-3}$ and a more dense phase $\sim 100 \text{ cm}^{-3}$ at about 100 K. Later, McKee and Ostriker (1977) showed that supernovas contribute significantly to the ISM energy and pressure balance; supernovas explosions produce three distinct ISM phases (which are still characterized by rough pressure equilibrium). In the three-phase ISM model, the majority of the ISM volume is filled with the intercloud medium, a hot ($T \sim 10^5-10^6$ K) and tenuous ($n \sim 10^{-3}-10^{-2} \text{ cm}^{-3}$) gas which emits soft X-rays. Embedded within the hot phase are the two other phases which are similar to those in the earlier two-phase models.

1.2.2 The Local Interstellar Medium

The local interstellar medium (LISM) is reviewed by Cox and Reynolds (1987). They define it as the region of space having H column densities $\leq 10^{19} \text{ cm}^{-2}$. The distances to this column density, as determined from interstellar absorption spectroscopic studies and H 21 cm observations, range from about 30 pc in the Galactic plane to 200 pc

at the North Galactic Pole. The volume of space occupied by the LISM is therefore elongated, but is roughly equivalent to the volume occupied by a sphere of radius 100 pc. Most of the LISM appears to be filled with a gas similar to the hottest phase of the ISM. It is observed to emit soft X-rays and appears to be spatially bounded, defining what is sometimes referred to as the local bubble. The local bubble has a particle number density $\sim 4 \times 10^{-3} \text{ cm}^{-3}$ and a temperature $\sim 10^6 \text{ K}$. It may be a remnant of a single supernova explosion which occurred roughly 10^5 years ago (McKee and Ostriker, 1977; Cox and Anderson, 1982)

1.2.3 The Very Local Interstellar Medium

It appears that the region within 3 to 10 pc of the Sun is more dense than the gas in the Local Bubble as a whole. McClintock et al. (1978) show that Copernicus satellite observations of interstellar absorption spectra of stellar H Ly α and D Ly α emission features are consistent with a homogenous region within 3.5 pc of the Sun. The H density is 0.10–0.15 cm^{-3} and flows past the sun at about 22 km s^{-1} from the direction $\alpha = 252^\circ$ and $\delta = -15^\circ$. This region within about 3.5 pc of the Sun is often referred to as the Local Fluff (Frisch, 1986). It is not currently known whether the Local Fluff is an equilibrium or transient structure within the Local Bubble. Frisch (1986) summarizes the empirically determined properties of the Local Fluff and cites a density of $\sim 0.1 \text{ cm}^{-3}$, temperature $\sim 11500 \text{ K}$ and magnetic field $\sim 3\text{--}5 \mu\text{G}$. Frisch et al. (1987) estimate the ionization fraction of the Local Fluff as determined from observations of nearby stars. They conclude that an appropriate upper limit to the electron density is $3 \times 10^{-3} \text{ cm}^{-3}$, implying an ionization fraction of $\leq 10\%$.

Holzer (1989) defines the VLISM as the innermost part of the Local Fluff, the region of space within 0.01 pc ($\sim 2000 \text{ AU}$) of the Sun. The VLISM is the region of space of the appropriate scale to impose boundary conditions when addressing the

penetration of H and He and Galactic cosmic rays into the solar system. It is believed to be large enough to effectively contain the interaction region between the Local Fluff and the solar environment, which includes the heliosphere and associated structures.

1.3 The Heliosphere

The term heliosphere was introduced in a review of the solar wind and interplanetary magnetic field by Dessler (1967), who defined it as “the region of interplanetary space where the solar wind is flowing supersonically.” Here, this definition is not employed literally, but is retained in spirit. The heliosphere is believed to be composed of several distinct parts. The specific definition of the terms heliosphere as well as inner and outer heliosphere are deferred until the end of this section, after these distinct parts are discussed.

Several detailed studies of the interaction between the VLISM and the solar environment have been conducted since 1955. Excellent summaries are available in the reviews written in the last 20 years (Baranov, 1990; Holzer, 1989; Thomas, 1978; Holzer, 1977; Fahr, 1974; and Axford, 1972). The prevailing picture involves the interaction between the supersonic solar wind and the interstellar plasma as two highly conductive fluids. The guiding principle is the same as for the two and three-phase ISM models: the various phases of the system tend toward pressure equilibrium. Heliospheric distributions of H and He are affected primarily by gravitation, radiation pressure, momentum and charge exchange collisions, and photoionization.

Fundamentally, the interaction between the solar wind and the VLISM involves the relaxation toward pressure equilibrium between the two magnetized plasma fluids. The effects of neutrals on the plasma flow have typically been neglected, but probably are significant as well (Holzer, 1989). Several interaction models have been constructed over the last three decades and are reviewed in detail by Holzer (1989, 1977), Baranov (1990), Fahr (1974) and Axford (1972). Figure 1.1 shows an schematic di-

agram of the plasma interaction taken from Holzer (1989). The pertinent features are the solar wind termination shock, a collisionless hydromagnetic shock where the supersonic solar wind is believed to decelerate to subsonic speeds, and the heliopause, an idealized discontinuity between the VLISM and solar wind plasmas. The region between the SWTS and the heliopause is called the heliosheath. In models where the VLISM flow is supersonic, there is an additional interstellar shock (ISS) upstream of the interaction region.

1.3.1 The Solar Wind

Evidence for the existence of “solar corpuscular radiation” existed before and during the 1950’s in observations of the terrestrial aurora, outwardly directed cometary tails, the disruption of the outer geomagnetic field during geomagnetic storms, and inhomogeneities in the solar coronal electron density. Direct measurements of the interplanetary ion flux were not made until the late 1950’s and early 1960’s. These measurements confirmed that the plasma flow is supersonic and directed radially outward. Investigations of the solar wind and heliomagnetic field are too numerous and detailed to review here. The *Proceedings of the 6th International Solar Wind Conference* (Pizzo et al., 1987) is a useful summary of the research up to the mid-1980’s. For earlier reviews see Hundhausen (1970; 1979).

Hydrodynamic expansion of the solar corona is the source of the solar wind (Parker 1963). The expansion starts at relatively low speeds beneath the corona, accelerating steadily outward and exceeding the sound speed at a few solar radii. The expansion speed eventually levels off to a few hundred km s^{-1} and remains relatively constant beyond.

The solar wind is not homogenous. It is primarily composed of protons, but alpha particles (He^{++}) represent about 5% of the total ion flux. There are significant variations in density and speed as well as latitudinal and longitudinal structure. Fast

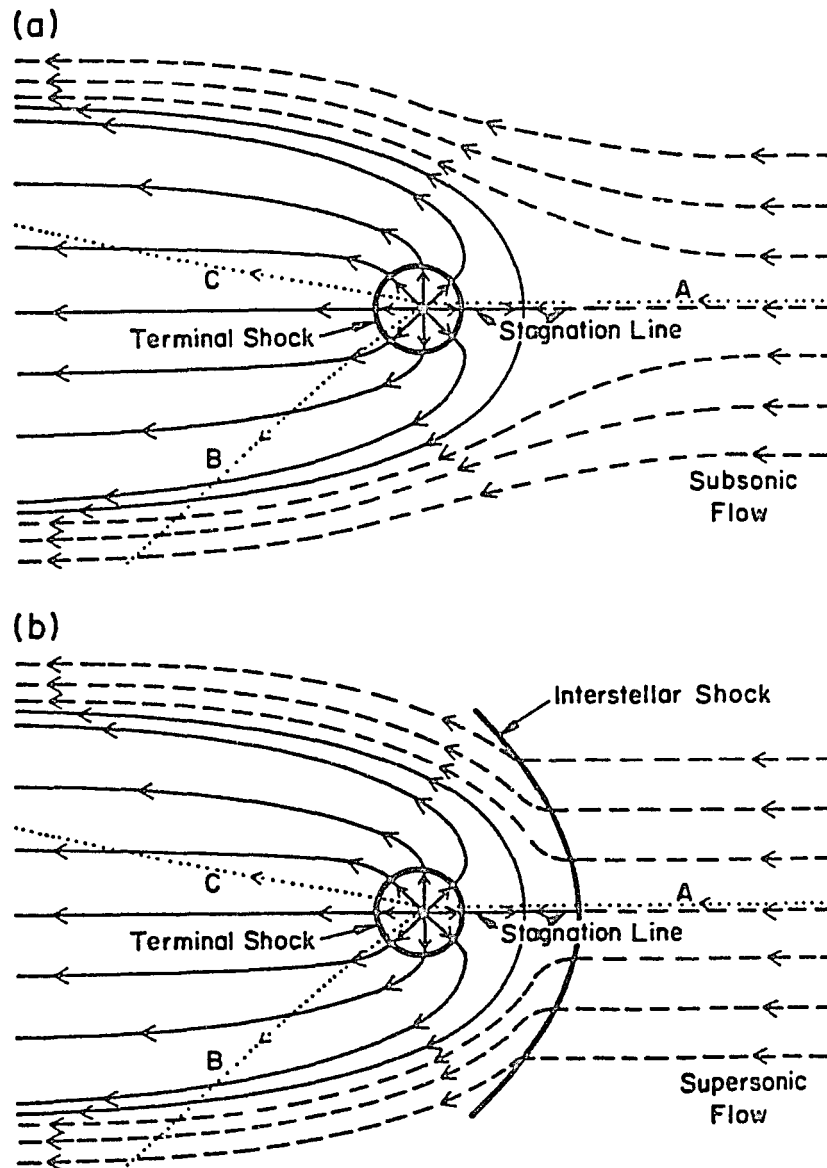


Figure 1.1: Two schematic diagrams of the VLISM and solar wind plasma interaction where the VLISM flow is subsonic (a) and supersonic (b). The solid lines with arrows show streamlines of the solar wind flow. The dashed lines show streamlines of the VLISM flow. The bold lines with no arrows show the SWTS and ISS shock structures. The dotted lines labeled A, B and C show VLISM neutral particle trajectories (Reproduced with permission from Holzer, 1989).

ion streams are observed, sometimes associated with interplanetary shocks. The flow carries highly variable magnetic fields, which resemble the Archimedean spiral structure during solar minimum conditions (i.e. those periods when the minimum number of sunspots are observed). The flow is generally organized by the dipole component of the solar magnetic field, except at times of solar maximum. Relatively low speed flows emanate from the dipole equator. Higher speed flows come from the poles; these are sometimes referred to as coronal holes.

For the purposes of this research, the details of the solar wind and heliomagnetic field will be described only when the need is apparent. Otherwise typical or average solar wind parameters will be used. Protons are the dominant constituent of the flow. The solar wind radial speed, v_{sw} , varies between 300 and 700 km s⁻¹, with a typical value of ≈ 400 km s⁻¹. Because of the nearly constant radial speed, conservation of mass implies that the proton density falls as the inverse square of the heliocentric distance, r :

$$n_p(r) = n_{pe} \left(\frac{r_e}{r} \right)^2, \quad (1.1)$$

where r_e is 1 AU and n_{pe} is the proton density at the earth. Representative values of n_{pe} are 4 to 10 cm⁻³. The flow is highly supersonic. Its Mach number is >10 at 1 AU and increases at larger heliocentric distances. The ratio of the solar wind ram pressure to thermal pressure is ~ 200 at 1 AU for typical solar wind conditions and also increases with r . So the solar wind may be reasonably approximated as a cold flow and the thermal pressure neglected.

1.3.2 The Solar Wind Termination Shock

Because of the highly supersonic nature of the solar wind, any significant obstruction induces deceleration to subsonic speeds via a hydrodynamic shock. A variety of different types of shocks are observed propagating along with inhomogeneities within the solar wind (see the collection of reviews in Tsurutani and Stone, (1985) and references

therein). Many of these are created by a violent expansion of the solar corona and/or interactions between fast and slow solar wind streams. Standing shocks are associated with relatively stationary obstacles (such as planets and comets) embedded in the solar wind. The shocks are generally abrupt discontinuities, having thicknesses of order the smallest pertinent interaction distance. In the case of neutral atmospheric shocks (created by supersonic aircraft, for instance) this is the collisional length scale. In the solar wind, the pertinent distance is the minimum of the plasma species' gyro radii. This scale is much smaller than the collisional length scale and so solar wind shocks are referred to as collisionless.

Planetary magnetospheric bow shocks occur roughly in the region where the ram pressure of the solar wind is balanced by the combined magnetic and thermal pressure inside the planetary magnetosphere. Similarly, the solar wind termination shock is thought to exist roughly in the region where the ram pressure of the solar wind balances the pressure beyond. Considering contributions from VLISM magnetic field, cosmic ray, thermal and ram pressures, Holzer (1989) estimates the distance to the SWTS to be between 50 and 200 AU. The major source of uncertainty is the poorly constrained VLISM magnetic field strength.

The SWTS probably has a complicated shape that varies significantly with time. The observed spatial and temporal variability of the solar wind implies significant variations in the SWTS heliocentric distance. Transient low and high speed solar wind flows imply a “bumpy” SWTS. The surfaces of the bumps probably move radially inward or outward with speeds $\geq 100 \text{ km s}^{-1}$. Observed latitudinal solar wind structure (i.e. high speed flows from polar coronal holes) suggests the SWTS should bulge outward at high latitudes over most of the solar cycle. The minimum SWTS distance should lie upstream or toward the incoming VLISM flow—the general direction where the Voyager spacecraft are headed. Because the expected $\geq 100 \text{ km s}^{-1}$ radial

speed of the SWTS is much greater than typical spacecraft speeds ($\leq 20 \text{ km s}^{-1}$), the most likely initial encounter is one where the SWTS moves inward past the spacecraft. Subsequent encounters with the same spacecraft may also occur because of short term SWTS radial oscillations.

At the SWTS, the radially outward motion of the solar wind plasma is converted mostly into random thermal motion. The shock is well approximated as a strong collisionless shock because of the large Mach number and weak magnetic fields (Parker, 1963; Axford, 1972). Applying the principles of mass, momentum and energy conservation across the shock (i.e. the Rankine-Hugoniot relations) and using an adiabatic index $\gamma_a = 5/3$ appropriate for a pure proton/electron plasma, yields a ratio of 4 between the bulk flow speeds and densities across the shock:

$$\frac{v_{p1}}{v_{p2}} = \frac{n_{p2}}{n_{p1}} = \frac{\gamma_a + 1}{\gamma_a - 1} = 4. \quad (1.2)$$

Here the subscripts 1 and 2 refer to the regions just inward of the shock (supersonic) and just outward (subsonic) respectively. The thermal pressure of the post-shock gas is

$$p_2 = \frac{2m_p n_{p1} v_{sw}^2}{\gamma_a + 1} = \frac{3m_p n_{p1} v_{sw}^2}{4}, \quad (1.3)$$

where m_p is the proton mass. This pressure is due to both the electron and ion gasses. The exact temperature partitioning between the electrons and protons is unspecified (Tidman and Krall, 1971). Assuming the subsonic electron and the proton temperatures are equal and using the perfect gas law equation of state yields

$$T_{p2} = \frac{(\gamma_a - 1) m_p n_{p1} v_{sw}^2}{k_B (\gamma_a + 1)^2} \approx \frac{m_p v_{sw}^2}{10k_B}, \quad (1.4)$$

where k_B is Boltzmann's constant. For typical solar wind parameters $T_{p2} \geq 10^6 \text{ K}$. The subsonic solar wind is a low Mach number flow and may be reasonably well approximated as an incompressible fluid (Parker, 1963).

1.3.3 The Heliopause

In idealized models of the plasma interaction, the heliopause is a contact surface separating the subsonic solar wind plasma from the plasma in the VLISM flow (see the review by Suess, 1990). A simple but elucidating derivation of its shape is given by Parker (1963) who employs several assumptions, including incompressible plasma flows and a SWTS with zero radius. The Parker (1963) solution has the same general form as shown in panel (a) of Figure 1.1. Along the flow axis upstream of the Sun, a stagnation point in the flow exists where the plasma has no net velocity. This point lies on the “nose” of the heliopause, and separates the subsonic solar wind and VLISM plasma on the flow axis. From there, the heliopause widens as it extends back in the downstream direction. In this idealized picture, the heliopause eventually reaches a final asymptotic width and extends to infinite distance downstream bounding what is referred to as the heliotail. Suess and Nerney (1990, 1991) have modified the Parker model to include a SWTS of finite size.

The idealized Parker model is not likely valid in reality. In fact, Parker himself suggests several differing heliopause geometries. Yu (1974) points out that the heliotail may be unstable to kinking, buckling and bifurcation. Neutsch and Fahr (1983) and Fahr and Neutsch (1983a, 1983b) model the heliopause as a roughly ellipsoidal surface, where the heliotail is closed off by a variety of plasma diffusion processes across the heliopause. In this case, the downstream heliopause becomes a somewhat imaginary surface, as the solar wind and VLISM plasmas diffuse into one another (see Fahr et al., 1986a). Fahr et al. (1986b) include the effects of a homogenous interstellar magnetic field, which yields a flattened paraboloid-like heliopause. Suess et al. (1987) suggest that the size of the upstream heliospheric cavity is only 2/3 that of the downstream cavity. The complicated and variable SWTS morphology should further modify the details of the solution. Also, VLISM neutrals (specifically H) in-

teract with the subsonic solar wind via momentum and charge exchange collisions and contribute to the turning of flow. Finally, Baranov et al. (1979) and Baranov (1990) model the system using a supersonic VLISM flow which implies an interstellar shock and changes the nature of the subsonic flow region and heliopause as well.

Even though a distinct heliopause surface may be an idealized concept, it still serves a useful function. The nature of the strongly shocked subsonic solar wind plasma and the subsonic VLISM plasma is radically different. In the subsonic VLISM case, the heliopause separates the tenuous subsonic solar wind with temperature $\geq 10^6$ K from the VLISM plasma with a temperature $\sim 10^4$ K. The VLISM plasma must be much more dense to achieve pressure equilibrium across the heliopause. In reality, diffusion and other interactions blur the heliopause, making it a region of finite extent, but one which separates two distinctly different plasmas nonetheless. Any reference to the heliopause must be regarded with this in mind.

1.3.4 The Inner and Outer Heliosphere

Given the above discussion of the plasma interaction between the VLISM and the solar wind, the terms inner and outer heliosphere may now be specifically defined. The inner heliosphere is the region that Dessler et al. (1967) originally defined: the region where the solar wind is flowing supersonically. In other words, the inner heliosphere is the region inside the SWTS, which, as mentioned above, is probably variable and has complicated morphology. The outer heliosphere is the region within the heliopause or the general region where the solar wind and VLISM plasmas intimately mix. The outer heliosphere is therefore a somewhat nebulous region with no precise boundaries, except in idealized models of the interaction. Suess and Nerney (1990, 1991) label the region between the upstream SWTS and the heliopause the heliosheath which connects to the downstream heliotail, in accordance with magnetospheric convention.

1.4 Penetration of VLISM H and He into the Heliosphere

The two dominant neutral species in the heliosphere are hydrogen and helium atoms. The dominant fraction of the neutrals found outside a few AU (and not in the immediate vicinity of a comet or planet) are believed to originate in the VLISM flow (Holzer, 1977). Because they are not electrically charged, the neutrals are not affected by the heliomagnetic environment. Their motion is determined by solar gravitation and radiation pressure. The processes of charge exchange and photoionization also affect the distributions.

1.4.1 H-p Charge Exchange

In order for VLISM neutrals to penetrate into the inner heliosphere, they must traverse the plasma structures described above. The principal interaction between the plasma and neutral species is the resonant charge exchange reaction between hydrogen and protons. The distribution of helium is probably not significantly affected by charge exchange reactions. The H-p charge exchange reaction



is both a source and a loss process for the H atoms. In the outer heliosphere a certain fraction of H atoms originating in the VLISM are replaced by newly created H atoms which have very nearly the same velocity as the parent subsonic solar wind protons. So part of the VLISM H flow with bulk speed $\approx 22 \text{ km s}^{-1}$ and temperature $\approx 10^4 \text{ K}$ is replaced by a distinct H distribution with bulk speeds of up to 100 km s^{-1} and temperatures $\geq 10^6 \text{ K}$. Similarly the subsonic solar wind proton flow is partially replaced by a distribution having the VLISM bulk velocity and temperature. The latter effect helps to cool the plasma in the heliosheath as well as turn the bulk flow toward the downstream direction.

Inside the SWTS, charge exchange replaces H atoms originating in the VLISM with ones directed radially outward at the solar wind speed, creating the splash component of the H distribution (Fahr, 1974; Holzer, 1977). Holzer (1972) points out that charge exchange slows and heats the solar wind. Solar wind protons are replaced with protons which are effectively motionless with respect to the solar wind flow. These are then accelerated outward by the heliomagnetic field. This pick-up process requires energy and therefore slows the solar wind flow. As they are accelerated up to the solar wind speed, the pick-up protons gain as much random thermal energy as bulk translational energy. So the pick-up process also implies a net heating of the solar wind.

The charge exchange loss rate of H atoms inside the SWTS, $\beta_{H,ex}$, is proportional to the proton flux, which decreases as r^{-2} :

$$\beta_{H,ex}(r) \approx n_{pe} v_{sw} \sigma_{ex} \left(\frac{r_e}{r} \right)^2, \quad (1.6)$$

where σ_{ex} is the charge exchange cross section. Assuming $v_{sw} = 450 \text{ km s}^{-1}$, then $\sigma_{ex} \approx 1.7 \times 10^{-15} \text{ cm}^2$ (using the cross section fit of Maher and Tinsley, 1977). For a proton density of 8 cm^{-3} at 1 AU, the loss rate is $6 \times 10^{-7} \text{ s}^{-1}$. However, the significant temporal and spatial variations in the solar wind imply similar variations in the H loss rate. A detailed investigation by Ajello et al. (1987) shows that this rate varies from 5 to $9 \times 10^{-7} \text{ s}^{-1}$ over the solar cycle.

1.4.2 Photoionization

As VLISM neutrals approach the Sun they may also be photoionized by Extreme Ultraviolet (EUV) solar radiation. The rate of photoionization is proportional to the EUV flux and therefore also falls as r^{-2} . The significant temporal variations in the solar wind and in the solar EUV flux (see the review by Lean, 1990) imply that these rates are also variable. Estimates of the photoionization rates are calculated

by integrating the solar flux multiplied by the photoionization cross section over the EUV spectral region. The estimates are generally about 10 to 20% of the value for charge exchange loss and vary over the solar cycle by a factor of two or more (Ajello et al., 1987). Axford (1972) gives a useful compilation of photoionization rates for both H and He. Typical values are $\beta_{\text{H},pi} \approx 1.5 \times 10^{-7} \text{ s}^{-1}$ and $\beta_{\text{He},pi} \approx 4.0 \times 10^{-8} \text{ s}^{-1}$.

1.5 Solar H Ly α

Both H and He atoms resonantly scatter UV radiation. During the scattering process the photon may transfer momentum to the scattering atom. Thus the resonance scattering of the solar photons exerts a net outward force on the neutrals. The only solar line that exerts significant force is H Ly α . Therefore the solar Ly α plays a dual role in the heliospheric Ly α scattering process. First, it provides the source photons for the Ly α radiation field. Second, it exerts significant radiation pressure on the H atoms, and thereby shapes their distribution.

1.5.1 The Integrated Solar H Ly α Flux

Direct measurements of solar Ly α from the ground are not possible because of the strong UV absorption of the terrestrial atmosphere; measurements must be conducted from spacecraft. Fortunately, there are several solar indices which can be measured from Earth's surface and correlate well with directly observed solar Ly α .

The Solar Mesospheric Explorer (SME) Earth-orbiting satellite measured the total Ly α flux from 1981 until 1989 (Rottman et al., 1982; Barth et al., 1990). The He 10.8 μm solar chromospheric absorption feature measured from Earth's surface correlates well with the Ly α variations observed by SME (Donnelly et al., 1986; Skinner et al., 1988). Figure 1.2 shows the solar Ly α fluxes as determined from the He 10.8 μm proxy. The observed flux varies on three time scales. Variations of about 5% are observed from day to day. These may be due to either noise in the measure-

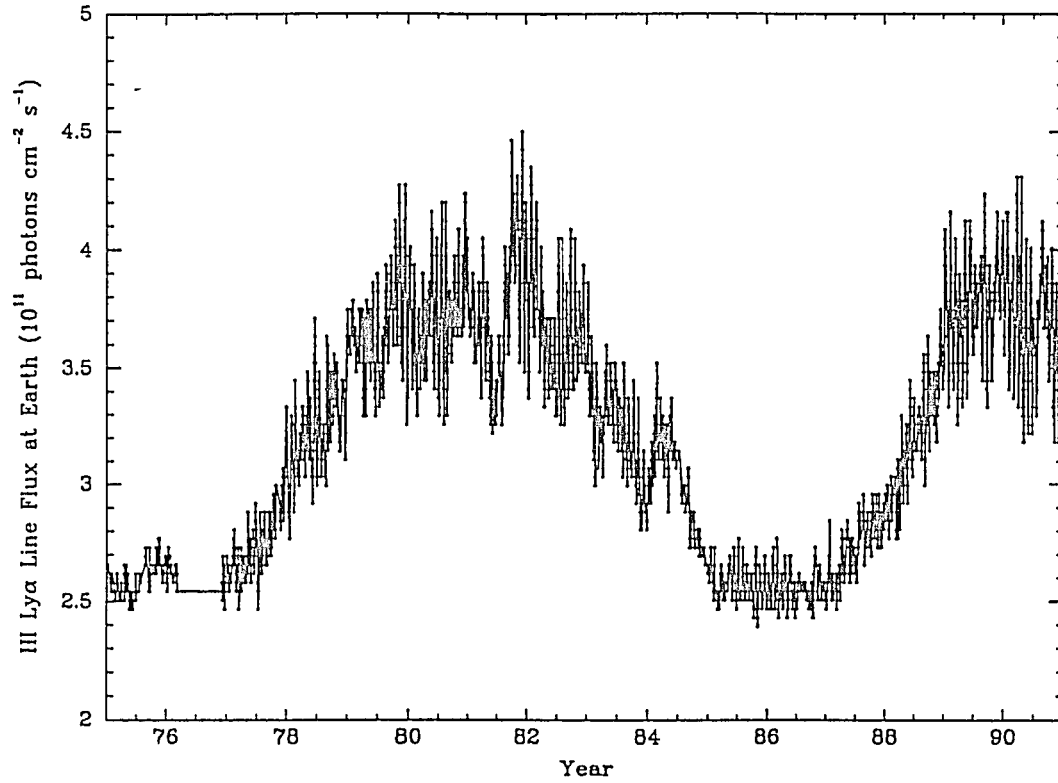


Figure 1.2: The total solar H Ly α flux at the Earth as determined by correlating to the solar He 10.8 μm chromospheric feature (Skinner et al., 1988). The flux varies by a factor of ≈ 1.5 over the 11 year solar cycle.

ments or short term variations in the solar atmosphere. More significant variations of up to 15% are correlated with the 25 day solar rotation period. (As seen from the Earth, the Sun appears to rotate in about 27 days, because of Earth's orbital motion.) These variations are most pronounced at solar maximum; they are probably associated with sunspots and plage regions mostly confined to the equatorial regions. The 25 day variations have also been observed in heliospheric $\text{Ly}\alpha$ (Shemansky et al., 1984).

The largest variation in solar $\text{Ly}\alpha$ is associated with the 11 year solar cycle. The integrated line flux increases by a factor of about 1.5 from solar minimum to solar maximum. Near solar maximum, the integrated flux shows longitudinal variability associated with spatially confined active areas near the solar equator. These same regions also cause a latitudinal anisotropy; the flux decreases significantly over the solar poles (Cook et al., 1981). This effect has been observed reflected in the heliospheric $\text{Ly}\alpha$ glow observed by the Galileo spacecraft (Pryor et al. 1992) and suggests that much of the $\text{Ly}\alpha$ enhancement observed at solar maximum may be confined to equatorial regions.

1.5.2 The Solar H $\text{Ly}\alpha$ Line Shape

Figure 1.3 shows the solar H $\text{Ly}\alpha$ line shape measured at 1 AU (Lemaire et al., 1978). It is the average of a solar disk center measurement in August, 1976 and a solar limb measurement from May, 1977 obtained by the OSO 8 spacecraft. The solar $\text{Ly}\alpha$ line has a central, self-reversed feature characteristic of lines emitted from deep source regions in stellar atmospheres. Unfortunately, $\text{Ly}\alpha$ line shape measurements are difficult to perform and few in number, whereas the integrated flux has been monitored more frequently.

The relationship between the integrated and line center fluxes is important in the study of heliospheric $\text{Ly}\alpha$ because the singly scattered intensity is proportional

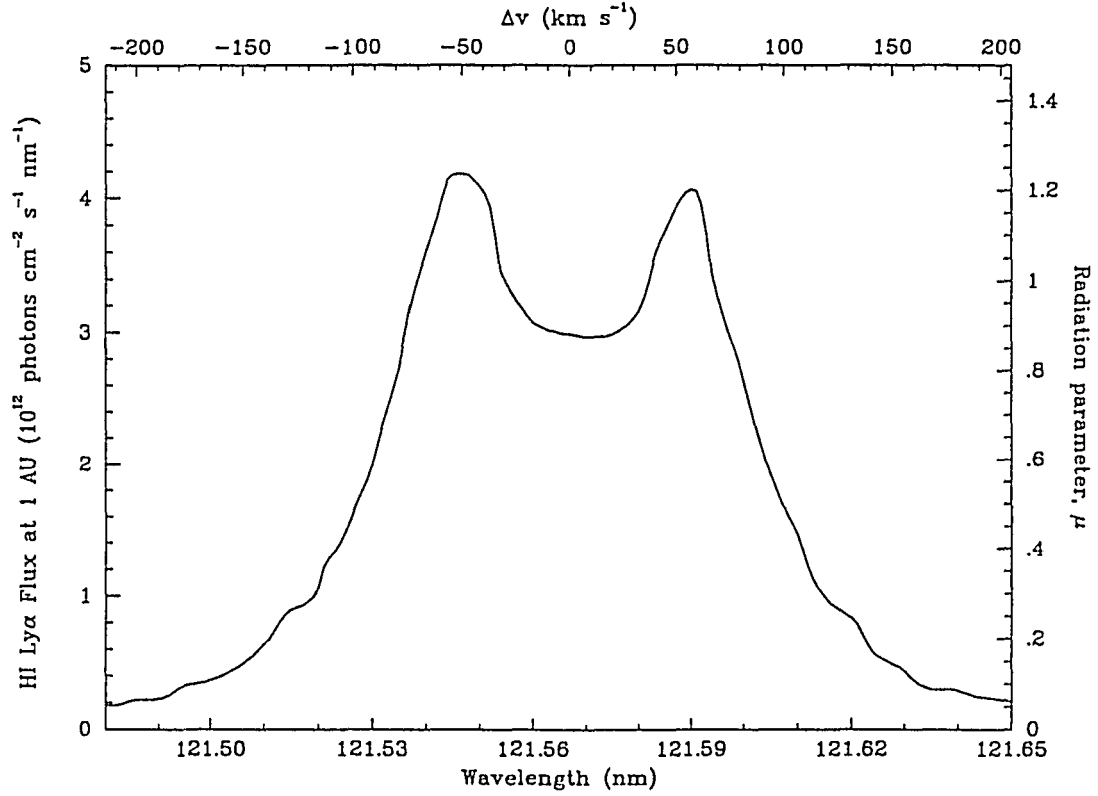


Figure 1.3: The solar H Ly α line observed at 1 AU (Lemaire et al., 1978). The solar line has a characteristic self reversed shape and a total width of $\sim 0.1 \text{ nm}$. The radiation pressure parameter is also shown.

to the flux within ≈ 0.02 nm of line center. Vidal-Madjar et al. (1973) and Vidal-Madjar (1975) show that the line shape varies in time. For instance, 50% changes in integrated flux may produce changes as large as 80% at line center. However, Ajello et al. (1987) find that the such enhanced line center flux modulations are too large when compared to heliospheric Ly α variations observed by the Pioneer-Venus spacecraft. The solar Ly α line shape is also observed to vary spatially over small portions of the solar disk, even at times of solar minimum (Lemaire et al., 1978). Here, for simplicity, the line shape shown in Figure 1.3 is taken to be representative over the entire solar cycle and all solar longitudes and latitudes.

1.5.3 H Ly α Radiation Pressure

The force exerted on an H atom by solar Ly α is proportional to the flux and, at small optical depths from the Sun, falls as r^{-2} . As a first approximation, the forces of due to gravity and radiation have the same dependence on heliocentric distance and radiation pressure may be taken into account by introducing an effective gravitational constant of $(1 - \mu_{\odot})G$, where μ_{\odot} is the ratio of the force on an atom from radiation to the force of gravity. For helium, $\mu_{\odot} \ll 1$. Solar Ly α variations suggest that for H, μ_{\odot} varies from 0.7 to 1.2 over the solar cycle (Ajello et al., 1987). So there are times when H atoms are attracted to the Sun and times when they are repelled. This effect is rather important in the downstream region where the H atoms tend to be focused at times when $\mu_{\odot} < 1$ and tend to be excluded when $\mu_{\odot} > 1$.

The actual radiation pressure force felt by an H atom, however, is not this simple; there are several important effects in addition to direct scattering of solar Ly α . First, the solar H Ly α line shape is not flat in wavelength and Doppler shifts imply that the actual radiation force depends on the radial component of the H atom's velocity. Second, spatial and temporal variations in the solar flux imply associated variations in μ_{\odot} . Finally, at large H Ly α optical depths from the Sun, the solar flux

is considerably attenuated and multiply scattered photons are responsible for much of the radiation pressure. The combined radiation pressure due to solar and multiply scattered photons, in general, does not fall as r^{-2} . This means that the H atom trajectories depend on the multiply scattered Ly α radiation field as well.

1.6 Heliospheric H and He Distributions

The processes of gravitation, radiation pressure, photoionization and charge exchange all affect the distribution of neutrals in the heliosphere. Neutrals originating in the VLISM follow hyperbolic orbits through the heliosphere. Those that approach the Sun too closely are likely to be ionized. The difference between the H and He distributions is considerable, mostly due to the differences in ionization rates and radiation pressure forces. For instance, VLISM atoms approaching the Sun should be able to penetrate to within a distance of order $R_i \sim \beta_e r_e^2 / v$ where β_e is the total loss rate at $r_e = 1$ AU and $v \approx 22$ km s $^{-1}$ is the velocity of the neutral atom (Axford, 1972). Using typical parameters yields $R_i \approx 5$ AU for H and $R_i \approx 0.3$ AU for He. Therefore, a cavity near the Sun with dimension of order 5 AU is expected in the H distribution. The prevailing VLISM flow elongates the H ionization cavity in the downstream direction—creating a roughly teardrop shaped cavity. The typical dimension of the He cavity is more than an order of magnitude smaller. Moreover, He atoms feel little or no repulsive radiation pressure. So the flow streamlines all tend to cross the downstream axis. This effect (often referred to as “gravitational focusing”) significantly enhances helium density on the downstream axis.

Several models of the neutral distributions have been presented over the last few decades. There is the cold model that considers a VLISM flow with negligible temperature, neutral loss rates that vary as r^{-2} and a constant radiation pressure parameter (Danby and Camm, 1957; Fahr, 1968; Holzer and Axford, 1971). Detailed summaries of the cold model are given in Axford (1972) and Fahr (1974). Also, there are the

hot models that employ the same assumptions but consider a VLISM flow with finite temperature (see reviews by Holzer, 1977 and Thomas, 1978). Finally there are the more complicated models that include drag-like effects, interactions with outer heliospheric plasma structures and variations in time (Ripken and Fahr, 1983; Fahr et al., 1985; Bleszynski, 1987; Fahr and Scherer, 1990; Scherer and Fahr, 1990; Baranov et al., 1991). The Ripken and Fahr (1983), Bleszynski (1987) and Baranov et al. (1991) models predict a significant filtering of the H gas at the heliospheric interface region. However, when such details are included, the problem becomes extremely difficult (see Fahr and Ripken, 1984).

1.7 Resonantly Scattered Radiation

The first maps of the of heliospheric H Ly α sky background were conducted by the OGO 5 spacecraft in 1969 (Thomas and Krassa, 1971; Bertaux and Blamont, 1971). Since then, both H and He heliospheric resonance emissions have been observed by several spacecraft. The majority of these were obtained from within 2 AU of the Sun (see Ajello et al., 1987 for a comparative review). The only Ly α observations outside 5 AU are those from the Pioneer and Voyager spacecraft. These data are presented and examined in this dissertation. Inner solar system observations (i.e. those performed inside 5 AU) have been investigated thoroughly by many authors and will not be analyzed here.

Briefly described, heliospheric resonance scattering has the following characteristics. Solar photons in one of the H or He resonance lines propagate outward into the heliosphere. As they travel outward they may resonantly scatter from heliospheric H or He atoms. In general, photons may be scattered more than once. In the VLISM the Ly α scattering path length is of order 10 AU. For He 58.4 nm it is ~ 200 AU. The resonance line intensity observed by a spacecraft UV instrument is equal to the rate photons are scattered along the instrument's line of sight plus whatever "Galactic"

background may exist.

The principal goal of observing heliospheric resonance emissions is to determine or constrain the properties of the heliosphere and VLISM. In fact, the VLISM flow velocity vector and temperature have been determined mainly by modeling the pattern of the H and He resonance line intensities (see Lallement, 1990 and references therein). One particularly important parameter is the density of hydrogen in the unperturbed VLISM, $n_{\text{H}\infty}$. The absolute intensity of $\text{Ly}\alpha$ sky background should depend on this parameter as well as the solar source flux. The complicating factor is the absolute calibrations of the instruments measuring the heliospheric intensities as well as the solar source flux are typically difficult to determine. Estimates of $n_{\text{H}\infty}$ based on inner solar system observations vary from 0.02 to 0.20 cm^{-3} with most estimates falling in the interval 0.04 to 0.08 cm^{-3} (Ajello et al., 1987). This large range very likely represents a combination of calibration errors and flaws in the models employed in the analysis.

1.7.1 Inner Solar System Observations

Multiple spacecraft have observed heliospheric resonance lines from within 5 AU, including (in rough chronological order): OGO 5, Mars 7, Mariner 10, Copernicus, Prognoz 5 and 6, Pioneer 10 and 11, Voyager 1 and 2, the International Ultraviolet Explorer, Pioneer-Venus, Venera 11 and 12. The publications spawned by these multiple missions are too numerous and detailed to cite here. Consult the reviews by Lallement (1990), Ajello et al. (1987) and Bertaux (1984) for references and more information. The spacecraft launched most recently that has performed inner solar system observations is Galileo (Pryor et al., 1992). The Hubble Space Telescope has probably also obtained measurements, but these are not yet in the literature.

The analysis of observations made within 5 AU of the Sun have increased our knowledge of the nature of the VLISM and heliosphere considerably. Heliospheric

resonance line observations are of two basic types: photometric and spectrometric. The former measure the total line intensities whereas the latter measure line shapes as a function of wavelength or frequency. As is summarized by Lallement (1990), the VLISM flow velocities and temperatures obtained from analyses of H and He spectrometric and photometric data are not always in agreement. A variety of methods of reconciling the disagreements have been suggested, but basically the disagreements suggest that the models employed are flawed in some way.

Nonetheless, several general characteristics of the heliospheric H distribution are well determined by the accumulated inner solar system observations. These include: 1) the region of maximum H Ly α emission is observed to lie 2 to 3 AU upstream of the Sun which verifies that the H ionization cavity is elongated in the downstream direction, 2) the observations favor a H lifetime at 1 AU of about 2×10^6 s which is in reasonable agreement with determinations from cometary studies (Smyth et al. 1991), 3) the Ly α glow shows large enhancements at medium and high latitudes which imply significant ($\approx 30\%$) solar wind anisotropies, probably associated with the polar coronal holes (see Ajello, 1990). A more recent result from inner solar system observations is reported by Pryor et al. (1992) on the basis of coordinated analysis of Galileo and Pioneer-Venus data. The data require a solar Ly α latitudinal anisotropy at times of solar maximum, with the Ly α flux approximately 25% lower over the solar poles than at the equator. This is consistent with the work of Cook et al. (1981).

1.7.2 Outer Solar System Ly α Observations

Three spacecraft have conducted Ly α observations beyond 5 AU: Voyager 1 and 2 and Pioneer 10. The Voyagers are equipped with nearly identical Ultraviolet Spectrographs (UVS), whereas Pioneer 10 has a two channel UV photometer system. These instruments measure integrated Ly α line intensities, not line shapes. On January 1, 1992 the heliocentric distances of these spacecraft were 47, 36 and 53 AU

respectively. Each is leaving the solar system at a rate of a few AU per year. The two Voyager spacecraft are heading generally into the VLISM flow whereas the Pioneer 10 trajectory very nearly parallels the downstream direction. The combined Voyager and Pioneer observations therefore provide a more global view of the heliosphere than either data set taken independently.

The Pioneer 10 spacecraft spins about the Earth-spacecraft line collecting Ly α data on a cone with a half-angle of $\approx 20^\circ$ measured from the anti-Earth direction. These data have been reduced and published by various members of the Pioneer 10 UV photometer team (Wu et al. 1981; 1988, Gangopadhyay et al., 1989 and Gangopadhyay and Judge, 1989). Both Voyager spacecraft periodically perform special Cruise Maneuver observing sequences, designed to produce partial maps of the sky in Ly α . The observations from these maneuvers may be accumulated to produce data comparable to that of Pioneer 10. Most of the Voyager Cruise Maneuver Ly α data have not been previously reduced or published.

Perhaps the most significant new result determined in this research project is summarized in Figure 1.4. The figure shows the Voyager (upstream) and Pioneer 10 (downstream) observations adjusted for solar flux variations and normalized at 15 AU. The combined Voyager data, measured on cones 65° from the antisolar direction, are plotted in the upper panel. The lower panel shows the Pioneer 10 data collected on 20° anti-Earth cones. All of the data fall as a function of heliocentric distance, r , but the Pioneer 10 intensities fall more quickly. The Pioneer 10 data fall as $r^{(-1.07 \pm 0.1)}$ (the two dashed lines in the lower panel of the Figure correspond to $r^{-1.0}$ and $r^{-1.1}$ respectively). The combined Voyager intensities between 15 and 35 AU fall as $r^{(-0.75 \pm 0.05)}$ (the dashed lines in the top panel show $r^{-0.7}$ and $r^{-0.8}$). This is a significant difference and is independent of instrument calibrations. In addition, the Voyager observations tend to show a flatter signature as a function of r starting at about 30 AU.

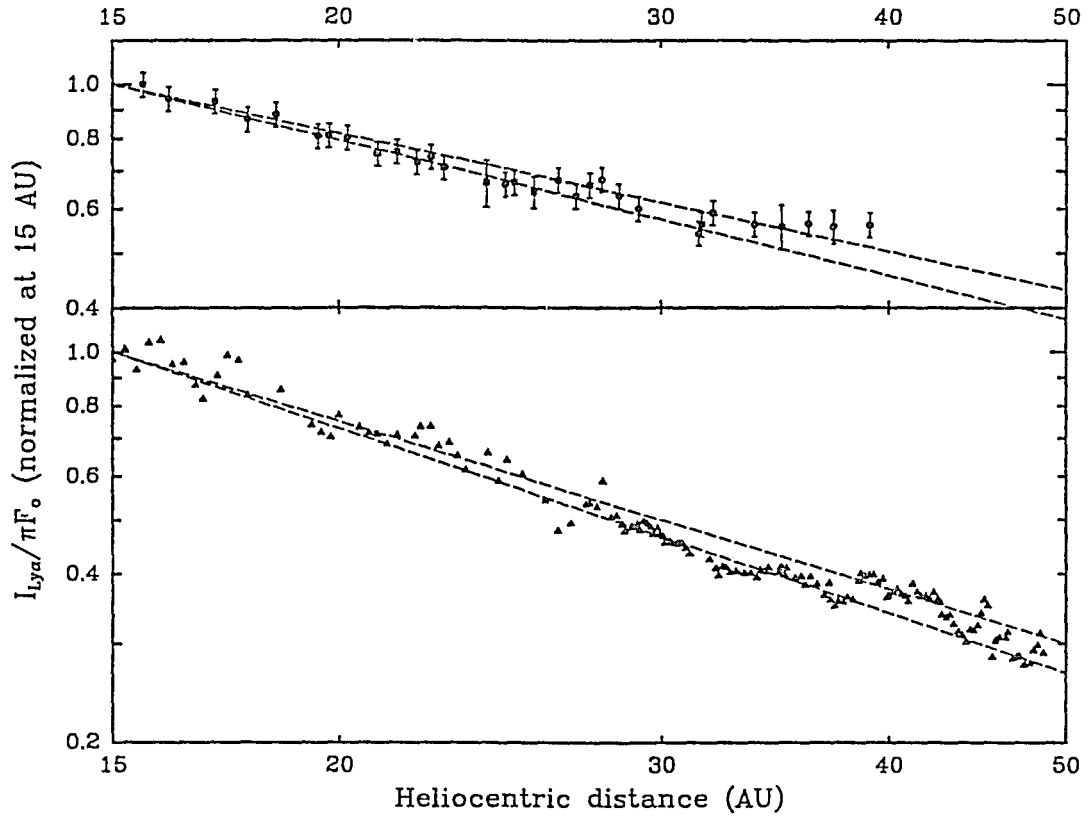


Figure 1.4: Voyager and Pioneer 10 heliospheric Ly α observations adjusted to constant solar flux and normalized at 15 AU. In the top panel the 65° antisolar cone Voyager 1 and 2 data are shown. The dashed lines show how the power laws $r^{-0.7}$ and $r^{-0.8}$ fall. In the lower panel, the Pioneer 10 observations (collected on 20° anti-Earth cones) are shown with $r^{-1.0}$ and $r^{-1.1}$ power laws.

Heliospheric $\text{Ly}\alpha$ radiative transfer models using the “conventional” heliospheric H distribution (which does not include the effects of charge exchange in the heliosheath) cannot match both data sets simultaneously. The data are more satisfactorily reproduced if a $\text{Ly}\alpha$ background is added in the upstream region, but not downstream. Such an asymmetry could be due to a Galactic background with an anisotropy that happens to coincide with the VLISM flow direction—but this possibility seems coincidental and unlikely. So the asymmetric background suggested by these data probably is associated with the heliosphere. Specifically, it may be caused by steep H density gradients or suprathermal H gas predicted by models which include the effects of charge exchange in the heliosheath. These data suggest the existence of the solar wind termination shock and associated outer heliospheric structures.

CHAPTER 2

THE DISTRIBUTION OF H AND He IN THE HELIOSPHERE

To investigate the heliospheric H distribution beyond 5 AU the dominant H production and loss processes must be identified. Because of the similarity of the H and He distribution problems, it is worthwhile to consider both concurrently. Holzer (1977) investigates various H and He sources and sinks in detail. The sources include the Sun, planets, comets, interplanetary dust and the VLISM flow. All but the last of these are negligible at heliocentric radii larger than ~ 1 AU and outside the immediate environments of comets and planets. Holzer (1977) also concludes the dominant loss processes outside ~ 0.5 AU are charge exchange and photoionization. These are the production and loss mechanisms examined here.

The formal problem of determining the H distribution is considerably more complicated than for He. The H-p charge exchange process couples the distributions of the protons and the H atoms. The radiation pressure exerted by the multiply scattered Ly α photons couples the Ly α radiation field to the distribution of H. And observed latitudinal variations in solar wind and EUV fluxes suggest that the H distribution is not axially symmetric about the interstellar wind axis. If one were to include all of these effects, the plasma fluid, Boltzmann and radiative transfer equations would need to be solved simultaneously in 3-dimensions—a daunting task—which necessarily implies the use of numerical techniques. No such coupled solution is pursued here. Instead the H distribution is approximated by solving the Boltzmann equation using several simplifying assumptions. First the general theory is presented. Then, several simple restricted problems having both spherical and axial symmetry are investigated using the relevant components of the general theory. In the final section, the algorithm

and some results of a numerical model of the H distribution are presented.

2.1 Distribution Theory: The Boltzmann Formulation

As described by Fahr (1990) and Ripken and Fahr (1983), the distribution of VLISM neutrals penetrating the heliosphere (with a fixed plasma distribution) may be calculated by solving the Boltzmann transport equation. The Boltzmann equation in differential form is an expression for the total time derivative of a particle distribution function, f , as a function of particle position, \mathbf{r} , velocity, \mathbf{v} , and time, t .

$$\frac{df(\mathbf{r}, \mathbf{v}, t)}{dt} = \frac{\partial f}{\partial t} + (\mathbf{v} \cdot \nabla) f + \left(\frac{\mathbf{F}}{m} \cdot \nabla_{\mathbf{v}} \right) f = P - L, \quad (2.1)$$

where \mathbf{F} is the vector force acting on the particle with mass m . The symbols ∇ and $\nabla_{\mathbf{v}}$ denote the vector gradient operators in position and velocity space respectively. The terms P and L represent the production and loss of particles at $(\mathbf{r}, \mathbf{v}, t)$. Generally, both the production and loss depend on the distribution function. The loss term in all the cases to be examined here has the form:

$$L(\mathbf{r}, \mathbf{v}, t) = f(\mathbf{r}, \mathbf{v}, t) \beta(\mathbf{r}, \mathbf{v}, t), \quad (2.2)$$

where β is the total loss rate in s^{-1} .

The volumetric density of particles (particles cm^{-3}) is obtained by integrating the distribution function over all velocities:

$$n(\mathbf{r}, t) = \int d^3\mathbf{v} f(\mathbf{r}, \mathbf{v}, t). \quad (2.3)$$

The average or mean value of a quantity $g(\mathbf{r}, \mathbf{v}, t)$ is

$$\bar{g}(\mathbf{r}, t) = \frac{1}{n(\mathbf{r}, t)} \int d^3\mathbf{v} g(\mathbf{r}, \mathbf{v}, t) f(\mathbf{r}, \mathbf{v}, t). \quad (2.4)$$

In a uniform system in thermodynamic equilibrium with temperature T and flowing with bulk velocity \mathbf{v}_{bulk} , the distribution function has the Maxwell-Boltzmann

form:

$$f_{\text{MB}}(\mathbf{v}) = n (\sqrt{\pi} v_{th})^{-3} \exp \left[- \left(\frac{\mathbf{v} - \mathbf{v}_{bulk}}{v_{th}} \right)^2 \right], \quad (2.5)$$

where the thermal speed, v_{th} is related to the temperature, T ,

$$v_{th} = \sqrt{\frac{2k_B T}{m}}. \quad (2.6)$$

For the Maxwell-Boltzmann distribution, the average velocity dispersion about the bulk velocity is related to the temperature as follows:

$$\overline{(\Delta v)^2} = \overline{(\mathbf{v} - \mathbf{v}_{bulk})^2} = \frac{3k_B T}{m}. \quad (2.7)$$

This relationship provides a means of defining an effective temperature of a non-Maxwellian gas.

2.1.1 The Integral Form of the Boltzmann Equation

The formal solution the differential Boltzmann equation (2.1) may be obtained by integrating over the past trajectories of the particles. The result is the integral equation

$$f(\mathbf{r}, \mathbf{v}, t) = \int_{-\infty}^t dt' P(\mathbf{r}', \mathbf{v}', t') e^{-\Lambda(t', t)}, \quad (2.8)$$

where t' denotes past times. The past trajectory of the particle at $(\mathbf{r}, \mathbf{v}, t)$ is given by $(\mathbf{r}', \mathbf{v}', t')$. The quantity $\Lambda(t', t)$ represents the loss of particles between times t' and t . It is calculated by integrating the decay rate as defined in equation (2.2) over the trajectory.

$$\Lambda(t', t) = \int_{t'}^t dt'' \beta(\mathbf{r}'', \mathbf{v}'', t''), \quad (2.9)$$

where the functional dependence of Λ on (\mathbf{r}, \mathbf{v}) is suppressed.

Often it is convenient to impose a boundary condition that the distribution function at some past time t_o (or alternatively at some position \mathbf{r}_o) is a known function, f_o . In this case the equation (2.8) assumes the form

$$f(\mathbf{r}, \mathbf{v}, t) = f_o(\mathbf{r}_o, \mathbf{v}_o, t_o) e^{-\Lambda(t_o, t)} + \int_{t_o}^t dt' P(\mathbf{r}', \mathbf{v}', t') e^{-\Lambda(t', t)} \quad (2.10)$$

Heliospheric neutral distributions may be calculated using equation (2.10). The boundary condition distribution is usually assumed to be Maxwellian with the VLISM density, temperature and bulk velocity as parameters. The boundary condition is imposed either at infinite heliocentric distance or at a distance large compared to characteristic heliospheric length scales.

Along the trajectory $(\mathbf{r}', \mathbf{v}', t')$ particles are affected by physical processes (such as photoionization) or they may be scattered on to (or off of) the trajectory by momentum or charge exchange collisions. Here the momentum exchange collisions are neglected and only the charge exchange and photoionization processes are considered.

2.1.2 H-p Charge Exchange

The H-p charge exchange process, reaction (1.5), has been investigated by Dalgarno and Yadav (1953). For low relative velocities, the differential scattering cross section is very sharply peaked in the forward direction. The process may be approximated as a transfer of an electron from an H atom to a proton with no accompanying transfer of momentum. After the charge transfer, the motion of the newly produced proton is directly influenced by the electromagnetic environment. The new neutral H atom is not. Charge exchange processes are especially important in environments where the plasma and neutral distributions have distinct distributions (i.e. are not in thermodynamic equilibrium, or have different temperatures and bulk velocities). In these environments, the H distribution is partially replaced by the distinct p distribution and vice versa. One such environment is the heliosheath, where the proton temperature is $\geq 10^6$ K but the net H distribution (as will be seen later on) has a temperature of $\sim 10^4$ K. In other words, charge exchange in the heliosheath creates a “suprathermal” population of H atoms.

The H-p Charge Exchange Cross Section

The H-p charge exchange cross sections used here are taken from Maher and Tinsley (1977) who fit empirically determined cross sections for interaction energies 0.005 to 130 eV (or relative velocities 1 to 500 km s⁻¹). The fit has the form

$$\sigma_{ex}(v_{rel}) = [A_{ex} + B_{ex} \log_{10}(v_{rel})]^2 \quad [\text{cm}^2] \quad (2.11)$$

where $A_{ex} = 1.64 \times 10^{-7}$, $B_{ex} = 1.6 \times 10^{-8}$ and v_{rel} is measured in [cm s⁻¹]. The fit is used here because the energy range is appropriate for the problem. The cross section does not vary rapidly in the velocity range of interest for heliospheric problems, changing by less than a factor of 2 between relative velocities of 10 and 100 km s⁻¹.

Charge Exchange Production and Loss

Ripken and Fahr (1983) describe the production and loss due to charge exchange. The H loss rate is obtained by integrating over the proton distribution function:

$$\beta_{ex}(\mathbf{r}, \mathbf{v}, t) = \int d^3\mathbf{v}_p f_p(\mathbf{r}, \mathbf{v}_p, t) v_{rel,p} \sigma_{ex}(v_{rel,p}), \quad (2.12)$$

where \mathbf{v}_p denotes proton velocities and f_p the proton distribution function. The relative speed of the H atom and proton is given by:

$$v_{rel,p} = |\mathbf{v} - \mathbf{v}_p|. \quad (2.13)$$

When momentum transfer in the charge exchange process is neglected, the H production term has the same form as the proton distribution function:

$$P_{ex}(\mathbf{r}, \mathbf{v}, t) = f_p(\mathbf{r}, \mathbf{v}, t) \int d^3\mathbf{v}_H f_H(\mathbf{r}, \mathbf{v}_H, t) v_{rel,H} \sigma_{ex}(v_{rel,H}), \quad (2.14)$$

where

$$v_{rel,H} = |\mathbf{v} - \mathbf{v}_H|. \quad (2.15)$$

In equation (2.14), the H distribution function is denoted f_H for clarity.

If the proton distribution is a cold flow with constant velocity $\mathbf{v}_{p,cold}$, its distribution function is written as a δ -function in velocity space:

$$f_p(\mathbf{r}, \mathbf{v}, t) = n_p(\mathbf{r}, t) \delta^3(\mathbf{v} - \mathbf{v}_{p,cold}). \quad (2.16)$$

Then the integral in equation (2.12) collapses to

$$\beta_{ex}(\mathbf{r}, \mathbf{v}, t) = n_p(\mathbf{r}, t) v_{rel,p} \sigma_{ex}(v_{rel,p}), \quad (2.17)$$

where here $v_{rel,p} = |\mathbf{v} - \mathbf{v}_{p,cold}|$.

If the proton distribution has finite temperature and is a Maxwellian of the form given in equation (2.5), the average velocity of the protons relative to an H atom with velocity \mathbf{v} is (see Ripken and Fahr, 1983):

$$\bar{v}_{rel,p} = v_{p,th} \left[\frac{e^{-w_p^2}}{\sqrt{\pi}} + \left(w_p + \frac{1}{2} \right) \text{erf}(w_p) \right], \quad (2.18)$$

where

$$w_p = \left(\frac{1}{v_{p,th}} \right) |\mathbf{v} - \mathbf{v}_{p,bulk}|. \quad (2.19)$$

The error function is defined as

$$\text{erf}(x) \equiv \frac{2}{\sqrt{\pi}} \int_0^x dt e^{-t^2}. \quad (2.20)$$

The quantity $\bar{v}_{rel,H}$ is expressed in an analogous fashion.

Ripken and Fahr (1983) show that if both the H and p distribution functions are Maxwellian then the charge exchange production and loss may be approximated to within $\sim 5\%$ by the expressions

$$P_{ex}(\mathbf{r}, \mathbf{v}, t) \approx f_p(\mathbf{r}, \mathbf{v}, t) [n_H(\mathbf{r}, t) \bar{v}_{rel,H} \sigma_{ex}(\bar{v}_{rel,H})], \quad (2.21)$$

and

$$\beta_{ex}(\mathbf{r}, \mathbf{v}, t) \approx n_p(\mathbf{r}, t) \bar{v}_{rel,p} \sigma_{ex}(\bar{v}_{rel,p}). \quad (2.22)$$

Charge Exchange Rates in the Solar Wind

Equation (2.17) is appropriate for the supersonic solar wind, which is reasonably approximated as a cold flow. Since typical solar wind velocities are much greater than VLISM flow velocities and remain relatively constant with heliocentric distance, the loss rate of VLISM neutrals penetrating the supersonic solar wind may be expressed by combining equations (1.1) and (2.17):

$$\beta_{ex} \approx n_{pe} \left(\frac{r_e}{r} \right)^2 v_{sw} \sigma_{ex}(v_{sw}). \quad (2.23)$$

Typical solar wind parameters give H loss rates of $(4-10) \times 10^{-7} \text{ s}^{-1}$. For He, the rates are typically an order of magnitude smaller.

2.1.3 Solar EUV Photoionization

In order for a solar photon to ionize a species it must have energy greater than the ionization potential for that species. In the case of H and He the ionization potentials are 13.6 eV and 24.5 eV. These correspond to threshold wavelengths of 91 and 51 nm respectively. Only photons with wavelengths shorter (or frequencies higher) than the threshold value are capable of ionizing. Thus photons in the EUV region of the spectrum are responsible for the ionization. The photoionization rate is calculated by integrating the EUV flux multiplied by the photoionization cross section, $\alpha_{pi}(\nu)$, over all ionizing frequencies (i.e. for $\nu > \nu_c$, where ν_c is the threshold frequency).

The Photoionization Cross Sections

The photoionization cross sections for H and He are compiled by Osterbrock (1989). Generally, they rise from zero at the threshold frequency very quickly to a sharp peak. The peak values for H and He are $6.4 \times 10^{-18} \text{ cm}^2$ and $7.9 \times 10^{-18} \text{ cm}^2$ respectively. At the peak frequency, solar photons are expected to penetrate into the VLISM a distance of order $(n\alpha_{peak})^{-1}$ where n is the mean density of the absorbing species

and α_{peak} is the peak photoionization cross section. Using typical VLISM values of $n_H = 0.1 \text{ cm}^{-3}$ and $n_{He} = 0.01 \text{ cm}^{-3}$ the penetration distance is $\sim 10^5 \text{ AU}$ for H and $\sim 10^6 \text{ AU}$ for He. These distances are much larger than the pertinent heliospheric length scales so the solar EUV flux does not suffer significant absorption due to photoionization and falls as r^{-2} .

The Solar EUV Spectrum

The EUV wavelength region is difficult to monitor continuously because the observations need to be performed from spacecraft above Earth's EUV absorbing atmosphere. However, as noted by Lean (1987, 1990), the EUV irradiance is essential in studies of planetary atmospheres, and periodic measurements have been conducted by various spacecraft. The solar EUV spectrum is composed of several emission lines lying on top of a relatively weak continuum. For wavelengths shortward of 90 nm, the spectrum is highly variable over the 25 day solar rotation period and the 11 year sunspot cycle. The EUV spectrum and variability are reviewed in detail by Lean (1987).

Photoionization Loss Rates

The photoionization rate is calculated by integrating the solar EUV flux multiplied by the photoionization cross section over all ionizing frequencies:

$$\beta_{pi}(\mathbf{r}, t) = \left(\frac{r_e}{r}\right)^2 \int_{\nu_c}^{\infty} d\nu \alpha_{pi}(\nu) F_{\odot}(\nu, \lambda, \beta, t), \quad (2.24)$$

where ν is the frequency (Hz), F_{\odot} is the solar EUV flux ($\text{photons cm}^{-2} \text{ s}^{-1} \text{ Hz}^{-1}$) measured at $r_e = 1 \text{ AU}$ and emitted from the Sun at heliocentric longitude and latitude (λ, β) . The integral in equation (2.24) is the loss rate at 1 AU, $\beta_{pi,e}$.

Observations of the solar EUV spectrum are not continuous enough to allow a detailed calculation of β_{pi} for either H or He at a specific time or emission angle from the Sun. Because of this, average photoionization rates representing particular phases

of the solar cycle are generally the best that are available. Torr et al. (1979) and Torr and Torr (1985) give representative EUV fluxes measured during the 1970's. Ajello et al. (1987) estimate that the H photoionization rate at 1 AU varies over the range $(0.55\text{--}1.2) \times 10^{-7} \text{ s}^{-1}$ during the solar cycle. A typical value for He is $4.0 \times 10^{-8} \text{ s}^{-1}$ (Axford, 1972).

2.2 Distributions Neglecting Production Terms

If one neglects the production term in the Boltzmann equation (2.10), the solution may be written by specifying the boundary condition distribution function, f_o , and calculating the associated losses, $\Lambda(t_o, t)$. This simplifies the problem considerably. Nonetheless the general problem neglecting production is still difficult because the combined effects of solar flux anisotropies and a net VLISM flow imply that the distributions are 3-dimensional in character. A discussion of simpler solutions possessing more fundamental symmetry is a useful exercise. It helps build a familiarity with the effects of the individual physical phenomena at work in the heliosphere. Moreover, restricted analytical solutions are needed to verify the performance of large numerical computer codes required by more general calculations.

The symmetry of the solution depends on the assumptions employed. For instance, assuming no solar flux anisotropies, no VLISM magnetic fields, and no net flow relative to the Sun, implies spherically symmetric distributions. Other assumptions, such as including a bulk VLISM flow, imply axially symmetric solutions. The utility of investigating both spherically and axially symmetric solutions may be evaluated by comparing the characteristic VLISM thermal speed, $v_{th,\infty}$, and bulk flow speed, v_∞ . If the thermal speeds are much greater than the bulk flow speed, one would expect the distribution to be roughly spherically symmetrical because the influence of the bulk flow would be small compared to the thermal dispersion. On the other hand, if $v_{th,\infty} \ll v_\infty$, an axially symmetric solution may be derived by approx-

imating the VLISM as a cold flow. Neither of these two extreme cases hold for the actual heliospheric distribution. Assuming a VLISM temperature of $T_\infty = 10^4$ K, the thermal speeds for H and He atoms are 12.8 km s^{-1} and 6.4 km s^{-1} respectively. These are somewhat less than, but roughly comparable to, the bulk VLISM flow speed, $v_\infty \approx 22 \text{ km s}^{-1}$. The H and He atoms penetrating directly from the VLISM are therefore expected to be distributed in an axially symmetric fashion. However, the component of the H distribution produced by charge exchange in the heliosheath is expected to have a temperature $\geq 10^6$ K, which corresponds to thermal speeds $\geq 100 \text{ km s}^{-1}$. For this component, the distribution is expected to bear at least some resemblance to the spherically symmetric solution.

2.2.1 Spherically Symmetric Distributions

If the Sun were immersed in a homogenous VLISM with no magnetic field and no net relative motion, and the solar wind and EUV fluxes were isotropic, the distribution of neutrals would be spherically symmetric about the Sun. However, in such an imaginary system, the physical processes of ionization, gravitation and radiation pressure still would contribute to a non-uniform distribution of the neutrals. In this section, two restricted spherically symmetric problems are addressed to demonstrate these general effects. The first solution demonstrates the effects of gravitation and radiation pressure on the distribution. The second illustrates the effects of ionization.

Solution with No Ionization

A simple solution that neglects the processes of charge exchange and photoionization demonstrates the effects of gravitation and radiation pressure. Three assumptions are employed here: 1) the production and loss terms are negligible, 2) the gravitation and radiation pressure forces are derivable from a spherically symmetric, conservative

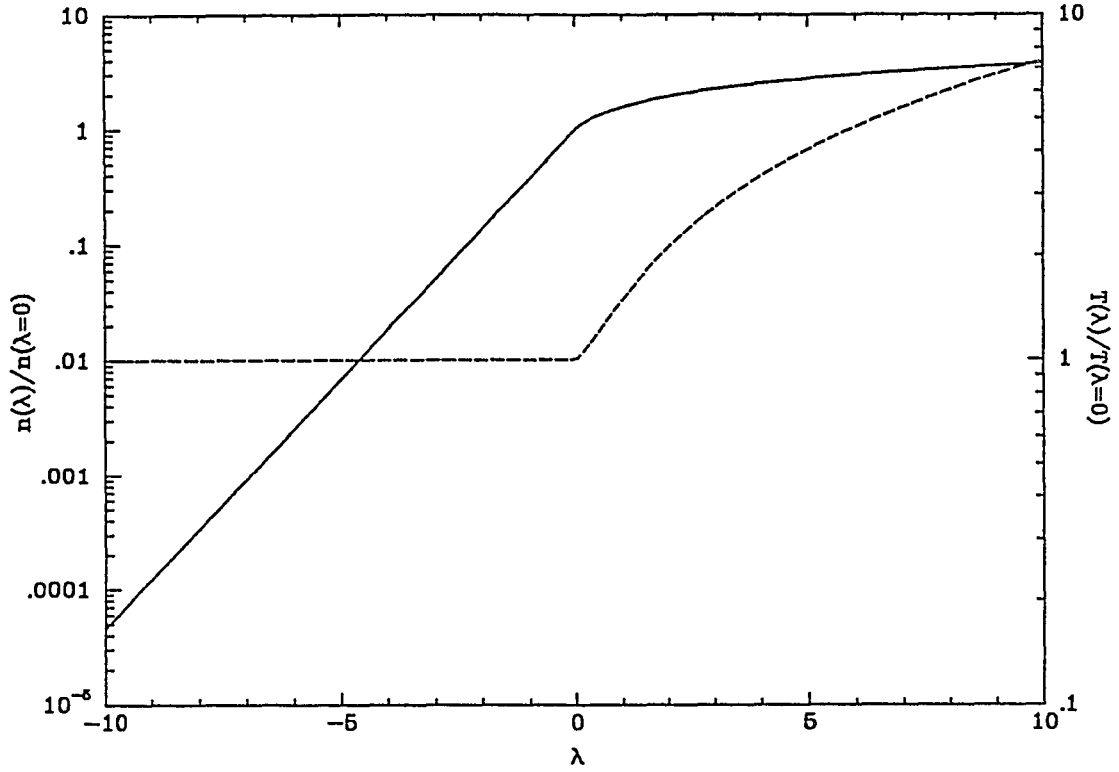


Figure 2.1: The normalized density and temperature of a neutral gas in a $1/r$ potential with no ionization. The density relative to the value at infinite distance is plotted as the solid curve and the normalized temperature as the dashed curve. For attractive potentials ($\lambda > 0$) the densities and temperatures are enhanced near the force center. Radiation pressure can create repulsive potentials ($\lambda < 0$), where the densities are diminished but the system is isothermal.

potential of the form

$$V(r) = -\frac{GM_{\odot}(1 - \mu_{\odot})}{r}, \quad (2.25)$$

where the radiation pressure parameter, μ_{\odot} is constant, and 3) the only source is the distant VLISM which is in thermal equilibrium. The last assumption implies that the boundary condition distribution function, f_{\odot} , used in equation (2.10) is a Maxwellian with no bulk velocity relative to the Sun and the boundary condition is imposed at infinite distance from the Sun. With these assumptions the distribution is written

$$f(r, v) = n_{\infty} (v_{th, \infty} \sqrt{\pi})^{-3} \exp \left[- \left(\frac{v_{\odot}}{v_{th, \infty}} \right)^2 \right] U_{step}(v_{\odot}^2), \quad (2.26)$$

where n_{∞} and $v_{th, \infty}$ are the density and thermal velocity at infinite distance from the Sun, and the step function, U_{step} , is defined

$$U_{step}(x) = \begin{cases} 0 & \text{if } x < 0 \\ 1 & \text{otherwise} \end{cases} \quad (2.27)$$

The velocity of the neutral at infinite distance, v_{\odot} , is obtained by applying the principal of conservation of energy along the trajectory:

$$v_{\odot}^2 = v^2 - \frac{2GM_{\odot}(1 - \mu_{\odot})}{r} = v^2 - v_e^2, \quad (2.28)$$

where v_e is the escape energy which is real only for non-repulsive potentials ($\mu_{\odot} \leq 1$). Negative values of v_{\odot}^2 imply that the particle does not have enough energy to escape from the solar gravitational well. Such bound particles cannot exist because the third assumption above states that all particles originate from the infinitely distant VLISM. This is mathematically included using the step function in equation (2.26). As can be seen in equations (2.26) and (2.28), the distribution function only depends on the magnitude of the velocity and not its direction. The distribution is therefore isotropic and bulk velocities vanish for all r . Integrating equation (2.26) over all velocities yields the density:

$$n(r) = n_{\infty} e^{\lambda(r)} \left[\frac{2u_c e^{-u_c^2}}{\sqrt{\pi}} + \text{erfc}(u_c) \right], \quad (2.29)$$

where the parameters $\lambda(r)$ and u_c are defined

$$\lambda(r) \equiv \frac{2GM_\odot m(1 - \mu_\odot)}{rk_B T_\infty}, \quad (2.30)$$

and

$$u_c \equiv \text{Re} \left[\sqrt{\lambda(r)} \right]. \quad (2.31)$$

Here $\text{Re}(x)$ denotes the real part of x . The complimentary error function is defined from the error function given in equation (2.20):

$$\text{erfc}(x) \equiv 1 - \text{erf}(x). \quad (2.32)$$

The quantity $\lambda(r)$ is familiar from the theory of extended planetary atmospheres (see Fahr and Shizgal, 1983; Chamberlain and Hunten, 1987). The problem of atoms escaping from planetary exospheres shares many similarities to the problem at hand. But here λ may be negative because of radiation pressure. Figure 2.1 shows a plot of $n(r)/n_\infty$ as calculated from equation (2.29). The density is enhanced for attractive potentials where $\lambda > 0$. For repulsive potentials, the density is diminished because the radiation pressure tends to exclude the particles. In the limit where the distant VLISM distribution has zero temperature ($v_{th,\infty} \rightarrow 0$), the region defined by $\lambda < 0$ has zero density because the repulsive potential excludes all particles. In the cases where the potential is attractive the distribution in velocity space has a spherical hole about the origin with a radius equal to the escape velocity (see equation (2.26)). This has the effect of increasing the effective temperature of the gas. Using equation (2.7) and (2.26) the effective temperature may be calculated:

$$T(r) \equiv \frac{m\overline{\Delta v^2}}{3k_B} = T_\infty \left(\frac{2e^{\lambda(r)}n_\infty}{3n(r)} \right) \left[\frac{2u_c e^{-u_c^2}}{\sqrt{\pi}} \left(u_c^2 + \frac{3}{2} \right) + \frac{3}{2} \text{erfc}(u_c) \right]. \quad (2.33)$$

Figure 2.1 shows a plot of T/T_∞ . For attractive potentials ($\lambda > 0$) the temperature is enhanced. For repulsive potentials the system is isothermal.

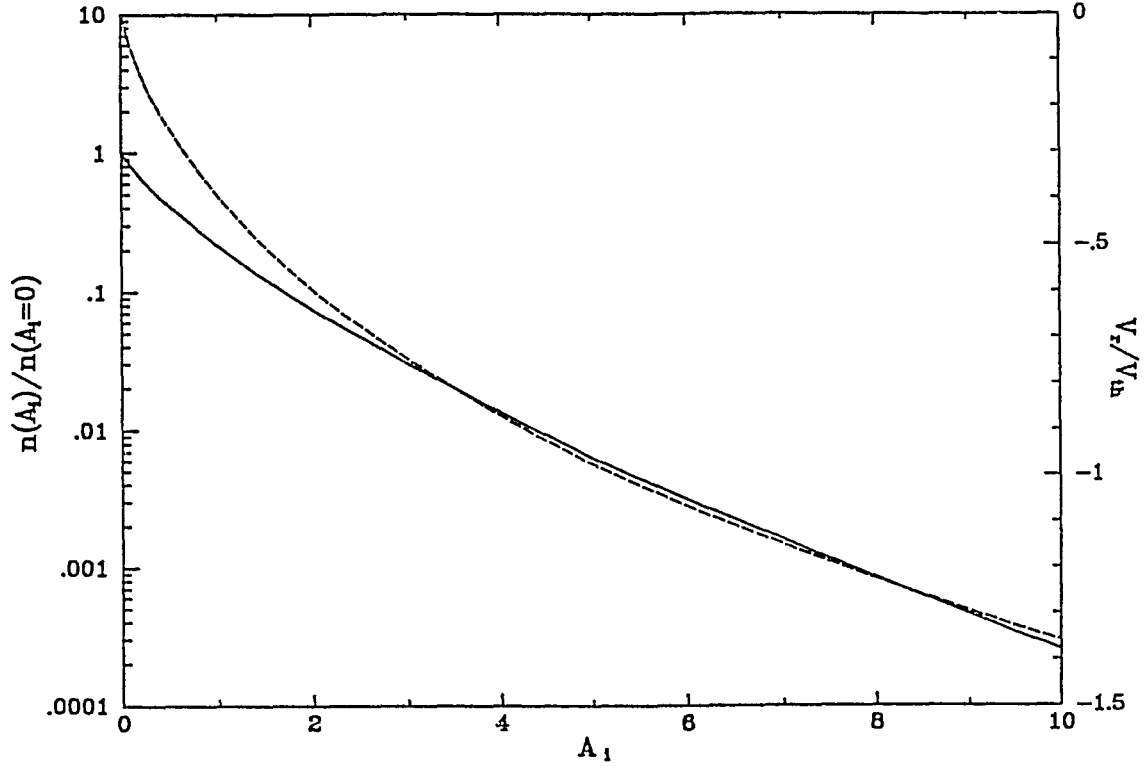


Figure 2.2: The normalized densities and radial velocities of a gas in a force-free system with a central ionization source. The density relative to the value at infinite distance is plotted as the solid line. As the ionization parameter, $A_i = (\beta_e r_e^2)/(rv_{th,\infty})$, is increased the density decreases. The radial speed relative to the thermal speed at infinity, $v_r/v_{th,\infty}$ is plotted as the dashed line.

Solution with No Gravitation or Radiation Pressure

To evaluate the effects of ionization, the effects of gravitation and radiation pressure may be eliminated by assuming that the repulsive radiation pressure force perfectly balances gravity ($\mu_{\odot} = 1$). This simplifies the problem considerably, because the particle trajectories are straight lines. Four assumptions are employed here: 1) the combined gravitation and radiation pressure forces vanish, 2) the production terms are negligible, 3) the loss rate has the form

$$\beta(r) = \frac{\beta_e r_e^2}{r^2}, \quad (2.34)$$

and 4) the only source is the distant VLISM which is uniform and is in thermal equilibrium. With these assumptions the distribution may be calculated from equation (2.10):

$$f(\mathbf{r}, \mathbf{v}) = n_{\infty} (v_{th,\infty} \sqrt{\pi})^{-3} \exp \left[- \left(\frac{v}{v_{th,\infty}} \right)^2 \right] e^{-\Lambda_{\infty}}. \quad (2.35)$$

The quantity Λ_{∞} represents the loss of the VLISM neutrals by ionization. Combining equations (2.9) and (2.34) and integrating yields:

$$\Lambda_{\infty} = \frac{\beta_e r_e^2 (\pi - \theta_v)}{rv \sin(\theta_v)}, \quad (2.36)$$

where θ_v is the angle between the velocity vector \mathbf{v} and the position vector \mathbf{r} . An order of magnitude estimate of how close the particles may approach the Sun before being ionized is obtained by equating this parameter to unity and assuming purely inward motion ($\theta_v = \pi$). This yields the penetration distance

$$R_i \sim \beta_e r_e^2 / v. \quad (2.37)$$

Using thermal and/or VLISM bulk flow speeds in this formula provides a handy estimate of the ionization cavity length scale. Faster particles penetrate farther into the system than slower ones. Also, from equation (2.36), it is evident that particles

traveling radially inward are less likely to be ionized than those travelling tangentially or outward. In fact, particles travelling radially outward have necessarily encountered the Sun at small radial distances and have a higher ionization probability because of the r^{-2} dependence of the ionization rate. Therefore, the distribution in velocity space is more populated for radially inward directed velocities than for the tangential and outward directions. This means that the net flow of the gas is inward toward the Sun. The density, bulk velocity and effective temperatures may be numerically calculated by integrating the distribution function over all velocities. They are functions of the dimensionless parameter

$$A_i = \frac{\beta_e r_e^2}{r v_{th,\infty}}. \quad (2.38)$$

Figure 2.1 shows a plot of the normalized densities and radial bulk flow speeds as a function of A_i . In the supersonic solar wind region, the ionization parameter for the penetration of VLISM H is $A_i \approx 6\text{AU}/r$. For VLISM He it is $A_i \approx 0.2\text{AU}/r$.

2.2.2 The Cold Heliospheric Distribution

As mentioned earlier, the VLISM thermal speeds of H and He are thought to be somewhat less than the bulk flow speed relative to the Sun. Idealizing the VLISM as a cold flow is therefore a reasonable first approximation, and should yield some of the general physical effects of introducing a net VLISM flow into the problem. (This approximation is superseded by a solution assuming a finite VLISM temperature as described in the next section.) Early work on the cold distribution was done by Fahr (1968), Blum and Fahr (1970), Holzer and Axford (1971), Holzer (1972) and others. An excellent summary is given by Axford (1972) where details on the early formulation of the theory may be found. Here a brief condensation of the theory is given, focused mainly on the points that provide insight on the structure of the distribution.

The usual formulation of the cold distribution assumes that VLISM magnetic

fields and solar flux anisotropies are negligible so the distributions of the neutrals are expected to be axially symmetric. The axis of symmetry passes through the Sun along the bulk VLISM flow direction. The motion of the particles is influenced by gravity and radiation pressure, as derived from the potential given in equation (2.25). The production terms are neglected, and the loss rate is assumed to fall as r^{-2} as given in equation (2.34).

The coordinate system used here is oriented such that the z -axis is pointed in the upstream direction. Axial symmetry requires a 2-dimensional solution of the Boltzmann equation. The two coordinates most often used are the radial distance, $r = |\mathbf{r}|$, and the axial angle, $\theta = \cos^{-1}(z/r)$. In some cases, it is more convenient to use cylindrical coordinates (ρ, z) where $\rho^2 = x^2 + y^2$.

The VLISM bulk flow vector at large distances from the Sun is:

$$\mathbf{v}_\infty = -\hat{z} v_\infty, \quad (2.39)$$

where \hat{z} is the unit vector in the direction of the positive z -axis. A cold VLISM flow means that the boundary condition distribution function, f_o , is given by a δ -function in velocity space:

$$f_o(\mathbf{r}_o, \mathbf{v}_o) = n_\infty \delta^3(\mathbf{v}_o - \mathbf{v}_\infty). \quad (2.40)$$

All of the source particles enter the system travelling parallel to the z -axis. Their trajectories are hyperbolae with the Sun as focus each characterized by the magnitude of their specific angular momentum, p_o :

$$p_o = v_\infty \rho_o, \quad (2.41)$$

where ρ_o is the impact parameter.

For net repulsive potentials ($\mu_\odot > 1$), there is a region from which the particles are excluded because their energy is inadequate to overcome the repulsive potential.

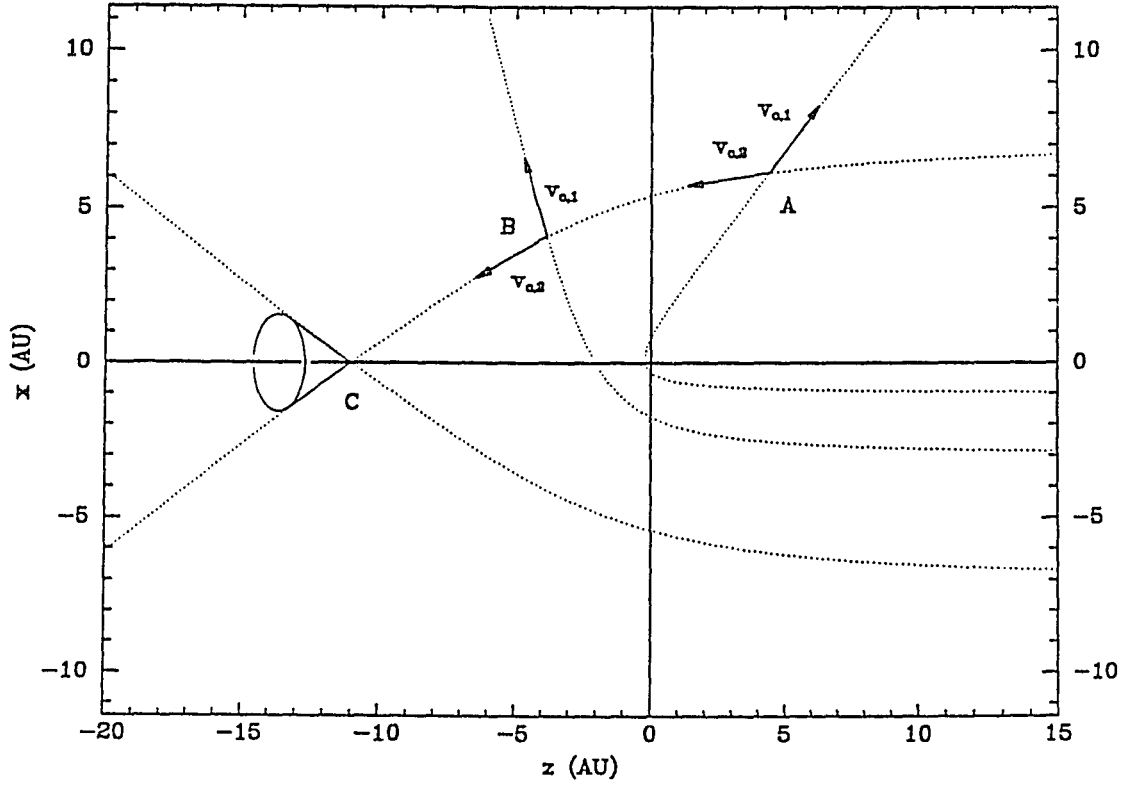


Figure 2.3: Representative trajectories in the Heliospheric cold distribution. Here four trajectories are shown as dotted lines defining the cold distribution at three points A, B and C. The density of the penetrating neutrals at the points A and B is given by the sum of the densities of particles travelling along each of the two trajectories. Point A lies in the upstream region, implying that particles on one of the two trajectories have passed their perihelia, are outbound and have suffered more ionization loss than the inbound stream. Point C is located on the downstream axis where an infinite number of cold trajectories intersect and whose velocities lie on the illustrated cone. This effect leads to a singularity on the downstream axis where the cold density diverges.

This forbidden region is defined by the expression:

$$r(1 + \cos \theta) \leq \frac{4GM_{\odot}(\mu_{\odot} - 1)}{v_{\infty}^2}, \quad (2.42)$$

and has a roughly parabolic shape extending into the downstream direction.

Any point (r, θ) not lying in the forbidden region or on the axis of symmetry is a point where two trajectories from the cold VLISM flow intersect. The distribution at these points is given by the sum of two δ -functions in velocity space:

$$f(\mathbf{r}, \mathbf{v}) = n_{c,1} \delta^3(\mathbf{v} - \mathbf{v}_{c,1}) + n_{c,2} \delta^3(\mathbf{v} - \mathbf{v}_{c,2}), \quad (2.43)$$

where the densities $n_{c,i}$ and velocity vectors $\mathbf{v}_{c,i}$ correspond to the two separate trajectories (see Axford, 1972, for the expressions). This is illustrated for two points **A** and **B** in Figure 2.3. The densities $n_{c,1}$ and $n_{c,2}$ are generally not equal because the two trajectories are distinct, and the ionization losses accumulated along the path are generally not the same. For instance, in the upstream region (point **A** in Figure 2.3), the particles on one of the two trajectories have necessarily passed their perihelion points and are proceeding outward. Particles on the other trajectory are proceeding inward. The former set of particles suffer much more ionization loss because of the r^{-2} dependence of the loss rate. So the density of the outbound particles is lower than the inbound particles.

On the upstream axis, only one trajectory incident from the upstream direction exists. Particles on the other trajectory would have necessarily encountered the Sun. On the downstream axis, in the case of attractive potentials, an infinite number of trajectories cross any given point and the total cold model density diverges (see point **C** in Figure 2.3). This downstream singularity is removed when the VLISM flow is assumed to have a non-zero temperature.

2.2.3 The Hot Heliospheric Distribution

The cold heliospheric distribution serves as a first approximation but is inadequate for two reasons. First, the rough comparability of the VLISM thermal speeds and bulk flow speed suggests that in the real heliosphere, departures from the cold distribution may be significant. This is especially true concerning the downstream density singularity and forbidden region inherent in the cold model. Second, the VLISM temperature may be estimated from heliospheric resonance observations only if it is included as a model parameter. Therefore the cold model is superseded by the heliospheric hot distribution. However, many of the concepts presented in the description of the cold model are useful here.

The influence of a finite VLISM temperature on the heliospheric distribution of neutrals is discussed by Danby and Camm (1957), Fahr (1971), Thomas (1972) and others. Meier (1977) and Thomas (1978) give detailed summaries. Here a brief description of the hot model is given, once again focusing on the physical effects rather than detailed derivations. The formulation is taken mostly from Meier (1977).

The Hot Distribution Function

The assumptions employed to derive the hot distribution are the same as in the cold model except the source distribution function, f_o , is assumed to be a Maxwellian:

$$f_o(\mathbf{r}_o, \mathbf{v}_o) = n_\infty (\sqrt{\pi} v_{th,\infty})^{-3} \exp \left[- \left(\frac{\mathbf{v}_o - \mathbf{v}_\infty}{v_{th,\infty}} \right)^2 \right], \quad (2.44)$$

where \mathbf{v}_∞ is given by equation (2.39). This source distribution is applied as a boundary condition at infinite heliocentric distance. Inserting equation (2.44) into (2.10), yields the distribution function:

$$f(\mathbf{r}, \mathbf{v}) = n_\infty (\sqrt{\pi} v_{th,\infty})^{-3} \exp \left[- \left(\frac{\mathbf{v}_o - \mathbf{v}_\infty}{v_{th,\infty}} \right)^2 \right] (e^{-\Lambda_\infty}) U_{step}(v_o^2), \quad (2.45)$$

where Λ_∞ represents the loss of particles as they travel in from infinite distance, v_o is given by equation (2.28) and the step function, $U_{step}(v_o^2)$, accounts for the fact that there are no bound particles in the system. By solving Kepler's equation for the trajectories, the term in the exponential in equation (2.45) is expressed:

$$\left(\frac{\mathbf{v}_o - \mathbf{v}_\infty}{v_{th,\infty}} \right)^2 = \frac{1}{(v_{th,\infty})^2} \left[v_o^2 + v_\infty^2 + 2v_\infty v_o \left(\frac{v_z(v_o - v_r) - V(r) \cos \theta}{v_o(v_o - v_r) - V(r)} \right) \right], \quad (2.46)$$

where v_r and v_z are the radial and z direction components of the velocity vector \mathbf{v} , and $V(r)$ is the potential given in equation (2.25). For ionization loss of the form given in equation (2.34), the loss integral may be written:

$$\Lambda_\infty = \frac{\beta_e r_e^2 \theta'}{v_o p_o}, \quad (2.47)$$

where θ' is the angle swept out by the atom on its Keplerian trajectory and $p_o = |\mathbf{r} \times \mathbf{v}|$ is the specific angular momentum.

Comparison of the Hot and Cold Distributions

The heliospheric H and He distributions are best described as warm because for each $v_{th,\infty}$ is less than, but comparable to, v_∞ . The concepts developed in the cold model help understand the structure of the hot distribution. In the limit $v_{th,\infty} \rightarrow 0$, the hot distribution function reduces to the double δ -function form given in equation (2.43)—except on the VLISM flow axis and in the forbidden region. Thus it makes sense that in the case of a warm flow, the distribution of particles in velocity space should be centered about the cold velocity vectors as shown in Figure 2.3; for points **A** and **B** there are two populated regions in velocity space centered on or near these vectors. These two regions generally have unequal size and density because of the different ionization losses suffered by the particles.

On the downstream axis, when $\mu_\odot < 1$, the populated region in velocity space actually assumes a form similar to a torus, which is centered on or near the rim of the

cone illustrated at point **C** in Figure 2.3. The downstream singularity is eliminated in the hot distribution. But the density on the downstream axis may be considerably enhanced over the VLISM value for low ionization and low radiation pressure (as is the case for the He distribution). Similarly, in the case where $\mu_{\odot} > 1$, the forbidden region is eliminated. But the corresponding region in the hot model may be substantially depleted.

2.2.4 “Standard” H and He Hot Distributions

The density of the hot distribution may be numerically calculated by integrating the distribution function (2.45) over all velocities. It is clear from the description above that the hot distribution function is not Maxwellian, nor is it simple in morphology. Accurately integrating the hot distribution function using numerical techniques requires careful attention. The hot distribution function has been integrated by several authors including Thomas (1978) and Wu and Judge (1979a). The latter authors report flow speeds and velocity dispersions along solar radii. These quantities are of interest because they determine the Doppler shifts and widths of singly scattered heliospheric H and He resonance line absorption and emission profiles. Here the hot distribution function is integrated using an algorithm similar to that of Wu and Judge (1979a). The results of both Thomas (1978) and Wu and Judge (1979a) are reproduced to within 5% for all heliocentric radii greater than 1 AU.

The parameters needed to calculate the hot distribution for a given neutral species are: 1) the total ionization rate at 1 AU, β_e , 2) the radiation pressure parameter, μ_{\odot} , 3) the VLISM flow speed relative to the Sun, v_{∞} , and 4) the VLISM temperature, T_{∞} . It is useful to define “standard” H and He distributions using what are believed to be typical values for these parameters. These will be used in the analyses in later chapters. As stated before, typical VLISM parameters are $v_{\infty} \approx 20 \text{ km s}^{-1}$ and $T_{\infty} \approx 10^4 \text{ K}$. Here two sets of parameters are selected to illustrate the solar

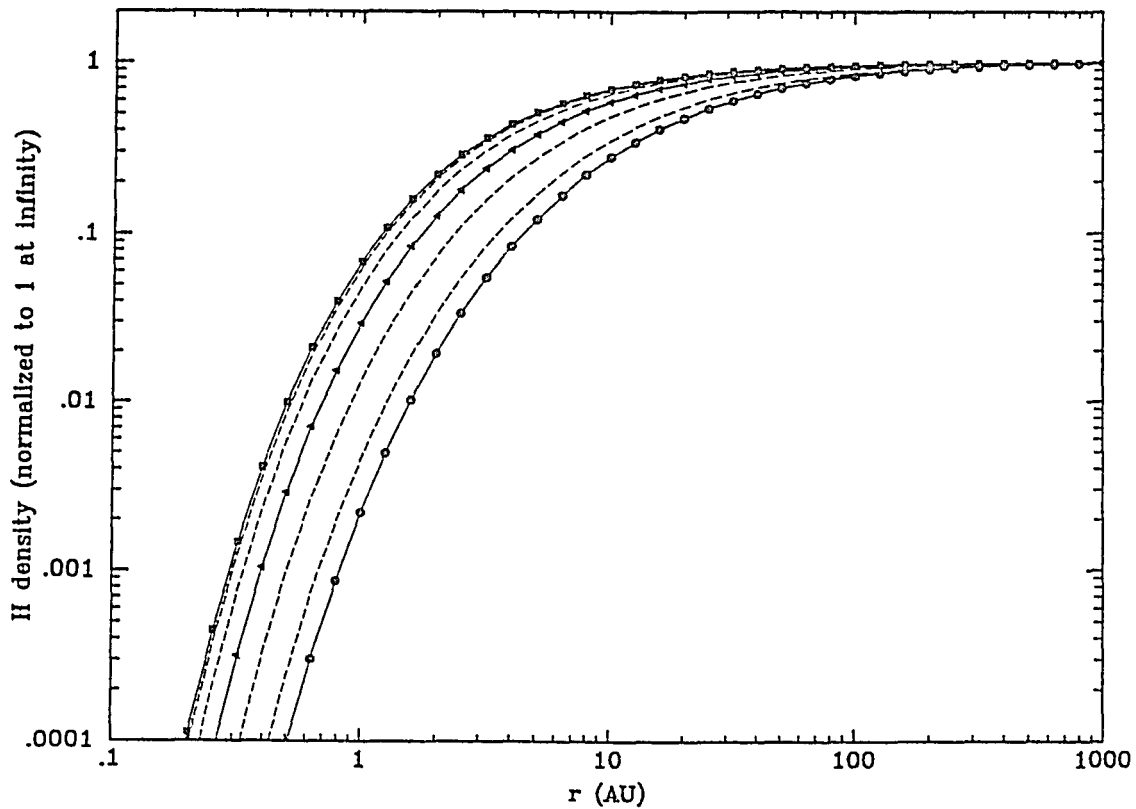


Figure 2.4: The solar minimum standard heliospheric H hot distribution. The integrated H densities relative to the value at infinity are plotted for several axial angles. The upstream ($\theta = 0^\circ$), sidestream ($\theta = 90^\circ$) and downstream ($\theta = 180^\circ$) distributions are marked with squares, triangles and circles respectively. Intermediate values of the axial angle $\theta = 30, 60, 120$ and 150° are shown as the intervening dashed lines. The parameters used for this distribution are: $v_\infty = 20 \text{ km s}^{-1}$, $T_\infty = 10^4 \text{ K}$, $\beta_e = 5 \times 10^{-7} \text{ s}^{-1}$, and $\mu_\odot = 0.75$.

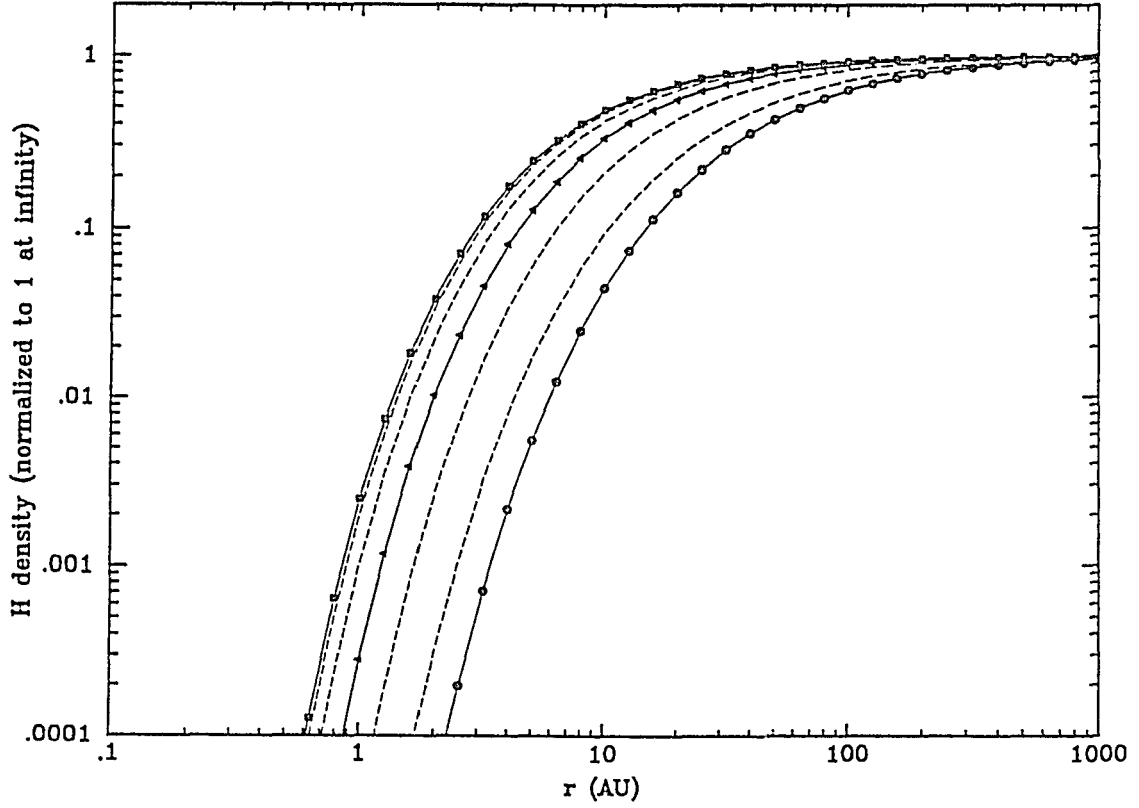


Figure 2.5: The solar maximum standard heliospheric H hot distribution. The integrated H densities relative to the value at infinity are plotted for several axial angles in the same format as described in the previous figure. The parameters used for this distribution are: $v_{\infty} = 20 \text{ km s}^{-1}$, $T_{\infty} = 10^4 \text{ K}$, $\beta_e = 10 \times 10^{-7} \text{ s}^{-1}$, and $\mu_{\odot} = 1.20$.

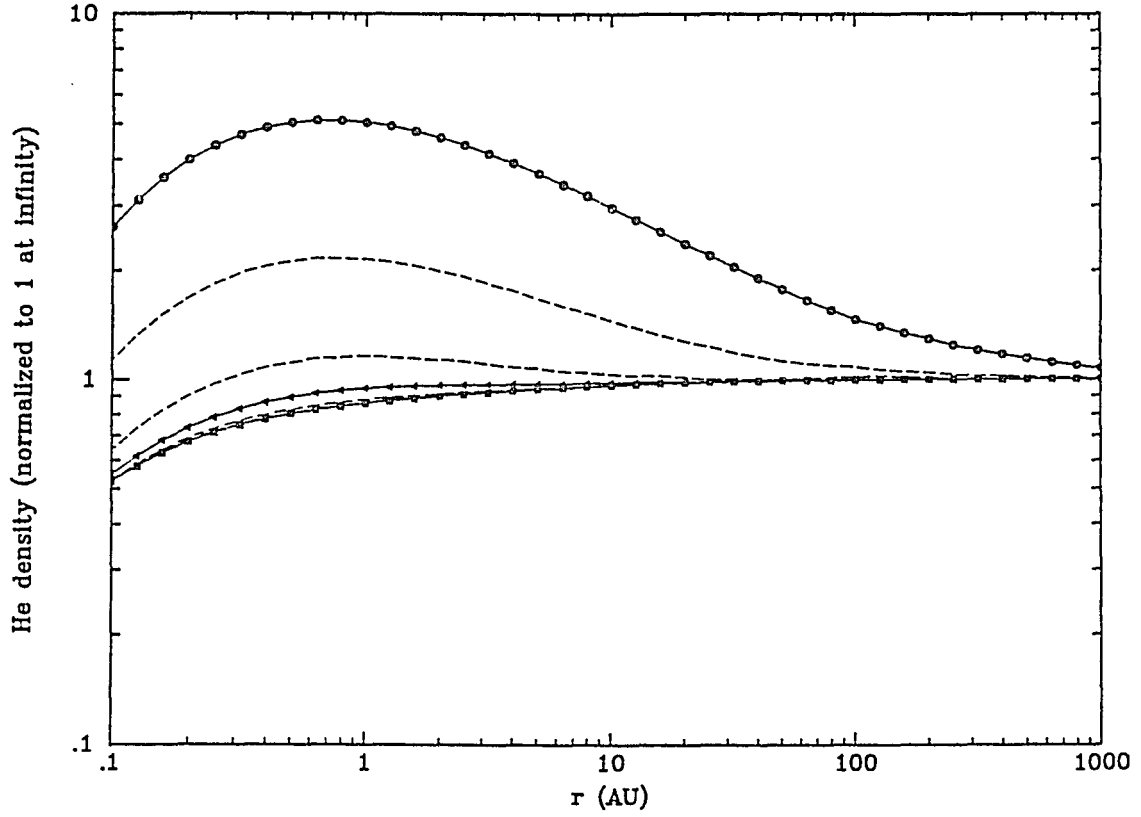


Figure 2.6: The standard heliospheric He hot distribution. The integrated He densities relative to the value at infinity are plotted for several axial angles in the same format as described in the two previous figures. The parameters are: $v_{\infty} = 20 \text{ km s}^{-1}$, $T_{\infty} = 10^4 \text{ K}$, $\beta_e = 7.5 \times 10^{-8} \text{ s}^{-1}$, and $\mu_{\odot} = 0.0$.

cycle variation of the hot H distribution (see Ajello et al., 1987). The solar minimum parameters are chosen to coincide with those of Thomas (1978): $\beta_e = 5 \times 10^{-7} \text{ s}^{-1}$ and $\mu_\odot = 0.75$. For solar maximum conditions the parameters are: $\beta_e = 10 \times 10^{-7} \text{ s}^{-1}$ and $\mu_\odot = 1.20$. Typical values for He are also from Thomas (1978): $\beta_e = 7.5 \times 10^{-8} \text{ s}^{-1}$ and $\mu_\odot = 0$. The integrated densities for these parameters are shown in Figures 2.4, 2.5 and 2.6. The major feature of the H distribution is the ionization cavity elongated in the downstream region. At times of large radiation pressure, the downstream region is further depleted. The He distribution clearly shows the density enhancement in the downstream region due to gravitational focusing.

2.3 A Multi-Component H Distribution Model

All of the distributions described above are derived assuming that the production term, P , in the Boltzmann equation is negligible. When production due to charge exchange is included two complications arise. First, the production terms in the Boltzmann equation (2.10) depend on the H distribution, resulting in a true integral equation; obtaining solutions requires either considerable analytical effort or numerical techniques. Second, the H-p charge exchange reactions occurring in the heliosphere produce two populations of H atoms that are distinctly different than the component penetrating from the VLISM. The H distribution is divided sensibly into three distinct components: 1) the H atoms penetrating from outside the heliopause, 2) H atoms created by charge exchange in the subsonic solar wind, and 3) those created in the supersonic solar wind. This section describes a model of the heliospheric H distribution that separately considers these three components. The first two components are referred to as “thermal” and “suprathermal” respectively, even though this is not a completely accurate description. The third, referred to as the splash component, is dismissed because it does not significantly affect heliospheric $\text{Ly}\alpha$.

The plasma flow model employed here is based mainly on that of Suess and Ner-

ney (1990, 1991) who generalize Parker's (1963) model to include a SWTS of finite size. They consider the interaction of the VLISM and subsonic solar wind as incompressible and irrotational fluids. The H distribution is calculated under the assumption that the plasma distribution does not depend significantly on the neutrals. In other words, the effects of the charge exchange process on the plasma flow are neglected. Holzer (1972) investigates the effect the neutrals have on the supersonic solar wind. The major effect is a deceleration and heating of the plasma flow by the introduction of pick-up protons created by charge exchange in the solar wind. In principal, this effect could lead to a shock-free transition from supersonic to subsonic flow but Holzer (1972) concludes that this is unlikely for $n_{\text{H}\infty} < 0.2\text{cm}^{-3}$. Here these effects are neglected; unless otherwise stated, the supersonic solar wind is approximated as a cold flow at constant velocity that terminates in a hydromagnetic shock.

Outside the SWTS, the validity of decoupling the neutrals and plasma has been investigated by Ripken and Fahr (1983). The process of charge exchange transfers momentum between protons and the H atoms. This momentum exchange acts as a volumetric force on the proton fluid. When comparing this force to the forces associated with magnetic and thermal pressures, Ripken and Fahr (1983) derive values for the critical VLISM H density above which the decoupled assumption is not valid. In the case of a subsonic VLISM flow they find the critical value to be 0.27 cm^{-3} . For a supersonic flow it is 0.55 cm^{-3} . However, by neglecting the effects that charge exchange has on the proton distribution, this calculation neglects an important cooling process in the post-shock solar wind. Therefore, the suprathreshold H densities and temperatures calculated in this model represent upper limits (A. J. Dessler, *private communication*, 1992).

The coupling between the $\text{Ly}\alpha$ radiation field and the H distribution is accounted for by using a radiation pressure parameter, μ_{\odot} , which may depend on the atoms'

velocity and optical depth from the Sun. The effects of multiple scattering on this parameter are investigated in Chapter 3. The parameter decreases with the optical depth from the Sun but does not decrease as quickly as the solar source flux is attenuated because the multiply scattered radiation field partially fills in the absorbed part of the solar source line. The radiative transfer calculations indicate that μ_{\odot} decreases to 80% of its unattenuated value at one line center optical depth from the Sun. At 10 optical depths, the corresponding reduction is 50%. For an H gas of density 0.10 cm^{-3} and temperature 10^4 K , one line center Ly α optical depth corresponds to a photon path length of $\sim 10 \text{ AU}$. Therefore the outer solar system H distribution may be affected by such reduction of the radiation pressure parameter.

2.3.1 The Plasma Model

As discussed in Chapter 1, several models of the VLISM and solar wind plasma interaction exist in the literature. The prevalent features are a termination shock and a transition region between the hot subsonic solar wind plasma and the cooler VLISM plasma. The penetration of VLISM neutrals into the heliosphere through these structures has been discussed extensively by Fahr and coauthors (see Ripken and Fahr, 1983; Fahr and Ripken, 1984; Fahr et al., 1985; Fahr, 1990). The plasma models vary in complexity and detail, but all seem to imply a filtering of VLISM neutrals at the heliospheric interface. This has been confirmed by other authors as well (Bleszinski, 1987; Baranov et al., 1991).

The goal here is to demonstrate the character of the effects of the heliospheric plasma on the H distribution. Neither a detailed nor self-consistent plasma model is employed here, because our poor knowledge of the VLISM magnetic field and proton density do not justify such an effort. The plasma flow is specified by a static proton distribution function, $f_p(\mathbf{r}, \mathbf{v})$. All other ions are neglected. The solar wind is assumed to be a cold, constant speed flow confined by a spherical SWTS. Outside the SWTS,

the plasma distribution function is assumed to be Maxwellian and temperatures are derived using Bernoulli's equation for steady, non-dissipative flow. The bulk flow velocities outside the SWTS are taken from Suess and Nerney (1990, 1991).

The Supersonic Solar Wind

The supersonic solar wind region is assumed to be bounded by a spherical SWTS with radius R_s . It is approximated as a cold, constant speed radial flow so the proton distribution function is δ -function in velocity space:

$$f_p(\mathbf{r}, \mathbf{v}, t) = n_{pe} \left(\frac{r_e}{r} \right)^2 \delta^3(\mathbf{v} - \hat{r} v_{sw}) \quad (r \leq R_s). \quad (2.48)$$

where \hat{r} denotes the radial unit vector. Integrating this over velocity space yields the familiar r^{-2} dependence of the solar wind proton density. The density of protons at $r_e = 1$ AU, n_{pe} , is an input parameter to the model. Typical values are 4 to 10 cm^{-3} .

Plasma Flow Outside the SWTS

The flow in all regions outside the SWTS is taken from Suess and Nerney (1990, 1991), who generalize Parker's (1963) calculation to include an SWTS of finite size (see section 1.3.3). Overall morphologies of the flow field and heliopause shape are determined by the dimensionless parameter

$$\epsilon_s = \left(\frac{v_\infty}{v_{p2}} \right)^{\frac{3}{2}}, \quad (2.49)$$

where the proton speeds in the VLISM and just outside the SWTS are v_∞ and v_{p2} respectively. Suess and Nerney (1990, 1991) emphasize that the details of their solution are not reliable for $\epsilon_s > 0.5$ because the assumption of an irrotational flow breaks down on the flanks of the SWTS. This is not a problem here, since $\epsilon_s \approx 0.10$ for the heliosphere.

The distance, z_c , to the stagnation point (the point on the upstream axis separating the subsonic solar wind from the VLISM flow) is calculated by finding the negative root of the cubic equation

$$\zeta_c^3 - \zeta_c - \epsilon_s = 0. \quad (2.50)$$

The stagnation point distance is

$$z_c = -\frac{R_s \zeta_c}{(\epsilon_s)^{\frac{1}{3}}}. \quad (2.51)$$

The bulk proton flow speeds outside the SWTS are expressed in terms of the cylindrical coordinate system \hat{z} and $\hat{\rho}$ components (see Suess and Nerney, 1990 and 1991, and note that their coordinate system has the z -axis reversed from that used here):

$$\mathbf{v}_{p,bulk}(\mathbf{r}) = \hat{\rho} v_\rho(\mathbf{r}) + \hat{z} v_z(\mathbf{r}), \quad (2.52)$$

where

$$v_z(\mathbf{r}) = v_{p2} \left[(\epsilon_s)^{\frac{2}{3}} \left(\frac{R_s^3 (z^2 - \rho^2/2)}{r^5} - 1 \right) + \frac{R_s^2 z}{r^3} \right], \quad (2.53)$$

and

$$v_\rho(\mathbf{r}) = v_{p2} \left[(\epsilon_s)^{\frac{2}{3}} \left(\frac{3R_s^3 \rho z}{2r^5} \right) + \frac{R_s^2 \rho}{r^3} \right]. \quad (2.54)$$

Given this velocity field, the plasma streamlines are calculated by numerically integrating the trajectories of test particles in the flow. To determine subsonic solar wind streamlines, the initial position of the test particle is somewhere on the sphere $r = R_s$. For VLISM streamlines, the initial position is somewhere far upstream of the interaction region. The shape of the heliopause may be calculated by placing the test particle at the stagnation point, $z = z_c$ and $\rho = 0$. Figure 2.7 shows the heliopause shape for several values of ϵ_s . As pointed out by Suess and Nerney (1990, 1991), larger values of ϵ_s imply smaller heliopause dimensions. Plasma streamlines for $\epsilon_s = 0.1$ are shown in Figure 2.8.

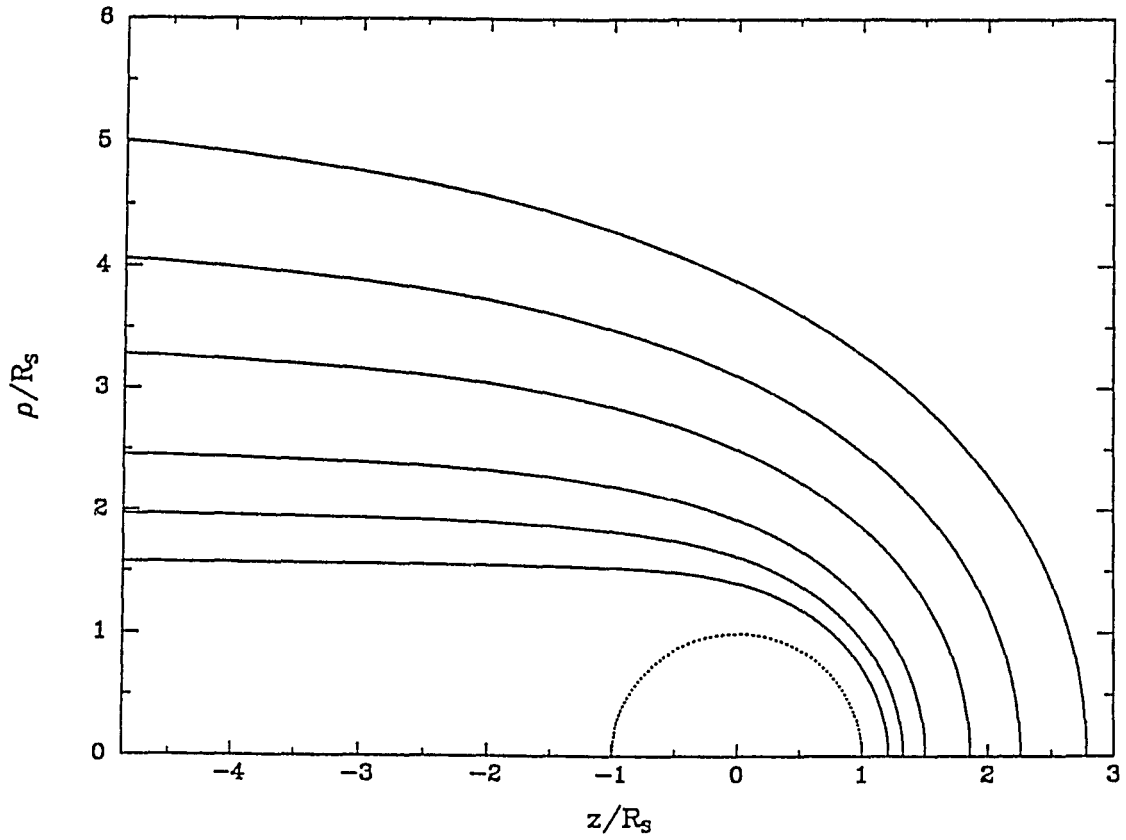


Figure 2.7: Heliopause shapes in the Suess and Nerney (1990, 1991) model for various values of ϵ_s . The shape of the heliopause is shown for $\epsilon_s = 0.05, 0.1, 0.2, 0.5, 1, 2$. The largest values of ϵ_s correspond to the smallest heliopause surfaces. For the heliosphere, $\epsilon_s \approx 0.1$.

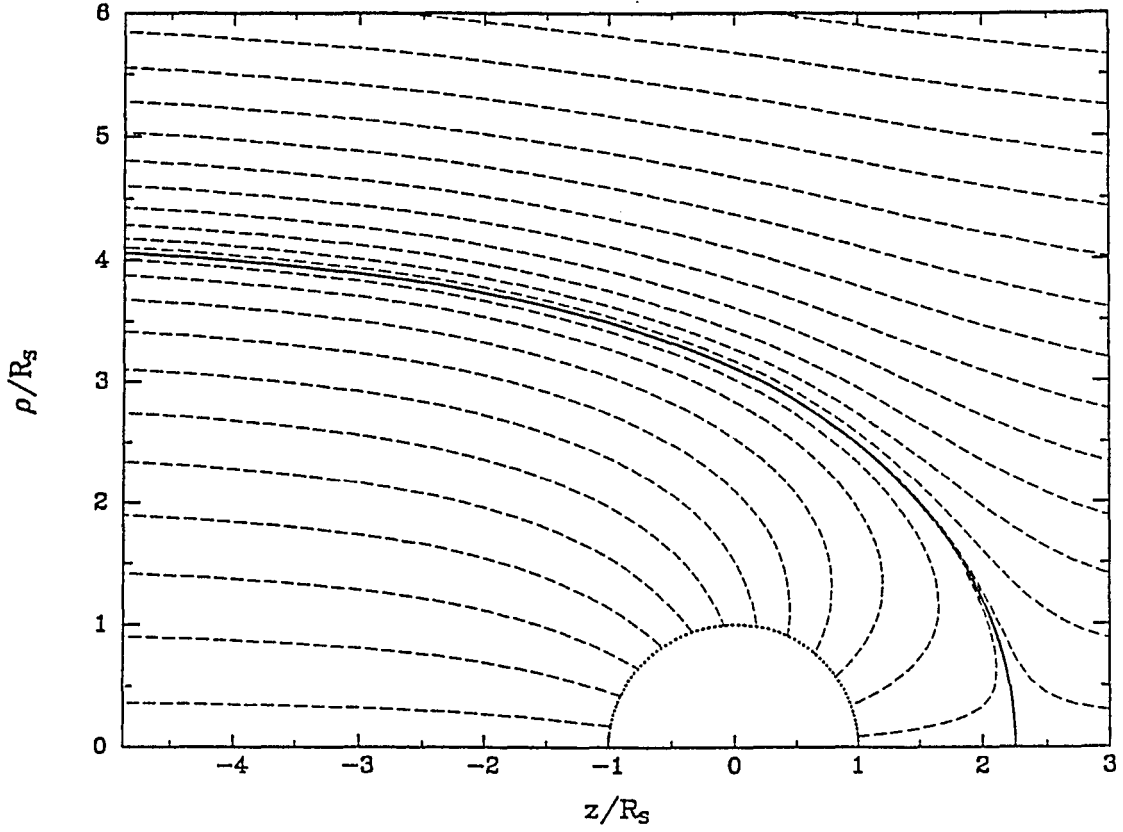


Figure 2.8: Plasma streamlines for the Suess and Nerney (1990, 1991) model for $\epsilon_s = 0.1$. The spherical SWTS is illustrated as the dotted line. Plasma streamlines are shown as the dashed lines. The heliopause is shown as the dark line separating the VLISM streamlines from the subsonic solar wind streamlines.

The Subsonic Solar Wind

The proton distribution in the subsonic solar wind region is assumed to be an incompressible flow. The distribution function is a Maxwellian of the form given in equation (2.5) with constant proton density, $n_p(\mathbf{r}) = n_{p2}$. The proton temperatures in the subsonic solar wind are derived by applying the Bernoulli equation for an incompressible flow (see Ripken and Fahr, 1983):

$$(C_b)_{\text{sw}} = \frac{m_p (v_{p,\text{bulk}})^2}{2} + 2n_{p2}k_B T_p, \quad (2.55)$$

where the factor of two in the second term represents the combined proton and electron pressures. Here $(C_b)_{\text{sw}}$ is the Bernoulli constant for the subsonic solar wind region. It is defined by using the known post-shock density, speed and temperature of the proton distribution given in equations (1.2) and (1.4). Proton temperatures between the SWTS and the heliopause may be calculated by using equations (2.52) and (2.55).

The VLISM Plasma

Following Ripken and Fahr (1983) the proton distribution outside the heliopause is also given by a Maxwellian with constant density and with bulk flow velocities as given in equation (2.52). The temperatures are derived using the Bernoulli equation but with the constant defined using distant VLISM parameters. Unless otherwise stated, the VLISM proton density is assumed to be $n_{p,\infty} = 0.003 \text{ cm}^{-3}$ which is consistent with the observations of Frisch et al. (1987). Pressure equilibrium at the heliopause is not considered explicitly. This is because there are several poorly constrained parameters contributing to the external pressure—the most important of which is the VLISM magnetic field (Holzer, 1989). To achieve a pressure equilibrium at the heliopause, the Bernoulli constants for the subsonic solar wind and VLISM plasmas would have to be equal. Suess and Nerney (1990, 1991) point out the effects of

magnetic field pressures are not likely to be important in the subsonic solar wind region. But the opposite is true in the region outside the heliopause. In addition, there are contributions to the VLISM pressure from galactic cosmic rays that are excluded from the heliospheric region (Holzer, 1989). Therefore a term, χ , which accounts for these pressures should be added to the expression for the VLISM Bernoulli constant:

$$(C_b)_{\text{VLISM}} = \frac{m_p (v_{p,\text{bulk}})^2}{2} + 2n_{p\infty} k_B T_p + \chi. \quad (2.56)$$

Here, χ is assumed *not* to vary with position and may be absorbed into the Bernoulli constant. If one neglects cosmic ray effects, then it is of order the magnetic pressure

$$\chi \sim \frac{B^2}{8\pi}. \quad (2.57)$$

An order-of-magnitude estimate of the VLISM magnetic field strength required to balance the pressure at the heliopause is obtained by equating the VLISM and solar wind Bernoulli constants:

$$B \sim \sqrt{8\pi} \left[\frac{m_p}{2} (v_{p2}^2 - v_\infty^2) + 2k_B (n_{p2} T_{p2} - n_{p\infty} T_\infty) \right]^{\frac{1}{2}}. \quad (2.58)$$

Using nominal solar wind and VLISM parameters, the VLISM field strengths implied by $R_s = 75, 100$ and 200 AU are about $9, 7$ and $3 \mu\text{G}$ respectively. These values are roughly comparable to the the estimated $(5 \pm 3) \mu\text{G}$ for the VLISM (Holzer, 1989).

Another important effect of a VLISM magnetic field is that it raises the fast-mode magneto-acoustic speed and thereby decreases the Mach number of the VLISM flow. In the case of no VLISM field, the VLISM flow likely is supersonic and the assumption of incompressibility is inappropriate (Suess, 1990; Suess and Nerney, 1990, 1991). However, invoking modest VLISM fields of magnitude $1 \mu\text{G}$ implies that the flow is sub-Alfvenic and justifies the assumption of incompressibility.

2.3.2 Multi-Component Theory

The three distinct components to the H distribution have all been discussed in the literature and are reviewed by Holzer (1972). Here we number the components 1, 2

and 3. The first component is composed of the H atoms penetrating from the region outside the heliopause. This “thermal” component has a distribution similar to the hot distribution described above. The second “suprathermal” component consists of the H atoms created in the heliosheath and heliotail, and was proposed as early as 1963 to explain observed Ly α lines which were wider than expected (Patterson, 1963). The third, “splash” component is produced in the supersonic solar wind. Upon examination, the splash component turns out to be negligible for the heliospheric Ly α problem.

The total H distribution function is written as the sum over the three distinct components:

$$f(\mathbf{r}, \mathbf{v}, t) = \sum_{k=1}^3 f_k(\mathbf{r}, \mathbf{v}, t). \quad (2.59)$$

For each, the integral Boltzmann equation (2.10) must be solved. For the thermal component, the boundary condition distribution function is a Maxwellian with the VLISM parameters (equation (2.44)). The production term, P_1 , has the same form given in equation (2.21) except it is non-zero only for positions outside the heliopause. The boundary condition distribution function for the suprathermal component is zero, and its production term, P_2 , is non-zero only between the SWTS and the heliopause. Finally, the splash component production is non-zero only inside the SWTS.

2.3.3 The Splash Component

The H atoms produced by charge exchange in the solar wind assume the cold character of the solar wind plasma flow. The production rate may be approximated (see section 2.1.2):

$$P_3(\mathbf{r}, \mathbf{v}, t) \approx n_H(\mathbf{r}, t) \left[n_{pe} \left(\frac{r_e}{r} \right)^2 v_{sw} \sigma_{ex}(v_{sw}) \right] U_{step}(r - R_s) \delta^3(\mathbf{v} - \hat{r} v_{sw}), \quad (2.60)$$

where n_H is the total H density. The step function restricts the production region to be inside the SWTS. The splash component distribution function may be written

using equation (2.10):

$$f_3(\mathbf{r}, \mathbf{v}, t) = \int_{t_0}^t dt' P_3(\mathbf{r}', \mathbf{v}', t') e^{-\Lambda(t', t)} \approx n_3(\mathbf{r}, t) \delta^3(\mathbf{v} - \hat{r} v_{sw}). \quad (2.61)$$

where n_3 is the splash component density. A useful upper limit to n_3 is given by using $n_{H\infty}$ for n_H , neglecting losses ($\Lambda(t', t) = 0$) and assuming the splash H atoms move outward at the solar wind speed. At the SWTS this yields

$$\left(\frac{n_3}{n_{H\infty}} \right) < \left(\frac{n_{pe} r_e^2 \sigma_{ez}(v_{sw})}{R_s} \right). \quad (2.62)$$

This is similar to the expression derived by Holzer (1977). Using representative solar wind parameters, $n_3/n_{H\infty}$ is less than 0.6% for all R_s greater than 50 AU. The splash component may be neglected here for two reasons (Holzer, 1977). First, the upper limit density is a very small fraction of the ambient VLISM density. Second, since the splash H atoms are moving radially outward at the solar wind speed, their Ly α absorption profile is Doppler shifted by 0.16 nm—completely off of the solar source Ly α line (see Figure 1.3). Therefore splash H atoms play little or no role in the resonance scattering processes.

2.3.4 Numerical Algorithm

Calculating the distribution of components 1 and 2 requires solving two coupled Boltzmann integral equations of the form given in equation (2.10). The production terms depend on the plasma distribution function as well as the total H density (see equation (2.21)). Here an iterative procedure is employed to calculate the distributions on a finite element grid. Each distribution is assumed to be Maxwellian, described by a local H density, temperature and bulk velocity. Temporal variations in the Sun and VLISM are neglected, so the distributions are static. However, the algorithm is general enough to handle the time dependent problem. The procedure is as follows: 1) A zeroth iteration H distribution is guessed for each point on the finite

element grid. This is taken to be a uniform medium with the VLISM parameters. 2) The production terms are calculated from equation (2.21) using this estimate of the H distribution. 3) A new H distribution is calculated from equation (2.10) for components 1 and 2, using the production terms calculated in the previous step. This entails integrating along the past trajectories of the particles accounting for both production and loss. 4) The densities, temperatures and bulk velocities are calculated for both components. These serve as the next estimate for an iterative procedure, which begins again at step 2. To generalize this algorithm for temporal variations, this procedure is repeated for a series of time steps covering the time interval of interest. The calculation converges rapidly: in all cases examined, the densities, temperatures and bulk velocities for both components of the H distribution converge to within $\sim 10\%$ at each grid point after 4 iterations.

The most computationally intensive step is integrating along the past trajectories of the particles. Given a particle initially at $(\mathbf{r}, \mathbf{v}, t)$, its past trajectory is denoted $(\mathbf{r}', \mathbf{v}', t')$, where $t' < t$. The trajectories are determined by solar gravity and radiation pressure. The integration algorithm is the adaptive step size, Runge-Kutta scheme taken from Press et al. (1986). The Runge-Kutta integration method allows the determination of a vector, \mathbf{A} , if its time derivative can be expressed:

$$\frac{d\mathbf{A}}{dt'} = \dot{\mathbf{A}}(\mathbf{A}(t'), t'). \quad (2.63)$$

Here, nine quantities are determined in the integration. The first six are the position and velocity of the particle. The seventh is the loss integral, $\Lambda(t', t)$. The eighth and ninth are the H produced along the trajectory for components 1 and 2 respectively. These nine quantities are expressed as a vector \mathbf{A} by making the following definitions:

$$A_1 \equiv x' \quad A_2 \equiv y' \quad A_3 \equiv z', \quad (2.64)$$

$$A_4 \equiv v'_x \quad A_5 \equiv v'_y \quad A_6 \equiv v'_z, \quad (2.65)$$

$$A_7 \equiv \Lambda(t', t) = \int_{t'}^t dt'' \beta(\mathbf{r}'', \mathbf{v}'', t''), \quad (2.66)$$

$$A_8 \equiv \int_{t'}^t dt' P_1(\mathbf{r}'', \mathbf{v}'', t'') e^{-\Lambda(t'', t)}. \quad (2.67)$$

and

$$A_9 \equiv \int_{t'}^t dt'' P_2(\mathbf{r}'', \mathbf{v}'', t'') e^{-\Lambda(t'', t)}. \quad (2.68)$$

The vector \mathbf{A} is formally a function of t' as well as $(\mathbf{r}, \mathbf{v}, t)$. Here the latter variables are suppressed, so $\mathbf{A} = \mathbf{A}(t')$.

Using these definitions, one may write the time derivatives of the position and velocities using Hamilton's equations of motion:

$$\dot{A}_1 = A_4 \quad \dot{A}_2 = A_5 \quad \dot{A}_3 = A_6, \quad (2.69)$$

$$\dot{A}_4 = \frac{F_x(\mathbf{r}', \mathbf{v}', t')}{m_H} \quad \dot{A}_5 = \frac{F_y(\mathbf{r}', \mathbf{v}', t')}{m_H} \quad \dot{A}_6 = \frac{F_z(\mathbf{r}', \mathbf{v}', t')}{m_H}, \quad (2.70)$$

where \mathbf{F} is the vector force on an H atom at $(\mathbf{r}', \mathbf{v}', t')$. The forces are calculated from the potential given in equation (2.25). The radiation pressure parameter, μ_\odot , is taken to be constant, although the algorithm allows time and velocity dependent forces to be used.

The derivatives of the remaining three components of \mathbf{A} are:

$$\dot{A}_7 = -\beta(\mathbf{r}', \mathbf{v}', t'), \quad (2.71)$$

$$\dot{A}_8 = -P_1(\mathbf{r}', \mathbf{v}', t') e^{-\Lambda(t', t)}, \quad (2.72)$$

and

$$\dot{A}_9 = -P_2(\mathbf{r}', \mathbf{v}', t') e^{-\Lambda(t', t)}. \quad (2.73)$$

Using the Runge-Kutta integration scheme, the past trajectory of a particle initially at $(\mathbf{r}, \mathbf{v}, t)$ is calculated. Typically the integration is truncated at a past time, t_o , corresponding to a distant point where the VLISM flow may be considered unperturbed (or, alternatively, where the loss integral $\Lambda(t_o, t)$ exceeds some large value).

The distribution of the component penetrating from outside the heliopause is then:

$$f_1(\mathbf{r}, \mathbf{v}, t) = f_o(\mathbf{r}_o, \mathbf{v}_o, t_o) e^{-A_7(t_o)} + A_8(t_o), \quad (2.74)$$

where the boundary condition distribution function, f_o , represents particles penetrating from the distant VLISM flow and is given by equation (2.44). The component created in the heliosheath is

$$f_2(\mathbf{r}, \mathbf{v}, t) = A_9(t_o). \quad (2.75)$$

Time dependencies are explicitly included in this formulation. However, if the Sun and the VLISM are static in time, the distributions calculated using equations (2.74) and (2.75) are static as well.

2.3.5 Calculated Results

The distribution of each of the two components is described by four quantities: the integrated density, the effective temperature, the bulk flow speed in the z direction, and the bulk flow speed in the ρ direction. As expected, the component 2 is more tenuous and hot than component 1. Results from a calculation with a SWTS at 70 AU are plotted in Figure 2.9 (component 1) and Figure 2.10 (component 2). The solar and VLISM input parameters for this calculation are: $R_s = 70 \text{ AU}$, $\mu_\odot = 0.80$, $v_{sw} = 400 \text{ km s}^{-1}$, $n_{pe} = 8 \text{ cm}^{-3}$, $n_{p\infty} = 0.003 \text{ cm}^{-3}$, $n_{H\infty} = 0.10 \text{ cm}^{-3}$, $T_\infty = 10^4 \text{ K}$, and $v_\infty = 20 \text{ km s}^{-1}$.

The qualitative distinction between component 1 and the standard hot distributions shown in Figures 2.4 and 2.5 is important. Including the Suess and Nerney (1990, 1991) plasma distribution implies a net filtering of H atoms penetrating from outside the heliopause. The density of the suprathermal component is much smaller than the thermal component everywhere except within $\sim 2 \text{ AU}$ of the Sun and in the downstream direction. Along the downstream axis the thermal density

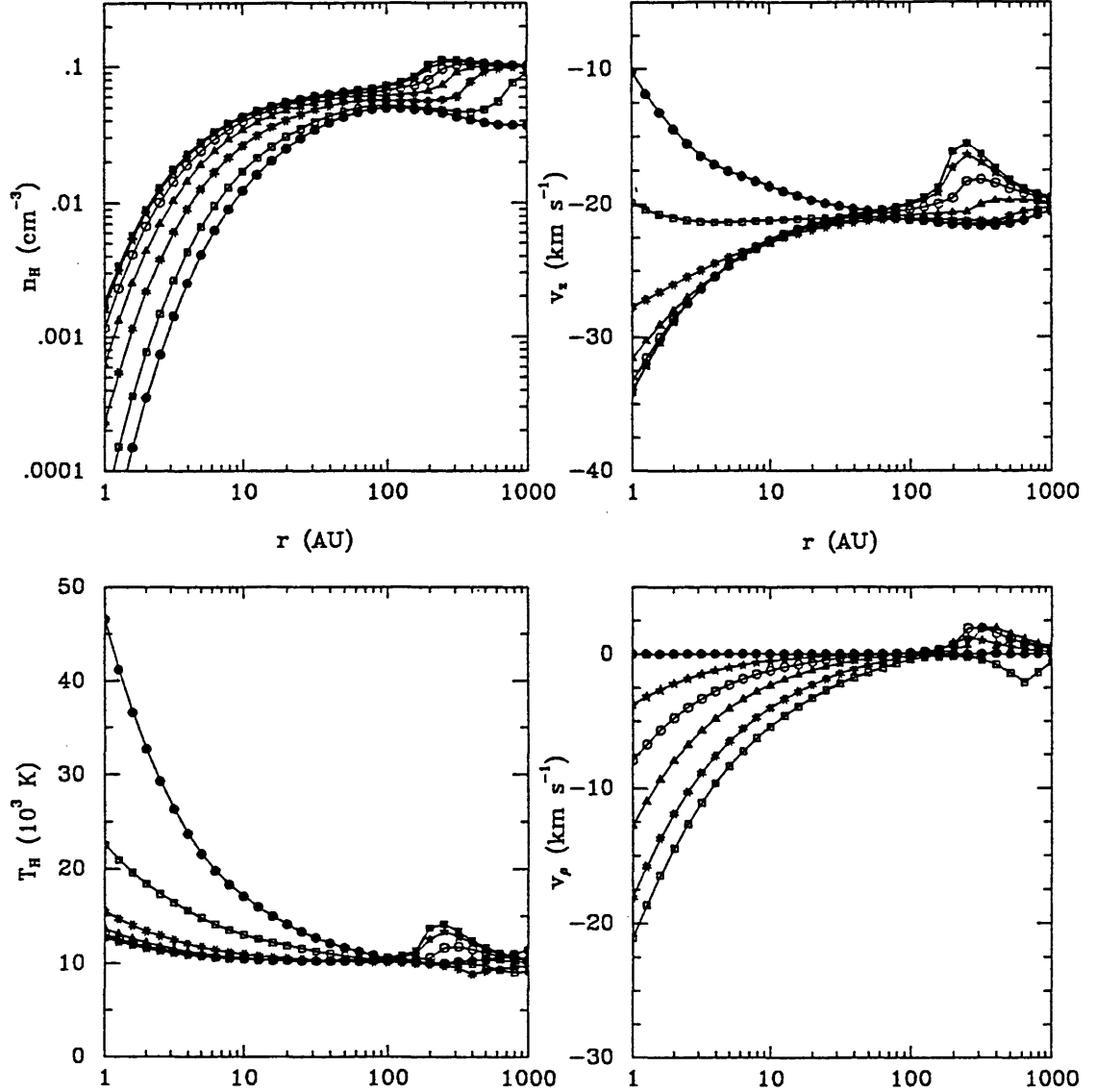


Figure 2.9: Densities, temperatures, and velocities for component 1 (the thermal component) of the heliospheric H distribution using solar and VLISM parameters: $R_s = 70$ AU, $\mu_\odot = 0.80$, $v_{sw} = 400$ km s⁻¹, $n_{pe} = 8$ cm⁻³, $n_{p\infty} = 0.003$ cm⁻³, $n_{H\infty} = 0.1$ cm⁻³, $T_\infty = 10^4$ K, and $v_\infty = 20$ km s⁻¹. Values for lines of constant axial angle, θ , are shown as a function of heliocentric radius. The symbols correspond to the following axial angles: solid squares (0°-upstream), stars (30°), open circles (60°), triangles (90°-sidestream), asterices (120°), open squares (150°), and solid circles (180°-downstream).

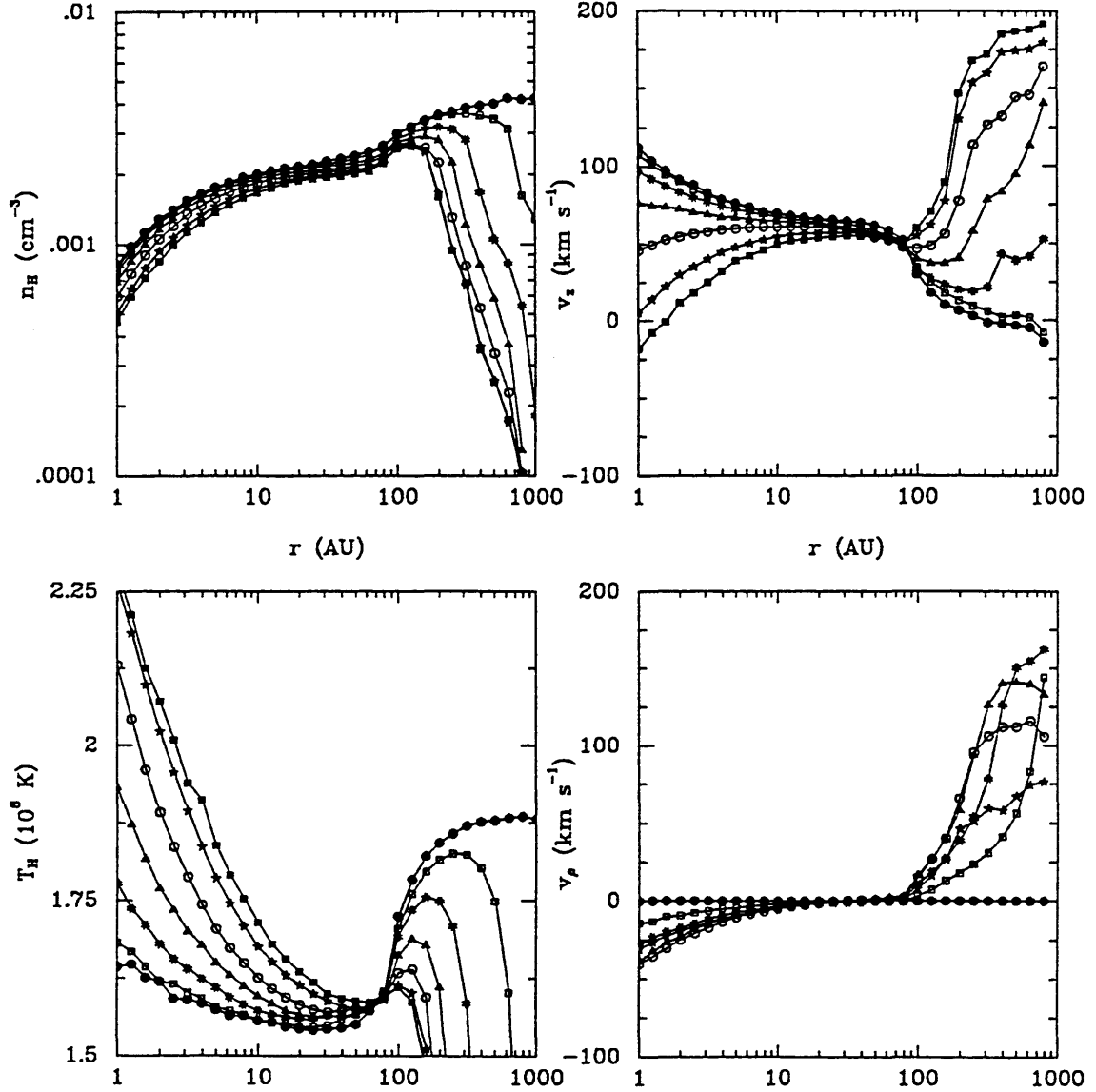


Figure 2.10: Densities, temperatures, and velocities calculated for component 2 (the suprathermal component) of the heliospheric H distribution. The same solar and VLISM parameters are used as in the previous figure (as are the plotted symbols). Comparing this to the previous figure reveals that thermal densities are much larger than suprathermal densities everywhere except for $r < 2$ AU and in the downstream direction. At 10 AU downstream, $n_2/n_1 \approx 0.1$; at 2 AU downstream $n_2/n_1 \approx 1$.

does not approach the unperturbed VLISM density; the effect of the heliotail is to carve an evacuated, downstream tube in the H distribution. Also, at a given radius, n_2 generally is larger in the downstream direction than upstream—exactly opposite the behavior of n_1 . This is because the source region for component 2 is the heliosheath and heliotail, which are more voluminous in the downstream direction.

The dependence of the densities n_1 and n_2 on the radius of the SWTS and the solar wind proton density is shown in Figures 2.11 and 2.12. The suprathermal density inside the SWTS varies strongly as a function of R_s . But the thermal component is not affected significantly. Both components are affected (but in opposite senses) by varying n_{pe} . These distinctions may eventually allow the determination of the SWTS distance, if the relative abundances of the two components can be estimated in the inner heliosphere. This may be done, for instance, by measuring the Ly α line shape. The large difference in temperature between the two suggests that the heliospheric Ly α line is a sum of wide and thin components. This is investigated in the next chapter, where the heliospheric resonance scattering process is discussed.

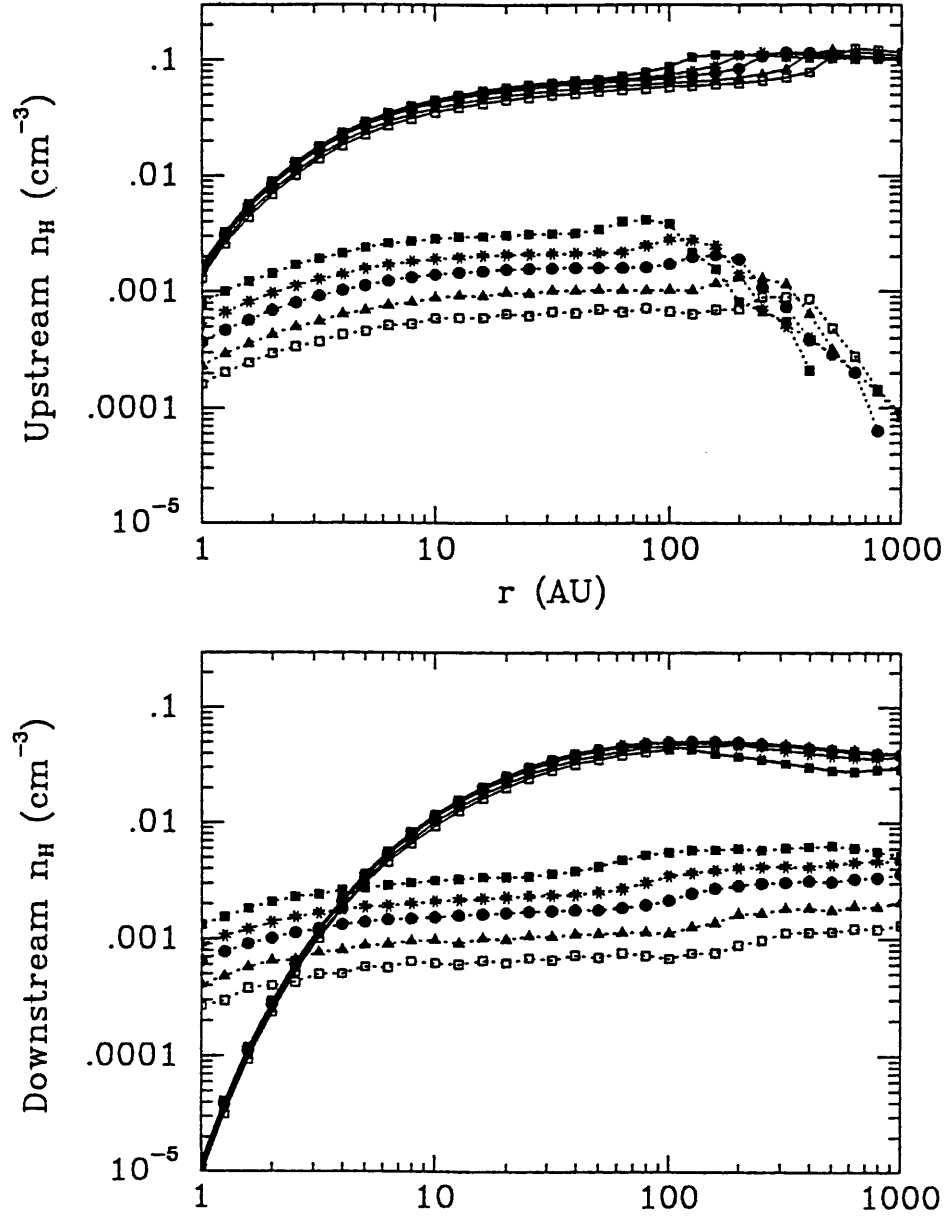


Figure 2.11: Upstream and downstream densities for H components 1 and 2 obtained by varying R_s . The other solar and VLISM parameters are: $\mu_\odot = 0.80$, $v_{sw} = 400 \text{ km s}^{-1}$, $n_{pe} = 6 \text{ cm}^{-3}$, $n_{p\infty} = 0.003 \text{ cm}^{-3}$, $n_{H\infty} = 0.1 \text{ cm}^{-3}$, $T_\infty = 10^4 \text{ K}$, and $v_\infty = 20 \text{ km s}^{-1}$. The thermal component is plotted with solid lines and the suprathermal component with dotted lines. The symbols correspond to the following SWTS radii in AU: solid squares (50), asterisks (75), solid circles (100), triangles (150), open squares (200).

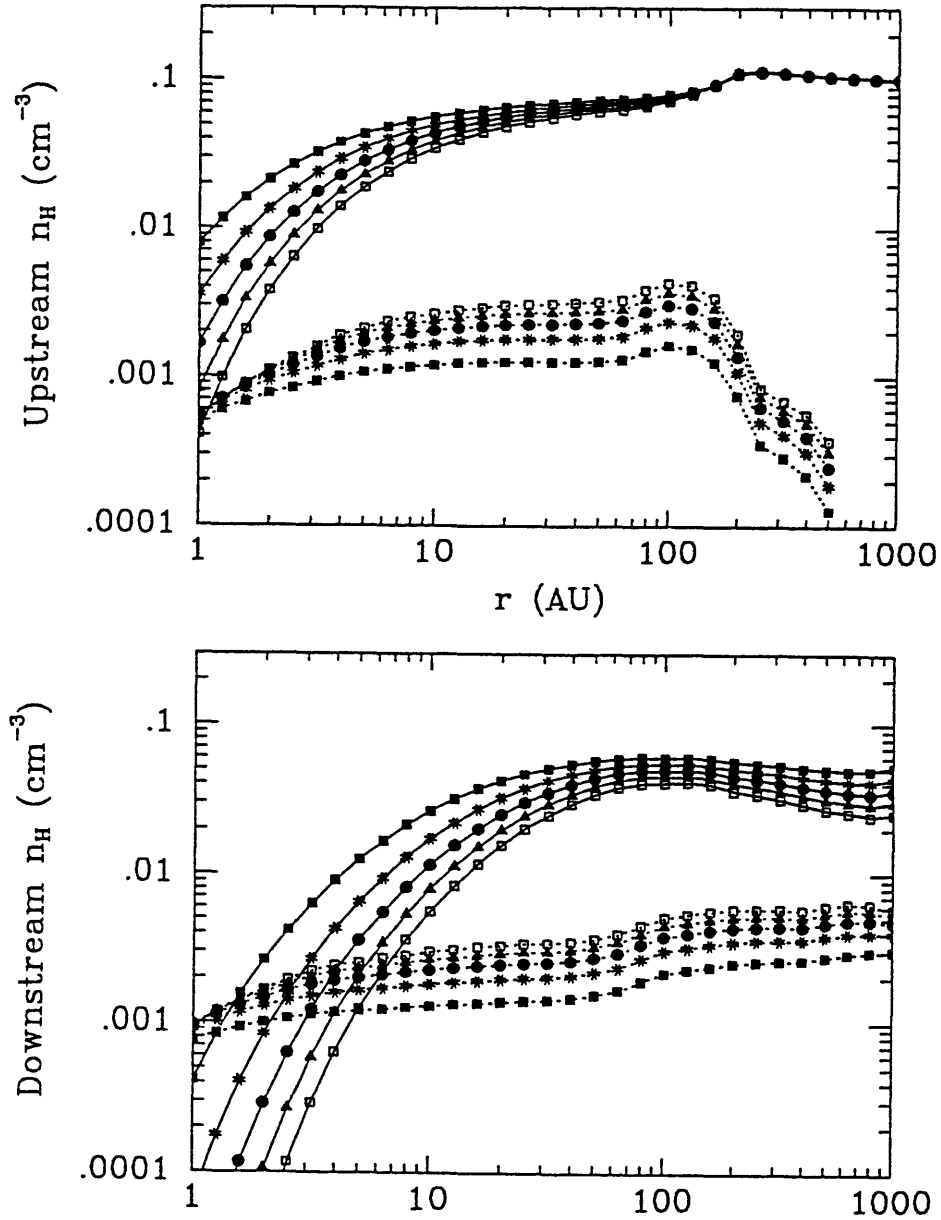


Figure 2.12: Upstream and downstream densities for the thermal and suprathermal components of the heliospheric H distribution obtained by varying the solar wind density, n_{pe} . The other solar and VLISM parameters are: $R_s = 70 \text{ AU}$, $\mu_\odot = 0.80$, $v_{sw} = 400 \text{ km s}^{-1}$, $n_{p\infty} = 0.003 \text{ cm}^{-3}$, $n_{H\infty} = 0.1 \text{ cm}^{-3}$, $T_\infty = 10^4 \text{ K}$, and $v_\infty = 20 \text{ km s}^{-1}$. Component 1 is plotted with solid lines and component 2 dotted lines. The symbols correspond to the following n_{pe} in cm^{-3} : solid squares (4), asterisks (6), solid circles (8), triangles (10), open squares (12). Inside the SWTS, the densities of both components vary strongly with n_{pe}

CHAPTER 3

HELIOSPHERIC RESONANCE SCATTERING

Heliospheric H Ly α resonance emissions were first detected in 1969 by two instruments aboard the Orbiting Geophysical Observatory (OGO 5) satellite (Thomas and Krassa, 1971; Bertaux and Blamont, 1971). Since then, several spacecraft have detected heliospheric H and He resonance lines. The majority of the measurements were obtained within 2 AU of the Sun. The Pioneer and Voyager spacecraft have obtained observations beyond 5 AU. Pioneer 10 is equipped with two UV photometers capable of measuring the H Ly α and He 58.4 nm intensities (Carlson and Judge, 1974). Voyagers 1 and 2 have Ultraviolet Spectrographs that measure spectra in the wavelength range 55 to 170 nm (Broadfoot et al., 1977). In addition to H Ly α and He 58.4 nm, the UVS instruments have detected H Ly β at 102.6 nm and H Ly γ at 97.2 nm (the latter only rises above instrumental noise in extremely long duration spectra). Figure 3.1 shows a long-duration Voyager 2 UVS spectrum observed in the direction of the North Galactic Pole (see Holberg, 1986). The H Lyman series lines α , β and γ are visible, as is the He 58.4 nm line.

Briefly described, heliospheric resonance scattering proceeds in the following manner. Solar photons in one of the resonance lines propagate outward into the heliosphere. As they travel outward, they may interact with heliospheric H or He atoms through the resonance scattering process (see Mitchell and Zemansky, 1934, for a detailed description). An observed resonance line intensity is due to photons scattered along the instrument's line of sight, plus whatever Galactic background may exist.

As in the case of the heliospheric distributions, there is a salient distinction between H and He heliospheric resonance scattering. The primary hydrogen line is H Ly α with wavelength 121.6 nm, while that for helium is at 58.4 nm. The impor-

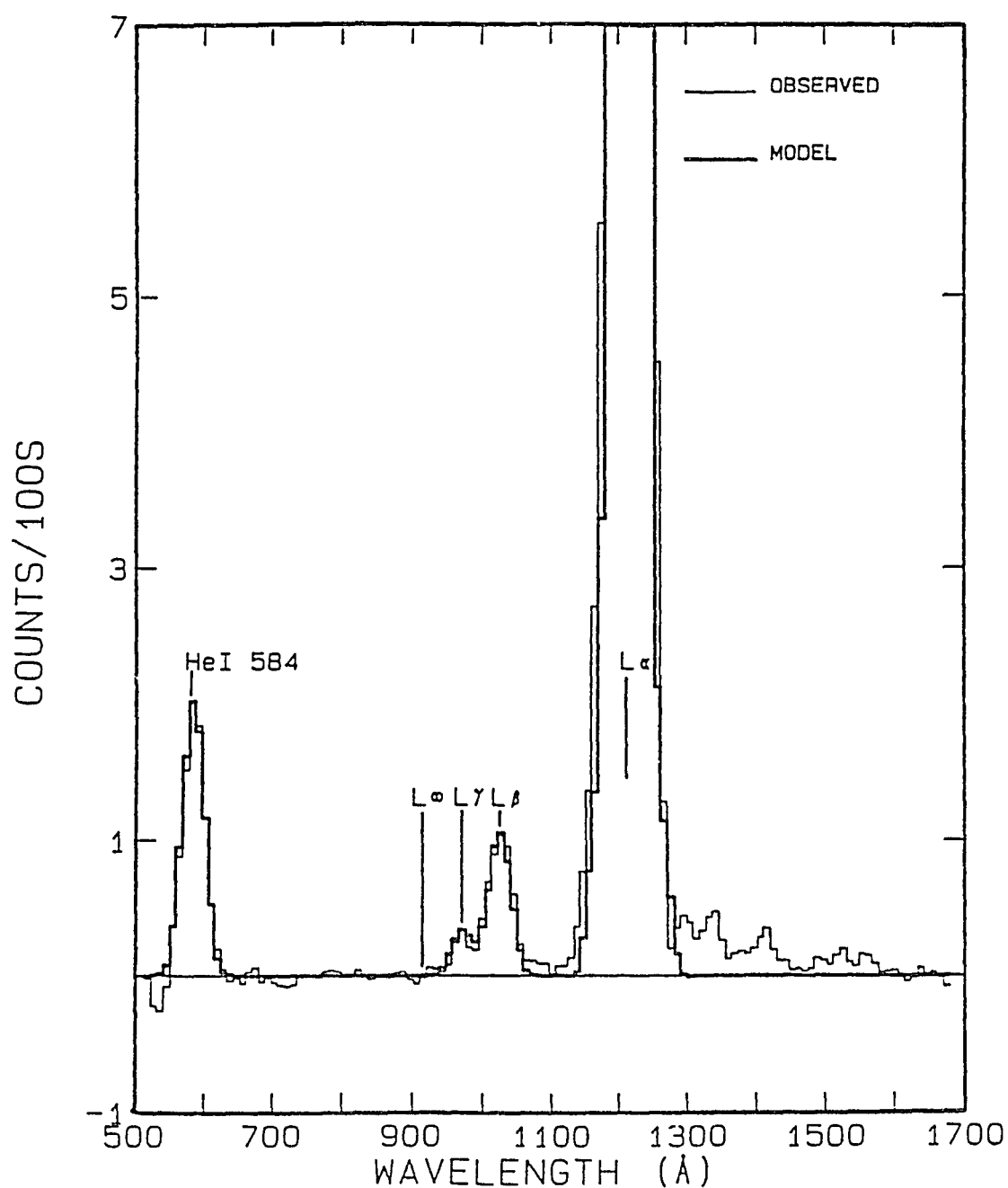


Figure 3.1: Voyager 2 UVS spectrum observed in the direction of the North Galactic Pole. The H Lyman series lines α (off scale), β and γ and the He 58.4 nm lines are produced by resonance scattering in the heliosphere. The total exposure duration is $\sim 1.5 \times 10^6$ seconds. (Reproduced with permission from Holberg, 1986.)

tant difference is the comparative optical depths in the heliosphere. For a Maxwellian gas at $T = 10^4$ K, one H Ly α line center optical depth corresponds to a column density of $\langle n\ell \rangle \approx 1.7 \times 10^{13} \text{ cm}^{-2}$. For a density $n_{\text{H}} = 0.1 \text{ cm}^{-3}$ this implies a path length of $\ell \approx 10 \text{ AU}$. One He 58.4 nm line center optical depth corresponds to $\langle n\ell \rangle \approx 2.7 \times 10^{13} \text{ cm}^{-2}$. For $n_{\text{He}} = 0.01 \text{ cm}^{-3}$, this gives $\ell \approx 200 \text{ AU}$. So the heliospheric length scale is probably much larger than one H Ly α optical depth, but roughly comparable to one He 58.4 nm optical depth. This distinction is important because within 50 AU of the Sun, the optically thin solution to the radiative transfer equation is justified for He 58.4 nm but not H 121.6 nm.

3.1 H and He Atomic Structure and Data

A resonance interaction may be idealized as a two step process (see Mitchell and Zemansky, 1934): absorption of a photon and emission of another. After absorption, the transition probability from some state “ k ” to a lower energy state “ i ” is given by the transition probability, $A_{ki} [\text{s}^{-1}]$, also referred to as the Einstein A-coefficient. The lifetime of the upper state due to spontaneous emission is the reciprocal of the sum of all of transition probabilities from that state to lower states. The transition probability (for dipole allowed transitions) is related to a dimensionless quantity called the absorption oscillator strength, f_{ik} . It represents the strength of the interaction between two atomic states when exposed to electromagnetic fields and may be calculated using quantum mechanical considerations (see Mitchell and Zemansky, 1934, and Rybicki and Lightman, 1979). Finally, the line strength, $S_{lr} [\text{cm}^2 \text{ Hz}^{-1}]$, is the integral of the scattering cross section over all frequencies and is also related to the oscillator strength.

The atomic structure of H and He is described in detail by Herzberg (1944). H Lyman series photons are associated with the $np \rightarrow 1s$ transitions in the hydrogen atom. The upper state for the Ly α line decays via only one channel, back to the

Table 3.1: Heliospheric Resonance Line Atomic Data.

	λ (nm)	Transition ($i - k$)	A_{ki} (s^{-1})	B_r	f_{ik}	S_{tr} ($cm^2 Hz^{-1}$)
H Ly α	121.567	1s - 2p	6.265×10^8	1.000	4.162×10^{-1}	1.104×10^{-2}
H Ly β	102.572	1s - 3p	1.672×10^8	0.882	7.910×10^{-2}	2.099×10^{-3}
H Ly γ	97.254	1s - 4p	6.818×10^7	0.839	2.889×10^{-2}	7.666×10^{-4}
He	58.433	1s ² - 1s2p	1.799×10^9	0.999	2.762×10^{-1}	7.329×10^{-3}

ground state. Because of this, Ly α photons cannot be destroyed by the resonance scattering process. Such scattering is called conservative. Ly β scattering is non-conservative. After a Ly β photon is resonantly absorbed, the H atom is in the 3p electronic state which may decay to either the 2s or the 1s states. This is called branching and the associated branching ratio is given by the transition probability multiplied by the upper state lifetime. In the case of Ly β , the branching ratio is $\approx 88\%$, meaning that about 12% of Ly β photons are lost in the resonance interaction and replaced by H α photons, which have wavelength ≈ 656 nm.

Transition wavelengths, probabilities, branching ratios, oscillator strengths and line strengths constitute the atomic data necessary to analyze resonance scattering observations. These data are compiled by Wiese et al. (1966) and are summarized in Table 3.1. The He 58.4 nm line has a branching ratio very close to unity so its scattering is nearly conservative.

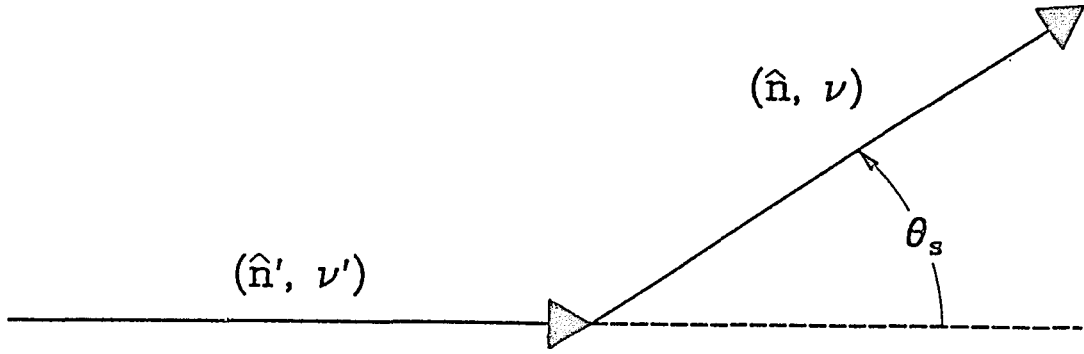


Figure 3.2: Schematic geometry of a resonance scattering interaction. The incident photon has direction and frequency (\hat{n}', ν') . The new photon has (\hat{n}, ν) . The two directions are separated by the scattering angle, θ_s .

3.2 Resonance Line Radiative Transfer

The theory of the transfer of radiation through space and matter is formally presented by Chandrasekhar (1960). Ivanov (1973) and Mihalas (1978) discuss the theory as applied to resonance radiation. The redistribution of photon directions and frequencies in the resonance scattering process is developed in detail by Hummer (1962). Here, the theory of resonance line radiative transfer (RT) is briefly described, focusing on the heliospheric problem.

3.2.1 The Resonance Scattering Process

Figure 3.2 illustrates the resonance scattering process. The primed quantities refer to the incident photon which travels along direction \hat{n}' with frequency ν' . The outgoing photon has direction \hat{n} and frequency ν . The scattering angle, θ_s , is the angle between the two directions: $\cos(\theta_s) = \hat{n} \cdot \hat{n}'$. The photon frequencies, ν' and ν , are measured in the global frame of reference, which is fixed with the Sun at the origin. The scattering atom is moving with velocity \mathbf{v} in this frame. In the atom's reference frame, the incident photon has frequency, ξ' , related to ν' by the Doppler shift:

$$\xi' = \xi'(\nu', \hat{n}', \mathbf{v}) = \nu' - \nu_o \left(\frac{\mathbf{v} \cdot \hat{n}'}{c} \right), \quad (3.1)$$

where ν_o is the line-center frequency and c is the speed of light. After the interaction, the frequency of the outgoing photon in the atom's frame is given by a similar relation:

$$\xi = \xi(\nu, \hat{\mathbf{n}}, \mathbf{v}) = \nu - \nu_o \left(\frac{\mathbf{v} \cdot \hat{\mathbf{n}}}{c} \right). \quad (3.2)$$

In equation (3.2) the change in the scattering atom's velocity caused by the resonance scattering process is neglected. One may estimate the change in the atom's speed by assuming that the all of the photon's momentum is transferred to the atom. This yields $\Delta v \leq 3 \text{ m s}^{-1}$ for both H Ly α and He 58.4 nm. This is much less than the typical heliospheric speeds $\sim 22 \text{ km s}^{-1}$, so the velocity changes may be safely neglected when calculating Doppler shifts. However, the cumulative transfer of momentum represents the force due to radiation pressure, which cannot be neglected for hydrogen.

3.2.2 The Scattering Coefficient and Optical Depth

If a monochromatic beam of photons (with frequency ν') passes in the direction $\hat{\mathbf{n}}'$ through a scattering medium from point \mathbf{r}_a to point \mathbf{r}_b , the fraction of the photons remaining unscattered is $e^{-\tau}$, where τ is the optical depth for scattering. It is the integral of the scattering coefficient, $k_s [\text{cm}^{-1}]$, along the path (see Rybicki and Lightman, 1979):

$$\tau(\mathbf{r}_a, \mathbf{r}_b, \nu') = \int_0^{r_{ba}} ds k_s(\nu', \hat{\mathbf{n}}'), \quad (3.3)$$

where $r_{ba} \equiv |\mathbf{r}_b - \mathbf{r}_a|$ and

$$\mathbf{r}' = \mathbf{r}_a + s \hat{\mathbf{n}}'. \quad (3.4)$$

The functional dependence of k_s on position is suppressed here.

The form of scattering coefficient appropriate for the heliospheric resonance lines is (Hummer, 1962; Mihalas, 1979)

$$k_s(\nu', \hat{\mathbf{n}}') = S_{tr} \int d^3\mathbf{v} f(\mathbf{r}, \mathbf{v}) \phi_L(\xi'), \quad (3.5)$$

where S_{lr} is the line strength [$\text{cm}^2 \text{ Hz}^{-1}$], f is the distribution function of the scattering species, ξ' is the frequency of the absorbed photon in the atoms frame and ϕ_L is the Natural or Lorentz profile given by:

$$\phi_L(\xi') = \frac{\Gamma_L}{\pi} [(\xi' - \nu_0)^2 + \Gamma_L^2]^{-1}. \quad (3.6)$$

The natural width of the line, Γ_L , is proportional to the total decay rate of the upper state; resonance lines with upper states that have short lifetimes have large natural line widths. (This may be understood by using Heisenberg's uncertainty principle, $\Delta E \Delta t \sim \hbar$. The finite line width is caused by the uncertainty in the upper state energy, $\sim \Delta E$, given that it decays in about one upper state lifetime, $\sim \Delta t$.) In the case of the heliospheric resonance lines, where collisional deactivation is negligible, the natural line width is proportional to the sum of all downward transition probabilities:

$$\Gamma_L = \frac{1}{4\pi} \sum_{i < k} A_{ki}. \quad (3.7)$$

The scattering cross section, σ_s , is the scattering coefficient divided by the number density,

$$\sigma_s(\nu', \hat{\mathbf{n}}') = \frac{k_s(\nu', \hat{\mathbf{n}}')}{n(\mathbf{r})} \quad (3.8)$$

which has dimensions [cm^2].

In section 3.2.4, the exact microscopic absorption coefficient, equation (3.5), is used along with the non-Maxwellian, hot H distribution to estimate interplanetary Ly α extinction. But this procedure requires too much computer time to use in the radiative transfer model that follows. Approximating the hot distribution as a Maxwellian allows the use of analytical expressions for the absorption coefficient which considerably speeds up the computation.

3.2.3 The Absorption Profile

The absorption profile is the normalized scattering coefficient:

$$\phi(\nu', \hat{\mathbf{n}}') = \frac{k_s(\nu', \hat{\mathbf{n}}')}{\int_0^\infty d\nu' k_s(\nu', \hat{\mathbf{n}}')}. \quad (3.9)$$

For a Maxwellian gas, the absorption is calculated by combining equations (2.5) and (3.5). This yields the Voigt profile:

$$\phi_v(\nu', \hat{\mathbf{n}}') = \frac{H_v(a, x')}{w_d \sqrt{\pi}}, \quad (3.10)$$

using the following definitions: the Doppler Width,

$$w_d \equiv \nu_o \left(\frac{v_{th}}{c} \right) = \nu_o \left(\frac{\sqrt{\frac{2k_B T}{m}}}{c} \right), \quad (3.11)$$

the Voigt Parameter,

$$a \equiv \frac{\Gamma_L}{w_d}, \quad (3.12)$$

the dimensionless frequency,

$$x' \equiv \frac{\xi' - \nu_o}{w_d}, \quad (3.13)$$

and, finally, the Voigt function,

$$H_v(a, x) \equiv a \int_{-\infty}^{\infty} dy e^{-y^2} [(x - y)^2 + a^2]^{-1}. \quad (3.14)$$

Hui et al. (1978) describe an algorithm for rapid computation of the Voigt function. In the limit where the Doppler width is much larger than the natural width, the Lorentz profile may be approximated by a δ -function and equation (3.10) reduces to the Doppler absorption profile:

$$\phi_d(\nu', \hat{\mathbf{n}}') = \frac{\exp[-(x')^2]}{w_d \sqrt{\pi}}, \quad (3.15)$$

which has the Gaussian form.

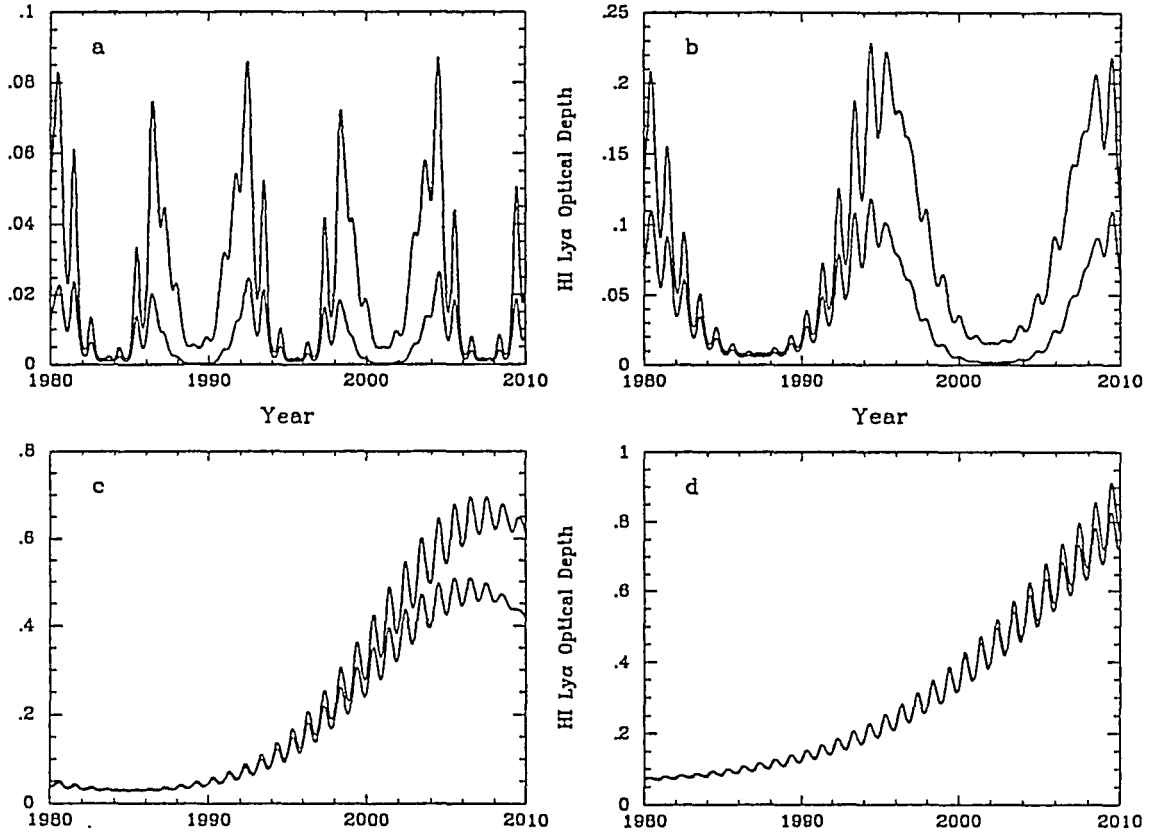


Figure 3.3: H Ly α line center optical depths between the Earth and the outer planets for the “standard” solar minimum and maximum H distributions shown in Figures 2.5 and 2.6. Shown are line center optical depths between Earth and Jupiter (panel a), Saturn (b), Uranus (c) and Neptune (d) (the solar maximum absorption is the lower curve in all cases). Cyclical variations associated with the orbital periods of both the Earth and the source planet are due to the Doppler shift associated with the net motion of the interplanetary H gas. All of these curves assume a VLISM H density of 0.10 cm^{-3} but optical depth scales linearly with this parameter.

3.2.4 Interplanetary Absorption of H Ly α

Wu and Judge (1979b) report the effect of interplanetary extinction on the solar H Ly α line. But a detailed treatment of the extinction of emissions *from the outer planets* is not available in the literature. This is an important consideration when observing outer planet Ly α emissions with near-Earth spacecraft (Clarke, 1982; McGrath and Clarke, 1992); the interplanetary extinction of planetary H Ly α lines could be significant because the path lengths are comparable to or larger than one Ly α line center optical depth (~ 10 AU). Due to the net VLISM flow and associated Doppler shift, the extinction is expected to vary significantly with observational geometry. Planetary Ly α emissions are generally close to line center and have widths much narrower than expected interplanetary absorption profiles. When a planet is situated upstream or downstream from the Earth, its Ly α emission line lies far from the peak of the interplanetary absorption profile (which is Doppler shifted about 22 km s^{-1} to either side of line center). In these cases, the net interplanetary extinction is low. However, when the planet lies in the sidestream direction, the Ly α photons traverse the H gas in a direction perpendicular to the net flow, there is no relative Doppler shift and the absorption is stronger.

Figure 3.3 shows Ly α line center optical depths between the outer planets and Earth. The curves are calculated using the microscopic formulation of the absorption coefficient, equation (3.5), and the standard solar minimum and maximum hot distributions with $n_{\text{H}\infty} = 0.10 \text{ cm}^{-3}$. In all cases, the optical depths for the solar minimum distribution are larger. Panels *a* through *d* show the optical depth for Jupiter, Saturn, Uranus and Neptune respectively. The curves show cyclic absorption patterns associated with the orbital period of the Earth and the outer planets.

This calculation probably is not correct in detail. First, the optical depths scale linearly with $n_{\text{H}\infty}$, which is an uncertain quantity. Second, these curves show the opti-

cal depth at line center, but planetary Ly α lines have finite width and may be shifted from line center. Finally, this calculation uses the hot heliospheric H distribution which probably is not correct in detail. However, these curves do illustrate the effects of observational geometry and are useful in helping to decide whether particular observations are likely to be strongly or weakly affected by interplanetary extinction effects. Also, they show that the absorption of Jovian Ly α probably never exceeds $\approx 10\%$, whereas emissions from the more distant planets may suffer observationally significant interplanetary extinction.

3.2.5 The Redistribution Function

Assuming no branching occurs, the probability that a photon with frequency ν' propagating in the element of solid angle $d\Omega'$ centered about the unit vector $\hat{\mathbf{n}}'$ is resonantly scattered into a photon with frequency ν travelling in $d\Omega$ centered about $\hat{\mathbf{n}}$ is (Hummer, 1962; Mihalas, 1978)

$$R(\nu', \hat{\mathbf{n}}', \nu, \hat{\mathbf{n}}) d\nu d\Omega d\nu' d\Omega', \quad (3.16)$$

where R is the frequency redistribution function. In general, R may be a function of position and time but these dependencies are suppressed here. By convention, the redistribution function is normalized as follows:

$$\oint \frac{d\Omega'}{4\pi} \oint \frac{d\Omega}{4\pi} \int_0^\infty d\nu' \int_0^\infty d\nu R(\nu', \hat{\mathbf{n}}', \nu, \hat{\mathbf{n}}) = 1. \quad (3.17)$$

The redistribution function depends on the distribution of the scattering species in velocity space:

$$R(\nu', \hat{\mathbf{n}}', \nu, \hat{\mathbf{n}}) = \frac{1}{n(\mathbf{r})} \int d^3\mathbf{v} f(\mathbf{r}, \mathbf{v}) R_o(\nu', \hat{\mathbf{n}}', \nu, \hat{\mathbf{n}}; \mathbf{v}), \quad (3.18)$$

where R_o is the redistribution function for a single atom travelling with velocity \mathbf{v} . The exact form of R_o is derived by Hummer (1962) and summarized by Miha-

las (1978); these authors also give the angle dependent form of R for a Maxwell-Boltzmann distribution. Cooper et al. (1989) formulate the coupled redistribution in the $\text{Ly}\alpha$, $\text{Ly}\beta$ and $\text{H}\alpha$ transition system of atomic hydrogen.

The distinction between R_o and R is important. R_o contains the microscopic properties of individual scattering events, and is constrained by the Heisenberg uncertainty principle. R is an ensemble average, so it accounts for the velocity dispersion of large numbers of atoms; it does not apply to individual scattering events. R may indicate that frequencies change by significantly more than one natural line width, but this does not violate the Heisenberg uncertainty principle.

Using the detailed form of R given by equation (3.18), is computationally expensive. Even the angle dependent functions for a Maxwell-Boltzmann gas developed by Hummer (1962) seriously complicate the numerical analysis. It is difficult to justify the necessary effort to include these complications, given that some of the basic input parameters (such as solar source line shapes and fluxes) are so poorly constrained. However, in the case of He 58.4 nm, where the relatively simple optically thin solution to the RT equation is a more valid approximation than for H $\text{Ly}\alpha$, such a detailed treatment of the redistribution process is possible and has been done by Meier (1977).

Complete Frequency Redistribution

A convenient approximation that is often used in planetary atmosphere calculations (Yelle and Wallace, 1989) is to assume complete frequency redistribution (CFR):

$$R(\nu', \hat{\mathbf{n}}', \nu, \hat{\mathbf{n}}) \approx P_h(\hat{\mathbf{n}}, \hat{\mathbf{n}}') \phi(\nu, \hat{\mathbf{n}}) \phi(\nu', \hat{\mathbf{n}}'). \quad (3.19)$$

Here P_h is the angular phase function. As discussed by Mihalas (1978), the CFR approximation is rigorously justified in environments where the collisional time scale is short compared to the radiative lifetime of the upper state (which is not true in the heliosphere). However, for small to moderate optical depths (less than 100 or

so), it yields reasonable approximations in the central cores of lines in non-collisional, Maxwellian gases (Wallace and Yelle, 1989). For non-Maxwellian gases, the CFR approximation may not be justified and could possibly lead to erroneous results. This is a consideration for the downstream region of the heliosphere, where the distribution may differ significantly from a Maxwellian.

For a multi-component gas, as used in Chapter 2 to describe the heliospheric H distribution, the CFR approximation has the following form:

$$R(\nu', \hat{\mathbf{n}}', \nu, \hat{\mathbf{n}}) \approx \frac{P_h(\hat{\mathbf{n}}, \hat{\mathbf{n}}')}{n(\mathbf{r})} \sum_k n_k(\mathbf{r}) \phi_k(\nu, \hat{\mathbf{n}}) \phi_k(\nu', \hat{\mathbf{n}}'), \quad (3.20)$$

where the subscript k refers to quantities associated with the k th component of the gas.

The Phase Function

The angular phase function, P_h , expresses the distribution of photons as a function of scattering angle. For isotropic scattering $P_h = 1$ for all scattering angles. Resonance scattering is not isotropic. The phase function has forward and backward scattering lobes. The form of P_h appropriate for heliospheric resonance scattering is

$$P_h(\hat{\mathbf{n}}, \hat{\mathbf{n}}') = A_p + B_p |\hat{\mathbf{n}} \cdot \hat{\mathbf{n}}'|^2. \quad (3.21)$$

The constants for He 58.4 nm are $A_p = B_p = 3/4$. These apply to general dipole scattering as well as Thompson and Rayleigh scattering (Mihalas 1978). For H Ly α they are $A_p = 11/12$ and $B_p = 1/4$ (Brandt and Chamberlain, 1959). The Ly α phase function is enhanced in the forward and backward directions by a factor of 16.7% over the isotropic value. He 58.4 nm scattering is even more anisotropic, having forward and backward enhancements of 50%.

3.2.6 The Specific Intensity

One of the fundamental quantities in radiative transfer theory is the specific intensity or intensity of the radiation field, $I(\mathbf{r}, \hat{\mathbf{n}}, \nu)$. It is the number of photons with frequency between ν and $\nu + d\nu$ travelling past the point \mathbf{r} in a differential element of solid angle centered on the direction $\hat{\mathbf{n}}$. (For a more detailed description see Chandrasekhar, 1960, Mihalas, 1978 or Rybicki and Lightman, 1979.) Even though the intensity often is defined in terms of the energy in the radiation field, here it measures the number of photons and has units [photons $\text{cm}^{-2} \text{ s}^{-1} \text{ Hz}^{-1} \text{ ster}^{-1}$]. In the heliosphere, the total intensity may be divided into distinct parts: a background component due to sources external to the heliosphere, I_{B} , the solar flux, I_0 , and the intensity due to solar photons which have scattered m times, I_m . The total intensity is the sum of these:

$$I(\mathbf{r}, \hat{\mathbf{n}}, \nu) = I_{\text{B}} + I_0 + \sum_{m=1}^{\infty} I_m = I_{\text{B}} + I_0 + \mathcal{I}, \quad (3.22)$$

where the total scattered intensity, \mathcal{I} , is defined,,

$$\mathcal{I} \equiv \sum_{m=1}^{\infty} I_m. \quad (3.23)$$

In the case of a resonance line with no underlying continuum the line intensity, I_{L} , is the specific intensity integrated over frequency:

$$I_{\text{L}}(\mathbf{r}, \hat{\mathbf{n}}) = \int_0^{\infty} d\nu I(\mathbf{r}, \hat{\mathbf{n}}, \nu). \quad (3.24)$$

Resonance line intensities are often reported in spectroscopic intensity units called *Rayleighs* (R). The line intensity in Rayleighs is equal to $4\pi I_{\text{L}}(\mathbf{r}, \hat{\mathbf{n}})/10^6$ (see Chamberlain, 1961, for a detailed explanation of Rayleighs).

The Galactic Background

Some component of the heliospheric resonance emissions may be due to a Galactic background. Thomas and Blamont (1976) use the results of Galactic $\text{H}\alpha$ mea-

surements to estimate an $\text{Ly}\alpha$ upper limit of ~ 10 R. Wu et al. (1988) include a background $\text{Ly}\alpha$ line intensity in their model of Pioneer 10 observations obtained between 30 and 40 AU. They find best fits for background intensities less than 20 R, but note that serious discrepancies exist between their model and the data. Background intensities for the other heliospheric lines are not constrained as well as for $\text{Ly}\alpha$. Henry (1991) reviews the level of the background EUV continuum in between the heliospheric resonance lines which, as can be seen in Figure 3.1, is negligible compared to the resonance lines.

Using typical VLISM parameters, one can show that distance scales of 3 to 10 pc correspond to large ($\gg 1$) line center optical depths in all of the heliospheric resonance lines. So background resonance lines probably have strongly reversed line shapes, characteristic of self-absorption optically thick media. One may reasonably assume that the central absorption feature of the background lines is completely saturated, and all of the photons are located on the extreme wings of the heliospheric absorption profiles where they are not expected to scatter on heliospheric length scales. If this is the case, the background lines do not participate in the heliospheric resonance scattering process. If one further assumes that the background is isotropic in the neighborhood of the VLISM, the background may be included in a radiative transfer model simply by specifying an integrated line intensity. This is the method of including the background in models developed here. However, it is important to note that even if the $\text{Ly}\alpha$ background line is severely self-reversed, it may be scattered in the heliosphere by the suprathermal component of the heliospheric H distribution created by charge exchange in the heliosheath.

The Solar Flux

The Sun is the dominant source of resonantly scattering photons in the inner heliosphere. If the Sun is approximated as a point source, the solar intensity field, I_0 , is non-zero only in the radial direction. It is written as a δ -function specifying the radial direction, $\delta^2(\hat{\mathbf{n}} - \hat{\mathbf{r}})$ [ster⁻¹], multiplied by the differential solar flux:

$$I_0(\mathbf{r}, \hat{\mathbf{n}}, \nu) = \delta^2(\hat{\mathbf{n}} - \hat{\mathbf{r}}) \left[(\pi \mathcal{F}_\odot) \Phi_\odot(\nu) \left(\frac{r_e}{r} \right)^2 \right] \exp[-\tau_\odot(\mathbf{r}, \nu)], \quad (3.25)$$

where $\pi \mathcal{F}_\odot$ [photons cm⁻² s⁻¹] is the unattenuated solar line flux at $r_e = 1$ AU, Φ_\odot [Hz⁻¹] is the normalized solar emission line shape, and τ_\odot is the optical depth for photons at frequency ν travelling from the Sun to the point \mathbf{r} . Here the solar source line shape and flux are written to be independent of the solar longitude and latitude which is not likely the case. No time dependencies are specified, even though the UV solar fluxes and line shapes are variable.

3.2.7 The Equations of Resonance Radiative Transfer

Problems in radiative transfer may be solved by calculating the intensity field or, alternatively, calculating the volume emission rate, $E(\mathbf{r}, \hat{\mathbf{n}}, \nu)$. It is the rate photons are emitted (per unit volume and frequency) into a differential solid angle and has dimensions [photons cm⁻³ s⁻¹ Hz⁻¹ ster⁻¹]. For the heliospheric RT problem it is more convenient to calculate the emission rate rather than the intensity field. An auxiliary function called the Source Function is defined as the emission rate divided by the absorption coefficient.

Assuming the Sun is the only source of photons, heliospheric emission is conveniently divided into components corresponding to the scattering order. For instance, the singly scattered emission rate is denoted E_1 . For photons scattered m times, it

is E_m . The total rate is written as a sum

$$E(\mathbf{r}, \hat{\mathbf{n}}, \nu) = \sum_{m=1}^{\infty} E_m. \quad (3.26)$$

The emission rate for the photons scattered m times is calculated by integrating over the intensity field of photons scattered $m-1$ times (see Mihalas 1978 and Ivanov 1973):

$$E_m(\mathbf{r}, \hat{\mathbf{n}}, \nu) = n(\mathbf{r}) B_r S_{tr} \oint \frac{d\Omega'}{4\pi} \int_0^\infty d\nu' I_{m-1}(\mathbf{r}, \hat{\mathbf{n}}', \nu') R(\nu', \hat{\mathbf{n}}', \nu, \hat{\mathbf{n}}). \quad (3.27)$$

The intensity is calculated by integrating the volume emission rate along the path of the incident photons:

$$I_m(\mathbf{r}, \hat{\mathbf{n}}, \nu) = \int_0^\infty ds E_m(\mathbf{r}', \hat{\mathbf{n}}, \nu) \exp[-\tau(\mathbf{r}', \mathbf{r}, \nu)]. \quad (3.28)$$

The point \mathbf{r}' lies a distance s from \mathbf{r} :

$$\mathbf{r}' \equiv \mathbf{r} - s\hat{\mathbf{n}}. \quad (3.29)$$

Combined, equations (3.28) and (3.27) are the radiative transfer equations of resonantly scattered radiation. They provide the means for solving the heliospheric RT problem by directly calculating each scattering order in sequence. Given the solar flux field, equation (3.25), one may use equation (3.27) to calculate E_1 . Then, using equation (3.28), I_1 may be calculated which could be inserted into equation (3.27) to calculate E_2 and so on. Such a calculation is necessarily numerical, but otherwise completely general. However, it is appropriate only for positions within a few peak optical depths of the source. (Here peak optical depth refers to the maximum value of τ as a function of ν . For a motionless medium, the peak occurs at the line center.) For larger peak optical depths, it becomes increasingly computationally expensive. Using the diffusion approximation for conservative scattering (see Ivanov, 1973; Chamberlain and Hunten, 1987), the mean scattering order is $\bar{m} \sim \sqrt{\tau_0}$, where τ_0 is the peak optical depth from the source. For VLISM Ly α scattering, the heliospheric length

scale of ~ 100 AU corresponds to ~ 10 peak optical depths. Traversing this distance, H Ly α photons typically scatter 100 times. So accurately modeling heliospheric Ly α using this technique requires sequentially calculating hundreds of scattering orders. Clearly, other less taxing methods are preferable.

The emission rate E_m may be expressed in terms of E_{m-1} by combining equations (3.27) and (3.28):

$$E_m(\mathbf{r}, \hat{\mathbf{n}}, \nu) = \frac{n(\mathbf{r})B_r S_{tr}}{4\pi} \int \frac{d^3\mathbf{r}'}{|\mathbf{r} - \mathbf{r}'|^2} \int_0^\infty d\nu' E_{m-1}(\mathbf{r}', \hat{\mathbf{n}}', \nu') [R e^{-\tau}], \quad (3.30)$$

where the functional arguments of R and τ are suppressed. Summing this equation over all m yields an integral form of the RT equation:

$$E(\mathbf{r}, \hat{\mathbf{n}}, \nu) = E_1(\mathbf{r}, \hat{\mathbf{n}}, \nu) + \frac{n(\mathbf{r})B_r S_{tr}}{4\pi} \int \frac{d^3\mathbf{r}'}{|\mathbf{r} - \mathbf{r}'|^2} \int_0^\infty d\nu' E(\mathbf{r}', \hat{\mathbf{n}}', \nu') [R e^{-\tau}]. \quad (3.31)$$

This form often is appropriate for resonance scattering problems—especially when employing the Green's function solution method (see Ivanov, 1973).

3.2.8 Singly Scattered Photons

The volume emission rate of singly scattered photons is calculated by combining the emission rate equation (3.27) with the solar flux equation (3.25):

$$E_1(\mathbf{r}, \hat{\mathbf{n}}, \nu) = B_r S_{tr} n(\mathbf{r}) \left[\pi \mathcal{F}_\odot \left(\frac{r_e}{r} \right)^2 \right] \int_0^\infty d\nu' \Phi_\odot(\nu') R(\nu', \hat{\mathbf{n}}, \nu, \hat{\mathbf{n}}) \exp[-\tau_\odot(\mathbf{r}, \nu')]. \quad (3.32)$$

Using the CFR approximation, equation (3.19), this reduces to

$$E_1(\mathbf{r}, \hat{\mathbf{n}}, \nu) = \left(\frac{n(\mathbf{r})}{4\pi} \right) P_h(\hat{\mathbf{n}}, \hat{\mathbf{r}}) \phi(\nu, \hat{\mathbf{n}}) g_\odot(\mathbf{r}), \quad (3.33)$$

where the g_\odot is the singly scattered g-value:

$$g_\odot(\mathbf{r}) = B_r S_{tr} \left[\pi \mathcal{F}_\odot \left(\frac{r_e}{r} \right)^2 \right] \int_0^\infty d\nu' \Phi_\odot(\nu') \phi(\nu', \hat{\mathbf{r}}) \exp[-\tau_\odot(\mathbf{r}, \nu')]. \quad (3.34)$$

The g-value has dimensions of s^{-1} ; it is the number of photons emitted into all solid angles per atom per second. The total g-value is given by the sum of the singly and multiply scattered components.

3.2.9 Multiply Scattered Photons

Summing the m th scatter order volume emission rate, equation (3.27), over all m yields an equation for the total emission rate:

$$E(\mathbf{r}, \hat{\mathbf{n}}, \nu) = E_1(\mathbf{r}, \hat{\mathbf{n}}, \nu) + B_r S_{tr} n(\mathbf{r}) \oint \frac{d\Omega'}{4\pi} \int_0^\infty d\nu' R(\nu', \hat{\mathbf{n}}', \nu, \hat{\mathbf{n}}) \mathcal{I}(\mathbf{r}, \hat{\mathbf{n}}', \nu'), \quad (3.35)$$

where \mathcal{I} is the summed resonantly scattered intensity (equation (3.23)). Using the CFR and isotropic scattering approximations for multiply scattered photons, this becomes:

$$E(\mathbf{r}, \hat{\mathbf{n}}, \nu) = \left(\frac{n(\mathbf{r})}{4\pi} \right) \phi(\nu, \hat{\mathbf{n}}) [P_h(\hat{\mathbf{n}}, \hat{\mathbf{r}}) g_\odot(\mathbf{r}) + g_{\text{MU}}(\mathbf{r})], \quad (3.36)$$

where the multiply scattered g-value is

$$g_{\text{MU}}(\mathbf{r}) = B_r S_{tr} \oint d\Omega' \int_0^\infty d\nu' \phi(\nu', \hat{\mathbf{n}}') \mathcal{I}(\mathbf{r}, \hat{\mathbf{n}}', \nu'). \quad (3.37)$$

The total emission rate, E_{TOT} [photons $\text{cm}^{-3} \text{s}^{-1}$], is defined as the integral of E over all solid angles and frequencies:

$$E_{\text{TOT}}(\mathbf{r}) = \oint d\Omega \int_0^\infty d\nu E(\mathbf{r}, \hat{\mathbf{n}}, \nu) = n(\mathbf{r}) [g_\odot(\mathbf{r}) + g_{\text{MU}}(\mathbf{r})] \quad (3.38)$$

3.2.10 The Optically Thin Approximation

To obtain complete and detailed solutions to the RT equation requires numerical techniques as well as several approximations. However, in systems where typical length scales correspond to small line center optical depths, a useful approximate solution is obtained by neglecting the multiply scattered component and all optical depths. This is the optically thin approximation and may be calculated from equations (3.33) and (3.34):

$$E_{\text{TH}}(\mathbf{r}, \hat{\mathbf{n}}, \nu) = \left(\frac{n(\mathbf{r})}{4\pi} \right) P_h(\hat{\mathbf{n}}, \hat{\mathbf{r}}) \phi(\nu, \hat{\mathbf{n}}) g_{\text{TH}}(\mathbf{r}), \quad (3.39)$$

where the optically thin g-value is

$$g_{\text{TH}}(\mathbf{r}) = B_r S_{tr} \left[\pi \mathcal{F}_\odot \left(\frac{r_e}{r} \right)^2 \right] \int_0^\infty d\nu' \Phi_\odot(\nu') \phi(\nu', \hat{\mathbf{r}}). \quad (3.40)$$

The optically thin intensities are

$$I_{\text{TH}}(\mathbf{r}, \hat{\mathbf{n}}, \nu) = \int_0^\infty ds E_{\text{TH}}(\mathbf{r}', \hat{\mathbf{n}}, \nu). \quad (3.41)$$

The optically thin approximation is useful for several reasons. First, given the solar flux and scattering species distribution, it is directly calculable—requiring no iterative or matrix inversion methods that optically thick RT solutions typically require. Complicated RT computer codes may be validated by comparing the results for optically thin systems with the optically thin approximation. Also, the thin approximation does not require extensive computer time to calculate. This means that the detailed effects of the complicated forms of the frequency redistribution function—like equation (3.18) or the angle dependent formulae developed by Hummer (1962)—may be investigated. Since exact line shapes depend on the redistribution function, this is especially important for high spectral resolution observations of resonance lines. Finally, the optically thin approximation reduces to a simple and convenient form in a uniform, motionless medium.

Meier (1977) calculates the optically thin approximation for the 58.4 nm line. He employs the hot distribution (as presented in section 2.2.3) and a frequency redistribution function as given in equation (3.18). The line shapes in the downstream direction can have complicated shapes and, in general, are not well represented by a Gaussian.

3.2.11 Radiation Pressure

Each resonance scattering event transfers momentum between the scattering atom and the photon. The change in a photon's momentum is related to a change in its frequency. The scattering atom's velocity also is affected. The cumulative effect may be expressed as a net radiation force on each atom. Since force is the change in momentum per unit time, radiation force is the momentum transferred from photon

to atom per scattering event multiplied by the frequency of the scattering events per atom. However, representing the cumulative effect as a continuously acting force is not justified if the time between scattering events is comparable to the time it takes for an atom to travel a length equivalent to its heliocentric distance. The time between scattering events is inversely proportional to the g -value, so it is proportional to r^2 . The time scale for an atom to travel a distance r is proportional to r . At some value for r , the times scales become comparable. Beyond this radius, the use of a continuously acting radiation force is not a reasonable representation of the photon-to-atom momentum transfer. For H Ly α this distance is ~ 5000 AU. Since the heliosphere probably has a length scale of a few hundred AU, the continuous radiation force representation is justified.

The force exerted on an atom due the cumulative effect of resonance scattering events, \mathbf{F}_R , is calculated by summing the rate momentum is transferred from the radiation field to the atoms:

$$\mathbf{F}_R(\mathbf{r}) = \frac{hS_{tr}}{c} \oint d\Omega' \hat{\mathbf{n}}' \int_0^\infty d\nu' \nu' \phi(\nu', \hat{\mathbf{n}}') \mathcal{I}(\mathbf{r}, \hat{\mathbf{n}}', \nu'). \quad (3.42)$$

In all of the cases to be investigated here, this vector is closely aligned with the radial direction so

$$F_R(\mathbf{r}) \approx \mathbf{F}_R \cdot \hat{\mathbf{r}} = \frac{hS_{tr}}{c} \oint d\Omega' (\hat{\mathbf{n}}' \cdot \hat{\mathbf{r}}) \int_0^\infty d\nu' \nu' \phi(\nu', \hat{\mathbf{n}}') \mathcal{I}(\mathbf{r}, \hat{\mathbf{n}}', \nu'). \quad (3.43)$$

The radiation pressure force exerted directly by of the solar flux, $F_{R,1}$, is obtained by combining the above equation with the solar flux intensity field, equation (3.25). This yields

$$F_{R,1}(\mathbf{r}) = \frac{hS_{tr}}{c} \left[\pi \mathcal{F}_\odot \left(\frac{r_e}{r} \right)^2 \right] \int_0^\infty d\nu' \nu' \phi(\nu', \hat{\mathbf{n}}') \Phi_\odot(\nu') \exp[-\tau_\odot(\mathbf{r}, \nu')]. \quad (3.44)$$

The optically thin approximation for the radiation pressure force may be calculated by neglecting the optical depth in equation (3.44). The result is that the force

falls as r^{-2} . Thus the ratio of the optically thin radiation force to the gravitational force, μ_{TH} , is independent of position. Furthermore, if the solar line profile is constant over the absorption profile (which is not satisfied in general), μ_{TH} may be written

$$\mu_{\text{TH}} = \left(\frac{h S_{tr} \lambda_o r_e^2}{G M_{\odot} m c} \right) (\pi \mathcal{F}_{\lambda_o}), \quad (3.45)$$

where $\pi \mathcal{F}_{\lambda_o}$ is the differential solar flux at 1 AU. Evaluating this numerically for H Ly α implies that $\mu_{\text{TH}} = 1$ for a differential flux of 3.37×10^{12} photons $\text{cm}^{-2} \text{s}^{-1} \text{nm}^{-1}$ at 1 AU. As can be seen in Figure 1.3, the measured differential flux near line center is in this neighborhood. Given the observed variations in solar Ly α , it is likely that μ_{TH} oscillates above and below unity over the solar cycle.

3.2.12 An Iterative, Finite-Element RT Method

Using the assumptions which yield equation (3.36), the entire heliospheric RT problem is solved by calculating the multiply scattered g-value, $g_{\text{MU}}(\mathbf{r})$. Here an iterative, finite element algorithm is used to iteratively calculate g_{MU} . The process goes as follows: 1) Divide the system into an array of grid points defining regions of finite volume. In the case of spherically symmetric problems, an array in radial distance r is appropriate. For axially symmetric systems, a grid in (r, θ) may be employed. (No 3-dimensional solutions are investigated here.) 2) Calculate the singly scattered and optically thin g-values for all of the grid points using equations (3.34) and (3.40). 3) Estimate the zeroth iteration multiply scattered g-values by using the difference between the optically thin and the singly scattered g-values. 4) Calculate new estimates of g_{MU} on the grid by using equation (3.37). Here the intensity, \mathcal{I} , is calculated with the previous estimate of g_{MU} . Step 4 is repeated iteratively until the multiply scattered g-values converge over the grid. Unfortunately, the convergence can be slow—especially for conservative scattering. In order to speed convergence, a form of the solution at large optical depths from the Sun may be introduced artificially

at radii that correspond to large line peak optical depths from the Sun. In the case of conservative scattering, using such a boundary condition is essential to obtain reasonable computation times.

3.3 RT in a Uniform Medium with a Point Source

Heliospheric H Ly α radiative transfer is complicated by several factors: the net VLISM motion with respect to the Sun (which introduces Doppler shifts), the details of the heliospheric H distribution, and, finally, the complicated shape of the solar source line. In order to be able to write an RT computer program based on the algorithm given in the previous section, analytical solutions for simpler cases are required to validate the computer code performance. This basic strategy is used by Keller and Thomas (1979); they point out that Ivanov (1973) gives analytical solutions for a system consisting of a point source in a uniform, isothermal and motionless medium in which photons isotropically scatter according to the CFR approximation. The total volume emission rate in such a system is a function only of the line center optical depth from the source, τ_o . Since the medium is motionless, there are no Doppler shifts and the absorption profile, ϕ , is only a function of frequency and not of direction. The solar source is assumed to have the same line shape as the absorption profile (i.e. $\Phi_\odot = \phi$) and the Doppler profile is used for both. Equation (3.3) implies that τ_o is the radial distance multiplied by the line center scattering coefficient, k_o :

$$\tau_o = r k_o = r \left(\frac{n S_{tr}}{w_d \sqrt{\pi}} \right). \quad (3.46)$$

3.3.1 The Optically Thin Solution

Using the above assumptions, the optically thin approximation for the volume emission rate is simplified considerably and may be written as a function of τ_o and ν :

$$E_{TH}(\tau_o, \nu) = C_e \frac{\phi(\nu)}{\tau_o^2}, \quad (3.47)$$

where C_e is a constant factor with dimensions [photons $\text{cm}^{-3} \text{s}^{-1} \text{ster}^{-1}$] and the τ_o^{-2} factor is introduced by the r^{-2} dependence of the solar flux. The dimensionless emission rate is defined:

$$\epsilon(\tau_o) \equiv \frac{1}{C_e} \int_0^\infty d\nu E(\tau_o, \nu). \quad (3.48)$$

The optically thin dimensionless emission rate is $\epsilon_{\text{TH}} = \tau_o^{-2}$.

The optically thin intensity is calculated by integrating through the optically thin emission rate. Total line intensities fall as τ_o^{-1} or r^{-1} :

$$I_L(r, \hat{\mathbf{n}}) = I_e \left(\frac{r_e}{r} \right) \left[\frac{\Theta}{\sin(\Theta)} \right], \quad (3.49)$$

where Θ is the angle between $\hat{\mathbf{n}}$ and the radially inward direction, and I_e is the intensity for $r = r_e$ and $\Theta = 0$.

3.3.2 Ivanov's Solution for Conservative Scattering

The RT equation (3.31) is a convenient form for solving the uniform medium problem; it is considerably simplified by using the isotropic scattering and CFR approximations. For instance the triple integration over volume ($d^3\mathbf{r}$) reduces to a single integral over radial distance (or τ_o). Ivanov (1973) obtains solutions in both the small and large τ_o limits. The details of the derivation are not reproduced here.

For conservative scattering the dimensionless emission in the large- τ_o limit is:

$$\epsilon(\tau_o) \approx \frac{8}{\tau_o^2} \sqrt{\frac{2 \ln(\tau_o)}{\pi^3}} \quad (\tau_o \gg 1). \quad (3.50)$$

The dominant dependence is τ_o^{-2} , as in the optically thin case. The ratio of the multiply scattered emission rate to the optically thin value is proportional to $\sqrt{\ln(\tau_o)}$ which varies relatively slowly. In this limit, the multiply scattered g-value divided by the optically thin g-value is:

$$\frac{g_{\text{MU}}}{g_{\text{TH}}} \approx 8 \sqrt{\frac{2 \ln(\tau_o)}{\pi^3}} \approx 2.03 \sqrt{\ln(\tau_o)} \quad (\tau_o \gg 1). \quad (3.51)$$

This result is used as a boundary condition on the multiply scattered g -values in the heliospheric $\text{Ly}\alpha$ RT models.

3.3.3 Numerical Solution of the Uniform Problem

The uniform medium problem can be solved for conservative scattering by calculating the multiply scattered g -values as described in section 3.2.12. The calculations are performed here using a computer program written to handle the axially symmetric problem. This spherically symmetric application is a simple case that verifies the code's performance. The calculation uses the Ivanov (1973) large τ_o limit as a boundary condition for $\tau_o \geq 10$. Calculated dimensionless emission rates are shown in Figure 3.4. The salient result is that the total volume emission rate is larger than the optically thin approximation everywhere.

3.3.4 Line Intensities in a Uniform Medium

The Voyager and Pioneer 10 spacecraft UV instruments measure integrated line intensities. Typically, optically thin models have been employed to model observations. This is reasonably justified for all of the lines except $\text{Ly}\alpha$. Therefore it is of interest to determine how the line intensities in a multiple scattering environment behave relative to the optically thin approximations. Using the solution from in the previous section, the intensities that would be detected by an instrument looking radially outward in a uniform medium may be calculated. (These are referred to as antisolar or radially outward intensities.) A plot of the antisolar intensities relative to their optically thin counterparts is shown in Figure 3.5. This is an accurate reproduction of the results of Keller et al. (1981). The fundamental result is that, whereas for small optical depths the antisolar intensity follows the optically thin τ_o^{-1} dependence, at large optical depths, it falls as τ_o^{-2} . Understanding this is not difficult. The intensity field at τ_o basically is a measure of the volume emission rate within a few optical

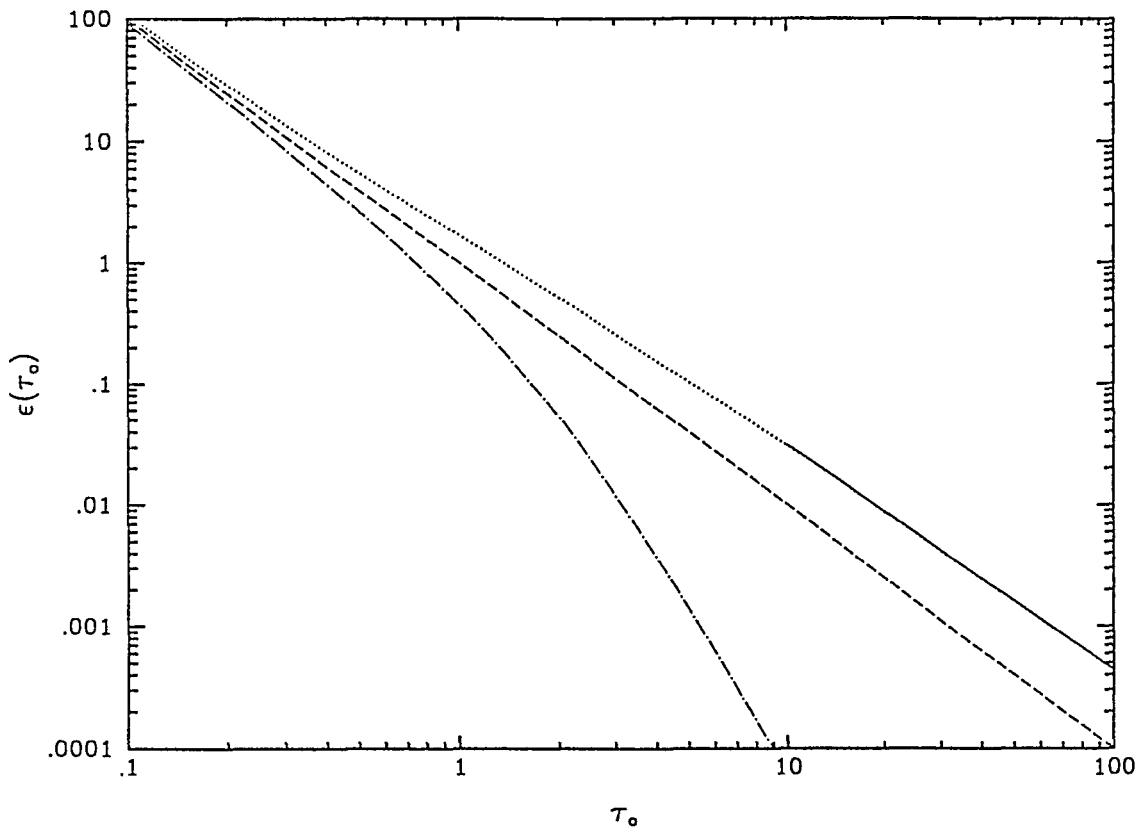


Figure 3.4: The dimensionless emission rate for a uniform, motionless, conservative, isotropic and CFR scattering medium as a function of line center optical depth from a point source. The optically thin rate, τ_0^{-2} , is shown as the dashed line. The dash-dot line is the singly scattered emission rate, which falls rapidly because of attenuation of the solar source flux. The dotted line is the total emission rate calculated using an iterative, finite-element computer code. As a boundary condition, the solution is forced to match the Ivanov (1973) large- τ_0 asymptote (shown as the solid line) for $\tau_0 > 10$.

depths. Thus, for values of τ_o significantly larger than a few, the intensity field should assume the same functional dependence as the volume emission rate, which is very nearly τ_o^{-2} .

3.3.5 Radiation Pressure in a Uniform Medium

The radiation pressure given by equation (3.43) may be calculated using the numerical solution for a uniform system. The optically thin radiation force falls as τ_o^{-2} which means that the optically thin radiation pressure parameter, μ_{TH} , is a constant. The calculated ratio of the radiation pressure parameter, μ_\odot , to μ_{TH} is shown in Figure 3.6. Evidently, the effects of multiple scattering make this ratio fall as a function of τ_o^{-2} . This effect may be significant for the heliospheric H distribution where $\tau_o = 1$ corresponds to a path of ~ 10 AU. Ideally, this effect should be incorporated into the numerical models of the H distribution given in Chapter 2. Unfortunately this links the RT problem to the distribution problem and would require considerably more effort. Here, this effect is ignored but acknowledged as being a deficiency that could be fixed in the future.

3.4 A Heliospheric H Ly α RT Model

An RT model is the necessary tool to analyze Voyager and Pioneer 10 Ly α observations obtained from beyond $r = 5$ AU. The iterative, finite-element algorithm described in section 3.2.12 is employed to determine emission rates and intensities in axially symmetric heliospheric H distributions. The shape of the solar source line used is that measured by Lemaire et al. (1978)—see Figure 1.3. The particle densities, bulk flow velocities and effective temperatures of the gas are used as input parameters in the model. The RT calculation is performed for the “standard” hot distributions (see Figures 2.4 and 2.5) as well as for the two-component distributions described in section 2.3. In both cases, the ratio g_{MU}/g_{TH} for the dominant H component (i.e. the H

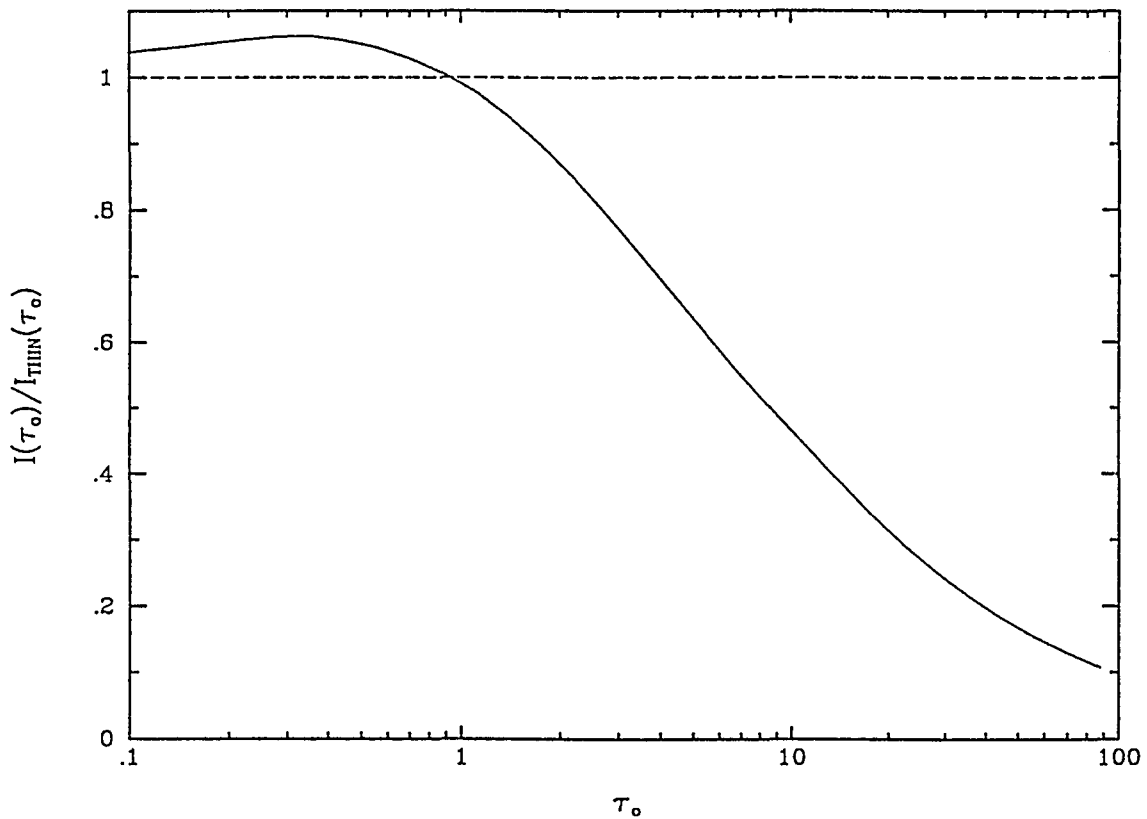


Figure 3.5: Line intensities looking radially outward, relative to the optically thin approximation. The multiply scattered intensities are within $\approx 10\%$ of the optically thin approximation for τ_0 less than about 2. At larger τ_0 , the ratio falls as τ_0^{-1} . Since optically thin intensities already fall as τ_0^{-1} , this implies that for outside a few line center optical depths, intensities measured in the antisolar direction in a uniform medium should fall as τ_0^{-2} , or alternatively as r^{-2} .

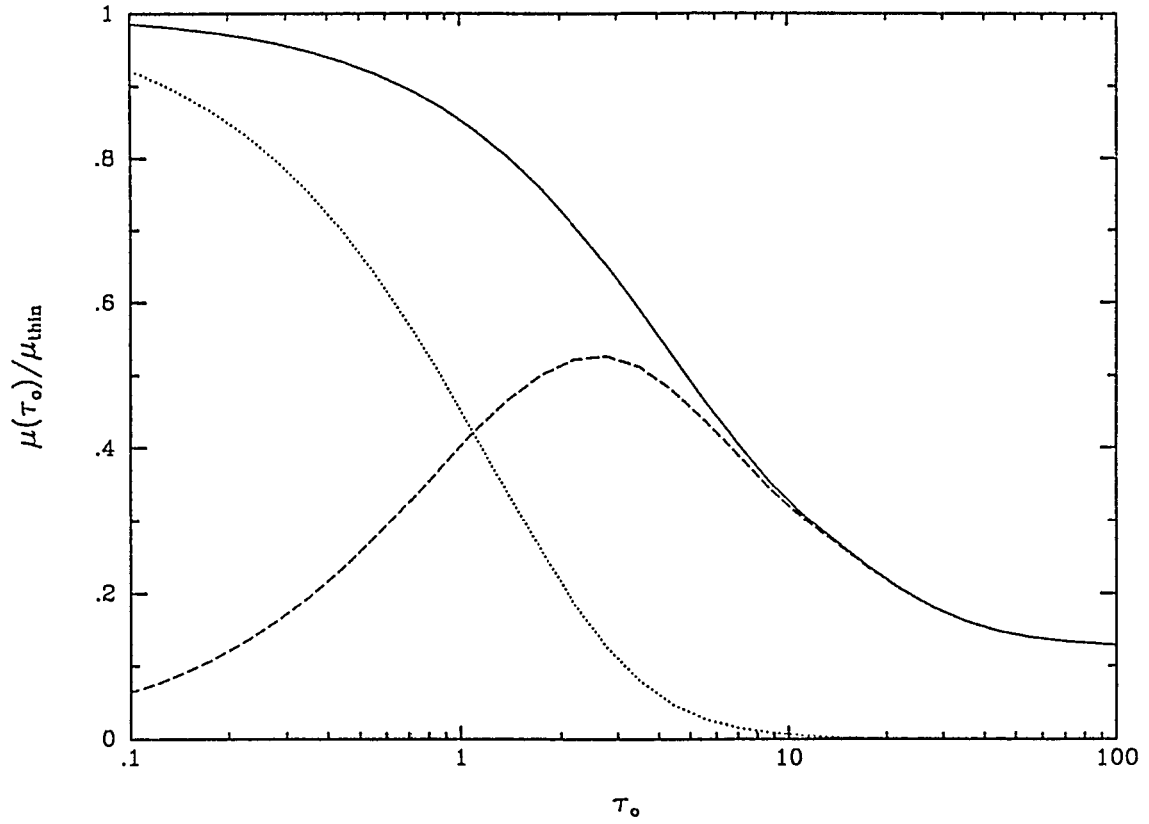


Figure 3.6: The ratio of the radiation pressure parameter to the optically thin approximation. The solid line shows the ratio for the total radiation force, while the dotted and dashed line show the singly and multiply scattered values respectively. The total ratio is reduced by about 20% at $\tau_0 \approx 1$. At $\tau_0 \approx 10$, the reduction is $\approx 70\%$. This effect could be significant for the heliospheric H distribution, where one line center optical depth corresponds to a path of order 10 AU.

atoms penetrating from outside the heliopause) is constrained to be equal to Ivanov's asymptotic value for line peak optical depths greater than 10. This boundary condition may not be correct in detail for the 2-dimensional heliospheric problem. However, without this imposed boundary condition, the code seems to converge to this limit anyway—but almost two orders of magnitude more slowly. Detailed comparisons of the RT calculation and the spacecraft data are given in Chapter 4. Here, only the character of the solutions are discussed.

3.4.1 Results for the “Standard” Hot H Distributions

Figure 3.7 shows H Ly α total emission rates and antisolar line intensities for the standard solar minimum hot heliospheric distribution shown in Figures 2.4. The parameters used are: $n_{\text{H}\infty} = 0.10 \text{ cm}^{-3}$, $v_{\infty} = 20 \text{ km s}^{-1}$, $T_{\infty} = 10^4 \text{ K}$, $\beta_e = 5 \times 10^{-7} \text{ s}^{-1}$, $\mu_{\odot} = 0.75$ and $\pi\mathcal{F}_{\odot} = 2.5 \times 10^{11} \text{ photons cm}^{-2} \text{ s}^{-1}$. The top panel shows the total volume emission rates at several angles from the upstream direction. The lower panel shows the antisolar intensities. Figure 3.8 shows Ly α total emission rates and antisolar line intensities for the solar maximum distribution in the same format. The parameters used are: $n_{\text{H}\infty} = 0.10 \text{ cm}^{-3}$, $v_{\infty} = 20 \text{ km s}^{-1}$, $T_{\infty} = 10^4 \text{ K}$, $\beta_e = 10 \times 10^{-7} \text{ s}^{-1}$, $\mu_{\odot} = 1.2$ and $\pi\mathcal{F}_{\odot} = 4.0 \times 10^{11} \text{ photons cm}^{-2} \text{ s}^{-1}$.

The pertinent results are in the lower panels of Figures (3.7) and (3.8). In either H distribution, the antisolar line intensities are expected fall more rapidly as a function of r in the upstream direction than in the downstream direction for heliocentric radii less than 30 AU. This is because the H ionization cavity is elongated in the downstream direction. In fact, no set of parameters for the hot distribution can reverse this basic trend. This is important because the Voyager and Pioneer 10 spacecraft, which are heading upstream and downstream respectively, measure the *opposite* trend. This is a strong indication that the hot distribution is not correct in detail. One possibility is that the effects of outer heliospheric plasma structures,

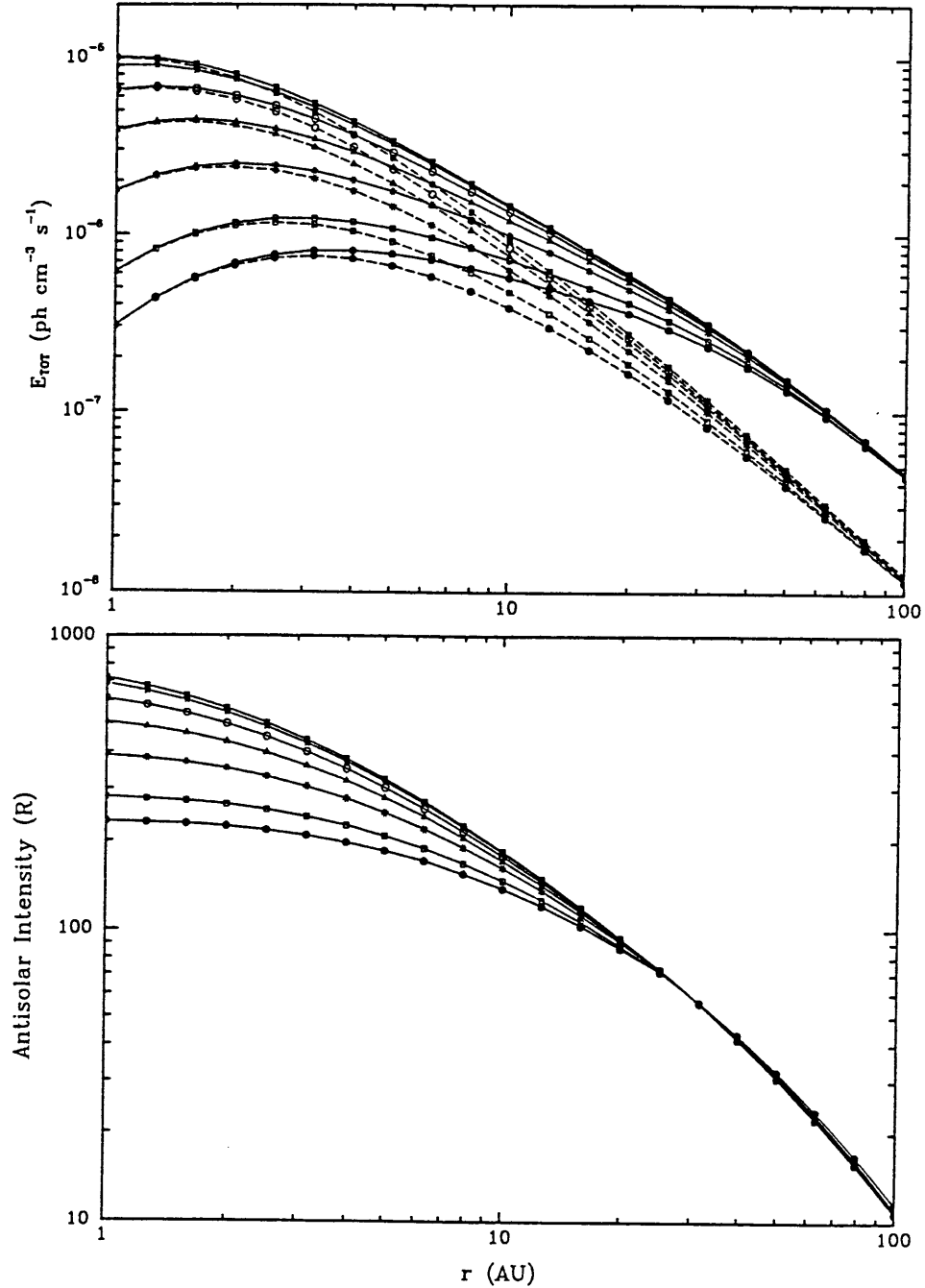


Figure 3.7: The volume emission rates and antisolar line intensities for $\text{Ly}\alpha$ scattering in the standard solar minimum hot H distribution shown in Figure 2.4. The symbols correspond to the following values of θ : solid squares (0°), stars (30°), open circles (60°), triangles (90°), asterices (120°), open squares (150°), solid circles (180°). In the top panel, the emission rates are shown as the solid lines. The dashed lines show the optically thin approximation. The lower panel shows the antisolar intensities, which tend to remain constant within the ionization cavity.

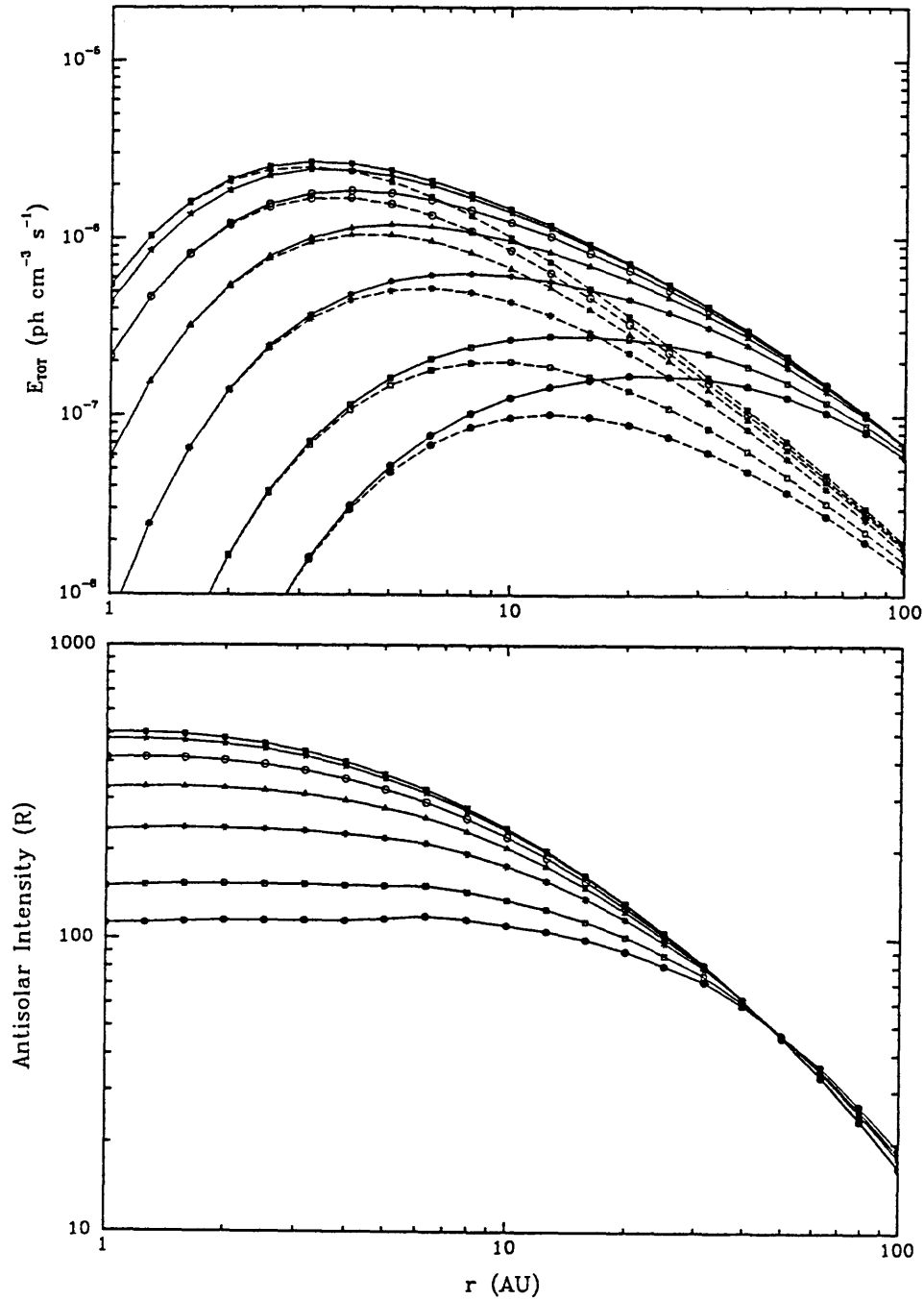


Figure 3.8: The total volume emission rates and antisolar line intensities for $\text{Ly}\alpha$ scattering in the standard solar maximum hot H distribution shown in Figure 2.5. The symbol and line format is the same as in the previous figure. Because the ionization cavity is larger and more depleted in this distribution than the previous case, the antisolar line intensities tend to remain constant further out from the Sun.

which are not included in the hot model, can account for the discrepancy.

3.4.2 Results for the Multi-Component H Distribution

The multi-component H distribution given in section 2.3 is distinct from the hot distribution in that it includes the filtering of the thermal component (which is analogous to the hot distribution) at the heliospheric interface, as well as including the suprathermal component. Because the thermal component dominates scattering at large heliocentric radii, its g -values are constrained to follow Ivanov's asymptote for $\tau_o > 10$. The RT results for the distribution shown in Figures 2.9 and 2.10 are shown in Figure 3.9. In the top panel the total volume emission rates for both components are plotted. The lower panel shows that the antisolar intensities have basically the same general pattern as seen in the standard hot distributions above—the downstream intensities fall more slowly as a function of heliocentric distance than upstream. Unfortunately, the extensive computer time required to calculate both the multi-component distributions and the associated multiply scattered radiation fields has prevented a detailed exploration of the parameter space of the multi-component model. This is deferred for future investigation.

An interesting result of the multi-component RT calculation is that inside ≈ 2 AU the total emission rate from the suprathermal component may be comparable to or larger than that from the thermal component, especially in the downstream region. This suggests that the Ly α line shape measured in the downstream direction could be significantly wider than the upstream line shapes. Figure 3.10 shows H Ly α line shapes calculated from the RT model shown in Figure 3.9. Given accurate line shape measurements, an RT analysis like the one presented here could be used to estimate the relative densities of the thermal and suprathermal components of the heliospheric H distribution. As can be seen in Figure 2.11, the mixing ratio of the two components in the upstream and downstream directions is extremely sensitive to

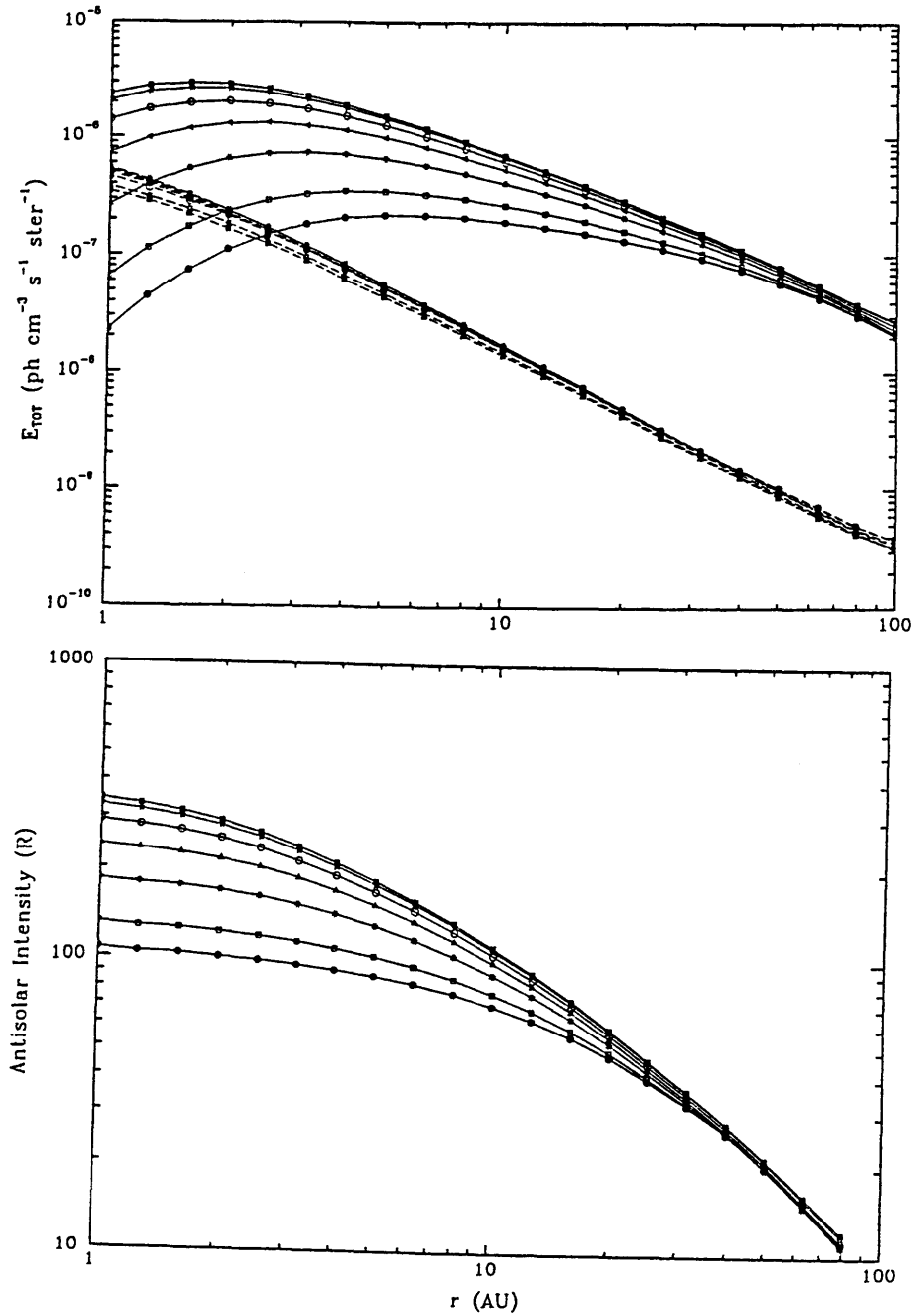


Figure 3.9: The total volume emission rates and antisolar line intensities for $\text{Ly}\alpha$ scattering in the multi-component heliospheric H distribution shown in Figures 2.9 and 2.10. The symbol format is the same as in the previous 2 figures. In the upper panel the solid and dashed lines correspond to the thermal and suprathermal H gases respectively. The general pattern of antisolar intensities is similar to that of the hot distribution. The critical difference is that a fraction of the $\text{Ly}\alpha$ intensity here is caused by scattering from the suprathermal component of the H distribution.

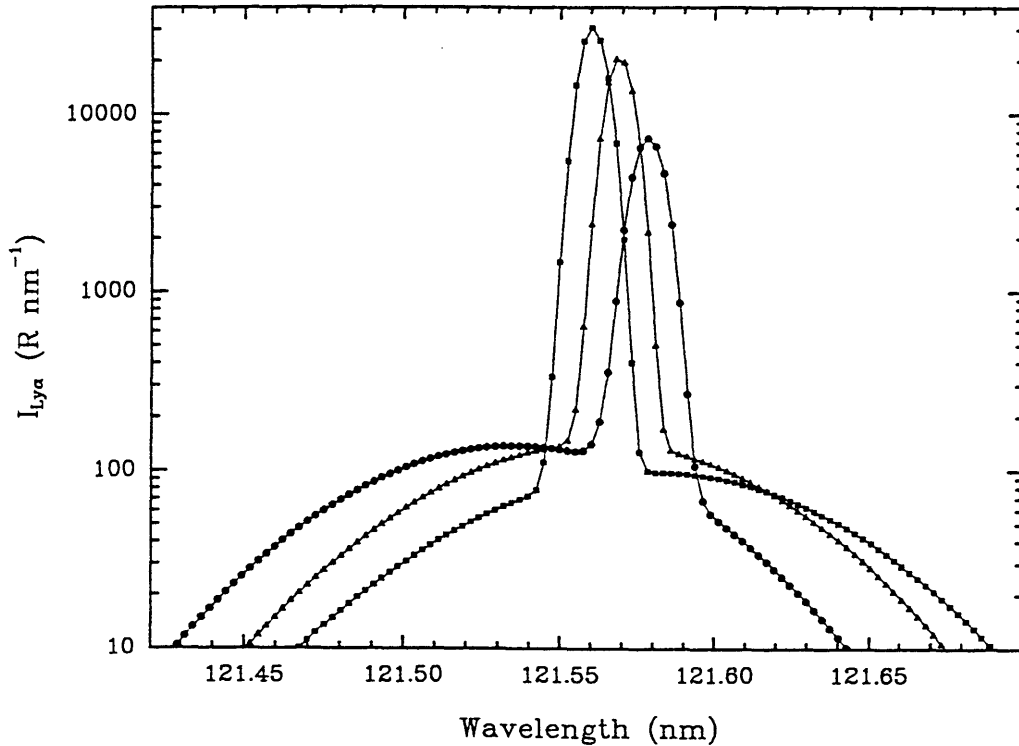


Figure 3.10: The H Ly α line shapes calculated in the upstream, sidestream and downstream directions in the multi-component heliospheric H distribution shown in Figures 2.10 and 2.11. The line shapes looking radially outward from 1 AU are shown for observation points lying upstream (squares), sidestream (triangles) and downstream (circles). The two H components combined produce line shapes that have two distinct parts. The central, thinner parts are due to scattering from component 1 of the H distribution. The wider parts are from the suprathermal component 2. In the downstream region, component 2 comprises a larger fraction of the total H density than in the upstream region; so the wide part of the line in the downstream direction makes up a larger part of the total line intensity. This effect could provide a means of estimating the density of component 2, which is sensitive to the distance to the solar wind termination shock.

the distance to the solar wind termination shock. Accurate high-resolution Ly α line shape measurements made from 1 AU could provide a diagnostic tool to constrain outer heliospheric geometry. Preliminary analysis shows that an instrument with spectral resolution better than about 0.02 nm and sensitive enough to detect an intensity of about 50 R nm⁻¹ on the wings of the Ly α line is required.

CHAPTER 4

PIONEER AND VOYAGER H Ly α OBSERVATIONS

On January 1, 1992 the heliocentric distances of the Voyager 1 and 2 and Pioneer 10 spacecraft were 47, 36 and 53 AU respectively. Each is leaving the solar system at a rate of a few AU per year and continues to collect heliospheric Ly α observations. Figure 4.1 illustrates their trajectories projected onto the ecliptic plane. The direction of the VLISM flow, which lies within about 7° of the ecliptic, is also shown. Both Voyagers are heading generally upstream, whereas the Pioneer 10 trajectory very nearly parallels the downstream direction. The combined Voyager and Pioneer observations therefore provide a more global view of the heliosphere than either data set taken independently.

The cones on each trajectory in Figure 4.1 schematically illustrate the directions the UV instruments aboard each spacecraft obtained Ly α observations. Pioneer 10 spins about the Earth-spacecraft line, collecting data on a cone approximately 20° from the anti-Earth direction. At each point marked on the Voyager trajectories, the spacecraft performed Cruise Maneuver observing sequences, obtaining partial maps of the sky in Ly α . These are combined to produce averages over the illustrated 65° antisolar cones. The Ly α intensities observed on the cones illustrated in Figure 4.1 constitute the main data of this dissertation. Pioneer 10 Ly α data have been reduced and published by various members of the Pioneer 10 UV photometer team (Wu et al. 1981; 1988, Gangopadhyay et al., 1989 and Gangopadhyay and Judge, 1989). Many of the Voyager Ly α data obtained beyond 5 AU have not been previously reduced or published. The Voyager UVS instruments and data reduction procedure are described in detail in Appendix A. Voyager Cruise Maneuver H Ly α observations are tabulated in Appendix B.

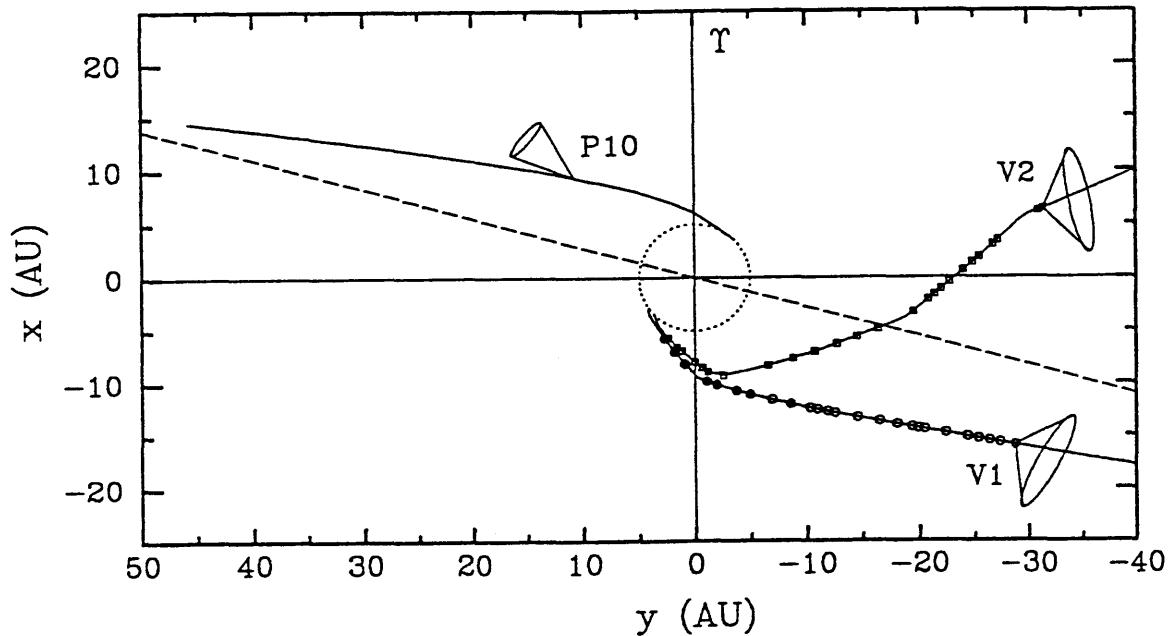


Figure 4.1: The trajectories of the Voyager 1, Voyager 2, and Pioneer 10 spacecraft projected onto the ecliptic plane. For scale, the dotted circle represents the orbit of Jupiter. Both Voyagers are heading generally upstream, into the VLISM flow direction, illustrated as the dashed line. The Pioneer 10 trajectory lies nearly in the ecliptic plane directed downstream. Since its encounter with Saturn (≈ 10 AU), Voyager 1 has travelled northward of the ecliptic plane. Voyager 2 was redirected southward at Neptune (≈ 30 AU). The cones illustrate the directions the UV instruments aboard each spacecraft obtained $\text{Ly}\alpha$ observations. Pioneer 10 collects data averaged on a cone 20° from the anti-Earth direction. At each point marked on the Voyager trajectories, the spacecraft performed Cruise Maneuver observing sequences which are combined to produce averages over the schematically illustrated 65° antisolar cones.

4.1 Instrument Calibrations: Issues and Limitations

Comparing Ly α data obtained from different spacecraft is complicated by the fact that absolute UV instrument sensitivity calibrations are difficult to validate. An example of how extreme instrument-to-instrument calibration differences can be is given in an analysis of heliospheric Ly α observations by Shemansky et al. (1984). By comparing Voyager 2 and Pioneer 10 data obtained during 1982, they derive a Ly α calibration difference of a factor of 4.4 ($I_{V2} = 4.4I_{P10}$). This analysis may be somewhat flawed in that it relies on a relatively simple model of the heliospheric H distribution and an approximate solution to the RT equations, but it shows that calibration differences can be uncomfortably large.

Even cross calibrating the two nearly identical Voyager UVS instruments is difficult. The Voyager 1 UVS suffered significant radiation damage during its encounter with Jupiter. Since then, the UVS have been periodically pointed at standard, bright stars to calibrate the instruments (see Holberg et al., 1982 and 1991). Unfortunately, this technique does not work at Ly α for three reasons. First, there is the variable foreground heliospheric Ly α line which is difficult to accurately subtract from the stellar spectra. Second, near the Ly α wavelength, the UVS instruments are equipped with a long wavelength filter which affects the net instrument response near 121.6 nm, and complicates cross calibration. Finally, the collimated design of the UVS instruments (Broadfoot et al., 1977) means that the instrumental response to point sources (stars) and extended field sources (like heliospheric Ly α) is distinctly different. So any in-flight adjustments to the UVS instrument calibrations based on stellar observations cannot be directly applied to Ly α . However, the stellar calibration analyses by Holberg et al. (1991; 1982) do yield one important piece of information: since the Jupiter encounters, the sensitivities of both UVS instruments have remained stable to within detectable limits. So the pattern of Ly α emissions observed by each UVS

beyond 5 AU is not in question, only the absolute and relative scaling.

Such difficulties with cross-calibration suggest that preliminary analysis the Voyager and Pioneer 10 Ly α observations should be based on the pattern of the observed emission. This is unfortunate because perhaps the most important parameter that one would want to determine from heliospheric Ly α observations is the ambient VLISM H density, $n_{\text{H}\infty}$. The most straightforward way to determine $n_{\text{H}\infty}$ is to compare observed intensities with those calculated from a model. But this technique relies on absolute instrument calibrations and requires a knowledge of the absolute solar Ly α flux. A better way to proceed is to base all initial estimates of $n_{\text{H}\infty}$ on the detected pattern of Ly α emissions. If the models predict the pattern reasonably well, then the observed and modeled intensities may be compared afterwards to validate or adjust cross calibrations (or at least to evaluate self-consistency). No analyses of the Voyager and Pioneer 10 data relying on absolute calibrations are presented here; this work is deferred for future investigations.

4.2 The Pioneer Spacecraft and H Ly α Observations

The Pioneer 10 and 11 spacecraft were launched in the early 1970's. The primary scientific objectives of the missions were to 1) characterize interplanetary phenomena, 2) study the asteroid belt and, most importantly, 3) the *in situ* measurement of the environments of Jupiter and, in the case of Pioneer 11, Saturn (Hall, 1975). The spacecraft are spin stabilized. The spin axis coincides with the axis of the high-gain antenna, which is usually pointed towards the Earth to maintain radio contact. Both spacecraft carry a compliment of ten or more scientific instruments, but the ultraviolet photometers are no longer operational on Pioneer 11. As of mid-1992, both spacecraft continue to operate, even though power reserve problems on Pioneer 11 threaten to discontinue its operational lifetime, perhaps before 1995.

4.2.1 The Pioneer 10 UV Photometer Experiment

The design and performance of the Pioneer 10 UV instrument is described in detail by Judge and Carlson (1974) and Carlson and Judge (1974). It is a two-channel photometer capable of measuring both H 121.6 nm and He 58.4 nm. The optical axis is fixed at a 20.24° angle to the spacecraft spin axis. So the data are collected on a cone $\approx 20^\circ$ from the anti-Earth direction. This is illustrated in Figure 4.1. Beyond 10 AU or so, the anti-Earth direction is very nearly coincident with the antisolar direction.

4.2.2 Pioneer 10 H Ly α Heliospheric Observations

The Pioneer 10 Ly α heliospheric observations beyond the orbit of Jupiter have been summarized and analyzed by Wu et al. (1981; 1988), Gangopadhyay et al. (1989) and Gangopadhyay and Judge (1989). The Pioneer 10 photometers are sensitive to particles and gamma radiation as well as UV photons. Within 5 AU of the Sun, the Ly α channel signal was affected significantly by solar wind particles. However, Wu et al. (1981) conclude that outside of 5 AU, particle contamination is negligible except during periods of intense solar activity. P. Gangopadhyay (*personal communication*, 1992) reports that in 1991 the signal in the Ly α channel was ≥ 150 counts s^{-1} with a noise contribution of ≈ 3 counts s^{-1} . In addition to the particle noise, the Pioneer 10 instrument suffers from transient sensitivity changes that occur when the instrument is turned off and on. This transient instrument response provides an internal means of estimating the Ly α sensitivity degradation over long periods of time. These effects are accounted for in the data presented here.

Early in the mission, the Pioneer 10 UV photometer field of view traced a circle in the upstream VLISM direction. Since 1978 (≥ 15 AU) the field of view has traced a cone within 30° of the downstream direction. The Ly α intensities, averaged over spin

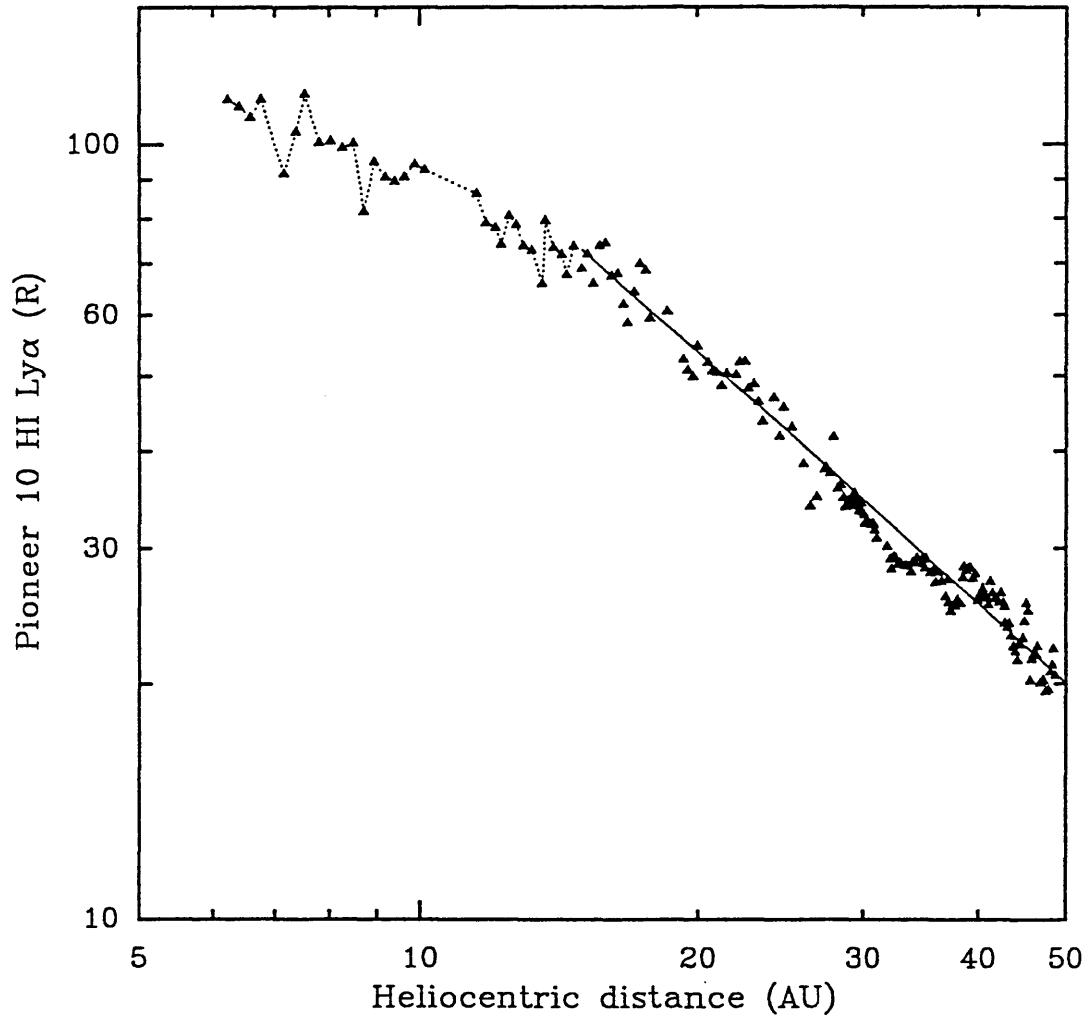


Figure 4.2: Pioneer 10 heliospheric H Ly α observations adjusted to constant solar Ly α flux. The absolute intensity scale is determined by the calibration factors reported in Wu et al. (1981). The solar Ly α flux variation has been removed from the data via multiplication by the factor $(3 \times 10^{11} \text{ photons cm}^{-2} \text{ s}^{-1})/\pi\mathcal{F}_{\odot}$, where $\pi\mathcal{F}_{\odot}$ is the estimated sub-spacecraft, monthly averaged solar Ly α flux. Between 5 and 15 AU, the intensities decrease relatively slowly as a function of heliocentric distance. Beyond 15 AU, the data fall off as $r^{(-1.07 \pm 0.1)}$

angle, show two basic trends (Wu et al., 1981; 1988): 1) they decrease with increasing heliocentric distance and 2) they tend to vary with the solar Ly α line integrated flux. The daily averaged Pioneer 10 Ly α observations between 5 and 50 AU are plotted in Figure 4.2. These data were obtained from P. Gangopadhyay (*personal communication*, 1991). Solar Ly α flux variations have been removed from the data by multiplying by the factor $(3 \times 10^{11} \text{ photons cm}^{-2} \text{ s}^{-1})/\pi\mathcal{F}_{\odot}$, where $\pi\mathcal{F}_{\odot}$ is the sub-spacecraft, monthly averaged solar flux. The inaccuracy of the solar flux adjustment may be responsible for part of the coherent structure in the 30 to 50 AU range.

Between 5 and 15 AU, the Pioneer 10 intensities decrease more slowly as a function of heliocentric distance than beyond 15 AU, where the data fall off as $r^{(-1.07 \pm 0.1)}$. An understanding of the general sense of these two trends is straightforward. Using the RT theory given in Chapter 3, one can show that from the inside of an idealized spherical, completely empty cavity, the antisolar intensity should be a constant for all radii less than the cavity radius. In this regard, the gentle slope of the Pioneer 10 intensities between 5 and 15 AU suggests that the spacecraft is still inside a considerably evacuated cavity in the heliospheric H distribution. Beyond 15 AU, the Pioneer 10 Ly α intensities fall as r^{-1} , to within uncertainty. Again, the general behavior is understandable. As a spacecraft leaves the evacuated cavity, intensities should begin to fall. Antisolar intensities fall as r^{-1} in an optically thin, uniform system. This suggests that the Pioneer 10 spacecraft entered a region of more nearly uniform density at about 15 AU. However this does not account for the effects of multiple scattering. As mentioned in section 3.3.2, beyond a few line center optical depths from the Sun, antisolar intensities in a uniform medium should fall as r^{-2} . Therefore the r^{-1} dependence of the Pioneer 10 observations probably is due to a combination of a non-uniform H distribution and the effects of multiple scattering. A comparison of the Pioneer 10 observations and RT models is given in section 4.6.

4.3 The Voyager Spacecraft and Ultraviolet Spectrographs

The Voyager spacecraft were launched in the late 1970's. A possible extended mission objective was to encounter all four of the gaseous giant planets, Jupiter, Saturn, Uranus and Neptune. This objective was completed when Voyager 2 encountered Neptune and Triton in 1989, and then began to head southward out of the ecliptic plane. Voyager 1 flew by Jupiter and then Saturn, where the encounter redirected it northward. Both spacecraft are leaving the solar system at about 3 AU per year. As of January 1, 1992 the heliocentric distances of Voyager 1 and 2 were 47 and 36 AU respectively. In January of 2000 they will have travelled to 76 and 60 AU respectively.

Each Voyager spacecraft is equipped with a host of scientific instruments, including magnetometers, particle detectors and imaging cameras (see Stone, 1983). The UVS instruments were included to obtain spectra in the 50 to 170 nm range. Their primary goal was to define the upper atmospheres of outer solar system bodies. An auxiliary goal was to observe resonance UV lines to constrain heliospheric structure. The UVS instruments are described in detail by Broadfoot et al. (1977, 1981). A useful summary is given by Holberg and Watkins (1992) and a brief description is given in Appendix A. The optical assembly is a compact, Wadsworth mounted design in which a grating disperses UV light entering the instrument onto a linear multi-channel detector.

Converting a UVS spectrum from raw counts registered on the detector array into a spectrum from which $\text{Ly}\alpha$ intensities may be calculated involves three steps (see Appendix A for details). First, the spectra are flat fielded by accounting for the inherent channel-to-channel sensitivity variations. This step entails multiplying the raw spectrum by a Fixed Pattern Noise (FPN) spectrum in a channel-by-channel fashion. Second, dark counts are removed. These are mostly caused by the response of the UVS to radiation in the spacecraft environment, mostly generated by the spacecraft nuclear power supply system. Dark count spectra are observed periodically

on each spacecraft by pointing the UVS at an optically neutral calibration plate mounted on the spacecraft body. The third step in reducing UVS spectra is accounting for the light that is (non-dispersively) scattered in the instrument assembly. Such scattering creates faint but extended skirts at the base of strong lines. This step is called descattering, and is performed by multiplying the spectra by a matrix operator. After these three steps, UVS spectra of the sky typically look like the one plotted in Figure 3.1. The UVS design and data reduction procedures are discussed in more detail in Appendix A.

4.4 Voyager UVS H Ly α Calibration

As discussed earlier, the Voyager UVS Ly α instrument sensitivity calibrations are difficult to validate. The laboratory calibration for Voyager 1 cannot be used due to the radiation damage suffered during Jupiter encounter. Stellar observations cannot be used for cross calibration at or near the wavelengths of the variable heliospheric resonance lines, especially at the relatively bright Ly α line. Other complicating factors include the possibilities of errors in the laboratory calibrations, changes in instrument sensitivities between the laboratory calibration period and the early post-launch period or a unique response in the UVS Ly α channels caused by the greatly elevated total photon exposure in those channels relative to adjacent channels. See Appendix A for a more complete description of these details.

Several separate UVS stellar observations indicate that, since their respective Jupiter encounters, each UVS has remained stable in the wavelength regions adjacent to 121.6 nm (Holberg et al., 1991). This strongly suggests that the UVS response to Ly α has not changed during the same period. The task at hand is to estimate the Voyager 1 Ly α UVS response *relative* to Voyager 2 for the post-Jupiter period. This may be combined with the an estimated absolute Ly α calibration for the Voyager 2 UVS, to determine the absolute Voyager 1 calibration for the post-Jupiter

period. Several methods of estimating the relative Ly α calibrations of the two instruments are investigated in Appendix A. These include 1) comparing the Voyager 1 Ly α line shapes observed before and after encounter, 2) comparing concurrent Voyager and International Ultraviolet Explorer (IUE) observations of the Saturn equatorial Ly α airglow, and 3) comparing Voyager 1 and 2 heliospheric Ly α observations conducted when the two spacecraft were in nearly the same position in the solar system looking in nearly the same direction. These methods yield estimates which are reasonably consistent with one another, and therefore yield a reasonably reliable estimate of the relative Voyager 1 and 2 Ly α sensitivities for the post-Jupiter phases of the mission. This is combined with the original laboratory Ly α calibration for Voyager 2 to establish a new, post-Jupiter Voyager 1 Ly α sensitivity calibration. As is discussed in Appendix A, the absolute Ly α calibration factor adopted for the Voyager 2 UVS is taken from the pre-flight laboratory calibration:

$$\epsilon_2 = \frac{172 \text{ Rayleighs}}{\text{counts/s in channels 72-80}}, \quad (4.1)$$

for spectra reduced using FPN 76 (see Appendix A for details on FPN). The absolute Voyager 1 calibration is estimated using the Ly α cross calibration for the two UVS instruments. The adopted value is:

$$\epsilon_1 = \frac{(218 \pm 33) \text{ Rayleighs}}{\text{counts/s in channels 70-78}}. \quad (4.2)$$

This is valid for spectra obtained after Jupiter encounter and reduced using FPN 47 or 49. The error of $\approx 15\%$ on the Voyager 1 calibration refers to the uncertainty in the UVS Ly α cross calibration. The uncertainty on both of these absolute calibrations is determined by the accuracy of the estimated Voyager 2 calibration. As is discussed in Appendix A, this is difficult to determine and is not reported here. However, the adopted absolute Voyager 2 Ly α calibration is consistent with that of IUE on the basis of concurrent observations of Jupiter's equatorial Ly α airglow (Shemansky and Judge, 1988).

4.5 Voyager Cruise Maneuver H Ly α Observations

Both Voyager spacecraft periodically conduct special maneuvers to map the heliospheric resonance emissions over large portions of the sky. The sequences are called the Cruise Maneuvers and are described in detail in Appendix B. During the maneuvers, the spacecraft are instructed to spin about their yaw and/or the roll axes for a period of 4 to 20 hours. As the spacecraft spin, the UVS gather spectra, which may be compiled into partial maps of the sky in the resonance lines H Ly α , Ly β , and He 58.4 nm, even though the signal-to-noise ratios for the latter two lines are much poorer than for Ly α . Maneuvers conducted within 5 AU of the Sun have been analyzed and published elsewhere (see Lallement, 1990 and references therein). Voyager Cruise Maneuver Ly α observations conducted beyond 5 AU are described and presented in tabular form in Appendix B. To date, these data have not been analyzed in detail. Ultimately, they should be compared in a spectrum-by-spectrum fashion with the predictions of a detailed model which combines multi-component H distributions (like those from Chapter 2) and radiative transfer algorithms (as given in Chapter 3). Here the Cruise Maneuver data are described and analyzed in a preliminary fashion.

4.5.1 A Simple Fit to the Cruise Maneuver Data

The Cruise Maneuver Ly α intensities are most conveniently organized using three variables: the spacecraft heliocentric distance, r , the half-cone angle between the UVS optical axis and the antisolar direction, Θ , and the angle of the UVS optical axis around the antisolar direction, Ψ (see Appendix B for more specific definitions). Antisolar observations correspond to $\Theta = 0^\circ$; $\Theta = 180^\circ$ denotes the direction toward the Sun. Observed intensities may be expressed $I(r, \Theta, \Psi)$. The cone-average intensities are defined:

$$I(r, \Theta) \equiv \frac{1}{2\pi} \int_0^{2\pi} d\Psi I(r, \Theta, \Psi) \quad (4.3)$$

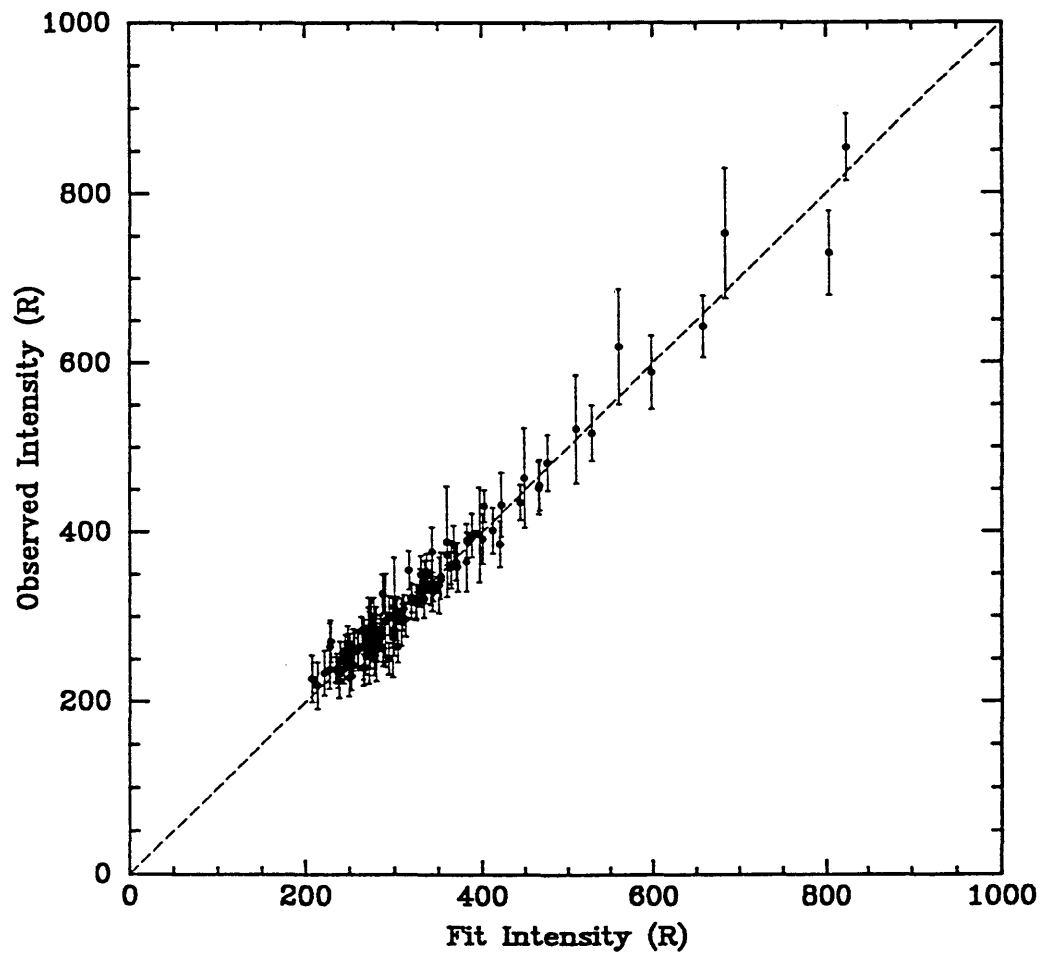


Figure 4.3: A scatter diagram showing the overall quality of a simple fit to the Voyager Cruise Maneuver cone-average intensities obtained between 15 and 35 AU. Despite the relative simplicity and phenomenological nature of the expansion, most of the data are reproduced to within error.

Here a simple, phenomenological fit to the cone-average Cruise Maneuver data obtained between 15 and 35 AU is presented. Not all of the Cruise Maneuvers provide complete, 360° sampling over the angle Ψ . In these cases, the averages are estimated from the available data. Fortunately, beyond 15 AU most of the observed intensities do not vary significantly with Ψ , so this approximation is reasonably justified.

As is shown in Chapter 3, the intensities in an optically thin, isotropically scattering uniform medium illuminated by a static point source vary with r and Θ as follows:

$$I(r, \Theta) = I_o \left(\frac{\Theta}{\sin \Theta} \right) \left(\frac{r_o}{r} \right), \quad (4.4)$$

where I_o is the antisolar intensity observed at heliocentric distance r_o . A reasonable expansion should have a functional form similar to this. One that works remarkably well is:

$$I(r, \Theta) = I_o \left[J(\Theta) \left(\frac{r_o}{r} \right)^\kappa \right] \left(\frac{\pi \mathcal{F}_\odot}{3 \times 10^{11} \text{ photons cm}^2 \text{ s}^{-1}} \right), \quad (4.5)$$

where $J(\Theta)$ is a function normalized such that $J(\Theta = 0) \equiv 1$. The last factor accounts for the variation in solar Ly α flux, where $\pi \mathcal{F}_\odot$ is the estimated sub-spacecraft solar flux at 1 AU (see Figure 1.2 and Appendix B). The parameters I_o , κ and $J(\Theta)$ are determined by using a least-squares algorithm to obtain the best fit to the cone-average Cruise Maneuver data obtained between 15 and 35 AU. Figure 4.3 shows a scatter diagram between the observed and best fit intensities. Despite the relative simplicity of the expansion, most of the data are reproduced to within error. For $r_o = 15$ AU, the best fit values of I_o are 397 and 365 R for Voyager 1 and 2 respectively. The overall best fit value for κ is (0.79 ± 0.09) . Figure 4.4 shows the best fit $J(\Theta)$.

This simple analysis yields two physically important results. First, it implies that the Voyager Ly α intensities fall with heliocentric distance as $r^{(-0.79 \pm 0.09)}$. Second, the best fit $J(\Theta)$ shown in Figure 4.4 differs significantly from the prediction for an optically thin uniform medium (shown as the dotted line). Qualitatively, this is

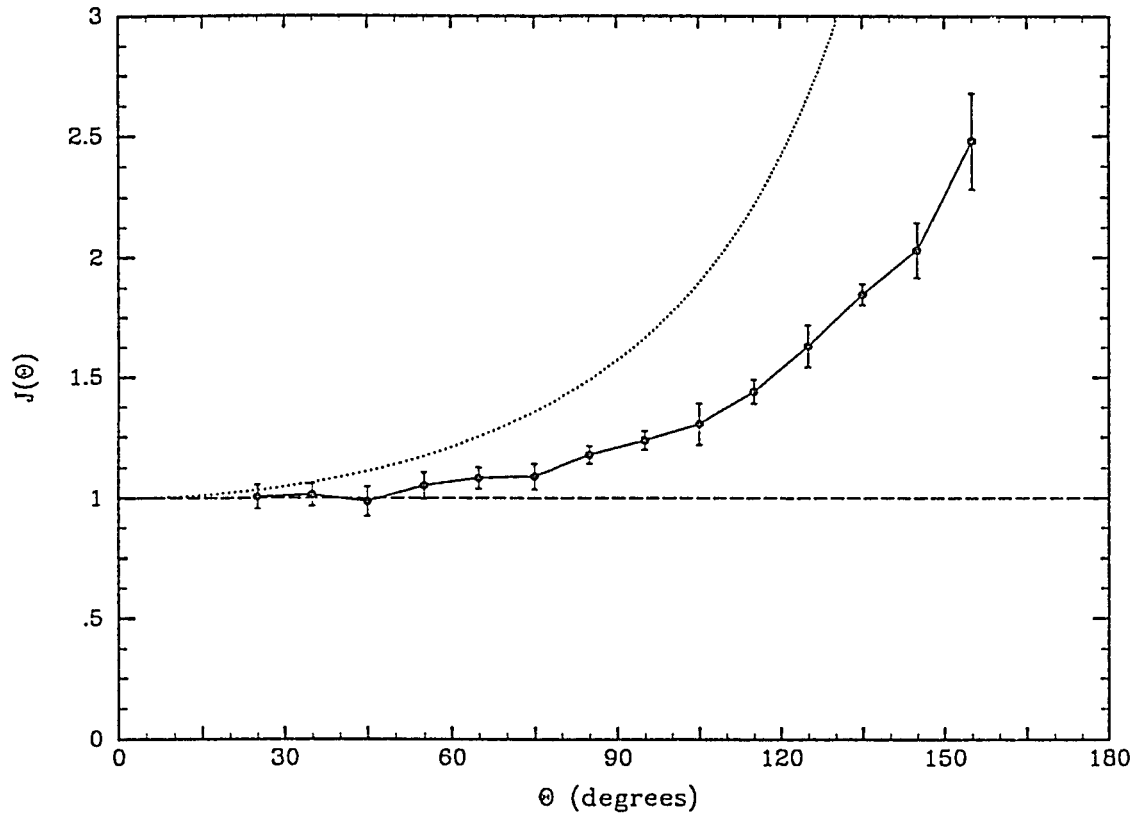


Figure 4.4: The best fit function $J(\Theta)$ derived from the combined Voyager 1 and 2 Cruise Maneuver $\text{Ly}\alpha$ data obtained between 15 and 35 AU. In an optically thin uniform system $J(\Theta) = \Theta / \sin \Theta$, shown as the dotted line. The best fit to the observations (points with error bars) indicates that the observed intensities increase less quickly than the optically thin result as the Θ approaches 180° . This probably is due to a combination of the H ionization cavity and radiative transfer effects.

consistent with the existence of the H ionization cavity. As the UVS observe Ly α closer to the Sun, their lines of sight pass through more evacuated regions of the ionization cavity, making the observed intensities smaller than those predicted for a uniform medium. However, this effect may also be caused by multiple scattering. In either case, optically thin uniform models clearly fail to reproduce the data between 15 and 35 AU.

4.5.2 H Ly α Observations on 65° Antisolar Cones

Voyager 1 and 2 Cruise Maneuver Ly α intensities collected on or near 65° antisolar cones between 5 and 40 AU are shown in Figure 4.5. These are the best estimates given by the least squares analysis of the previous section. The solar Ly α flux variation has been removed by multiplying by the factor $(3 \times 10^{11} \text{ photons cm}^{-2} \text{ s}^{-1})/\pi\mathcal{F}_{\odot}$, where $\pi\mathcal{F}_{\odot}$ is a 6-day average of the estimated sub-spacecraft solar flux as shown in Figure 1.2. There are three notable trends in the data: 1) Between 5 and 10 AU the Voyager 1 intensities are consistently lower than those for Voyager 2. This is unexpected, considering the similarities between the two spacecraft trajectories (see Figure 4.1). 2) Between 15 and 30 AU the intensities observed by each spacecraft as a function of heliocentric distance are nearly the same and fall with the same slope to within error. In fact, in this region, the two data sets are within the 15% estimated uncertainty for the UVS Ly α cross calibration. The error bars in Figure 4.5 are statistical uncertainties and do not include the uncertainty in calibration. Finally, 3) the Voyager 1 intensities beyond about 30 AU show a distinctive flat signature.

4.5.3 Observations from 5 to 10 AU

From 5 to 10 AU the Voyager 1 65° cone-average intensities are consistently lower than those for Voyager 2. Moreover, the shapes of the two data sets differ significantly in this range. This is surprising considering the similarity of the two spacecraft

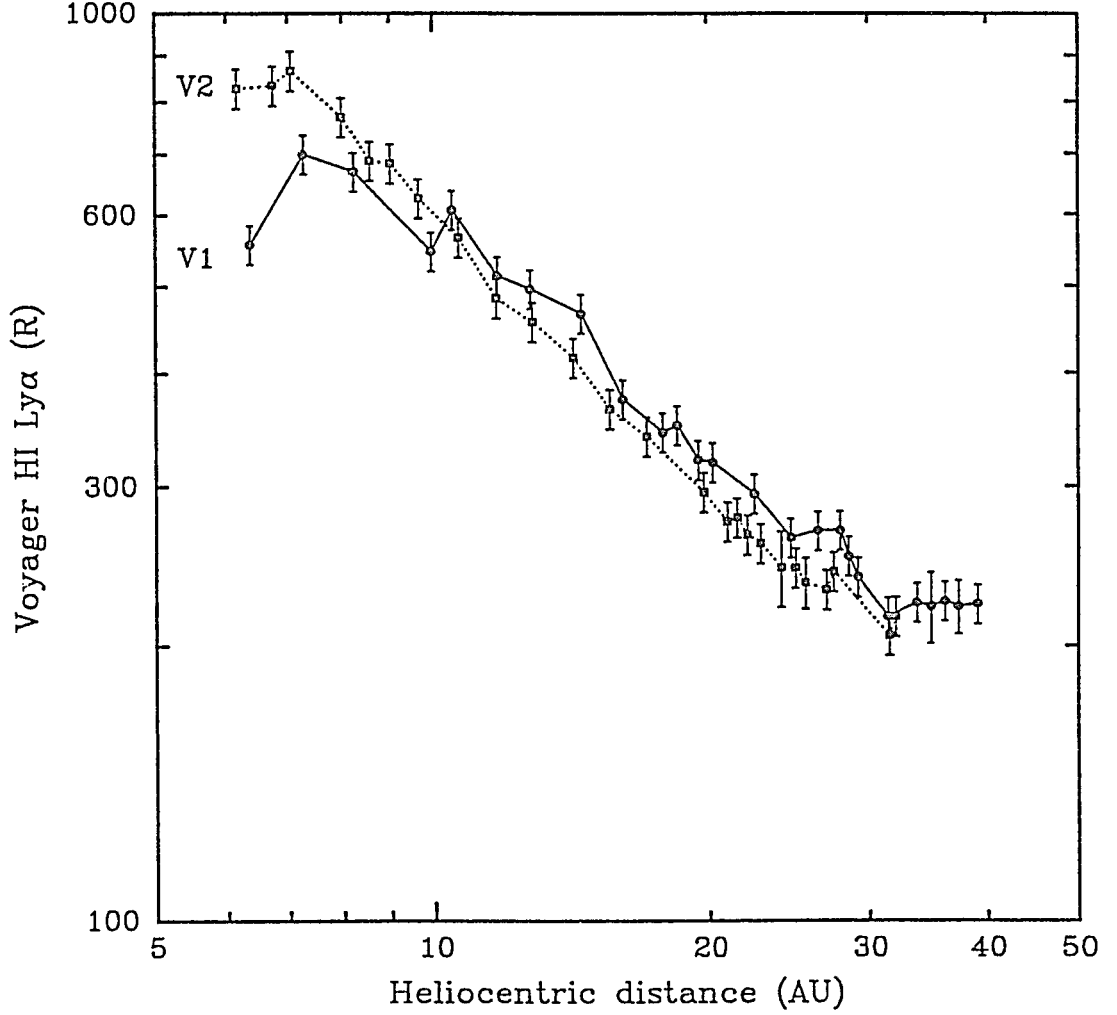


Figure 4.5: Voyager heliospheric 65° $\text{Ly}\alpha$ cone-average observations adjusted to constant solar $\text{Ly}\alpha$ flux. The solar $\text{Ly}\alpha$ flux variation has been removed from the data via multiplication by the factor $(3 \times 10^{11} \text{ photons cm}^{-2} \text{ s}^{-1})/\pi\mathcal{F}_\odot$, where $\pi\mathcal{F}_\odot$ is a 6-day average of the estimated sub-spacecraft solar $\text{Ly}\alpha$ flux. Between 5 and 10 AU the Voyager 1 intensities are consistently lower than for Voyager 2. From 15 to 35 AU the intensities observed by each spacecraft are the same to within cross calibration uncertainty. The Voyager 1 intensities beyond ≈ 30 AU show a flat signature.

trajectories (see Figure 4.1). At equivalent radii, the spacecraft were looking into very nearly the same region of the heliosphere. The only notable difference between the data is when they were gathered. The Voyager 1 Jupiter to Saturn cruise period lasted from day 65 of 1979 to day 317 of 1980. For Voyager 2 it was day 190 of 1979 to day 238 of 1981. This means that the spacecraft reached equal heliocentric radii at different times. For instance, Voyager 2 reached 7 AU about 6 months after Voyager 1. At 9.6 AU, Voyager 2 followed Voyager 1 by an entire year. So the differences in intensities indicate a significant change in the heliospheric Ly α on a time scale of 6 months to one year.

The variations in the integrated Ly α solar flux have been removed from the data plotted in Figure 4.5. Inaccuracies in this adjustment are doubtfully large enough to account for the observed difference. Therefore, the short period change in Ly α indicates real changes in the heliospheric H distribution—perhaps in the dimension of the ionization cavity. The data are consistent with the ionization cavity shrinking considerably during the ≤ 1 year interval between the spacecraft. This would require a considerable change in the H atom ionization lifetime, which is determined primarily by the solar wind and EUV fluxes. However significant changes in the heliospheric H cavity caused by solar flux variations are expected to have time scales ≥ 2 years (Fahr and Scherer, 1990). Another speculative interpretation is that these data imply a previously unknown clumpiness in the heliospheric H distribution. Blum et al. (1992) recently have suggested the existence of solar-driven H density waves which tend to have the largest amplitudes in the downstream region.

4.5.4 Observations from 15 to 35 AU

The Cruise Maneuver 65° cone-average Ly α intensities between 15 and 35 AU from both spacecraft fall off in a very similar fashion. The combined data fall as $r^{(-0.75 \pm 0.05)}$. This is within error of the $r^{(-0.79 \pm 0.09)}$ dependence determined in the alternate analy-

sis given in section 4.5.1. In addition, between 15 and 35 AU, the absolute differences in intensities are within the estimated UVS cross calibration uncertainty, suggesting that the two Voyager spacecraft are travelling through similar H distributions. So an $r^{-0.75}$ Ly α dependence may be considered reasonably representative of the upstream region. It is notably different than the $r^{(-1.07 \pm 0.1)}$ dependence observed by Pioneer 10 downstream. This has significant implications about the heliospheric H distribution. These trends are precisely opposite those predicted by either the “standard” hot models of the heliospheric H distribution (see sections 3.4.1 and 3.4.2), where intensities in the downstream direction are predicted to fall off more gently than upstream. This fundamental disagreement only relies on the observed pattern of the data, so it is a calibration independent result. The simplest solution is to add a constant intensity to the models in the upstream region. Radiative transfer models of the Voyager and Pioneer 10 data incorporating the specific trajectories of each spacecraft are discussed in section 4.6.

4.5.5 Voyager 1 Observations Beyond 35 AU

Perhaps the most suggestive trend in Figure 4.5 is the flattening of the Voyager 1 intensities that occurs beyond 30 to 35 AU. (The Voyager 2 data in this region have not yet been reduced.) This trend is suggestive in that it implies a considerable steepening of the Ly α volume emission rate (or H density) as a function of r and/or the existence of an additive background Ly α in the upstream direction. Either of these possibilities suggest the effects of the solar wind termination shock or related structures. The flattening trend cannot be due to inaccurate removal of solar Ly α flux variations because the errors introduced would need to be larger than the adjustments themselves. Moreover, removal of solar Ly α variations does not introduce such trends in the Pioneer 10 data.

The rate that outward looking intensities fall with r may be understood qual-

itatively by writing the expression for the antisolar line intensity in a spherically symmetric, isotropically scattering medium using the monochromatic approximation (see Chapter 3 for details):

$$I(r) = I_B + \frac{1}{4\pi} \int_r^\infty dr' n(r') g(r') e^{-\tau(r,r')}, \quad (4.6)$$

where I_B is a constant background, $n(r)$ is the H density, $g(r)$ is the Ly α g-value and $\tau(r, r')$ is the optical depth between radii r and r' . There are two ways to interpret the change that occurs at 30 to 35 AU. First, if the background is negligible and $g \propto r^{-2}$, then the transition from an $r^{-0.75}$ dependence to a considerably flatter signature, suggests that the density profile steepens near 30 AU. The transition could reflect a change from $n(r) \propto r^{0.25}$ to $r^{1.00}$. This is a considerable steepening, and most likely only could be explained as an effect associated with outer heliospheric plasma structures. Such a steepening in upstream H densities appears inside the solar wind termination shock in the two component H distributions given in section 2.3.5. The two-shock models of Baranov et al. (1991) also show similar gradients, but these usually appear in the heliosheath region.

On the other hand, if the flat signature starting at 30 to 35 AU were caused by an additive background, then $I_B/I(15 \text{ AU}) \approx 0.25$, which corresponds to $I_B \approx 100 \text{ R}$ (note that the latter number is calibration dependent). This background could be either Galactic in nature or caused by heliospheric resonance scattering somewhere beyond 40 AU. Thomas and Blamont (1976) use Galactic H α measurements to estimate an Ly α Galactic background upper limit of $\sim 10 \text{ R}$. This is a factor of ~ 10 less than the upstream background suggested by this analysis, and exceeds any likely cross calibration error. Therefore, should the flattening be caused by a background, it probably is associated with outer heliospheric structure.

It is difficult to discern which of these possibilities is the actual explanation. But both suggest the existence of outer heliospheric plasma structures. This is a significant

and new result. It is the first indication of outer heliospheric structure from Ly α data.

4.6 Models of Voyager and Pioneer 10 H Ly α Observations

Extensive computer time is required to calculate the H distribution and Ly α radiative transfer models of Voyager and Pioneer 10 data (this is especially true for the multi-component H distribution of section 2.3). A systematic exploration of the model parameters to find a best fit to the observations has yet to be performed. This is the next logical step in the analysis of these data, but is deferred until either the available computing hardware or the efficiency of computer codes is improved. Here, a preliminary RT analysis is given, primarily based on the two “standard” solar minimum and maximum H distributions shown in Figures 2.4 and 2.5. The details of the RT calculation are given in section 3.4.1. This analysis is calibration independent because it is based on the shapes of the observations, and not their absolute intensities. A calibration dependent RT analysis is also deferred for later work.

Figures 4.6 and 4.7 show the hot distribution models of the observations plotted on a scale normalized at 15 AU. These RT simulations account for the individual spacecraft trajectories and UV instrument orientations. In the top panels, the 65° Voyager 1 and 2 data (adjusted to constant solar Ly α flux) are shown as the circles and squares respectively. The solid and dotted lines show the simulations for Voyager 1 and 2 respectively. In the lower panels, the Pioneer 10 observations and models are shown. Five models are shown for each spacecraft, using the VLISM densities $n_{H\infty} = 0.04, 0.06, 0.08, 0.10, 0.12$ and 0.14 cm^{-3} , which lie from top to bottom in all cases. The basic disagreement between the data and the RT models is that the upstream data fall more gently than the downstream data, whereas both models predict the opposite.

As can be seen in Figures 4.6 and 4.7, the solar minimum distribution fits the Pioneer 10 data the best, whereas the solar maximum distribution is marginally better

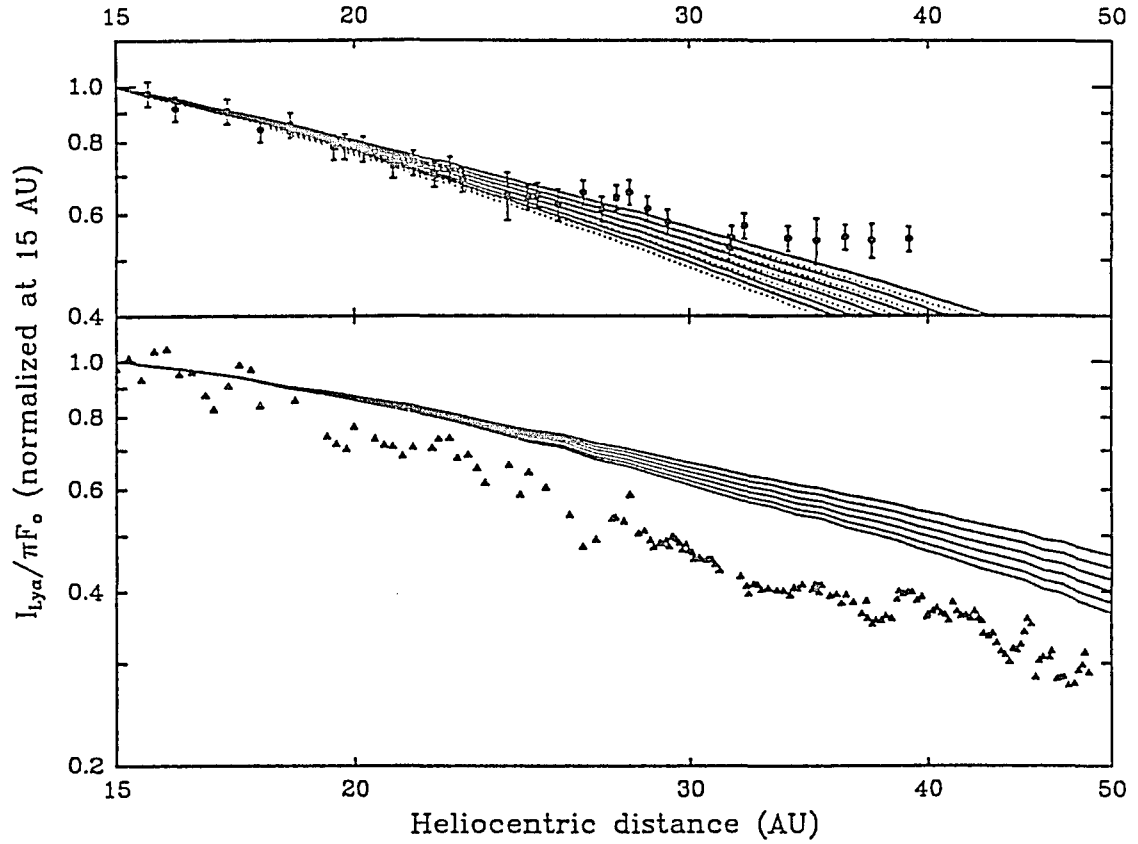


Figure 4.6: Voyager and Pioneer 10 heliospheric $\text{Ly}\alpha$ observations adjusted to constant solar flux and normalized at 15 AU plotted with solar minimum RT simulations. In the top panels the 65° Voyager 1 and 2 data are shown as circles and squares respectively. The solid and dotted lines show the solar minimum Voyager 1 and 2 simulations respectively. In the lower panels, the Pioneer 10 observations and models are shown. Five models are shown for each spacecraft, using the VLISM densities 0.04, 0.06, 0.08, 0.10, 0.12 and 0.14 cm^{-3} , from top to bottom in all cases.

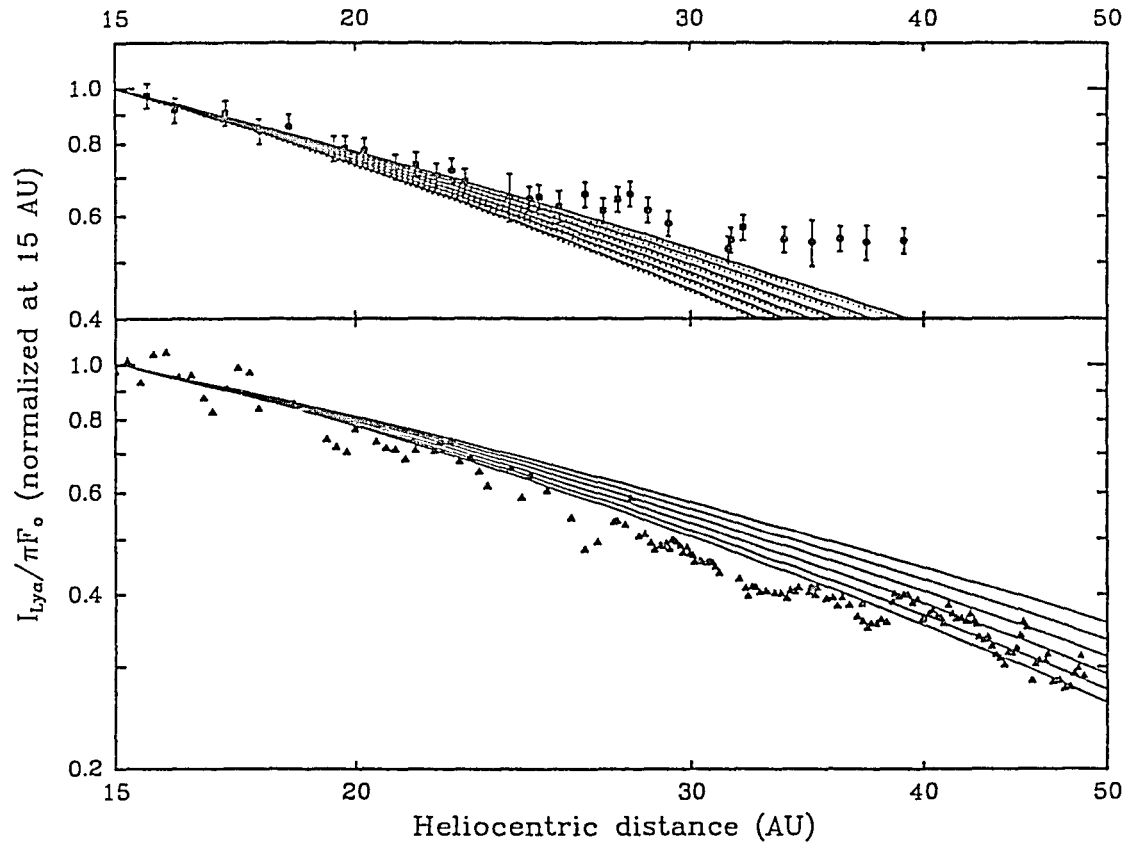


Figure 4.7: Voyager and Pioneer 10 heliospheric Ly α observations adjusted to constant solar flux and normalized at 15 AU plotted with solar maximum RT simulations. See the previous figure for a description.

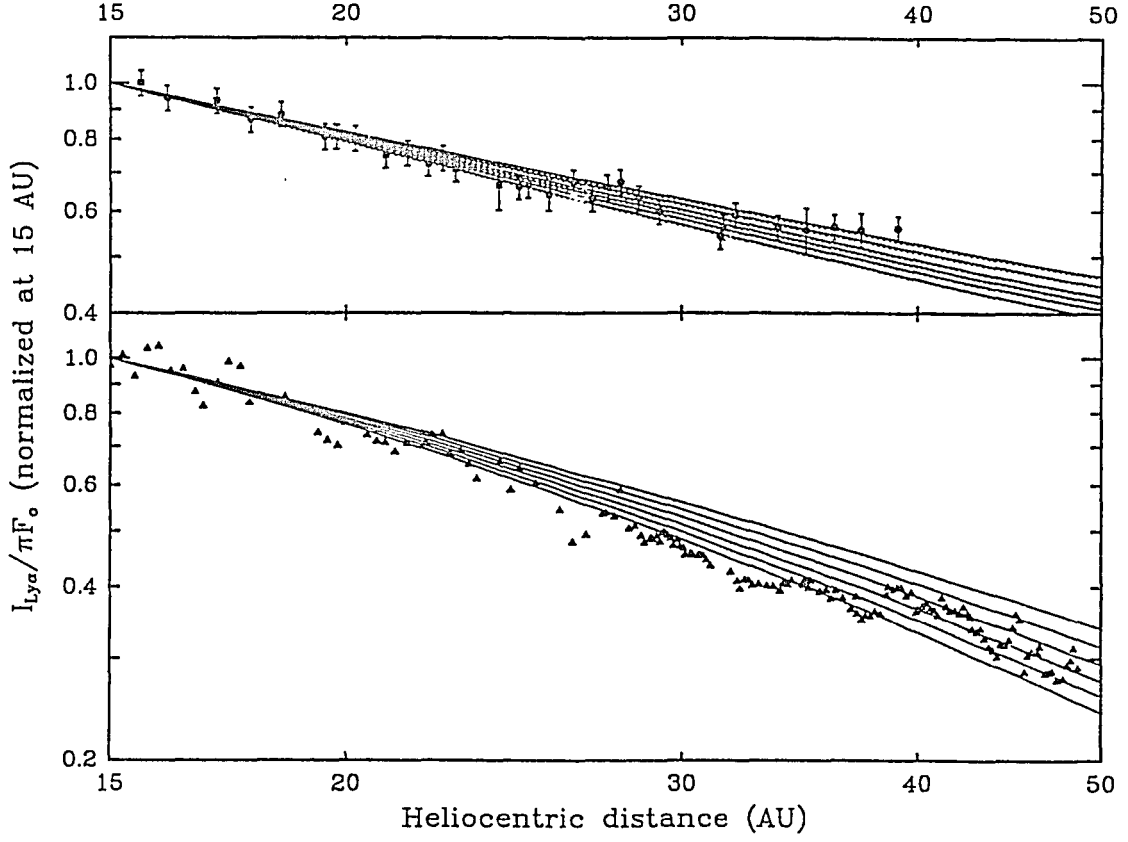


Figure 4.8: Voyager and Pioneer 10 heliospheric $\text{Ly}\alpha$ observations adjusted to constant solar flux and normalized at 15 AU plotted with RT simulations using the hot heliospheric distribution and including an additive upstream $\text{Ly}\alpha$ background. The line and symbol formats are the same as in the previous two figures. The parameters for the hot distribution are $v_{\infty} = 20 \text{ km s}^{-1}$, $T_{\infty} = 10^4 \text{ K}$, $\beta_e = 4 \times 10^{-7} \text{ s}^{-1}$, and $\mu_{\odot} = 0.75$. The upstream background is equal to 25% of the intensity observed at 15 AU.

for the Voyager data. The fits to the Voyager data beyond ~ 30 AU are improved in all cases by including a constant additive intensity of about 20 to 30% of that observed at 15 AU. However, the Pioneer 10 fits are degraded by including such a background, but improved by decreasing the H atom ionization rate, β_e . Figure 4.8 shows an improved fit to the combined data. The H distribution is the hot model using the standard solar minimum parameters but with the H loss rate decreased to $4 \times 10^{-7} \text{ s}^{-1}$. A constant intensity equal to 25% of that observed at 15 AU is added to the upstream Voyager models.

These adjustments probably indicate how the real heliospheric H distribution deviates from the hot model. For instance, decreasing the loss rate to $\beta_e = 4 \times 10^{-7} \text{ s}^{-1}$ improves the agreement in the downstream direction. In the hot model, this makes the downstream cavity less elongated than in the standard solar minimum distribution. Thus, the real downstream distribution may be characterized by a more truncated downstream cavity than indicated by the solar minimum model. Another possibility is that the downstream data are showing the signature of suprathermal H gas, which is not included in the hot model. The multi-component model from Chapter 3 predicts that the mixing ratio of the suprathermal H gas is largest in the downstream region.

The additive upstream background suggests that there is a Ly α source beyond 40 AU upstream that is unaccounted for in the hot model. This could be due to a Galactic background with an anisotropy that happens to coincide with the VLISM flow—but this possibility seems coincidental and unlikely. So the asymmetric background probably is associated with the heliosphere; specifically, it may be due to steep gradients in the H density near 30–40 AU or to a layer of suprathermal H gas in the upstream region. Both of these effects are predicted by the multi-component model of Chapter 3. Alternatively, the two shock model of Baranov et al. (1991) predicts

a large “wall” of hydrogen near the upstream heliosheath. Such a structure could produce a considerable Ly α intensity and, thus, may provide an improved fit to the data.

CHAPTER 5

VOYAGER MUTUAL OBSERVATIONS

As is discussed in Chapter 4 and Appendix A, a significant limitation in determining absolute VLISM H densities is establishing valid instrument sensitivity calibrations. In addition, to calculate $n_{H\infty}$ by comparing measured intensities to model values, several boundary condition parameters are required including the structure of the solar Ly α flux in latitude and longitude, the detailed solar wind and EUV flux fields which determine the H lifetimes, the Galactic Ly α background, and the details of the outer heliospheric H distribution. Currently no model exists which contains all of these ingredients. Even if such a sophisticated model were developed which matched the available data, one could reasonably argue that the solution obtained is not unique. Therefore a method of estimating heliospheric H densities which is as independent as possible of instrument calibrations, solar flux fields, outer heliospheric structure and Galactic Ly α background is highly desirable. Here such a method is introduced. The technique involves using both UVS instruments to measure simultaneously Ly α intensities along the line between the two Voyager spacecraft; the observations are called Voyager Mutual Observations (VMOs).

The concept behind of the Mutual Observation method is simple. Each Voyager spacecraft measures intensities toward and away from the other. Through a combination of subtracting and dividing these four intensities, the density of the scattering material in the region between the spacecraft may be estimated. Unfortunately, the overall effectiveness of the VMO technique suffers from three separate effects. First, it requires a good estimate of the relative UVS Ly α calibration. As discussed in Appendix A, this cross calibration is known to an accuracy of no better than 15%. This is a severe limitation on the VMO technique. Second, the VMO method may

suffer from solar rotational and longitudinal $\text{Ly}\alpha$ variability. Equatorial solar $\text{Ly}\alpha$ can vary by $\approx 15\%$ over the 25 day solar rotation period (see Figure 1.2). Ideally, all four VMO intensities should be measured in a time period short compared to the solar rotation period. Spacecraft and Deep Space Network scheduling constraints have required that the two VMO measurements performed thus far be spread over 10 and 29 day intervals. Moreover, the VMO concept was originally conceived in late 1989. So both sets of the VMOs were conducted at or near solar maximum, when the solar rotational variations are largest in amplitude. Finally, the effectiveness of the VMO technique is doubtful if the spacecraft are separated by a large number of $\text{Ly}\alpha$ optical depths, in which case one spacecraft would not be able to “see” the other. The first VMO was performed when the spacecraft were separated by 34.7 AU. Since nominal VLISM parameters imply that one line center optical depth is ~ 10 AU, this suggests the spacecraft could have been separated by 3 or more line center optical depths. It is unfortunate that the VMO technique was not conceived earlier in the Voyager mission, when the interspacecraft separation was smaller and solar variations were less extreme.

Because of these limitations, the two sets of VMOs performed thus far are difficult to interpret. The results are ambiguous because they do not yield a unique inter-spacecraft H density. Ultimately, this may be due to the large interspacecraft separation.

5.1 The Mutual Observation Method

Figure 5.1 schematically illustrates the two Voyager spacecraft and the four VMO intensities. The $\text{Ly}\alpha$ line intensity measured by Voyager 1 when its UVS is pointed inward towards Voyager 2 is defined as A_i . This total line intensity is the differential intensity, $A_i(\nu)$, integrated over frequency ν . The Voyager 1 intensity measured in the opposite direction (i.e. outward) is defined as A_o . The Voyager 2 intensities B_i

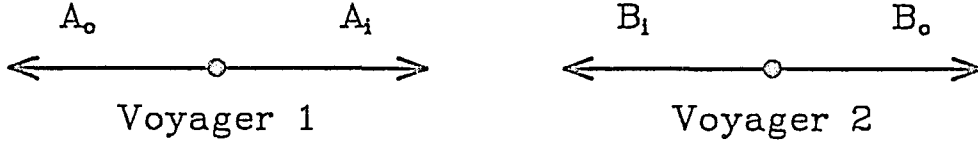


Figure 5.1: An illustration of the Voyager Mutual Observation $\text{Ly}\alpha$ measurements. The $\text{Ly}\alpha$ line intensity measured by Voyager 1 when its UVS is pointed inward towards Voyager 2 is defined as A_i . The Voyager 1 intensity measured in the opposite direction is A_o . The Voyager 2 intensities B_i and B_o are defined similarly. The region between the spacecraft is filled with H gas that both scatters and absorbs $\text{Ly}\alpha$ photons. The goal of these measurements is to estimate the interspacecraft H density.

and B_o are defined similarly.

The fundamental concept behind the Mutual Observations is that a certain component of the intensity B_o is transmitted through the medium between the spacecraft and measured as part of A_i ; in addition, some part of A_i is created by $\text{Ly}\alpha$ resonance scattering in the region between the spacecraft. This corresponds to the following relationship:

$$A_i(\nu) = B_o(\nu)e^{-\tau(\mathbf{r}_2, \mathbf{r}_1, \nu)} + \int_0^D ds E(\mathbf{r}, -\hat{\mathbf{n}}, \nu) e^{-\tau(\mathbf{r}, \mathbf{r}_1, \nu)}, \quad (5.1)$$

where \mathbf{r}_1 and \mathbf{r}_2 are the positions of the spacecraft, and E and τ are the $\text{Ly}\alpha$ volume emission rate and optical depth as defined in Chapter 3. The spacecraft are separated by distance D . The parameter s measures the distance from Voyager 1 toward Voyager 2 such that the vector $\mathbf{r}(s)$ traverses the interspacecraft region:

$$\mathbf{r} = \mathbf{r}(s) = \mathbf{r}_1 + s\hat{\mathbf{n}}, \quad (5.2)$$

where $\hat{\mathbf{n}}$ is the unit vector pointing from Voyager 1 to 2. A relationship analogous to equation (5.1) exists for intensities measured in the opposite direction.

Equation (5.1) may be simplified by making the following assumptions: 1) all absorption, emission and line profiles are Doppler profiles, $\phi(\nu)$, given by the temperature $T = 10^4$ K, 2) the H gas in the region between the spacecraft has uniform density n , and 3) the volume emission rate between the spacecraft is $E = ng(r)\phi(\nu)/(4\pi)$, where the Ly α g-value falls as $r^{-\gamma}$, with $\gamma \approx 2$. These are sweeping assumptions, which may not be valid in detail. But a more sophisticated analysis is not justified, considering that the limiting factor in the overall effectiveness of the VMO technique is the accuracy of the UVS Ly α cross calibration. Using these assumptions, equation (5.1) is considerably simplified by integrating over frequency:

$$A_i = \alpha + TB_o, \quad (5.3)$$

where α is the component of A_i created by Ly α scattering between the spacecraft and T is the net transmission of Ly α through the inter-spacecraft H gas. The analogous equation for the other direction is

$$B_i = \beta + TA_o, \quad (5.4)$$

where β is the component of B_i due to Ly α scattering between the spacecraft. To make the VMO analysis independent of solar Ly α flux, the ratio $M \equiv \alpha/\beta$ is modeled. This ratio is independent of the solar flux if the four VMO intensity measurement are conducted simultaneously and the solar flux does not vary significantly over the heliocentric longitudes and latitudes spanned by the segment joining the spacecraft. As stated earlier, these conditions may be violated by the observed $\approx 15\%$ longitudinal and solar rotational variations (see Figure 1.2). Using equations (5.3) and (5.4), M may be expressed:

$$M \equiv \frac{\alpha}{\beta} = \frac{A_i - TB_o}{B_i - TA_o}. \quad (5.5)$$

The ratio α/β may be calculated using the assumptions stated above. It is a function of the interspacecraft H density, n . Similarly, the transmission, T , is also a function

of n . Thus, equation (5.5) may be rewritten:

$$f(n) \equiv \frac{\alpha}{\beta} - \frac{A_i - TB_o}{B_i - TA_o} = 0. \quad (5.6)$$

The interspacecraft density may be estimated by finding the root of the function $f(n)$.

In practice, $f(n)$ is very sensitive to the estimated relative UVS Ly α calibration, which seriously limits the accuracy of the densities measured by the VMO technique.

5.2 Voyager Mutual Observation Measurements

Two sets of VMO measurements have been performed. These are summarized in Table 5.1. The first set were performed in late 1990 when the spacecraft were separated by 34.7 AU. The second set were obtained in early 1992, when $D = 41.3$ AU. The Ly α intensities given Table 5.1 are derived using the UVS Ly α calibration factors given in equations (4.1) and (4.2).

5.3 Results and Limitations

Figure 5.2 shows the average interspacecraft densities as a function of, ϵ_1 , the Voyager 1 calibration factor. The range shown for ϵ_1 corresponds to the estimated uncertainty in the relative UVS calibration. The solid line is the calculated interspacecraft H density for the first set of VMOs performed in 1990. The dashed line is for the VMOs conducted in 1992. The range in ϵ_1 corresponds to interspacecraft densities $n < 0.08 \text{ cm}^{-3}$ and $n < 0.13 \text{ cm}^{-3}$ respectively.

Ideally, the two curves in Figure 5.2 would cross at some value of ϵ_1 , indicating a unique interspacecraft density that satisfies both sets of observations. But this does not occur. For this reason the results are ambiguous. This ambiguity may be caused by several effects including: 1) an incorrect assumption in the VMO modeling process, 2) solar Ly α variability, 3) a large spacecraft separation in Ly α optical depth, and/or 4) a real change in the interspacecraft density between 1990 and 1992. Because of the

Table 5.1: H Ly α Voyager Mutual Observations.

VMO days 297–308, 1990		D = 34.7 AU
$r_1 = 42.8$ AU	$\lambda_1 = 242.7^\circ$	$\beta_1 = 33.0^\circ$
$r_2 = 33.1$ AU	$\lambda_2 = 281.7^\circ$	$\beta_2 = -4.0^\circ$
Measured Ly α (R)	Start time	End time
$A_i = 339$	90/305 13:33	308 02:45
$A_o = 190$	90/297 16:09	299 11:53
$B_i = 297$	90/305 12:34	308 22:11
$B_o = 242$	90/298 20:40	305 11:36
VMO days 86–115, 1992		D = 41.3 AU
$r_1 = 48.2$ AU	$\lambda_1 = 244.6^\circ$	$\beta_1 = 33.4^\circ$
$r_2 = 37.0$ AU	$\lambda_2 = 282.8^\circ$	$\beta_2 = -9.4^\circ$
Measured Ly α (R)	Start time	End time
$A_i = 250$	92/106 06:18	111 09:00
$A_o = 149$	92/086 10:23	093 10:00
$B_i = 247$	92/092 10:50	093 20:00
$B_o = 219$	92/105 10:34	111/10:00

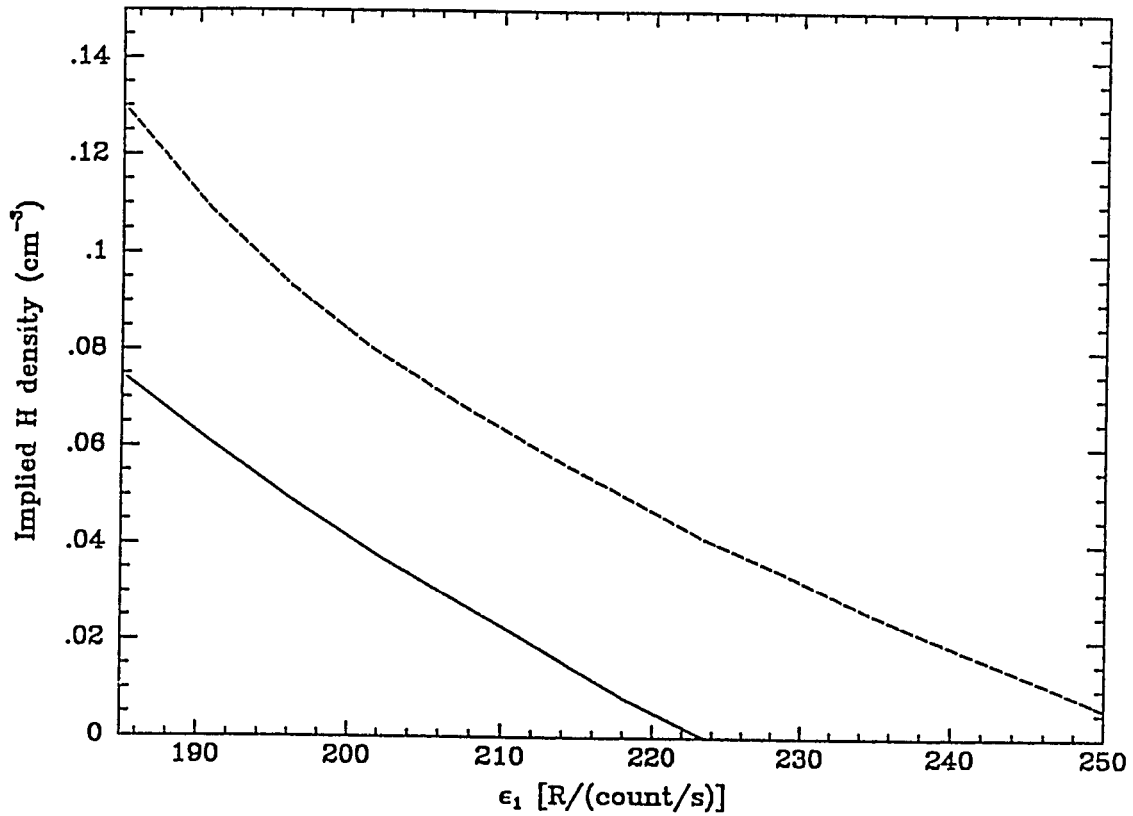


Figure 5.2: The interspacecraft H density determined from the Voyager Mutual Observations as a function of the Voyager 1 UVS Ly α sensitivity calibration factor. The Voyager 1 calibration factor is 218 ± 33 , where the error refers to the cross calibration uncertainty between the two UVS instruments. The densities calculated from measurements performed in 1990 and 1992 are shown as the solid and dashed lines respectively. The densities derived from the VMO observations are strong functions of the UVS Ly α cross calibration. The 15% cross calibration error dominates the uncertainty of the VMO determinations.

ambiguity, the results are difficult to interpret. The measurements seem to suggest that the interspacecraft density in the 1990 to 1992 (33 to 48 AU upstream) period was less than $(0.08\text{--}0.13)\text{ cm}^{-3}$. This density range lies a bit above the range Ajello et al. (1987) estimate for the parameter $n_{\text{H}\infty}$ based on a review of observations performed by multiple spacecraft over more than a decade.

However, if the interspacecraft density is larger than $\approx 0.04\text{ cm}^{-3}$, the spacecraft are separated by more than two line center $\text{Ly}\alpha$ optical depths. The Mutual Observation method is inherently unstable at either large or small spacecraft separation. This may be why the VMOs do not yield a unique result. Obtaining another set of VMO measurements is not justified, considering the expense of Deep Space Network coverage and data processing. However, this is not necessarily a fatal flaw in the Mutual Observation method. Its application to the Voyager mission may have failed, but the concept may yet be proven viable.

CHAPTER 6

CONCLUSIONS AND FUTURE WORK

The most significant advance in this work is the identification of a distinct difference between upstream and downstream heliospheric $\text{Ly}\alpha$ as measured by the Voyager and Pioneer 10 spacecraft. The observations, adjusted for solar flux variations, are characterized as follows: Voyager intensities fall as $r^{(-0.75 \pm 0.05)}$ between 15 and 35 AU, whereas between 15 and 50 AU Pioneer 10 observations fall as $r^{(-1.07 \pm 0.1)}$. A radiative transfer calculation using the conventional (i.e. hot) model of the heliospheric H distribution does not reproduce these trends. The hot model (which does not include the solar wind termination shock) predicts that upstream $\text{Ly}\alpha$ intensities should fall more quickly as a function of heliocentric distance than downstream. This is precisely opposite to the trends observed by the spacecraft. The observations require a significant additional $\text{Ly}\alpha$ component emanating from beyond 40 AU upstream that is not accounted for in the hot H model. The additional $\text{Ly}\alpha$ probably is due to a combination of H density gradients and suprathermal H gas, both of which are predicted to be associated with the solar wind termination shock in the upstream region.

These results are significant because they are the first indication of outer heliocentric structure. Moreover, should the excess upstream $\text{Ly}\alpha$ be caused mainly by a gradient in the thermal H distribution (rather than suprathermal H gas), then it must be coming from within a few $\text{Ly}\alpha$ optical depths. Using an H density of 0.1 cm^{-3} and temperature 10^4 K , this suggests that the solar wind termination shock is within about 30 AU of the Voyager 1 spacecraft, at a heliocentric distance of $\approx 75 \text{ AU}$ in the upstream direction. Therefore, continued acquisition and analyses of Voyager and Pioneer heliospheric $\text{Ly}\alpha$ measurements during the next decade are vital in monitoring outer heliospheric structure.

It is not surprising that the first indication of outer heliospheric structure is apparent in $\text{Ly}\alpha$ observations obtained beyond 5 AU. Observations obtained within 5 AU are reproduced reasonably well by the hot model because solar processes dominate the H distribution in this region. Further out, the H distribution is expected to be coupled to the heliospheric plasma by the hydrogen-proton charge exchange process. Specifically, H-p charge exchange is predicted to create 1) significant gradients in the bulk (i.e. thermal) H density in the vicinity of the solar wind termination shock, 2) a suprathermal population of heliospheric H atoms, and 3) an extended (>100 AU) region in the downstream direction with a significantly reduced thermal H density and an elevated suprathermal H gas mixing ratio. In a model that includes the effects of a supersonic VLISM flow, Baranov et al. (1991) also predict large upstream density gradients and an extended downstream depleted region.

Most published estimates of the VLISM H density have been obtained by comparing measured $\text{Ly}\alpha$ intensities to those calculated using the hot H model. These estimates need to be reevaluated in light of the new results presented here. However, Shemansky et al. (1984) estimate $n_{\text{H}\infty}$ using a calibration independent method that does not rely on the hot model. They present Voyager 2 and Pioneer 10 observations obtained in 1982 when the spacecraft were located at 13 and 30 AU respectively. Both data sets clearly show 25 day variations in backscattered $\text{Ly}\alpha$ that are directly associated with an active $\text{Ly}\alpha$ sector on the solar disk. The relative amplitudes of the variations are used to estimate the asymptotic H density beyond the spacecraft, yielding $n_{\text{H}\infty} = 0.16 \text{ cm}^{-3}$ for Voyager 2 and 0.11 cm^{-3} for Pioneer 10. Their results are consistent with those presented here, in that they cannot be reconciled with the hot H model—which predicts the same value of $n_{\text{H}\infty}$ upstream and downstream. The lower density derived from the Pioneer 10 data implies an extended downstream depleted region, as predicted by models including the solar wind termination shock. A

unified reanalysis of the Shemansky et al. (1984) data and the data presented here promises to yield both the global distribution and the absolute density of heliospheric hydrogen. This is the next logical step in the analysis of the Voyager and Pioneer 10 heliospheric Ly α data.

Heliospheric Ly α lines are expected to be composed of two distinct parts: a bright line core scattered by the dominant, thermal component of the H gas, and a wider part due to the suprathermal component. The mixing ratio of the suprathermal component is very sensitive to the solar wind termination shock distance and should be larger in the downstream region. High-resolution Ly α line shape measurements made from 1 AU could provide a diagnostic tool for outer heliospheric structure. Preliminary analysis suggests that such measurements require a UV instrument with spectral resolution better than 0.02 nm and sensitive enough to detect ≈ 50 R/nm Ly α line wings. Such an instrument, mounted on a low-orbit satellite or a sounding rocket, could make the necessary measurements if Ly α from Earth's geocorona is properly removed.

Finally, the Voyager Mutual Observations are particularly sensitive to the relative UVS Ly α calibration, which is known to an accuracy of about 15%. A preliminary analysis of two sets of measurements performed in 1990 and 1992 yields ambiguous results, probably because the spacecraft are separated by too many Ly α optical depths. On this basis, repeating the observations is not justified.

APPENDIX A

VOYAGER UVS DATA AND H Ly α CALIBRATION

Each Voyager spacecraft is equipped with a host of scientific instruments, including magnetometers, particle detectors and imaging cameras (see Stone, 1983). The Ultraviolet Spectrograph (UVS) instruments were included to obtain spectra in the 50 to 170 nm range. Their primary goal was to define the upper atmospheres of outer solar system bodies. An auxiliary goal was to observe heliospheric UV lines to help constrain heliospheric structure.

A.1 UVS Instrument Design and Parameters

The UVS instruments are described in detail by Broadfoot et al. (1977, 1981). A useful summary is given by Holberg and Watkins (1992). The UVS is an objective grating spectrograph covering the wavelength range 50 to 170 nm. The objective grating design is commonly used to observe point sources. However, the UVS instruments were adapted to observe extended emission sources by using a collimator to restrict the field of view. Because of this, the UVS has two distinctly different responses for point source targets and extended sources. For extended sources the spectral resolution is about 3 nm while for point sources it is 1.8 nm.

The UVS each have two apertures. The smaller of these, the occultation port, is devoted to solar and stellar occultation studies of planetary atmospheres. The larger airglow port is used for planetary airglow, stellar and heliospheric observations. The collimated design of the UVS instruments restricts the airglow field of view to $0.10^\circ \times 0.87^\circ$ (full width at half maximum). The occultation port is offset at an angle of $\approx 19^\circ$ from the airglow port. During some observations, light from the occultation port can contaminate spectra of targets observed through the airglow port. However,

this contamination usually affects measured H Ly α intensities by less than 5%; it is only explicitly considered when the occultation port lies near a strong source, such as a planet, star or the Sun.

The UVS optical assembly is a compact, Wadsworth mounted design. The grating is a platinum coated replica, ruled at 540 lines mm⁻¹ which disperses the UV light entering the instrument onto a linear 128-element detector. The detector assembly is a self-scanned anode array which counts packets of photoelectrons produced by a microchannel plate (MCP) electron multiplier (Broadfoot and Sandel, 1977). Two of the 128 anodes are unused, so the UVS is a photon counting instrument with 126 channels, each spanning a wavelength interval of 0.926 nm. In the 50 to 125 nm region, the photoelectrons are produced by the incident UV radiation focused on the bare MCP. From 125 to 170 nm, an MgF₂ filter coated with CuI acts as a supplementary photoelectron source for the MCP.

A.2 UVS Data Reduction

The UVS data reduction procedure is described by Holberg and Watkins (1992) in the *Voyager Ultraviolet Spectrometer Guest Observer and Data Analysis Handbook*. Converting a UVS spectrum from raw counts registered on the detector array into a spectrum from which H Ly α intensities may be calculated involves three steps. First, the spectra are flat fielded to account for the inherent channel-to-channel variations in the detector response. Second dark counts are removed. Finally, the unwanted (i.e. non-dispersive) scattering of the UV light that occurs on the ruled grating and in the instrument assembly must be removed. This operation is called descattering.

A.2.1 Fixed Patterned Noise

The linear array detectors have a characteristic, patterned response to a uniform field of electrons. This reproducible pattern is called the fixed pattern noise (FPN),

and indicates the response of each anode as an individual photomultiplier. Each raw UVS spectrum must be multiplied by this pattern in a channel-by-channel fashion to account for the individual anode response variations. This step is analogous to what is often called flat fielding spectra or images. The procedure is to multiply the raw UVS spectrum by an FPN spectrum. Several FPN spectra exist for each spacecraft, so they are numbered for tabulation purposes. For all of the Voyager 2 data reported here, FPN 76 is used. Similarly for Voyager 1, FPN 49 is used (even though basically the same results are given by FPN 47).

A.2.2 UVS Dark Counts

The UVS detectors are sensitive to energetic photon and particle radiation. Solar and Galactic cosmic rays and radiation from the spacecraft nuclear power supply combine to create a dark count background which must be removed from the spectra. The shape of the dark count spectra are measured by pointing the UVS at an optically neutral calibration plate mounted in the solar shadow on the body of the spacecraft. Dark count spectra are collected periodically during the mission, but do not change shape significantly over time.

A.2.3 Internal Instrument Scattering

The Voyager UVS dispersive elements are ruled gratings which exhibit more non-dispersive scattering than modern holographic gratings. In addition some scattering may occur in the instrument assembly. An effective means of correcting for such unwanted scattering is by using a matrix operator. The instrumental response to scattering is modeled by a 126×126 matrix, S_{ij} , which describes the count rate at channel j given a monochromatic source at the wavelength of channel i . The scattering matrices for each spacecraft were measured in the laboratory before launch using 50 individual emission lines covering the entire UVS bandpasses. Descattering

UVS spectra involves multiplying the spectra by the inverse of the laboratory scattering matrix. This descattering algorithm assumes only photon events are present in the spectrum, so dark counts must be removed prior to the descattering operation.

The descattering matrix operator for the Voyager 1 UVS recently has undergone reanalysis because of apparent overcorrection in some spectral regions (D. E. She-mansky, *personal communication*, 1992). Improved Voyager 1 descattering matrices should not change H Ly α intensities by more than a few percent. But the effects on Ly β and He 58.4 nm intensities could be significantly larger. These modifications to the scattering matrices have not been incorporated into this work; only laboratory scattering matrices are used here. Like FPN spectra, the descattering matrices are numbered. All of the data reported here were descattered using matrices 21 and 35 for Voyager 1 and 2 respectively.

A.3 Voyager UVS H Ly α Sensitivity Calibrations

The Voyager UVS H Ly α instrument sensitivity calibrations are difficult to validate. The laboratory calibration for Voyager 1 cannot be used because of the radiation damage suffered by the spacecraft during its Jupiter encounter. Stellar observations cannot be used for cross calibration at or near the wavelengths of the variable helio-spheric resonance lines, especially at the relatively bright Ly α line. Other complicat-ing factors include the possibilities of errors in the laboratory calibrations, changes in instrument sensitivities between the laboratory calibration period and the early post-launch period, the presence of the filter edge at 125 nm and/or a unique response in the UVS Ly α channels caused by the greatly elevated total photon exposure in those channels relative to adjacent channels.

Several separate UVS stellar observations indicate that, since their respective Jupiter encounters, each UVS has remained stable in the wavelength regions adjacent to 121.6 nm (Holberg et al., 1991). This strongly suggests that the UVS response to

$\text{Ly}\alpha$ has not changed during the same period. So the task at hand is to determine the Voyager UVS $\text{Ly}\alpha$ sensitivity calibrations for post-Jupiter phases of the mission. This is accomplished in two steps. First, the Voyager 1 $\text{Ly}\alpha$ instrument response relative to Voyager 2 for the post-Jupiter period is estimated in several ways. This cross-calibration is then combined with the an estimated absolute $\text{Ly}\alpha$ calibration for the Voyager 2 UVS, to determine the absolute Voyager 1 calibration for the post-Jupiter period.

A.3.1 In-Flight Recalibration with Stellar Observations

Holberg et al. (1982, 1991) have adjusted the Voyager UVS point-source calibration curves on the basis of observations of UV standard stars for the post-Jupiter periods. The stellar recalibration technique works only for wavelengths longward of 91 nm and not near the stronger, variable heliospheric resonance lines. The calibration adjustments are as large as 50% in some wavelength regions. Unfortunately, the the in-flight stellar recalibrations cannot be directly applied to extended sources. However, similar adjustments may be needed for extended source sensitivity calibrations. Stellar observations performed during the decade after the Jupiter encounters indicate that each UVS has remained stable in the wavelength regions adjacent to 121.6 nm (Holberg et al., 1991). This strongly suggests that the UVS response to $\text{Ly}\alpha$ has also remained stable during the same period.

A.3.2 The Degradation at the Voyager 1 Jupiter Encounter

Jupiter's magnetosphere is a hostile radiation environment (see Dessler, 1983 for an extensive description of the Jovian magnetosphere). Before the Voyager encounters, the exact radiation dosage a spacecraft could expect to receive traversing the system, especially the Io plasma torus environment, was difficult to estimate. During the Voyager 1 encounter, the UVS count rate was elevated to saturation levels by mag-

netospheric particle radiation and photoelectron output of the microchannel plate (MCP) was degraded considerably before the instrument gain could be reduced to safe levels.

The relevant quantity for estimating MCP degradation is the total charge per unit area extracted from the MCP during its history (Sandel et al, 1977). Evidently the particle radiation at Jupiter ejected enough accumulated charge from the MCP to significantly change its gain characteristics. Because the MCP is uniform over the detector array, the most physically plausible scenario is that the total charge extracted from the MCP during the event was uniform as well. If this were the only degradation to have occurred during the lifetime of the instrument, the expected spectral signature for the damage is a uniform degradation in response for each channel. However, if a particular region of the MCP had already undergone significant degradation or were otherwise unique, then that region may have been degraded to a different extent during the Voyager 1 Jupiter encounter (see Sandel et al., 1977). This is especially important for the Ly α channels, which had been thoroughly saturated during periodic solar observations before the Jupiter encounter.

The earliest estimate of the degradation of the MCP was obtained by using observations of the bright star α Virgo (see Holberg and Watkins, 1992). Through comparison of spectra obtained by Voyager 1 before and after encounter, the loss of sensitivity in the wavelength intervals (100–119) nm and (130–145) nm was determined to be about 30%. A similar but independent analysis using the star α Leo reveals that the loss of sensitivity was $(32 \pm 7)\%$, where the error refers to the channel-to-channel variations. This means that for stellar spectra obtained after Jupiter encounter, raw count rates need to be multiplied by a factor of (1.47 ± 0.17) to be comparable to spectra obtained before Jupiter.

A.3.3 Non-Uniform Degradation in the Ly α Region

The possibility of non-uniform degradation for channels in the vicinity of a very strong line is mentioned by Sandel et al. (1977). Such non-uniform degradation at Ly α cannot be estimated using stellar observations because of the dual complications of the variable heliospheric Ly α foreground, and the proximity of the UVS long wavelength filter edge at 125 nm. By far the brightest UV source ever observed by the UVS instruments is the solar Ly α line. During pre-Jupiter solar observations, the UVS count rate at Ly α was elevated to saturation levels. This early exposure may have caused some degradation in the channels near 121.6 nm in both instruments before their Jupiter encounters. In addition, due to the pervasive heliospheric Ly α background, the quiescent count rate in the Ly α channels is two to three orders of magnitude larger than in any of the other UVS channels. These considerations suggest that the Ly α channel region of both instruments are unique compared to the other channels, even those directly adjacent.

There are two ways to test for a non-uniform degradation in the UVS channels at or near the Ly α line. First, the shape of the spectra in the channels near the bright core of Ly α lines observed before and after Jupiter may be compared. Second, the faint but detectable Ly α photons scattered into channels far from the Ly α line may be compared to those detected at or near the center of the line. Both of these tests indicate that at or near Jupiter encounter, the Ly α channels did undergo a net change in sensitivity different than the adjacent channels. This type of channel-to-channel sensitivity variation is usually accounted for by the FPN correction. Here the non-uniform nature of the degradation is empirically characterized, but no physical explanation for its existence is offered. New FPN spectra, adjusted to account for the effects of the Voyager 1 Jupiter encounter in and near the Ly α channels are currently being developed (D. E. Shemansky, *personal communication*, 1992) but are

not incorporated into the current analysis.

H Ly α Line Shape Changes

Long duration, sky background observations periodically conducted by each spacecraft provide high statistical quality measurements of the response of the UVS to a monochromatic Ly α line. If all of the Voyager 1 UVS channels were uniformly degraded at or near Jupiter encounter, the shape of the Ly α line detected before and after the encounter should not change. However, if the degradation were non-uniform, the detected Ly α line shape would change. Figure A.1 shows a comparison of the pre-Jupiter and post-Jupiter Ly α line shapes after FPN and dark count corrections (both spectra were reduced using FPN 47). The spectra are normalized such that the total count rate across the Ly α channels (70 through 78) is 2 counts per second. The Ly α line core and scattering wings are clearly visible. The histograms with the error bars are the spectra multiplied by 15 to show the detailed shapes of the scattering wings. The channels near the Ly β line at 102.5 nm are not included here and the contribution from the scattering wings of the Ly β line is negligible. (In typical heliospheric spectra, Ly β is usually a factor of ≈ 500 fainter than Ly α) The distinct difference between the shapes of the bright cores of the two lines indicates a non-uniform change in the sensitivity across the Ly α channels. A similar exercise for Voyager 2 indicates no statistically significant line shape changes.

H Ly α Scattered Photons

The signature of Ly α instrumental scattering is that of a faint “skirt” about the base of the core of the line. If changes in sensitivity are uniform across the detector, the ratio of the signal levels in the Ly α core and skirt should remain the same. However, as is shown in Figure A.1, this ratio changed for Voyager 1 during or near the Jupiter

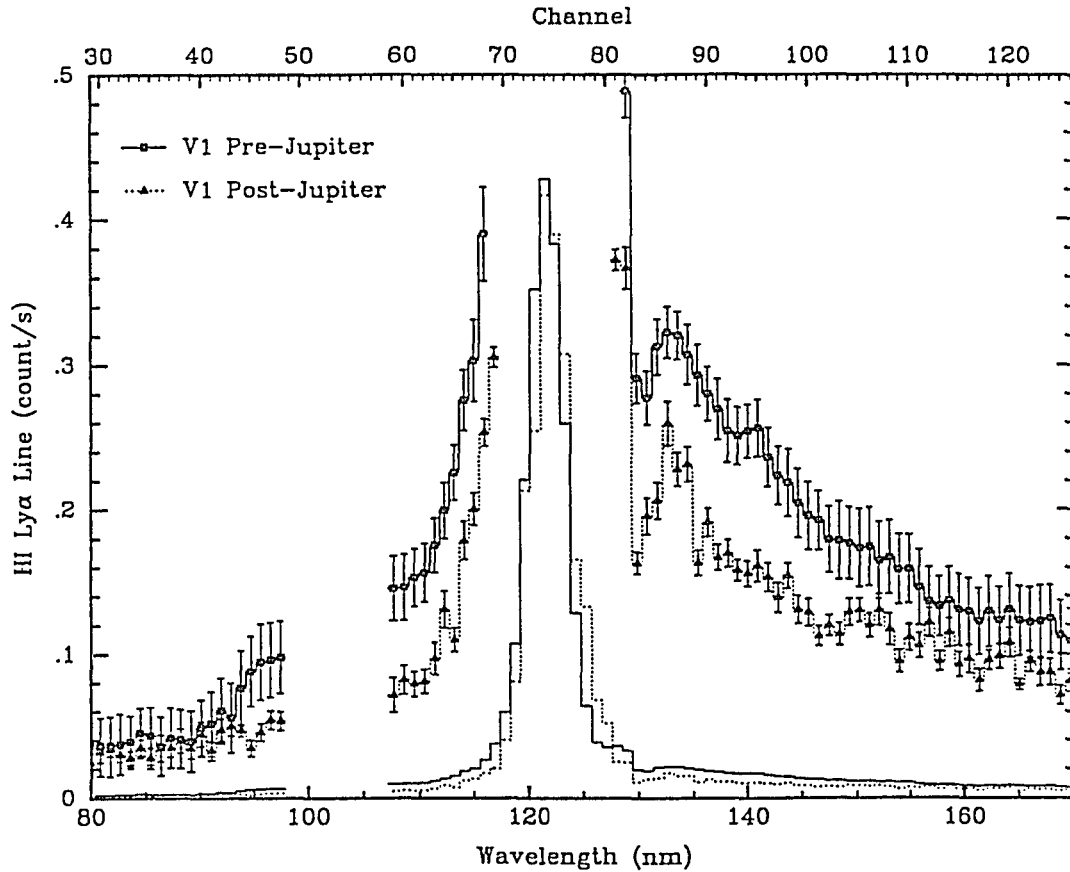


Figure A.1: The Voyager 1 UVS H Ly α line shape before and after Jupiter encounter. The solid and dotted lines show the Ly α line as detected in long duration sky background observation before and after Jupiter encounter. The line core and scattering wings are clearly visible. The histograms with the error bars show the spectra multiplied by a factor of 15 and illustrates the detailed shapes of the scattering wings. The cores of the lines (channels 70–78) are normalized to a count rate of 2 counts/sec. The difference in the spectral shapes in these core regions indicates that sensitivity changes that occurred at or near Jupiter encounter were non-uniform across the Ly α channels. The change in the ratio of the count rates in the scattering wings relative to the core indicates that the Ly α channels suffered a different level of degradation than adjacent channels. The channels near the Ly β line at 102.5 nm are not included, and the contribution from the scattering wings of the Ly β line is negligible.

encounter. The observed difference in Ly α scattering profiles indicates that the Ly α channels were degraded by a factor of (0.67 ± 0.07) less than the channels in the 130 to 140 nm wavelength region. A similar exercise for Voyager 2 indicates no significant changes in the Ly α scattering profile.

As mentioned above, the post Jupiter encounter sensitivity of the Voyager 1 UVS in the wavelength intervals (100–119) nm and (130–145) nm was assessed to be 68% of the pre-encounter sensitivity on the basis of comparing stellar spectra. However, the analysis of scattered Ly α photons indicates that the Ly α channels suffered 67% less degradation than those in these regions. These factors cancel one another to within error—indicating that the sensitivity at Ly α remained about the same before and after Jupiter encounter. No physical explanation for this result is tendered, but possible causes include the unique exposure history of the Ly α channels or the proximity of the long wavelength filter edge at 125 nm.

A.3.4 The Relative UVS H Ly α Calibrations

The two UVS instruments on the Voyager spacecraft are nearly identical and their sensitivities to equivalent laboratory illumination sources were measured to be similar. For instance, at 121.6 nm, the sensitivity of the Voyager 1 UVS was measured to be about 80% that of Voyager 2. On the basis of the observed scattered Ly α photons, the post-Jupiter Ly α sensitivity of the Voyager 1 UVS is apparently about the same as the pre-Jupiter sensitivity. Specifically, the ratio of Voyager 1 Ly α counts to Voyager 2 counts for equivalent Ly α intensities observed after Voyager 1 Jupiter encounter is (0.79 ± 0.12) . This cross calibration is a new result introduced here. It assumes that FPN 76 is used for the Voyager 2 spectral reduction and FPN 49 or 47 is used for Voyager 1. Formerly, most post-Jupiter Voyager 1 Ly α intensities were reported by incorrectly assuming that the 32% reduction in sensitivity indicated by the stellar observations applies to the Ly α channels as well. So intensities reported

previously need to be revised downward by 32% in order to be consistent with this new calibration. For instance, the ≈ 4.9 kR of Ly α Saturn day side equatorial airglow reported for the Voyager 1 encounter (Shemansky and Ajello, 1983; Yelle et al., 1986; 1987) should be revised downward to ≈ 3.3 kR. The UVS Ly α cross calibration introduced here relies on the observed level of scattered Ly α photons which indicates a non-uniform degradation near the Ly α channels. The physical explanation for the observed non-uniform degradation remains elusive. So a cautious approach is warranted, and suggests that the relative UVS Ly α calibrations be determined by other independent means. One way to cross check the calibrations of two instruments is to have them both observe the same target with a known (or separately measured) intensity. For the Voyager spacecraft there were only two different extended field Ly α sources observed by both spacecraft in the post-Jupiter mission phase: the heliosphere and Saturn. Neither of these sources should be considered “standard candles” because each is reasonably expected to be variable. However, judicious comparisons of the data yield estimates for the relative UVS Ly α sensitivities which are within error of the original relative laboratory sensitivities. These comparisons therefore verify the results obtained above by analyzing the scattered Ly α light in the Voyager 1 UVS.

Saturn Equatorial H Ly α

Voyager 1 encountered Saturn on day 317 of 1980. The Voyager 2 encounter occurred less than a year later, on day 238 of 1981. Both spacecraft observed H Ly α emissions from the equatorial regions of the planet. In addition, during or near each encounter, the International Ultraviolet Explorer (IUE) satellite observed the Ly α emissions as well (see McGrath and Clarke, 1992). The reported Voyager 1 Ly α intensities included the 32% degradation determined from stellar observations. By comparing the concurrent IUE and Voyager observations McGrath and Clarke (1992) suggest

that either the Voyager 1 UVS Ly α calibration is incorrect or the maximum optical depth between the Earth and Saturn for Ly α absorption is >0.6 . The optical depth for the absorption of Saturnian Ly α emissions is plotted in Figure 3.3. The largest optical depth is ≈ 0.2 . The calculation assumes a hot distribution for heliospheric H with a VLISM H density, $n_{\text{H}\infty} = 0.1 \text{ cm}^{-3}$. Even the highest estimates for $n_{\text{H}\infty}$ are less than 0.2 cm^{-3} which makes it unlikely that the optical depth ever exceeds 0.4. So, as indicated by McGrath and Clarke (1992), to make the concurrent Voyager and IUE observations consistent, the reported Voyager 1 Saturn intensity needs to be reduced by a factor of about 25%. This is close to the $(32 \pm 7)\%$ loss of sensitivity that was assumed to apply to the Ly α on the basis of stellar spectra. In other words, the Voyager and IUE Saturn equatorial observations are consistent (to within observational error) when the new UVS cross calibration introduced here is employed.

Heliospheric Ly α Observations

Heliospheric observations also provide a means of estimating the UVS Ly α cross calibration. The relative sensitivities at Ly α may be estimated through direct comparison of count rates in spectra obtained when the spacecraft were in nearly the same position in the solar system, looking in nearly the same direction. Such observations were performed within a year of one another just before the Saturn encounters. The Ly α intensities are taken from several long-duration sky background spectra obtained when the two spacecraft were within $\approx 0.3 \text{ AU}$ and when the UVS were pointed within 10° of one another. When the signals are adjusted for the observed variability of the solar Ly α line, the ratio of the Voyager 2 Ly α signal to that of Voyager 1 is (0.75 ± 0.07) . This is within error of the new cross calibration ratio (0.79 ± 0.12) .

A.4 The Absolute Voyager UVS H Ly α Calibrations

Voyager 2 presumably suffered little or no radiation damage at Jupiter. The demonstrated stability of the Voyager 2 UVS from the post-launch period onward suggests that, if no launch or post-launch instrumental changes occurred, the laboratory calibration at Ly α is the best estimate available. Here, the absolute Voyager 2 Ly α calibration factor is determined by using the laboratory calibration curve to calculate a synthetic Ly α line. The synthetic line is fit to a high-quality sky background line and the intensity related to the integrated count rate in channels 72 through 80 which span the Ly α line in the Voyager 2 UVS. This procedure yields the absolute calibration factor

$$\epsilon_2 = \frac{172 \text{ Rayleighs}}{\text{counts/s in channels 72-80}}, \quad (\text{A.1})$$

for spectra reduced using FPN 76. The error on this absolute calibration is difficult to determine and is not reported here. However, the absolute Voyager 2 Ly α calibration is consistent with the IUE calibration on the basis of concurrent observations of Jupiter's equatorial airglow (Shemansky and Judge, 1988).

Channels 70 through 78 span the Ly α line on the Voyager 1 UVS. Using the cross calibration factor (0.79 ± 0.12), the absolute Voyager 1 Ly α calibration is

$$\epsilon_1 = \frac{(218 \pm 33) \text{ Rayleighs}}{\text{counts/s in channels 70-78}}, \quad (\text{A.2})$$

for spectra obtained after Jupiter encounter and reduced using FPN 47 or 49. The $\approx 15\%$ error refers to the uncertainty in the UVS Ly α cross calibration, and not to the uncertainty of the absolute scale.

APPENDIX B

VOYAGER CRUISE MANEUVER $\text{Ly}\alpha$ OBSERVATIONS

Both Voyager spacecraft periodically conduct special maneuvers to map the heliospheric resonance emissions over large portions of the sky. The sequences are called the Cruise Maneuvers. During the maneuvers, the spacecraft are instructed to spin about their yaw and/or the roll axes for a period of 4 to 20 hours. As the spacecraft spin, the Ultraviolet Spectrographs (UVS) gather spectra, which may be compiled into maps of the sky in the resonance lines H $\text{Ly}\alpha$, $\text{Ly}\beta$, and He 58.4 nm, even though the signal-to-noise ratios for the latter two lines are much poorer than for $\text{Ly}\alpha$. The earliest maneuvers conducted within 5 AU of the Sun have been analyzed and published elsewhere (see Lallement, 1990 and references therein).

B.1 Voyager Spacecraft and Geometry

The Voyager spacecraft are the last of the Mariner probe design. Two sources of general information on their design and geometry are: the Science and Mission Systems Handbook (JPL Publication PD 618-128) and the Voyager Neptune Travel Guide (JPL Publication 89-24). Figure B.1 is an illustration of the spacecraft. Following aerospace convention, three orthogonal axes, called roll, yaw and pitch, are used for reference. The attitude of the spacecraft and the articulation of the scan platform are controlled by the spacecraft Attitude and Articulation Control System (AACS). During normal operation, the spacecraft are stabilized in a fixed orientation by the AACS through a combination of a two-axis Sun sensor for pitch and yaw control and a star tracker for roll reference. The High-Gain Antenna (HGA) is pointed along the roll axis, usually toward the Earth to maintain radio contact. During special maneuvers, the AACS may be commanded to use the hydrazine thrusters to spin the craft about

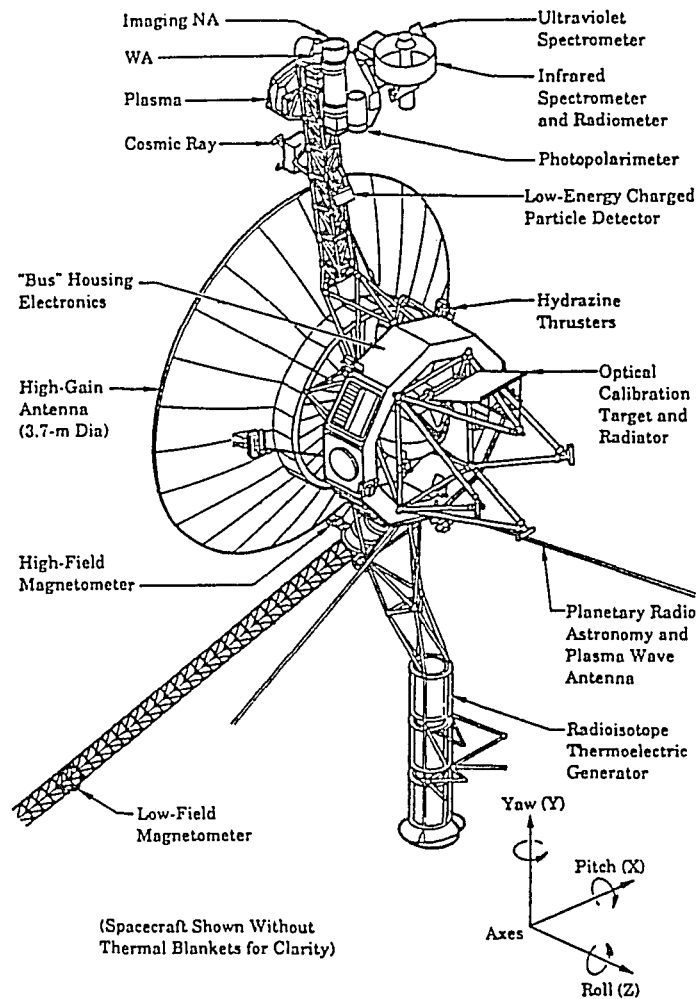


Figure B.1: A drawing of the Voyager spacecraft indicating the location of various components. The UVS is mounted on the scan platform at the end of the science boom. The orientation of the roll, yaw and pitch axes are shown at the lower right. The High-Gain Antenna lies along the roll axis. (Reproduced with permission from Holberg and Watkins, 1992.)

any of the three axes. In the case of a roll turn, the spacecraft need not lose radio contact with the Earth. Yaw and pitch turns swing the HGA along a great circle through the sky. The AACCS is designed for one primary spin rate, 1.8 revolutions per hour.

B.2 Cruise Maneuver Sequences

The Cruise Maneuver observations were designed to gather UVS observations of the heliospheric resonance emissions over large portions of the sky. They are composed of a series of yaw and then roll turns lasting from 4 to 20 hours. During the roll phase of the sequences, the scan platform (on which the UVS is mounted) sometimes is slewed. The combination of rolling and slewing swings the UVS through large portions of the sky. Figure B.2 shows the positions, in Earth Mean Equatorial (1950) Right Ascension and Declination coordinates, where UVS spectra were obtained during the roll phases of two Voyager 2 cruise maneuvers. Portions of the sky near the solar and antisolar directions are not mapped. During the yaw phase of the maneuvers, the scan platform is not slewed, so the UVS typically just traces a small circle in the sky.

Early in the mission, the cruise maneuvers consisted of 10 yaw turns followed by 25 roll turns and required about 20 hours to complete. The scan platform was slewed between each roll, allowing the UVS to map the sky (see the top panel of Figure B.2). These “maxi” maneuvers were much more extensive (and expensive) than the “mini” maneuvers performed later in the mission, which typically consisted of 4 yaw turns and 4 rolls with no scan platform slews. One Voyager 2 maneuver conducted near Uranus had an intermediate design (see the bottom panel of Figure B.2). In addition, the roll phases of earlier maneuvers were conducted with the HGA pointed towards the Sun rather than the Earth. Between the Jupiter and Saturn encounters this practice was discontinued on both spacecraft.

Reducing the raw Cruise Maneuver observations involves three principal steps:

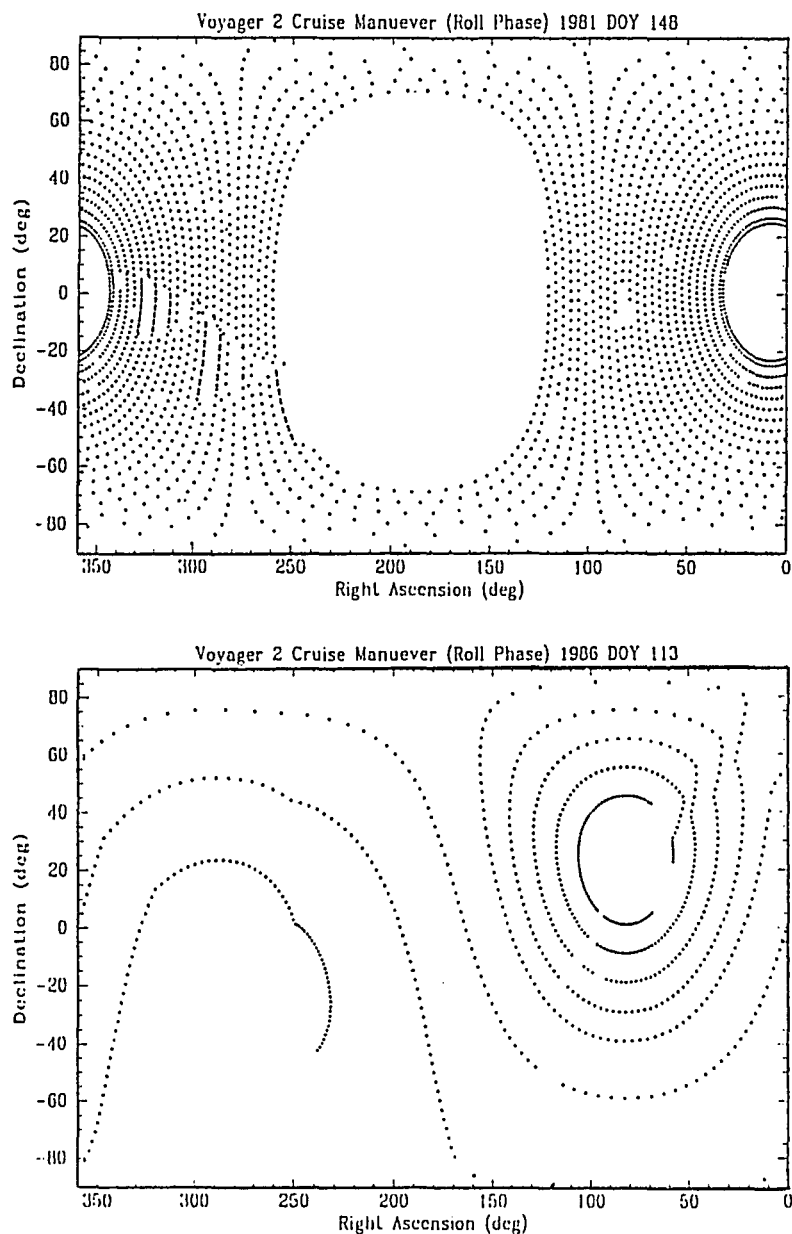


Figure B.2: The pattern of UVS observations during two Voyager 2 cruise maneuvers. Each dot represents a UVS spectrum obtained at a particular Right Ascension and Declination (Earth Mean Equatorial, 1950). The pattern of stars detected in the Cruise Maneuver Observations allows the spacecraft spin rate and orientation to be determined. The spectra not polluted by starlight may then be compiled into maps of the sky in the heliospheric emissions.

1) determining initial spacecraft orientation, 2) accumulating or “binning” the spectra according to position in the sky, and 3) determining the H Ly α intensity for each accumulated spectrum using the spectral reduction procedure and calibration factors given in Appendix A.

B.3 Initial Spacecraft Orientation and Spin Rate

As the AACS initializes the yaw or roll turn, the absolute spacecraft orientation becomes uncertain by a few degrees. In addition, the exact spin rate of the spacecraft varies (within design limits) by $\approx 0.5\%$ from one maneuver to the next. To accurately associate a particular UVS spectrum with a particular position in the sky, it is necessary to determine the initial spacecraft orientation and the exact spin rate. Fortunately, during most maneuvers, the UVS sweeps over several stars. By comparing the detected pattern of stars to the known distribution of stars in the sky, the initial orientations and spin rates may be determined. During a few maneuvers, the number of detected stars is inadequate to determine these parameters; the data from these maneuvers are not included here.

B.4 Binning the Spectra

Figure B.2 shows the positions where UVS spectra were gathered in Right Ascension and Declination coordinates. However, in this coordinate system the density of spectra is not equal in all sections of the sky covered during the maneuver. If the data are accumulated in these coordinates, the signal-to-noise ratios tend to vary greatly from one position to the next. Here, a more natural coordinate system is employed, where the signal-to-noise ratios are more evenly distributed. This system is also composed of two angles, which are defined by the position of the spacecraft with respect to the Sun. The first angle, Θ , is that between the UVS optical axis and the antisolar direction. The second angle, Ψ , measures the position of the UVS optical axis around

the antisolar direction. In this system $\Theta = 0^\circ$ corresponds to the direction away from the Sun and $\Theta = 180^\circ$ denotes the direction toward the Sun. Figure B.3 shows how these angles relate to the spacecraft heliocentric longitude λ , and latitude β . All heliocentric coordinates here are given in the Sun-centered, Earth Mean Ecliptic, epoch 1950, (EMEc50) system. In the EMEc50 system, the x - y plane is the ecliptic and the spacecraft position vector, \mathbf{r} is

$$\mathbf{r} = \begin{pmatrix} x \\ y \\ z \end{pmatrix} = R \begin{pmatrix} \cos \lambda \cos \beta \\ \sin \lambda \cos \beta \\ \sin \beta \end{pmatrix}, \quad (\text{B.1})$$

where R is the heliocentric distance. The three unit vectors, \hat{r} , $\hat{\lambda}$ and $\hat{\beta}$ are defined by the spacecraft position as shown in panel *a* of Figure B.3. The direction of the UVS optical axis in EMEc50 coordinates, $\hat{\ell}$, may be calculated from Θ and Ψ by using the expression (see panel *b* of Figure B.3):

$$\hat{\ell} = \hat{\lambda}(\cos \Psi \sin \Theta) + \hat{\beta}(\sin \Psi \sin \Theta) + \hat{r}(\cos \Theta). \quad (\text{B.2})$$

B.5 Cruise Maneuver H Ly α Observations

The Voyager Cruise Maneuver H Ly α observations are compiled in the tables B.1 through B.50. In the first two lines of each table, the spacecraft heliocentric distance (R), and EMEc50 longitude (λ) and latitude (β) are noted. Also a six day average of the estimated subspacecraft solar H Ly α integrated flux (photons $\text{cm}^{-2} \text{s}^{-1}$) at 1 AU is tabulated. These are taken from the record of He 10.8 μm solar observations, which correlate well with H Ly α variations observed directly by SME (Donnelly et al., 1986; Skinner et al., 1988). Following the first two lines of each table, the Ly α intensities (in Rayleighs) are tabulated in $20^\circ \times 20^\circ$ sections of the sky in the angles Θ and Ψ . The absolute Ly α intensities are derived using the spectral reduction procedure and

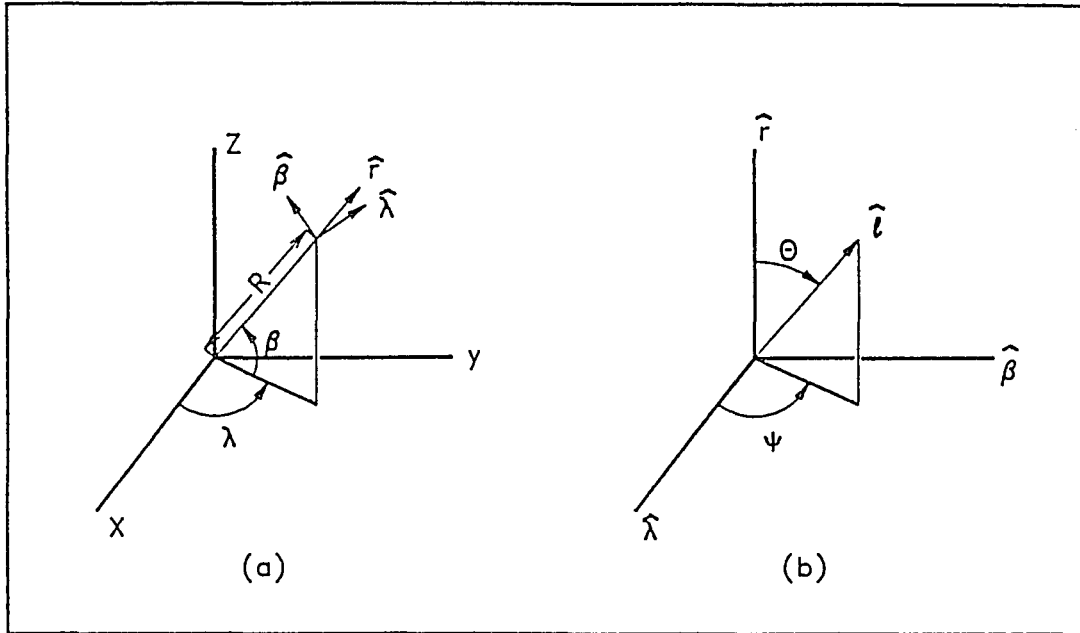


Figure B.3: The geometry of the coordinate system used to bin the Voyager Cruise Maneuver H $\text{Ly}\alpha$ observations. Panel a shows the EMEc50 coordinate system with the spacecraft at heliocentric radius R , and ecliptic longitude and latitude λ and β . Panel b shows how the angles Θ and Ψ are related to the local unit vectors \hat{r} , $\hat{\lambda}$ and $\hat{\beta}$. The Cruise Maneuver $\text{Ly}\alpha$ data are tabulated in the angles Θ and Ψ .

calibration factors given in Appendix A. In the lower part of the tables, the statistical errors on the Ly α intensities are given. These are calculated from the total number of counts observed in the UVS Ly α channels.

Reading the tables is straightforward. For instance, Table B.1 gives the H Ly α data for the Voyager 1 Cruise Maneuver performed on Day 288 in the year 1979. At this time the spacecraft was 6.4 AU from the Sun at longitude 154.5° and latitude 1.6° (EMEc50). The estimated subspacecraft Ly α solar flux at 1 AU for this time is 3.73×10^{11} photons cm⁻² s⁻¹. The Ly α intensity observed by the UVS when its optical axis was pointed in the direction given by $\Theta = 70^\circ$ and $\Psi = 10^\circ$ was (871 ± 86) Rayleighs. Similarly, the Ly α intensity in the direction $\Theta = 130^\circ$ and $\Psi = 210^\circ$ was (743 ± 42) Rayleighs.

Table B.1: Voyager 1 Cruise Maneuver: 1979 Day 288

Voyager 1		1979 Day 288				R = 6.4 AU			
Long. = 154.5°		Lat. = 1.6°				Flux = 3.73(11) cm ⁻² s ⁻¹			
Θ	10 30	50	70	90	110	130	150	170	
Ψ									
10			871	912	1263	1590	1890		
30			775	938	1131	1504	1679		
50			814	807	1134	1477	1637		
70			899	829	1120	1275	1480		
90				778	990	1224	1371		
110				844	934	1149	1279		
130				741	857	951	1077		
150			592	648	783	862	976		
170			831	595	567	723	809		
190			548	528	555	674	726		
210			601	644	665	743	797		
230			678	679	769	805	960		
250			747	709	812	964	1098		
270			753	823	895	1175	1263		
290			729	713	1002	1167	1371		
310			963	850	1027	1319	1506		
330			843	937	1144	1446	1666		
350			898	948	1239	1537	1728		
10			86	54	67	60	66		
30			77	56	60	59	63		
50			79	50	62	60	63		
70			109	54	63	53	60		
90				51	57	53	58		
110				52	54	52	54		
130				50	55	46	51		
150			76	49	55	45	49		
170			84	46	47	41	44		
190			65	43	49	39	43		
210			73	46	48	42	44		
230			73	50	50	43	48		
250			85	48	51	47	52		
270			76	52	54	53	56		
290			80	50	56	51	57		
310			105	53	58	55	60		
330			85	57	61	57	62		
350			88	55	64	59	64		

Table B.2: Voyager 1 Cruise Maneuver: 1980 Day 51

Voyager 1		1980 Day 51				R = 7.3 AU			
Long. = 165.8°		Lat. = 2.0°				Flux = 3.40(11) cm ⁻² s ⁻¹			
Θ	10 30	50	70	90	110	130	150	170	
Ψ									
10	740	852	962	1063	1273	1451	1800		
30	720	840	921	1083	1215	1541	1798		
50	658	837	897	992	1217	1398	1760		
70	727	772	817	980	1064	1406	1605		
90	842	751	802	870	1014	1214	1486		
110	850	741	803	827	903	1171	1367		
130	645	715	762	796	916	1025	1254		
150	645	747	741	820	761	852	1024		
170	789	725	768	700	727	763	926		
190	758	728	807	740	637	721	889		
210	644	694	779	791	694	784	888		
230	688	749	736	822	797	908	1029		
250	706	828	796	780	930	956	1134		
270	670	708	825	906	994	1160	1285		
290	507	762	827	847	1081	1234	1462		
310	880	797	907	964	1098	1241	1635		
330	739	789	883	1032	1111	1448	1835		
350	794	820	1024	1016	1244	1463	1949		
10	79	60	61	65	71	76	85		
30	75	58	60	65	68	77	82		
50	72	57	62	63	73	76	88		
70	69	59	57	64	65	74	81		
90	81	54	56	59	62	69	76		
110	81	54	58	57	61	69	74		
130	75	55	54	55	60	64	70		
150	71	55	54	59	55	58	63		
170	83	53	57	53	55	55	61		
190	77	55	57	54	51	54	59		
210	71	53	56	58	53	56	59		
230	77	55	56	58	57	60	64		
250	74	61	56	56	61	62	67		
270	72	54	59	63	62	67	71		
290	63	55	58	59	67	69	75		
310	87	58	59	62	72	71	81		
330	76	56	61	65	65	75	83		
350	78	57	67	63	71	75	89		

Table B.3: Voyager 1 Cruise Maneuver: 1980 Day 168

Voyager 1		1980 Day 168				R = 8.2 AU			
Long. = 173.8°		Lat. = 2.2°				Flux = 3.83(11) cm ⁻² s ⁻¹			
Θ	10 30	50	70	90	110	130	150	170	
Ψ									
10			1009	1071	1353	1646	1997		
30			964	1055	1244	1560	1983		
50			947	1084	1204	1463	1892		
70			883	953	1126	1331	1663		
90			794	954	1080	1284	1513		
110			752	939	1035	1184	1248		
130			886	930	898	1040	1148		
150			850	856	868	1018	1006		
170			788	820	827	845	912		
190			825	846	745	770	955		
210			813	857	908	854	923		
230			844	864	879	1022	1100		
250			875	848	1003	1162	1262		
270			835	938	1111	1297	1446		
290			949	917	1125	1361	1627		
310			945	1051	1235	1549	1792		
330			954	1128	1277	1630	1855		
350			1061	1199	1291	1600	1851		
10			57	58	66	66	88		
30			55	58	63	64	89		
50			56	60	63	65	85		
70			51	57	61	59	80		
90			51	56	59	59	77		
110			49	55	58	56	71		
130			53	55	55	54	67		
150			52	53	53	51	63		
170			51	51	51	48	60		
190			51	52	50	46	62		
210			52	57	55	47	60		
230			57	52	53	52	66		
250			56	51	58	55	71		
270			53	57	59	58	75		
290			57	53	60	60	80		
310			56	58	64	64	83		
330			57	61	63	65	86		
350			62	63	64	65	85		

Table B.4: Voyager 1 Cruise Maneuver: 1981 Day 41

Voyager 1			1981 Day 41			R = 9.9 AU			
Long. = 186.4°			Lat. = 5.8°			Flux = 3.83(11) cm ⁻² s ⁻¹			
Θ	10	30	50	70	90	110	130	150	170
Ψ									
10				734	880	1012	1281	1645	
30				757	802	969	1177	1540	
50				729	802	945	1207	1467	
70				672	745	940	1068	1326	
90				664	712	851	1001	1318	
110				642	766	819	964	1204	
130				709	735	840	910	1035	
150				704	770	813	864	929	
170				672	705	776	784	790	
190				688	709	762	763	813	
210				628	707	761	847	815	
230				730	766	795	881	1011	
250				738	759	818	939	1087	
270				702	736	824	962	1236	
290				726	770	963	1078	1397	
310				769	826	944	1221	1497	
330				785	828	1030	1214	1600	
350				821	859	1027	1229	1639	
10				56	53	56	57	72	
30				56	51	56	56	69	
50				57	51	56	56	68	
70				50	50	55	56	68	
90				49	49	54	51	64	
110				54	49	52	51	62	
130				55	49	52	49	57	
150				54	50	51	48	55	
170				55	48	50	45	51	
190				55	49	49	46	51	
210				53	50	53	48	51	
230				56	51	51	48	58	
250				61	50	51	50	59	
270				55	49	52	51	62	
290				57	51	57	54	68	
310				58	51	54	57	68	
330				58	51	58	57	71	
350				61	53	58	57	72	

Table B.5: Voyager 1 Cruise Maneuver: 1981 Day 134

Voyager 1		1981 Day 134				R = 10.5 AU			
Long. = 191.1°		Lat. = 9.1°				Flux = 3.44(11) cm ⁻² s ⁻¹			
Θ	10 30	50	70	90	110	130	150	170	
Ψ									
10			804	890	1019	1301	1763		
30			731	864	961	1209	1645		
50			781	797	878	1183	1537		
70			720	815	918	1150	1372		
90			675	672	847	1072	1205		
110			683	670	882	1082	1161		
130			639	758	782	951	1082		
150			702	723	800	982	1034		
170			715	753	856	793	864		
190			656	684	794	823	827		
210			707	680	860	869	931		
230			665	753	803	978	1001		
250			712	720	855	956	1179		
270			716	767	825	1098	1237		
290			700	839	845	1095	1306		
310			697	794	915	1076	1402		
330			711	812	996	1286	1570		
350			771	812	997	1326	1604		
10			58	54	57	58	75		
30			58	52	56	56	72		
50			60	53	54	58	69		
70			58	55	55	57	69		
90			59	48	53	53	61		
110			42	48	54	54	60		
130			42	49	51	51	60		
150			43	48	51	50	57		
170			44	50	53	48	53		
190			43	48	52	47	52		
210			44	49	55	48	54		
230			48	53	51	51	56		
250			56	53	53	50	62		
270			57	51	52	54	62		
290			57	53	52	54	66		
310			55	50	55	53	68		
330			58	50	57	58	73		
350			59	53	56	60	70		

Table B.6: Voyager 1 Cruise Maneuver: 1981 Day 320

Voyager 1		1981 Day 320				R = 11.7 AU			
Long. = 199.3°		Lat. = 14.5°				Flux = 4.20(11) cm ⁻² s ⁻¹			
Θ	10 30	50	70	90	110	130	150	170	
Ψ									
10			818	829	1048	1296	1593		
30			816	837	964	1226	1538		
50			694	813	936	1248	1438		
70			720	746	908	1124	1378		
90			692	692	858	1003	1218		
110			653	788	899	1001	1264		
130			667	747	878	1059	1037		
150			726	717	911	1018	1006		
170			755	772	867	959	1035		
190			750	767	881	975	1022		
210			739	760	915	989	1030		
230			679	740	889	1048	1198		
250			755	830	896	1097	1244		
270			701	724	873	1111	1294		
290			737	796	990	1143	1483		
310			803	931	971	1289	1539		
330			810	919	1017	1300	1525		
350			711	888	1012	1342	1590		
10			66	51	53	65	70		
30			66	52	52	62	72		
50			64	53	52	64	70		
70			62	49	50	60	65		
90			61	47	50	56	62		
110			57	51	51	57	67		
130			51	50	51	59	57		
150			54	48	49	57	62		
170			56	50	48	56	61		
190			54	50	49	57	56		
210			54	49	52	69	60		
230			63	55	54	59	61		
250			64	58	49	61	64		
270			65	48	49	62	67		
290			66	54	51	61	70		
310			67	55	51	64	69		
330			69	53	52	64	72		
350			65	54	51	66	72		

Table B.7: Voyager 1 Cruise Maneuver: 1982 Day 90

Voyager 1			1982 Day 90			R = 12.8 AU			
Long. = 204.3°			Lat. = 17.5°			Flux = 3.77(11) cm ⁻² s ⁻¹			
Θ	10	30	50	70	90	110	130	150	170
Ψ									
10				638	781	859	1074	1414	
30				591	730	773	1076	1334	
50				644	700	805	957	1256	
70				565	700	769	957	1275	
90				562	647	736	862	1194	
110				551	591	784	871	1119	
130				625	616	777	843	1021	
150				576	660	765	828	842	
170				641	652	807	867	895	
190				619	704	797	860	948	
210				595	614	715	986	1039	
230				610	727	805	915	1094	
250				617	692	822	954	1133	
270				725	693	822	927	1169	
290				681	667	816	1001	1287	
310				704	753	886	1032	1368	
330				728	779	911	1078	1369	
350				693	813	831	1053	1393	
10				47	49	54	59	68	
30				45	50	50	59	65	
50				47	48	50	55	62	
70				43	48	51	56	65	
90				45	45	48	53	62	
110				44	44	50	52	60	
130				45	46	51	53	58	
150				48	46	49	53	51	
170				48	43	52	55	54	
190				47	47	50	57	54	
210				43	47	50	56	59	
230				47	49	56	56	59	
250				45	50	52	55	59	
270				49	49	51	55	62	
290				50	48	51	57	64	
310				47	49	54	60	66	
330				50	50	55	59	66	
350				47	53	52	58	66	

Table B.8: Voyager 1 Cruise Maneuver: 1982 Day 300

Voyager 1		1982 Day 300					R = 14.5 AU			
Long. = 211.0°		Lat. = 21.2°					Flux = 3.47(11) cm ⁻² s ⁻¹			
Θ	10	30	50	70	90	110	130	150	170	
Ψ										
10		426	495	532		828	963	1021		
30		528						1199		
50		448						1257		
70		461						1157		
90		462						1136		
110		519	473				857	995		
130			552	530	600	685	804			
150										
170										
190										
210										
230										
250										
270										
290										
310										
330										
350				566	614	678				
10		33	36	84		89	50	49		
30		52						81		
50		43						66		
70		45						67		
90		48						74		
110		52	35				48	71		
130			45	31	34	36	47			
150										
170										
190										
210										
230										
250										
270										
290										
310										
330										
350				33	34	36				

Table B.9: Voyager 1 Cruise Maneuver: 1983 Day 117

Voyager 1			1983 Day 117			R = 16.1 AU			
Long. = 215.7°			Lat. = 23.6°			Flux = 3.45(11) cm ⁻² s ⁻¹			
Θ	10	30	50	70	90	110	130	150	170
Ψ									
10			468	464	544	690	932		
30			449	471	567	730	866		
50			438	474	535	627	898		
70			399	430	561	645	816		
90			396	430	532	644	824		
110			425	463	514	611	787		
130			399	435	460	660	771		
150			383	424	560	575	678		
170			455	497	521	684	700		
190			359	441	550	671	794		
210			394	459	554	728	803		
230			433	493	549	704	911		
250			402	595	555	701	860		
270			473	529	629	738	976		
290			523	536	599	753	987		
310			501	471	624	770	962		
330			505	505	614	818	987		
350			456	527	610	714	1010		
10			39	39	42	47	55		
30			39	39	43	49	53		
50			39	41	42	45	53		
70			35	38	44	46	53		
90			36	40	42	46	52		
110			38	39	41	45	51		
130			37	38	39	46	50		
150			36	38	43	44	47		
170			39	41	42	47	49		
190			35	38	43	49	56		
210			36	39	43	49	51		
230			39	41	44	48	58		
250			37	43	44	47	52		
270			41	43	46	50	58		
290			42	42	44	49	58		
310			41	39	46	50	60		
330			41	41	46	52	55		
350			39	42	44	48	57		

Table B.16: Voyager 1 Cruise Maneuver: 1986 Day 93

Voyager 1		1986 Day 93					R = 26.4 AU			
Long. = 232.2°		Lat. = 30.2°					Flux = 2.57(11) cm ⁻² s ⁻¹			
Θ	10	30	50	70	90	110	130	150	170	
Ψ										
10						256				
30						265				
50						234				
70						258				
90						233				
110						233				
130						229				
150						243				
170						264				
190						233				
210						216				
230						209				
250						277				
270						255				
290						262				
310						268	274	314		
330						209	258	341		
350						186	266	313		
10						24				
30						24				
50						23				
70						25				
90						28				
110						23				
130						23				
150						23				
170						24				
190						23				
210						22				
230						22				
250						25				
270						24				
290						24				
310						23	17	23		
330						17	25	22		
350						21	18	24		

Table B.17: Voyager 1 Cruise Maneuver: 1986 Day 246

Voyager 1		1986 Day 246					R = 27.9 AU			
Long. = 233.7°		Lat. = 30.7°					Flux = 2.53(11) cm ⁻² s ⁻¹			
Θ	10	30	50	70	90	110	130	150	170	
Ψ										
10			175	237	212	220	352			
30							361			
50							350			
70							307			
90							421			
110							366			
130							343			
150							377			
170							351			
190							352			
210							443			
230							366			
250							397			
270				242	284	336	396			
290			244	332		307	357			
310		246	230				358			
330		180					349			
350		211	234				368			
10			25	20	19	25	24			
30							24			
50							24			
70							23			
90							27			
110							26			
130							26			
150							27			
170							24			
190							25			
210							28			
230							25			
250							26			
270				31	22	24	26			
290			30	39		31	28			
310		26	27				21			
330		23					20			
350		34	26				19			

Table B.22: Voyager 1 Cruise Maneuver: 1988 Day 230

Voyager 1		1988 Day 230				R = 34.9 AU			
Long. = 238.9°		Lat. = 32.1°				Flux = 3.28(11) cm ⁻² s ⁻¹			
Θ	10	30	50	70	90	110	130	150	170
Ψ									
10					284				
30					271				
50					338				
70					272				
90					290				
110					286				
130					304				
150					269				
170					278				
190					234				
210					288				
230					256				
250					259				
270					281				
290					275				
310					281				
330					270				
350					275				
10					25				
30					24				
50					29				
70					25				
90					25				
110					25				
130					25				
150					24				
170					25				
190					25				
210					25				
230					25				
250					31				
270					26				
290					26				
310					25				
330					24				
350					24				

Table B.23: Voyager 1 Cruise Maneuver: 1988 Day 351

Voyager 1		1988 Day 351					R = 36.1 AU			
Long. = 239.6°		Lat. = 32.3°					Flux = 3.47(11) cm ⁻² s ⁻¹			
Θ	10	30	50	70	90	110	130	150	170	
Ψ										
10			202	273	302	316				
30			249	255		305	337			
50			248				343			
70			233				345			
90			232	254	287	328	416			
110			249							
130			237							
150			220							
170			220							
190			252							
210			236							
230			225							
250			246							
270			250							
290			278							
310			298							
330			215							
350			279							
10			21	21	21	23				
30			21	33		31	24			
50			24				26			
70			22				32			
90			19	23	20	27	30			
110			23							
130			23							
150			23							
170			22							
190			24							
210			23							
230			23							
250			23							
270			24							
290			27							
310			26							
330			22							
350			24							

Table B.24: Voyager 1 Cruise Maneuver: 1989 Day 104

Voyager 1		1989 Day 104				R = 37.3 AU			
Long. = 240.2°		Lat. = 32.5°				Flux = 3.75(11) cm ⁻² s ⁻¹			
Θ	10	30	50	70	90	110	130	150	170
Ψ									
10				282	344	334	341		
30			300	252			402		
50			263	217			410		
70			251	239			431		
90			249	280	283	366	428		
110				275					
130				251					
150				259					
170			305	270					
190			257						
210			283						
230			243						
250			302						
270				352					
290				335					
310				216					
330				283					
350				266					
10				25	23	27	37		
30			31	27			33		
50			25	23			29		
70			27	23			36		
90			20	19	20	24	22		
110				25					
130				23					
150				24					
170			30	32					
190			24						
210			25						
230			23						
250			27						
270				28					
290				29					
310				22					
330				24					
350				24					

Table B.25: Voyager 1 Cruise Maneuver: 1989 Day 279

Voyager 1		1989 Day 279					R = 39.1 AU			
Long. = 241.1°		Lat. = 32.7°					Flux = 3.62(11) cm ⁻² s ⁻¹			
Θ	10	30	50	70	90	110	130	150	170	
Ψ										
10			286	260		397	424			
30		221	218				457	519		
50		280					432	554		
70		245					456	511		
90		221	253				429			
110			269	251	287	316	386			
130							447			
150							502			
170							481			
190							471			
210							516			
230							415			
250							470			
270							523			
290							442			
310							461			
330							453			
350				295	291	352	499			
10			29	22		34	30			
30		26	49				29	45		
50		30					30	42		
70		27					35	36		
90		31	30				28			
110			25	21	23	24	34			
130							36			
150							36			
170							37			
190							36			
210							43			
230							34			
250							31			
270							35			
290							30			
310							31			
330							31			
350				23	23	28	32			

Table B.26: Voyager 2 Cruise Maneuver: 1980 Day 24

Voyager 2		1980 Day 24					R = 6.2 AU			
Long. = 157.5°		Lat. = 1.6°					Flux = 3.57(11) cm ⁻² s ⁻¹			
Θ	10	30	50	70	90	110	130	150	170	
Ψ										
10				1201	1401	1650	1935	2415		
30				1178	1358	1552	2018	2369		
50				1100	1305	1475	1815	2163		
70				1073	1247	1420	1615	2013		
90				1019	1163	1305	1571	1768		
110				1035	999	1208	1334	1624		
130				970	1036	1095	1296	1421		
150				932	940	989	1097	1281		
170				862	878	825	908	1107		
190				842	801	802	874	1092		
210				919	873	901	937	1153		
230				917	985	978	1105	1280		
250				969	1030	1160	1263	1519		
270				1077	1063	1296	1404	1733		
290				1026	1084	1356	1521	1865		
310				1118	1312	1475	1598	2081		
330				1098	1350	1612	1929	2248		
350				1202	1405	1590	2034	2401		
10				73	71	69	86	52		
30				71	76	70	94	49		
50				67	76	68	89	49		
70				58	73	68	82	48		
90				56	72	64	80	45		
110				58	64	62	79	43		
130				55	67	58	73	40		
150				54	64	55	70	38		
170				52	61	51	62	36		
190				52	60	51	60	35		
210				58	60	53	66	36		
230				53	66	55	67	38		
250				55	67	61	75	41		
270				59	67	64	77	44		
290				57	69	64	80	46		
310				60	76	69	84	49		
330				58	77	69	89	51		
350				62	78	73	94	52		

Table B.27: Voyager 2 Cruise Maneuver: 1980 Day 136

Voyager 2		1980 Day 136				R = 6.7 AU			
Long. = 166.5°		Lat. = 1.9°				Flux = 3.88(11) cm ⁻² s ⁻¹			
Θ	10 30	50	70	90	110	130	150	170	
Ψ									
10			1295	1393	1662	1948	2307		
30			1221	1308	1549	1888	2238		
50			1176	1236	1436	1767	2078		
70			1095	1258	1386	1523	1824		
90			1072	1105	1252	1469	1626		
110			1116	1149	1266	1384	1548		
130			1096	1137	1241	1285	1386		
150			1120	1048	1131	1105	1296		
170			997	1001	950	979	1071		
190			1087	990	868	862	1055		
210			1085	983	1048	1013	1099		
230			1158	1082	1200	1289	1282		
250			1138	1177	1236	1408	1457		
270			1209	1170	1345	1620	1673		
290			1182	1288	1457	1772	1874		
310			1304	1281	1527	1760	2108		
330			1299	1327	1583	1968	2168		
350			1226	1477	1603	2004	2374		
10			52	56	57	69	78		
30			51	57	56	66	75		
50			48	56	54	66	72		
70			67	56	54	62	67		
90			61	53	51	61	64		
110			61	55	52	58	62		
130			61	53	51	58	59		
150			61	53	48	52	57		
170			58	50	45	50	52		
190			61	51	43	47	52		
210			62	54	47	50	52		
230			71	50	50	58	57		
250			63	54	50	59	61		
270			67	54	53	65	65		
290			64	57	55	67	69		
310			68	57	56	66	73		
330			68	59	57	71	82		
350			65	62	58	71	85		

Table B.28: Voyager 2 Cruise Maneuver: 1980 Day 192

Voyager 2		1980 Day 192				R = 7.0 AU			
Long. = 170.5°		Lat. = 2.0°				Flux = 3.95(11) cm ⁻² s ⁻¹			
Θ	10	30	50	70	90	110	130	150	170
Ψ									
10		1110						2345	
30		1056						2170	
50		1049						1967	
70		1040						1806	
90		1027	1061				1327	1611	
110			1073	1095	1091	1163	1340	1491	
130								1278	
150								1148	
170								1080	
190								1058	
210								1025	
230								1141	
250								1480	
270								1602	
290								1711	
310								2014	
330				1313	1427	1758		2160	
350		1069	1143	1260		1959	2141	2257	
10		64						57	
30		58						45	
50		59						44	
70		63						50	
90		56	52				58	59	
110			41	39	39	40	46	48	
130								44	
150								43	
170								40	
190								41	
210								40	
230								42	
250								49	
270								49	
290								51	
310								58	
330				47	46	52		61	
350		43	49	97		108	66	60	

Table B.29: Voyager 2 Cruise Maneuver: 1980 Day 351

Voyager 2		1980 Day 351					R = 8.0 AU			
Long. = 179.9°		Lat. = 2.2°					Flux = 3.89(11) cm ⁻² s ⁻¹			
Θ	10	30	50	70	90	110	130	150	170	
Ψ										
10		828	996				2225	2034		
30		935						2132		
50		796						1880		
70		831						1741		
90		714	887	954		1178	1340	1747		
110				1030	1013	1248				
130										
150										
170										
190										
210										
230										
250										
270										
290										
310										
330										
350			963	1099	1224	1421	1860			
10		41	87				182	63		
30		51						94		
50		60						82		
70		41						53		
90		104	44	51		58	51	161		
110				39	37	52				
130										
150										
170										
190										
210										
230										
250										
270										
290										
310										
330										
350			45	38	41	44	61			

Table B.30: Voyager 2 Cruise Maneuver: 1981 Day 77

Voyager 2		1981 Day 77					R = 8.6 AU			
Long. = 184.5°		Lat. = 2.3°					Flux = 3.70(11) cm ⁻² s ⁻¹			
Θ	10	30	50	70	90	110	130	150	170	
Ψ										
10		791						2030		
30		673						1956		
50		749						1925		
70		739						1699		
90		730	733				1191	1421		
110			781	873	905	979	969	1504		
130								1327		
150								1138		
170								927		
190								980		
210								969		
230								1060		
250								1200		
270								1369		
290								1574		
310								1760		
330				880	1031	1128		1891		
350		805	824	962		1367	1628	2058		
10		54						64		
30		45						44		
50		49						43		
70		41						47		
90		38	41				52	49		
110			77	35	38	37	85	49		
130								45		
150								42		
170								38		
190								39		
210								40		
230								40		
250								43		
270								46		
290								49		
310								52		
330				41	42	46		55		
350		43	41	57		61	56	62		

Table B.31: Voyager 2 Cruise Maneuver: 1981 Day 148

Voyager 2		1981 Day 148				R = 9.0 AU			
Long. = 187.5°		Lat. = 2.4°				Flux = 3.46(11) cm ⁻² s ⁻¹			
Θ	10	30	50	70	90	110	130	150	170
Ψ									
10				908	1039	1219	1423	1855	
30				885	983	1138	1404	1763	
50				855	903	1073	1359	1706	
70				892	927	1000	1244	1492	
90				756	891	981	1106	1388	
110				810	785	957	1111	1227	
130				761	847	956	1054	1184	
150				766	860	873	915	998	
170				759	855	828	862	901	
190				769	800	820	783	789	
210				713	818	870	854	838	
230				769	781	850	941	992	
250				727	797	864	1009	1110	
270				773	781	933	1079	1334	
290				817	817	974	1220	1372	
310				835	948	1050	1302	1562	
330				936	1014	1201	1401	1712	
350				952	1040	1192	1444	1838	
10				43	48	57	52	71	
30				43	51	54	51	64	
50				41	50	54	54	64	
70				45	48	51	52	60	
90				42	48	51	48	59	
110				42	44	48	48	59	
130				39	47	50	47	54	
150				42	47	48	46	49	
170				50	47	46	42	48	
190				53	45	45	42	47	
210				50	47	55	43	46	
230				53	46	47	44	49	
250				53	46	47	46	54	
270				52	44	48	49	62	
290				53	47	50	51	60	
310				55	50	52	52	67	
330				49	53	55	55	66	
350				57	51	55	55	69	

Table B.32: Voyager 2 Cruise Maneuver: 1981 Day 302

Voyager 2		1981 Day 302					R = 9.6 AU			
Long. = 195.6°		Lat. = 2.3°					Flux = 4.02(11) cm ⁻² s ⁻¹			
Θ	10	30	50	70	90	110	130	150	170	
Ψ										
10	906									
30	865 968 1049									
50	835 891 1020									
70	867 870									
90	800									
110	726									
130	820									
150	797									
170	783									
190	749									
210	761									
230	732									
250	799									
270	820									
290	837									
310	899									
330	854									
350	935									
10	38									
30	26 22 34									
50	26 34 30									
70	37 28									
90	36									
110	33									
130	37									
150	35									
170	35									
190	35									
210	35									
230	38									
250	35									
270	40									
290	38									
310	38									
330	37									
350	43									

Table B.33: Voyager 2 Cruise Maneuver: 1982 Day 293

Voyager 2		1982 Day 293					R = 10.6 AU			
Long. = 218.3°		Lat. = 1.7°					Flux = 3.64(11) cm ⁻² s ⁻¹			
Θ	10	30	50	70	90	110	130	150	170	
Ψ										
10		637	651				1243	1316		
30		658						1240		
50		673						1223		
70		659	642				1055	1206		
90			637	676	698	826	999			
110										
130										
150										
170										
190										
210										
230										
250										
270										
290										
310										
330										
350			675	713	818	989	1070			
10		57	42				64	81		
30		37						55		
50		38						55		
70		41	40				52	55		
90			34	29	30	32	43			
110										
130										
150										
170										
190										
210										
230										
250										
270										
290										
310										
330										
350			32	30	34	41	42			

Table B.34: Voyager 2 Cruise Maneuver: 1983 Day 132

Voyager 2		1983 Day 132					R = 11.7 AU			
Long. = 229.0°		Lat. = 1.3°					Flux = 3.32(11) cm ⁻² s ⁻¹			
Θ	10	30	50	70	90	110	130	150	170	
Ψ										
10			496				897	976		
30		510					850	993		
50		503					833	1008		
70		466	445				801	851		
90			497	535	540	714	787			
110							867			
130							822			
150							744			
170							898			
190							800			
210							862			
230							794			
250							804			
270							833			
290							864			
310							860			
330							877			
350			476	562	655	718	933			
10			31				38	171		
30		31					37	45		
50		33					35	47		
70		36	33				40	61		
90			40	27	27	29	34			
110							37			
130							36			
150							34			
170							41			
190							35			
210							38			
230							37			
250							35			
270							37			
290							37			
310							37			
330							37			
350			30	26	29	29	33			

Table B.35: Voyager 2 Cruise Maneuver: 1983 Day 313

Voyager 2		1983 Day 313					R = 12.8 AU			
Long. = 236.8°		Lat. = 0.9°					Flux = 2.87(11) cm ⁻² s ⁻¹			
Θ	10	30	50	70	90	110	130	150	170	
Ψ										
10		430	435				681	835		
30		404						887		
50		391						831		
70		394	498				709	833		
90			400	385		609	659	898		
110				489	455	478		880		
130								773		
150								804		
170								790		
190								810		
210								752		
230								813		
250								796		
270								844		
290								790		
310								845		
330								907		
350			455	473	487	536	667	868		
10		30	35				49	34		
30		31						30		
50		31						28		
70		30	51				46	29		
90			30	26		30	37	38		
110				37	25	50		37		
130								36		
150								36		
170								38		
190								36		
210								35		
230								40		
250								36		
270								37		
290								36		
310								36		
330								37		
350			37	32	26	36	29	37		

Table B.36: Voyager 2 Cruise Maneuver: 1984 Day 145

Voyager 2		1984 Day 145					R = 14.2 AU			
Long. = 243.7°		Lat. = 0.7°					Flux = 3.23(11) cm ⁻² s ⁻¹			
Θ	10	30	50	70	90	110	130	150	170	
Ψ										
10			417				741	959		
30		415	466				795	951		
50		407						935		
70		405	373				682	869		
90			422	441	514	542	596	1001		
110								889		
130								973		
150								947		
170								913		
190								861		
210								827		
230								914		
250								927		
270								842		
290								920		
310								978		
330								985		
350			349	449	530	604	752	908		
10			28				36	38		
30		32	43				63	43		
50		29						41		
70		34	32				43	40		
90			32	23	26	26	39	41		
110								37		
130								40		
150								38		
170								43		
190								56		
210								42		
230								57		
250								42		
270								38		
290								38		
310								40		
330								43		
350			53	24	26	28	76	38		

Table B.38: Voyager 2 Cruise Maneuver: 1985 Day 150

Voyager 2		1985 Day 150					R = 17.1 AU			
Long. = 253.5°		Lat. = 0.2°					Flux = 2.59(11) cm ⁻² s ⁻¹			
Θ	10	30	50	70	90	110	130	150	170	
Ψ										
10	290									
30	288 317 363									
50	300 379									
70	278 337 385									
90	262									
110	265									
130	243									
150	298									
170	269									
190	273									
210	265									
230	294									
250	304									
270	281									
290	264									
310	301									
330	236									
350	312									
10	24									
30	18 14 20									
50	12 16									
70	17 21 22									
90	21									
110	22									
130	20									
150	23									
170	21									
190	21									
210	21									
230	22									
250	23									
270	22									
290	21									
310	22									
330	20									
350	24									

Table B.39: Voyager 2 Cruise Maneuver: 1986 Day 113

Voyager 2		1986 Day 113				R = 19.8 AU			
Long. = 260.5°		Lat. = 0.0°				Flux = 2.58(11) cm ⁻² s ⁻¹			
Θ	10	30	50	70	90	110	130	150	170
Ψ									
10		233		298	293	352	400	549	
30		203	251		225	369	388	512	
50		256	262		287	332	438	556	
70		228	216	262		361	436	648	
90		230		198	276	287	479	573	
110		309		178	288	357	404	542	
130		233		222	291	343	460	686	
150		222		298	284	340	475	635	
170		211		305	365	314	470	562	
190		244		300	296	361	398	600	
210		274		238	345	374	420	641	
230		258		311	287	412	370	530	
250				295	239	280	474	596	
270				242	281	310	477	613	
290				132	314	344	403	604	
310		237		212	254	385	422	543	
330		334		251	263	346	442	590	
350		294		370	297	396	396	507	
10		39		54	43	53	53	60	
30		35	50		40	52	51	58	
50		41	44		45	48	54	76	
70		38	46	43		54	53	65	
90		31		39	8	56	58	61	
110		46		35	43	49	50	73	
130		40		39	45	47	54	63	
150		41		45	43	46	54	62	
170		39		45	50	46	54	57	
190		43		44	43	48	50	59	
210		47		41	48	49	51	62	
230		46		46	43	52	49	57	
250				45	44	42	63	60	
270				41	42	46	60	80	
290				30	46	47	53	62	
310		58		39	42	51	53	63	
330		48		40	41	48	54	63	
350		42		62	45	56	53	63	

Table B.40: Voyager 2 Cruise Maneuver: 1986 Day 273

Voyager 2		1986 Day 273					R = 21.0 AU			
Long. = 264.3°		Lat. = 0.2°					Flux = 2.51(11) cm ⁻² s ⁻¹			
Θ	10	30	50	70	90	110	130	150	170	
Ψ										
10						278				
30						276				
50						283				
70						235	263	277		
90						231	253	285		
110							267			
130							285			
150							269			
170							281			
190							266			
210							262			
230							311			
250							271			
270						248	197			
290						270				
310						287				
330						236				
350						269				
10						20				
30						19				
50						24				
70						13	11	15		
90						11	11	12		
110							21			
130							22			
150							21			
170							22			
190							22			
210							21			
230							27			
250							21			
270						22	41			
290						21				
310						22				
330						20				
350						21				

Table B.41: Voyager 2 Cruise Maneuver: 1986 Day 339

Voyager 2			1986 Day 339			R = 21.5 AU			
Long. = 265.7°			Lat. = 0.3°			Flux = 2.56(11) cm ⁻² s ⁻¹			
Θ	10	30	50	70	90	110	130	150	170
Ψ									
10			234	260	240	318	317		
30			219				404		
50			203				437		
70			226				331		
90			247	218	258	288	333		
110			221						
130			260						
150			239						
170			192						
190			214						
210			257						
230			224						
250			260						
270			196						
290			232						
310			242						
330			256						
350			237						
10			21	21	17	24	24		
30			17				30		
50			14				26		
70			16				27		
90			21	19	18	23	24		
110			19						
130			21						
150			20						
170			18						
190			20						
210			21						
230			19						
250			21						
270			18						
290			20						
310			22						
330			21						
350			20						

Table B.42: Voyager 2 Cruise Maneuver: 1987 Day 42

Voyager 2		1987 Day 42				R = 22.1 AU			
Long. = 267.1°		Lat. = 0.3°				Flux = 2.61(11) cm ⁻² s ⁻¹			
Θ	10 30	50	70	90	110	130	150	170	
Ψ									
10		186	253	251	319	328			
30		224	180			361			
50		206	258			424			
70		184	239			405			
90		217	235	253	317	368			
110			264						
130			257						
150			238						
170			224						
190			223						
210			243						
230			305						
250			239						
270			227						
290			246						
310			211						
330			227						
350			272						
10		20	20	17	23	21			
30		18	17			27			
50		19	22			27			
70		20	21			32			
90		18	16	17	24	19			
110			23						
130			21						
150			20						
170			23						
190			20						
210			21						
230			24						
250			21						
270			19						
290			27						
310			19						
330			19						
350			21						

Table B.44: Voyager 2 Cruise Maneuver: 1987 Day 280

Voyager 2			1987 Day 280			R = 24.0 AU			
Long. = 271.5°			Lat. = 0.5°			Flux = 2.87(11) cm ⁻² s ⁻¹			
Θ	10	30	50	70	90	110	130	150	170
Ψ									
10						272			
30						254			
50						295			
70						266			
90						321			
110						295			
130						314			
150						301			
170						274			
190						453			
210									
230						288			
250						393			
270						222			
290						245			
310						316			
330						259			
350						254			
10						23			
30						25			
50						24			
70						22			
90						23			
110						23			
130						25			
150						26			
170						35			
190						119			
210									
230						61			
250						64			
270						43			
290						48			
310						58			
330						29			
350						23			

Table B.45: Voyager 2 Cruise Maneuver: 1988 Day 15

Voyager 2		1988 Day 15					R = 24.9 AU			
Long. = 273.1°		Lat. = 0.6°					Flux = 2.89(11) cm ⁻² s ⁻¹			
Θ	10	30	50	70	90	110	130	150	170	
Ψ										
10	248									
30	242 260 287									
50	241 310									
70	257 258 290									
90	250									
110	261									
130	260									
150	261									
170	245									
190	256									
210	266									
230	239									
250	281									
270	271									
290	241									
310	214									
330	279									
350	247									
10	20									
30	16 19 21									
50	15 15									
70	17 13 18									
90	21									
110	21									
130	21									
150	22									
170	20									
190	21									
210	21									
230	21									
250	25									
270	22									
290	20									
310	20									
330	22									
350	21									

Table B.46: Voyager 2 Cruise Maneuver: 1988 Day 88

Voyager 2		1988 Day 88				R = 25.5 AU			
Long. = 274.3°		Lat. = 0.6°				Flux = 2.95(11) cm ⁻² s ⁻¹			
Θ	10	30	50	70	90	110	130	150	170
Ψ									
10				211	268	206			
30			234	236	268	295	369		
50			232		263		383		
70			227	248	287	331	383		
90				265	267	276			
110					265				
130					294				
150					274				
170					295				
190					288				
210					271				
230					262				
250					321				
270					248				
290					267				
310					284				
330					283				
350					290				
10				30	16	21			
30			23	17	22	24	19		
50			17		21		22		
70			15	14	22	23	23		
90				21	16	17			
110					21				
130					23				
150					21				
170					23				
190					22				
210					21				
230					22				
250					24				
270					21				
290					21				
310					22				
330					22				
350					22				

Table B.48: Voyager 2 Cruise Maneuver: 1988 Day 300

Voyager 2		1988 Day 300					R = 27.4 AU			
Long. = 277.2°		Lat. = 0.8°					Flux = 3.37(11) cm ⁻² s ⁻¹			
Θ	10	30	50	70	90	110	130	150	170	
Ψ										
10	295									
30	314									
50	297									
70	299									
90	323									
110	300									
130	340									
150	372									
170	313									
190	372									
210	332									
230	331									
250	369									
270	322									
290	317									
310	338									
330	316									
350	343									
10	23									
30	24									
50	7									
70	22									
90	23									
110	22									
130	24									
150	25									
170	22									
190	26									
210	23									
230	24									
250	26									
270	24									
290	22									
310	24									
330	23									
350	24									

Table B.50: Voyager 2 Cruise Maneuver: 1990 Day 143

Voyager 2		1990 Day 143				R = 32.0 AU			
Long. = 281.4°		Lat. = -2.5°				Flux = 3.80(11) cm ⁻² s ⁻¹			
Θ	10	30	50	70	90	110	130	150	170
Ψ									
10		232	246				592	523	
30		202						592	
50		239						632	
70		236						635	
90		276						716	
110		270	266	289		313	468	565	
130				371	321	306			
150									
170									
190									
210									
230									
250									
270									
290									
310									
330									
350			234	275	302	316	365		
10		27	30				135	40	
30		26						42	
50		29						48	
70		29						48	
90		26						50	
110		27	24	24		29	32	33	
130				38	22	25			
150									
170									
190									
210									
230									
250									
270									
290									
310									
330									
350			22	20	21	28	24		

REFERENCES

- Ajello, J. M., Stewart, A. I., Thomas, G. E., and Graps A. (1987) Solar cycle study of interplanetary Lyman-alpha variations: Pioneer Venus orbiter sky background results. *Astrophys. Jour.* **317**, 964.
- Ajello, J. M. (1990) Solar minimum Lyman α sky background observations from Pioneer Venus orbiter ultraviolet spectrometer: solar wind latitude variation. *Jour. Geophys. Res.* **95**, 14,855.
- Axford, W. I., Dessler, A. J., and Gottlieb, B. (1963) Termination of solar wind and solar magnetic field. *Astrophys. Jour.* **137**, 1268.
- Axford, W. I. (1972) "The interaction of the solar wind with the interstellar medium" in *Solar Wind*, C. P. Sonett, P. J. Coleman, and J. M. Wilcox, eds. (NASA SP-308), pp. 609.
- Baranov, V. B., Lebedev, M. G., and Ruderman, M. S. (1979) Structure of the region of solar wind—interstellar medium interaction and its influence on the H atoms penetrating the solar wind. *Astrophys. & Spa. Sci.* **66**, 441.
- Baranov, V. B. (1990) Gasdynamics of the solar wind interaction with the interstellar medium. *Spa. Sci. Rev.* **52**, 89.
- Baranov, V. B., Lebedev, M. G., and Malama, Y. G. (1991) The influence of the interface between the heliosphere and the local interstellar medium on the penetration of the H atoms to the solar system. *Astrophys. Jour.* **375**, 347.
- Barth C. A., Tobiska, W. K., Rottman, G. J., and White, O. R. (1990) Comparison of 10.7 cm radio flux with SME solar Lyman alpha flux. *Geophys. Res. Letters* **17**, 571.
- Bertaux, J. L. and Blamont, J. E. (1971) Evidence for a source of an extraterrestrial hydrogen Lyman-alpha emission: the interstellar wind. *Astron. Astrophys.* **11**, 200.
- Bertaux, J. L. (1984) "Helium and hydrogen of the interstellar medium in the vicinity of the Sun" in *Local Interstellar Medium*, Y Kondo, F. C. Bruhweiler, and B. D. Savage, eds. (NASA SP-2345), pp. 3.
- Bleszynski, S. (1987) Filtering of the local interstellar medium at the heliopause. *Astron. Astrophys.* **180**, 201.

- Blum, P. W. and Fahr, H. J. (1970) Interaction between interstellar hydrogen and the solar wind. *Astron. Astrophys.* **4**, 280.
- Blum, P., Gangopadhyay, P., Ogawa, H. S., and Judge, D. L. (1992) Solar driven neutral density waves. In preparation.
- Brandt, J. C. and Chamberlain, J. W. (1959) Interplanetary gas. I. Hydrogen radiation in the night sky. *Astrophys. Jour.* **130**, 670.
- Broadfoot, A. L. and Sandel, B. R. (1977) Self-scanned anode array with a microchannel plate electron multiplier: the SSANACON. *Applied Optics* **16**, 1533.
- Broadfoot, A. L., Sandel, B. R., Shemasnky, D. E., Atreya, S. K., Donahue T. M., Moos, H. W., Bertaux, J. L., Blamont, J. E., Ajello, J. M., Strobel, D. F., McConnel, J. C., Dalgarno, A., Goody R., McElroy M. B., and Yung, Y. L. (1977) Ultraviolet spectrometer experiment for the Voyager mission. *Spa. Sci. Rev.* **21**, 183.
- Broadfoot, A. L., Sandel, B. R., Shemansky, D. E., McConnel, J. C., Smith, G. R., Holberg, J. B., Atreya, S. K., Donahue, T. M., Strobel, D. F., and Bertaux, J. L. (1981) Overview of the Voyager Ultraviolet Spectrometry results through Jupiter encounter. *Jour. Geophys. Res.* **86**, 8259.
- Carlson, R. W. and Judge, D. L. (1974) Pioneer 10 Ultraviolet Photometer observations at Jupiter encounter. *Jour. Geophys. Res.* **79**, 3623.
- Chamberlain, J. W. (1961) "Physics of the Aurora and Airglow," Academic Press: New York.
- Chamberlain, J. W. and Huntem, D. M. (1987) "Theory of Planetary Atmospheres," Academic Press: San Diego.
- Chandrasekhar, S. (1960) "Radiative Transfer," Dover Publications: New York.
- Clarke, J. T. (1982) Detection of auroral hydrogen Lyman-alpha emission from Uranus. *Astrophys. Jour.* **263**, L105.
- Cook, J. W., Meier, R. R., Bruecknew, G. E., and Van Hoosier, M. E. (1981) Latitudinal anisotropy of the solar far ultraviolet flux: effect on the Ly α sky background. *Astron. Astrophys.* **97**, 394.
- Cooper, J., Ballagh, R. J., and Hubeny, J. (1989) Approximate formulation of redistribution in the Ly α , Ly β and H α system. *Astrophys. Jour.* **344**, 949.

- Cox, D. P. and Anderson, P. R (1982) Extended adiabatic blast waves and a model of the soft x-ray background. *Astrophys. Jour.* **253**, 268.
- Cox, D. P. and Reynolds, R. J. (1987) The local interstellar medium. *Ann. Rev. Astron. Astrophys.* **25**, 303.
- Dalgarno, A. and Yadav, H. N. (1953) Electron capture II: resonance capture from hydrogen atoms by slow protons. *Proc. Phys. Soc* **66**, 173.
- Danby, J. M. A. and Camm, G. L. (1957) Statistical dynamics and accretion. *Mon. Not. Roy. Astron. Soc.* **117**, 50.
- Dessler, A. J. (1967) Solar wind and interplanetary magnetic field. *Rev. Geophys.* **5**, 1.
- Dessler, A. J., ed. (1983) "Physics of the Jovian Magnetosphere," Cambridge University Press: Cambridge.
- Dickey, J. M. and Lockman, F. L. (1990) HI in the Galaxy. *Ann. Rev. Astron. Astrophys.* **28**, 215.
- Donnelly, R. F., Hinteregger, H. E., and Heath, D. F. (1986) Temporal variations of solar EUV, UV and 10,830-Å radiations. *Jour. Geophys. Res.* **91**, 5567.
- Fahr, H. J. (1968) Neutral corpuscular energy flux by charge-transfer collisions in the vicinity of the Sun. *Astrophys. & Spa. Sci.* **2**, 496.
- Fahr, H. J. (1971) The interplanetary hydrogen cone and its solar cycle variations. *Astron. Astrophys.* **14**, 263.
- Fahr, H. J. (1974) The extraterrestrial UV-background and the nearby interstellar medium. *Spa. Sci. Rev.* **15**, 483.
- Fahr, H. J. and Shizgal, B. (1983) Modern exospheric theories and their observational relevance. *Rev. Geophys. Space Phys.* **21**, 75.
- Fahr, H. J. and Neutsch, W. (1983a) Stationary plasma-field equilibrium states in astropause boundary layers—I. general theory. *Mon. Not. Roy. Astron. Soc.* **205**, 839.
- Fahr, H. J. and Neutsch, W. (1983b) Pressure distribution at the inner boundary of an astropause caused by a compressible stellar wind. *Astron. Astrophys.* **118**, 57.

- Fahr, H. S. and Ripken, H. W. (1984) The physics of the heliospheric interface and its implications for LISM diagnostics. *Astron. Astrophys.* **139**, 551.
- Fahr, H. S., Nass, H. U., and Rucinski, D. (1985) Drag-like effects on heliospheric neutrals due to elastic collisions with solar wind ions. *Astron. Astrophys.* **142**, 476.
- Fahr, H. J., Neutsch, W., Grzedzielski, S., Macek, W., and Ratkiewicz-Landowska, R. (1986a) Plasma transport across the heliopause. *Spa. Sci. Rev.* **43**, 329.
- Fahr, H. J., Ratkiewicz, R., and Grzedzielski, S. (1986b) The heliopause as a pressure equilibrium surface separating two counterflowing magnetized plasmas. *Adv. Space Res.* **6**, 389.
- Fahr, H. S. and Scherer, K. (1990) Heliospheric neutral gases in three-dimensional and time-dependent solar force and ionization fields. *Astron. Astrophys.* **232**, 556.
- Fahr, H. J. (1990) "Filtration of the interstellar neutrals at the heliospheric interface and their coupling to the solar wind" in *Physics of the Outer Heliosphere*, S. Grzedzielski and D. E. Page, eds. Pergamon: Oxford, pp. 327.
- Field, G. B., Goldsmith, D. W., and Habing, H. J. (1969) Cosmic-ray heating of the interstellar gas. *Astrophys. Jour.* **155**, L149.
- Frisch, P. C. (1986) The physical properties of the "Local Fluff". *Adv. Space Res.* **6**, 345.
- Frisch, P. C., York, D. G., and Fowler, J. R. (1987) The local interstellar medium. VII. The local interstellar wind and interstellar material in front of the nearby star α Ophiuchi. *Astrophys. Jour.* **320**, 842.
- Gangopadhyay, P. and Judge, D. L. (1989) The heliospheric neutral hydrogen density profile in the presence of a solar wind shock. *Astrophys. Jour.* **336**, 999.
- Gangopadhyay, P., Ogawa, H. S., and Judge, D. L. (1989) Evidence of a nearby solar wind shock as obtained from distant Pioneer 10 ultraviolet glow data. *Astrophys. Jour.* **336**, 1012.
- Goldsmith, D. W., Habing, H. J., and Field, G. B. (1969) Thermal properties of interstellar gas heated by cosmic rays. *Astrophys. Jour.* **158**, 173.
- Gruntman, M. A. (1990) Two-step photionization of hydrogen atoms in interplanetary space. *Planet. Space Sci.* **38**, 1225.

- Hall, C. F. (1975) Pioneer 10. *Science* **183**, 301.
- Henry, R. C (1991) Ultraviolet background radiation. *Ann. Rev. Astron. Astrophys.* **29**, 89.
- Herzberg, G. (1944) "Atomic Spectra and Atomic Structure," Dover Publications: New York.
- Holberg, J. B., Forrester, W. T., Shemansky, D. E., and Barry, D. C. (1982) Voyager absolute far-ultraviolet spectrophotometry of hot stars. *Astrophys. Jour.* **257**, 656.
- Holberg, J. B. (1986) Far-ultraviolet background observations at high galactic latitude, II, diffuse emission. *Astrophys. Jour.* **311**, 969.
- Holberg, J. B., Ali, B., Carone, T. E., and Polidan, R. S. (1991) Absolute far-ultraviolet spectrophotometry of hot subluminous stars from Voyager. *Astrophys. Jour.* **375**, 716.
- Holberg, J. B. and Watkins, R. (1992) "Voyager Ultraviolet Spectrometer Guest Observer and Data Analysis Handbook," Lunar and Planetary Laboratory: Tucson.
- Holzer, T. E. and Axford, W. I. (1971) Interaction between interstellar helium and the solar wind. *Jour. Geophys. Res.* **76**, 6965.
- Holzer, T. E. (1972) Interaction of the solar wind with the neutral component of the interstellar gas. *Jour. Geophys. Res.* **77**, 5407.
- Holzer, T. E. (1977) Neutral hydrogen in interplanetary space. *Rev. Geophys. Space Phys.* **15**, 467.
- Holzer, T. E. (1989) Interaction between the solar wind and the interstellar medium. *Ann. Rev. Astron. Astrophys.* **27**, 199.
- Hui, A. K., Armstrong, B. H., and Wray, A. A. (1978) Rapid calculation of the Voigt and complex error functions. *J. Quant. Radiat. Transfer* **19**, 509.
- Hummer, D. G. (1962) Non-coherent scattering I. The redistribution functions with Doppler broadening. *Mon. Not. Roy. Astron. Soc.* **125**, 21.
- Hundhausen, A. J. (1970) Composition and dynamics of solar wind plasma. *Rev. Geophys. Space Phys.* **8**, 729.

- Hundhausen, A. J. (1972) "Coronal Expansion and Solar Wind," Springer-Verlag: Berlin.
- Hundhausen, A. J. (1979) Solar activity and the solar wind. *Rev. Geophys. Space Phys.* **17**, 2034.
- Ivanov, V. V. (1973) "Transfer of Radiation in Spectral Lines," National Bureau of Standards Special Publication 388, Vols. 1 and 2: U. S. Government Printing Office, Washington D.C.
- Johnson, H. E. (1972) Backscatter of solar resonance radiation-I. *Planet. Space Sci.* **20**, 829.
- Judge, D. L. and Carlson, R. W. (1974) Pioneer 10 observations of the ultraviolet glow in the vicinity of Jupiter. *Science* **183**, 317.
- Keller, H. U. and Thomas, G. E. (1979) Multiple scattering of solar resonance radiation in the nearby interstellar medium. I. *Astron. Astrophys.* **80**, 227.
- Keller, H. U., Richter, K., and Thomas, G. E. (1981) Multiple scattering of solar resonance radiation in the nearby interstellar medium. II. *Astron. Astrophys.* **102**, 415.
- Kohlhase, C., ed. (1989) "The Voyager Neptune Travel Guide," NASA JPL Publication 89-24.
- Lallement, R. (1990) "Scattering of solar UV on local neutral gases" in *Physics of the Outer Heliosphere*, S. Grzedzielski and D. E. Page, eds. Pergamon: Oxford, pp. 49.
- Lallement, R., Bertaux, J. L., Chassefiere, E., and Sandel, B. R. (1990) "Lyman-alpha observations from Voyager (1-18 AU)" in *Physics of the Outer Heliosphere*, S. Grzedzielski and D. E. Page, eds. Pergamon: Oxford, pp. 73.
- Lean, J. (1987) Solar ultraviolet irradiance variations: a review. *Jour. Geophys. Res.* **92**, 839.
- Lean, J. (1990) A comparison of models of the Sun's extreme ultraviolet irradiance variations. *Jour. Geophys. Res.* **95**, 11933.
- Lemaire, P., Charra, J., Jouchoux, A., Vidal-Madjar A., Artzner, G. E., Vial, J. C., Bonnet, R. M., and Skumanich, A. (1978) Calibrated full disk solar HI Lyman- α and Lyman- β profiles. *Astrophys. Jour.* **223**, L55.

- Maher, L. J. and Tinsley, B. A. (1977) Atomic hydrogen escape rate due to charge exchange with hot plasmaspheric ions. *Jour. Geophys. Res.* **82**, 689.
- Marsden, R. G., ed. (1986) "The Sun and the Heliosphere in Three Dimensions," D. Reidel Publishing Company: Dodrecht, Holland.
- McClintock, W., Henry, R. C., Linsky, J. L., and Moos, H. W. (1978) Ultraviolet observations of cool stars. VII. Local interstellar hydrogen and deuterium Lyman-alpha. *Astrophys. Jour.* **225**, 465.
- McCray, R. and Snow, T. P., Jr. (1979) The violent interstellar medium. *Ann. Rev. Astron. Astrophys.* **17**, 213.
- McKee, C. F. and Ostriker, J. P. (1977) A theory of the interstellar medium: three components regulated by supernova explosions in an inhomogeneous substrate. *Astrophys. Jour.* **218**, 148.
- McGrath, M. A. and Clarke, J. T. (1992) HI Ly α emission from Saturn *Jour. Geophys. Res.*, in press.
- Meier, R. R. (1977) Some optical and kinetic properties of the nearby interstellar gas. *Astron. Astrophys.* **55**, 211.
- Mihalas, D. (1978) "Stellar Atmospheres," W. H. Freeman and Company: New York.
- Mitchell, A. C. G. and Zemansky, M. W. (1934) "Resonance Radiation and Excited Atoms," Cambridge University Press: London.
- Neutsch, W. and Fahr, H. J. (1983) The magnetic and fluid environment of an ellipsoidal circumstellar plasma cavity. *Mon. Not. Roy. Astron. Soc.* **202**, 735.
- Osterbrock, D. E. (1989) "Astrophysics of Gaseous Nebula and Active Galactic Nuclei," University Science Books: Mill Valley, California.
- Parker, E. N. (1961) The stellar-wind regions. *Astrophys. Jour.* **134**, 20.
- Parker, E. N. (1963) "Interplanetary dynamical processes," Interscience Publishers: New York.
- Paresce, F. (1984) On the distribution of interstellar matter around the Sun. *Astron. Jour.* **89**, 1022.
- Patterson, T. N. L., Johnson, F. S., and Hanson, W. B. (1963) The distribution of interplanetary hydrogen. *Planet. Space Sci.* **11**, 767.

- Pizzo, V. J., Holzer, T. M., and Sime, D. G, eds. (1987) "Proceedings of the Sixth International Solar Wind Conference," NCAR/TN-306+Proc, Vol. 1 and 2.
- Press, W. H., Flannery, B. P., Teukolsky, S. A., and Vetterling, W. T. (1986) "Numerical Recipes," Cambridge University Press: Cambridge.
- Pryor, W. R., Ajello, J. M., Barth, C. A., Hord, C. W., Stewart, A. I. F., Simmons, K. E., McClintock, W. E., Sandel, B. R., and Shemansky, D. E (1992) The Galileo and Pioneer Venus Ultraviolet spectrometer experiments: solar Lyman- α latitude variation at solar maximum from interplanetary Lyman- α observations. *Astrophys. Jour.* **394**, 363.
- Ripken, H. W. and Fahr, H. J. (1983) Modification of the local interstellar gas properties in the heliospheric interface. *Astron. Astrophys.* **122**, 181.
- Rottman, G. J., Barth, C. A., Thomas, R. J., Mount, G. H., Lawrence, G. M., Rusch, D. W., Snaders, R. W., Thomas, G. E., and London, J. (1982) Solar spectral irradiance, 120 to 190 nm, October 13, 1981–January 3, 1982. *Geophys. Res. Letters* **9**, 587.
- Rybicki, G. B. and Lightman, A. P. (1979) "Radiative Processes in Astrophysics," John Wiley and Sons: New York.
- Sandel, B. R., Broadfoot, A. L., and Shemansky, D. E. (1977) Microchannel plate life tests. *Applied Optics* **16**, 1435.
- Scherer, K. and Hahr, H. J. (1990) Fluctuations in the heliospheric hydrogen distribution induced by generalized and time-dependent interstellar boundary conditions. *Planet. Space Sci.* **38**, 1487.
- Shemansky, D. E. and Ajello, J. M. (1983) The Saturn spectrum in the EUV–electron excited hydrogen. *Jour. Geophys. Res.* **88**, 459.
- Shemansky, D. E., Judge, D. L., and Jesson, J. M. (1984) "Pioneer 10 and Voyager observations of the He 584 Å and H Ly α 1216 Å lines" in *Local Interstellar Medium*, Y Kondo, F. C. Bruhweiler, and B. D. Savage, eds. (NASA SP–2345), pp. 24.
- Shemansky, D. E. and Judge, D. L. (1988) Evidence for change in particle excitation of Jupiter's atmosphere 1968–1979. *Jour. Geophys. Res.* **93**, 21.

- Skinner, T. E., DeLand, M. T., Ballester, G. E., Coplin, K. A., Feldman, P. D., and Moos, H. W. (1988) Temporal variation of the Jovian HI Lyman alpha emission (1979–1986). *Jour. Geophys. Res.* **93**, 29.
- Smyth, W. H., Combi, M. R., and Stewart, A. I. F. (1991) Analysis of the Pioneer-Venus Lyman- α image of the hydrogen coma of comet P/Halley. *Science* **253**, 1008.
- Stone, E. C. (1983) The Voyager mission: encounters with Saturn. *Jour. Geophys. Res.* **88**, 8639.
- Suess, S. T., Hathaway, D. H., and Dessler, A. J. (1987) Asymmetry of the heliosphere. *Geophys. Res. Letters* **14**, 977.
- Suess, S. T. (1990) The heliopause. *Rev. Geophys.* **28**, 97.
- Suess, S. T. and Nerney, S. (1990) Flow downstream of the heliospheric terminal shock, 1, irrotational flow. *Jour. Geophys. Res.* **95**, 6403.
- Suess, S. T. and Nerney, S. (1991) Correction to “Flow downstream of the heliospheric terminal shock, 1, irrotational flow”. *Jour. Geophys. Res.* **96**, 1883.
- Spitzer, L., Jr. and Jenkins, E. B. (1975) Ultraviolet Studies of the interstellar gas. *Ann. Rev. Astron. Astrophys.* **13**, 133.
- Spitzer, L., Jr. (1990) Theories of the hot interstellar gas. *Ann. Rev. Astron. Astrophys.* **28**, 71.
- Thomas, G. E. and Krassa, R. F. (1971) OGO 5 measurements of the Lyman alpha sky background. *Astron. Astrophys.* **11**, 218.
- Thomas G. E. (1972) “Properties of nearby interstellar hydrogen deduced from Ly- α sky background measurements” in *Solar Wind*, C. P. Sonett, P. J. Coleman, and J. M. Wilcox, eds. (NASA SP-308), pp. 668.
- Thomas, G. E. (1975) Interplanetary gas of nonsolar origin. *Rev. Geophys. Space Phys.* **13**, 1063.
- Thomas, G. E. and Blamont, E. (1976) Galactic Lyman alpha emission in the solar vicinity. *Astron. Astrophys.* **51**, 283.
- Thomas, G. E. (1978) The interstellar wind and its influence on the interplanetary environment. *Ann. Rev. Earth Planet. Sci.* **6**, 173.

- Tidman, D. A. and Krall, N. A. (1971) "Shock Waves in Collisionless Plasmas," John Wiley and Sons: New York.
- Torr, M. R., Torr, D. G., Ong, R. A., and Hinteregger, H. E. (1979) Ionization frequencies for major thermospheric constituents as a function of solar cycle 21. *Geophys. Res. Letters* **6**, 771.
- Torr, M. R. and Torr, D. G. (1985) Ionization frequencies for solar cycle 21: revised. *Jour. Geophys. Res.* **90**, 6675.
- Tsurutani, B. T. and Stone, R. G., eds. (1985) "Collisionless Shocks in the Heliosphere: Reviews of Current Research," Geophysical Monograph 35, American Geophysical Union: Washington, D.C.
- Vidal-Madjar, A., Balamont, J. E., and Phissamay, B. (1973) Solar Lyman alpha changes and related hydrogen density distribution at the Earth's exobase (1969–1970). *Jour. Geophys. Res.* **78**, 1115.
- Vidal-Madjar, A. (1975) Evolution of the solar Lyman alpha flux during four consecutive years. *Solar Phys.* **40**, 69.
- Voyager Neptune/Interstellar Mission (1987) "Flight Science Office Science and Mission Systems Handbook," NASA JPL Publication PD 618–128.
- Wallace, L. and Yelle, R. V. (1989) Resonance line transfer calculations by doubling thin layers. II. The use of the R_{II} redistribution function. *Astrophys. Jour.* **346**, 489.
- Wallis, M. K. (1984) Interstellar medium ahead of the heliosphere. *Astron. Astrophys.* **130**, 200.
- Wiese, W. L., Smith M. W., and Glennon, B. M. (1966) "Atomic Transition Probabilities, Vol. I, Hydrogen Through Neon," National Standard Reference Data Series, National Bureau of Standards 4, U.S. Government Printing Office: Washington D.C.
- Wu, F. M. and Judge, D. L. (1979a) Temperature and flow velocity of the interplanetary gases along solar radii. *Astrophys. Jour.* **231**, 594.
- Wu, F. M. and Judge, D. L. (1979b) Modification of solar lines propagating through the interplanetary medium. *Jour. Geophys. Res.* **84**, 979.

- Wu, F. M., Suzuki, K., Carlson, R. W., and Judge, D. L. (1981) Pioneer 10 ultraviolet photometer observations of the interplanetary glow at heliocentric distances from 2 to 14 AU. *Astrophys. Jour.* **245**, 1145.
- Wu, F. M., Gangopadhyay, P., Ogawa, H. S., and Judge, D. L. (1988) The hydrogen density of the local interstellar medium and an upper limit to the galactic glow determined from Pioneer 10 ultraviolet photometer observations. *Astrophys. Jour.* **331**, 1004.
- Yelle, R. V., Sandel B. R., Shemansky, D. E., and Kumar, S. (1986) Altitude variation of EUV emissions and evidence for proton precipitation at low latitudes in the Saturnian atmosphere. *Jour. Geophys. Res.* **91**, 8756.
- Yelle, R. V., McConnel, J. C., Sandel B. R., and Broadfoot, A. L. (1987) The dependence of electroglow on the solar flux. *Jour. Geophys. Res.* **92**, 15110.
- Yelle, R. V. and Wallace, L. (1989) Resonance line transfer calculations by doubling thin layers. I. Comparison with other techniques. *Astrophys. Jour.* **346**, 481.
- Yu, G. (1974) The interstellar wake of the solar wind. *Astrophys. Jour.* **194**, 187.